Strategic Advances in 2D Materials: Low-Temperature Plasma-Enhanced Chemical Vapor Deposition Growth of Graphene and Complementary Insights into MoS_2

Thesis by

Chen-Hsuan Lu

In Partial Fulfillment of the Requirements for

the Degree of

Doctor of Philosophy

CALIFORNIA INSTITUTE OF TECHNOLOGY

Pasadena, California

2024

(Defensed 11/06/2023)

© 2024

Chen-Hsuan Lu
ORCID: 0000-0002-4802-1332

ACKNOWLEDGEMENTS

I would like to express my deepest gratitude to those who have supported me during this incredible journey. I am particularly thankful to my advisor, Prof. Nai-Chang Yeh, for welcoming me into her group at Caltech. Her guidance has been invaluable, shaping my research and helping me navigate academic challenges.

I am deeply indebted to Prof. George Rossman for being so generous in sharing his facilities and showing me around some fascinating experiments in Geology. His open-minded approach and willingness to cross disciplinary boundaries have greatly expanded my horizons, and his passion for geology has been both inspiring and educational.

I would like to acknowledge Prof. Joseph Falson, Prof. Katherine Faber, and Prof. Bill Goddard for serving as my thesis committee.

My collaborators at ITRI, including Dr. Chyi-Ming Leu, Dr. Tsong-Ming Lee, Dr. Cheng-Chung Lee, and all other colleagues, have been a constant source of research support. Their extensive knowledge and experiences have been crucial to my Ph.D. study.

I must also thank our current and past lab members, including Aki, Chun-I, Daniel, Duxing, Wei-Hsiang, Chien-Chang, Deepan, Chen-Chih, David, and Wei-Shiuan. Their collaborative spirit, innovative ideas, and continuous feedback have significantly contributed to this research.

Additionally, I want to acknowledge our lab administrator, Loly, not only for her efficiency in handling administrative paperwork but also for her personal advice and support. Her kindness and wisdom have made the procedural aspects of this research smooth and provided guidance during critical times.

My experience at Caltech has been enriched by our materials science cohort, Ben, Magel, Yuchun, and Zac. Their mutual encouragement and shared moments on the softball field have made the pursuit of knowledge rewarding. I also appreciate Jennifer, our materials

science manager, for organizing many enriching department events that have brought us all closer as a community.

I am grateful for my friends in the Association of Caltech Taiwanese (ACT), specifically my roommates Meng-Jhang Fong, Kuang-Ming Shang, and Wen Chao, for the mahjong time; Especially MJ, who has been my roommate since joining Caltech; and Po-Hsuan Lin, for the interesting Red Door lunch chats. These moments of relaxation have provided a welcome break from the rigors of academic life.

A special mention goes to Chang-Chen Lee and Meng-Hsiang Liu, for their continuous friendship and professional insights. Our shared experiences during our formative years in the lab have fostered a bond that transcends academia. Their willingness to provide career advice and share in the joys and struggles of our respective journeys has been both comforting and inspiring.

Finally, I wish to express my heartfelt gratitude to my parents and relatives for their unwavering love, support, and confidence in my potential, which have been the cornerstones of my academic and personal development. I should thank my cousin Tiffany Lin, who was willing to help me draw the complicated table of contents figure, a task I don't think I would have been able to complete at that level. I must especially acknowledge my aunt, Dr. Patricia Lee. Her extensive experience and significant achievements in both the scientific and industrial sectors have not only guided my professional journey but have also greatly enriched my personal growth. The invaluable advice, strategic insights, and industrial connections provided by Dr. Lee have been instrumental in shaping the trajectory of my research and its real-world applications. My profound indebtedness to her for her wisdom and her substantial contributions cannot be overstated, and I am immensely grateful for the pivotal role her mentorship has played in the progress of my work.

ABSTRACT

This thesis explores the intricate details of the plasma-enhanced chemical vapor deposition (PECVD) technique for growing graphene on various substrates at low temperatures. The research begins by finely optimizing the PECVD growth conditions to produce high-quality graphene on copper ink, which can potentially be used in a wide range of flexible electronics and Internet of Things (IoT) devices. The study also showcases that PECVD is an effective technique for growing graphene directly on electroplated copper over polyimide substrates, which greatly improves the resilience and environmental stability of copper circuits.

Furthermore, the research investigates the possibility of using PECVD to grow graphene on gold, which can be a game-changer in anti-corrosion applications and increase the longevity of gold electrode-based biosensors. The study also makes a significant breakthrough by growing nanocrystalline multilayer graphene on silver in a single step, which demonstrates exceptional oxidation resistance and opens new opportunities for hybrid graphene-silver plasmonic technologies.

Lastly, the thesis examines the potential and complexities of using electrodeposited (ED) copper foil as a graphene growth substrate, showing significant transformations in the properties of the ED copper foil post PECVD process. Towards the latter part of this work, attention is briefly shifted to explore the unique dipole ordering properties of monolayer molybdenum disulfide (MoS_2) single crystals, which are synthesized using high-temperature chemical vapor deposition (CVD) and are van der Waals materials like graphene. Although not the main focus, this inclusion offers valuable insights into contrasting attributes and functionalities of graphene and MoS_2, especially in areas like high-density data storage and non-volatile memories, and also compares the status of synthesis methods of these two types of van der Waals materials.

Alongside these investigations, the thesis also touches upon the prospects of both large-area PECVD graphene growth and interfacial graphene growth, identifying future paths for

research and innovation. This comprehensive study highlights the versatility of low-temperature PECVD for graphene synthesis and provides insights that may reshape research and applications in flexible electronics, biosensing, and beyond. The findings of this research therefore pave ways for researchers, technology developers, and businesses to explore realistic technological applications of graphene and two-dimensional materials in various industries.

PUBLISHED CONTENT AND CONTRIBUTIONS

Lu, C. H.; Leu, C. M.; Yeh, N. C. Single-Step Direct Growth of Graphene on Cu Ink toward Flexible Hybrid Electronic Applications by Plasma-Enhanced Chemical Vapor Deposition. ACS Applied Materials & Interfaces 2021, 13 (5), 6951-6959, DOI: 10.1021/acsami.0c22207.

C.-H. L. conceived the project idea, grew the PECVD graphene, performed AFM and Raman measurements, interpreted the data, and wrote the draft manuscript.

Lu, C.-H.; Leu, C.-M.; Yeh, N.-C. Polymer-Compatible Low-Temperature Plasma-Enhanced Chemical Vapor Deposition of Graphene on Electroplated Cu for Flexible Hybrid Electronics. ACS Applied Materials & Interfaces 2021, 13 (34), 41323-41329, DOI: 10.1021/acsami.1c11510.

C.-H. L. conceived the project idea, grew the PECVD graphene, performed AFM, XPS and Raman measurements, interpreted the data, and wrote the draft manuscript.

Lu, C.-H.; Shang, K.-M.; Lee, S.-R.; Tai, Y.-C.; Yeh, N.-C. Graphene on Nanoscale-Thick Au Films: Implications for Anticorrosion in Smart Wearable Electronics. ACS Applied Nano Materials 2022, 5 (3), 4343-4349, DOI: 10.1021/acsanm.2c00401.

C.-H. L. conceived the project idea, grew the PECVD graphene, performed AFM, XPS and Raman measurements, interpreted the data, and wrote the draft manuscript.

Lu, C.-H.; Shang, K.-M.; Lee, S.-R.; Leu, C.-M.; Tai, Y.-C.; Yeh, N.-C. Low-Temperature Direct Growth of Nanocrystalline Multilayer Graphene on Silver with Long-Term Surface Passivation. ACS Applied Materials & Interfaces 2023, 15, 7, 9883–9891, DOI: 10.1021/acsami.2c21809

C.-H. L. conceived the project idea, grew the PECVD graphene, performed AFM, XPS, XRD and Raman measurements, interpreted the data, and wrote the draft manuscript.

Duxing Hao, Wen-Hao Chang, Yu-Chen Chang, Wei-Tung Liu, Chen-Hsuan Lu, Tilo H. Yang, Naoya Kawakami, Ming-Hao Liu, Chun-Liang Lin, Ting-Hua Lu, Yann-Wen Lan and Nai-Chang Yeh. Magnetic Field-Induced Ferroelectric Responses in Monolayer MoS_2 Transistors. In preparation.

C.-H.L. carried out the PF-KPFM measurements and estimated the carrier concentrations and sulfur vacancies.

Lu, C.-H.; Shang, K.-M.; Lee, S.-R.; Leu, C.-M.; Tai, Y.-C.; Yeh, N.-C. Feasibility and Structural Transformations of Electrodeposited Copper Foils for Graphene Synthesis by Plasma-Enhanced Chemical Vapor Deposition. Submitted

C.-H. L. conceived the project idea, grew the PECVD graphene, performed SEM, EBSD, XPS, and Raman measurements, interpreted the data, and wrote the draft manuscript.

Chen-Hsuan Lu; Duxing Hao; Nai-Chang Yeh. A Perspective of Recent Advances on PECVD-Grown Graphene Thin Films for Scientific Research and Technological Applications. Submitted.

C.-H. L.: Conceptualization, Writing – original draft, Writing – review & editing, visualization.

TABLE OF CONTENTS

Acknowledgements iii
Abstract v
Published Content and Contributions vii
Table of Contents ix
List of Illustrations and Tables x
Chapter I: Introduction 1
1. An overview of graphene and other Van der Waals materials 1
1.1 Interactions and Applications of Graphene with Various Materials 1
1.2 Technological and Economic Implications 2
1.3 Research Goals and Future Directions 3
1.4 Graphene lattice structure 4
2. Overview of graphene growth method 6
3. The scope of this thesis 7
Chapter II: Single-Step Direct Growth of Graphene on Cu Ink toward Flexible Hybrid Electronic Applications by Plasma-Enhanced Chemical Vapor Deposition. 8
1. Introduction 8
2. Experimental method 11
3. Results and discussion 14
4. Conclusion 27
Supporting information 28
Chapter III: Polymer-Compatible Low-Temperature Plasma-Enhanced Chemical Vapor Deposition of Graphene on Electroplated Cu for Flexible Hybrid Electronics 31
1. Introduction 31
2. Experimental method 34
3. Results and discussion 35
4. Conclusion 43
Supporting information 44
Chapter IV: Graphene on Gold for Anticorrosion in Smart Wearable Electronics 51
1. Introduction 51
2. Experimental method 53
3. Results and discussion 55
4. Conclusion 64
Chapter V: Graphene on Silver with Long-Term Surface Passivation 65
1. Introduction 66
2. Material and methods 68
3. Results and discussion 70
4. Conclusion 81
Supporting information 82
Chapter VI: Exploring the Feasibility and Structural Transformations of Electrodeposited Copper Foil in Plasma-Enhanced Chemical Vapor Deposition Graphene Synthesis 87

1. Introduction 88
2. Experimental method 90
3. Results and discussion 91
4. Conclusion 104
Supporting information 106
Chapter VII: Dipole Ordering in Monolayer MoS_2 113
1. Introduction 113
2. Growth methods of MoS_2 114
3. Dipole ordering responses in monolayer MoS_2 115
4. Work function measurements and estimating the density of sulfur vacancies 116
5. Mechanisms underlying dipole ordering response 118
6. Conclusion 119
Chapter VIII: Future Work and Summary 120
1. Large-area PECVD graphene growth 120
2. Interfacial graphene growth 130
Summary 138
Bibliography 140

List of Figures and Tables

Figure 1.1. Graphite structure (left). The interspacing between graphene layers is 3.35Å. (right) the hexagonal lattice of graphene. 5
Figure 1.2. Three common structural polymorphs of monolayer MX_2. M represents (Mo,W) and X represents (S, Se, Te). Reproduced from Ref[47]. Copyright © 2021, Springer Nature. 6
Figure 2.1: A schematic diagram of the PECVD system for direct graphene growth on Cu ink. The inset shows an image of PECVD graphene growth in process, where the sample was placed inside the plasma. 13
Figure 2.2: Raman spectral characteristics of graphene grown on Cu ink under different PECVD growth conditions: (a) Raman spectra of samples grown under a total gas pressure of 500 mtorr. (b) The intensity ratios of I(D)/I(G) for the spectra shown in (a) *vs* the H_2/CH_4 gas ratio. (c) Raman spectra of samples grown under a total gas pressure of 750 mtorr. (d) The intensity ratios of I(D)/I(G) for the spectra shown in (c) *vs* the H_2/CH_4 gas ratio. 15
Figure 2.3: Comparison of the I(D′)/I(G) and I(D)/I(D′) ratios of samples of graphene on Cu ink taken under a total pressure of 750mtorr: (a) I(D′)/I(G) *vs.* H_2/CH_4 (b) I(D)/I(D′) *vs.* H_2/CH_4 17
Figure 2.4: Raman spectral maps of graphene grown on Cu ink with three different H_2/CH_4 ratios of 8, 5 and 0.125 at 750 mtorr. The top row are the optical images with the red box indicating the mapped region of (15×15) μm^2. The second row correspond to maps of the I(D)/I(G) ratios taken over areas indicated above, and the third row are the histograms of the I(D)/I(G) maps. 18
Figure 2.5: SEM and STEM images (a) SEM image of Cu ink before PECVD. (b) HAADF-STEM image of Cu ink before PECVD. (c) SEM and (d) HAADF-STEM images of Cu ink after PECVD with H_2/CH_4 = 0.125 and total pressure = 750 mtorr. (e) SEM and (f) HAADF-STEM images of Cu ink after PECVD with H_2/CH_4 = 8 and total pressure = 750 mtorr. The red lines in (d) and (f) indicate the approximate heating depths of the PECVD process under H_2/CH_4 = 0.125 and 8, respectively. 20
Figure 2.6: Magnified HAADF-STEM images of graphene Cu ink after PECVD with a total pressure of 750 mtorr and H_2/CH_4 (a) = 0.125, (b) = 8. Here "a-C" refers to amorphous carbon and "Gr" represents graphene. The intensity slices (green rectangle region) for both (a) and (b) were included in Figure S2.3. 21
Figure 2.7: AFM images of the samples (a) after PECVD with H_2/CH_4 = 8, 750 mtorr; and (b) after H_2/CH_4 = 0.125, 750 mtorr. Here the values of the surface roughness obtained in the areas indicated by the red boxes in (a) and (b) were obtained by calculating the RMS roughness of the selected regions. (c) A schematic showing the observed roughness differences due to different H_2/CH_4 ratios. 23
Figure 2.8: XPS Cu-2p spectra taken on Cu-ink samples: (a) before PECVD; (b) after PECVD with growth conditions of H_2/CH_4 = 0.125 and total pressure = 750 mtorr; and (c) after PECVD with H_2/CH_4 = 8 and total pressure = 750 mtorr. 24
Figure 2.9: XAES Cu LMM spectra of samples after PECVD: (a) with H_2/CH_4 = 8, total pressure = 750 mtorr; (b) differential spectrum of (a); (c) with H_2/CH_4 = 0.125, total pressure = 750 mtorr; and (d) differential spectrum of (c). 26

Figure S2.1: Images of the Cu ink sample (a) before PECVD and (b) after PECVD. 28
Figure S2.2. I(2D)/I(G) vs H_2/CH_4 at (a) 500 mtorr and (b) 750 mtorr. 28
Figure S2.3: HAADF-STEM image of the Cu ink before and after PECVD of 750mtorr with the corresponding intensity slices. 29
Figure 3.1. Raman spectra measurement (a) Representative Raman spectra of PECVD graphene grown at different H_2/CH_4 ratios. (b) The I(D)/I(G) intensity ratio and graphene grain size L *vs.* H_2/CH_4 ratio. Here the error bar associated with each H_2/CH_4 ratio was calculated from analyzing 225 Raman spectra. 36
Figure 3.2. Peak Force Error image of electroplated Cu substrates after the PECVD process with (a) $H_2/CH_4 = 1$, (b) $H_2/CH_4 = 2$, (c) $H_2/CH_4 = 6$, and (d) $H_2/CH_4 = 12$. 38
Figure 3.3. HAADF-STEM image of PECVD graphene grown on electroplated Cu with the ratio of $H_2/CH_4 = 12$. Here "Gr" represents graphene. The inset shows the intensity slice of the indicated region from Cu through graphene to the protection layer. 40
Figure 3.4. XPS C1s spectra collected on PECVD graphene covered samples: (a) after PECVD with $H_2/CH_4 = 1$, (b) after PECVD with $H_2/CH_4 = 2$, (c) after PECVD with $H_2/CH_4 = 6$, (d) after PECVD with $H_2/CH_4 = 12$. 41
Figure 3.5. XPS Cu 2p spectra. Top panels: XPS Cu 2p peaks of (a) etched Cu substrate and (b-e) samples right after PECVD growth of graphene under different H_2/CH_4 ratios. Middle panels, XPS Cu 2p peaks of samples after stored under normal ambient condition for 4 weeks: (f) etched Cu substrate and (g-j) samples after PECVD growth of graphene under different H_2/CH_4 ratios. Bottom panels: XPS Cu 2p peaks of samples after stored under normal ambient condition for 8 weeks: (k) etched Cu substrate and (l-o) samples after PECVD growth of graphene under different H_2/CH_4 ratios. 42
Figure 3.6. Resistance of the Cu circuit *vs.* the number of folding cycles. Note that the reference sample failed after about 60,000 folding cycles. 43
Figure S3.1. Appearance of the PECVD and the temperature measurement. (Top panel) Photograph of the PECVD process in progress. (Bottom panel) The growth chamber temperature change as a function of time during the PECVD process was recorded via thermocouple attached on the quartz tube. 45
Figure S3.2. Optical images, I(D)/I(G) spatial maps and histograms of the I(D)/I(G) spatial maps of PECVD-grown graphene on electroplated Cu under different ratios of H_2/CH_4: (a,e,i) $H_2/CH_4 = 12$ (b,f,j) $H_2/CH_4 = 6$ (c,g,k) $H_2/CH_4 = 2$, and (d,h,i) $H_2/CH_4 = 1$. The size of the mapping area in (e-h), which corresponds to the red squares in (a-d), is $(30\times30)\ \mu m^2$. Each histogram from (i) to (l) consists of 225 point spectra, and each point spectrum is taken over a spot size with a radius of 0.5 μm. 45
Figure S3.3. I(2D)/I(G) spatial maps and histograms of the I(2D)/I(G) spatial maps of PECVD-grown graphene on electroplated Cu under different ratios of H_2/CH_4 flow rates: (a,e) $H_2/CH_4 = 1$, (b,f) $H_2/CH_4 = 2$, (c,g) $H_2/CH_4 = 6$, and (d,h) $H_2/CH_4 = 12$. The size of the mapping area in (a-d) is $(30\times30)\ \mu m^2$. Each histogram from (e) to (h) consists of 225 point spectra, and each point spectrum is taken over a spot size with a radius of 0.5 μm. 46
Figure S3.4. Optical image comparing the appearances of the electroplated Cu substrate on polyimide before and after the PECVD process. 46
Figure S3.5. Surface morphology of electroplated Cu substrates: (a) AFM image (top panel) and Peak Force channel (bottom panel) of an electroplated Cu substrate before PECVD. (b)

AFM image of an electroplated Cu substrate after PECVD with H_2/CH_4 = 1. (c) AFM image of an electroplated Cu substrate after PECVD with H_2/CH_4 = 2. (d) AFM image of an electroplated Cu substrate after PECVD with H_2/CH_4 = 6. (e) AFM image of an electroplated Cu substrate after PECVD with H_2/CH_4 = 12. The RMS roughness of the images were indicated. 47
Figure S3.6. HAADF-STEM image of the reference sample. Here a-C between Cu and the protection layer refers to amorphous carbon. 48
Figure S3.7. Cu2p XPS spectra of (a) as-received electroplated Cu substrate, and (b) the same electroplated Cu substrate after dilute H_2SO_4 etch. 48
Figure S3.8. The circuit pattern used for the folding test and resistance measurements (Left). The size for each electrical pad is (1×1) mm^2, and the expanded image of the area indicated by the red box is shown on the right, and the scale bar (white) is 20 μm. (Right) Photograph of the equipment for the folding test. The circuit pattern was attached to the center of the equipment. 49
Table S3.1. Electrical resistance (measured in Ω) of different samples after the indicated number (N) of folding cycles and comparison among samples grown under different H_2/CH_4 ratios. 50
Table S3.2. Electrical resistance (measured in Ω) of different samples after the indicated number (N) of folding cycles up to 200,000 cycles. 50
Figure 4.1. Raman spectra measurement (a) Graphene (lighter blue) transferred onto a SiO_2/Si substrate (darker blue) after its growth on Au/Ti/ SiO_2/Si. The scale bar is 1 cm. (b) Raman spectra of PECVD-grown graphene on Au/Ti/ SiO_2/Si under different H_2/CH_4 growth conditions. (c) The intensity ratios I(D)/I(G) and I(D)/I(D´) extracted from (b). (d) The calculated strain of graphene on Au from Eq. (4.2). 57
Figure 4.2. The AFM height images and peakforce error images of the sample surface (a,d) before PECVD, (b,e) after PECVD graphene growth at H_2/CH_4 = 0.2, and (c,f) after PECVD graphene growth at H_2/CH_4 = 2. Here the scale bar represents 200 nm. 58
Figure 4.3. XPS C-1s spectra of the graphene samples after the PECVD process under the growth condition with (a) H_2/CH_4 = 0.2, (b) H_2/CH_4 = 1, (c) H_2/CH_4 = 1.5, and (d) H_2/CH_4 = 2. 59
Figure 4.4. ADF-STEM images at a lower magnification (top row) and higher magnification (bottom row) of (a,f) a reference sample without the PECVD process, and samples after the PECVD process with the growth condition of (b,g) H_2/CH_4 = 0.2, (c,h) H_2/CH_4 = 1, (d,i) H_2/CH_4 = 1.5, and (e,j) H_2/CH_4 = 2. Here "PL", "Gr" and "a-C" represent protection layer, graphene, and amorphous carbon, respectively. 60
Figure. 4.5 Schematic of the growth mechanism of graphene on gold by PECVD 61
Figure 4.6. XRD measurement (a) XRD of Au (111) region (b) the extracted Au (111) peak intensity plotted versus H_2/CH_4 ratio. Note that the dashed line is for guidance only. 62
Figure 4.7. SEM images (a) Reference sample without graphene coverage. The red arrow indicates the damaged surface with bubbles. (b) Sample with PECVD graphene coverage grown under the condition H_2/CH_4 = 0.2. (c) Sample with PECVD graphene coverage grown under the condition H_2/CH_4 = 2. The top row shows the optical images before and after AST. The bottom row shows the SEM images taken after AST. The scale bar is 100 μm. 63

Figure 5.1. Schematic of flipping over the Ag/Ti/Si substrate and placing it onto the sample holder for direct PECVD-graphene growth on Ag. 69
Figure 5.2. Ramen spectra measurements (a) Representative Raman spectrum of the PECVD graphene on silver of different growth times of 5, 10 and 15 minutes. (b) Graphene transferred onto a SiO_2 target substrate after its growth. The growth substrate after the removal of graphene was also included side-by-side with the SiO_2 target substrate to demonstrate the full coverage of graphene on it before graphene removal. The scale bar is 1 cm. (c) The Raman intensity ratios I(D)/I(G) and I(2D)/I(G) for samples of different growth times. (d) The graphene grain sizes of different samples extracted from the I(D)/I(G) ratios and Eq (1). (e) The I(D)/I(D') ratios for samples of different growth times and (f) the FWHM of the 2D peaks for samples of different growth times. 72
Figure 5.3. 2D peak position “pos(2D)” versus G peak position “pos(G)” of the PECVD graphene on silver samples under growth times of (a) 15 min, (b) 10 min, and (c) 5 min, showing slight hole doping and compressional strain in all samples according to the analysis developed by Lee *et al.*[170] Here the light green solid dot in each panel denotes the strain-free and undoped graphene peak position, and the positive value of the strain corresponds to tensile strain. 73
Figure 5.4. A sideview of the gas velocity distribution around the flipped substrate for graphene growth, as obtained by CFD simulations. 74
Figure 5.5. XPS Ag-3d and O-1s spectra taken quickly after the PECVD process for growth times of (a,e) 15 min, (b,f) 10 min, (c,g) 5 min, and those of the reference sample (d,h), showing a much reduced silver oxide component for all samples after the PECVD process. 75
Figure 5.6. Cross-sectional ADF-STEM images for graphene samples with growth times of (a,d) 15 min, (b,e) 10 min, and (c,f) 5 min. The insets showed the averaged intensity profile within the boxed region. The orange dash lines were for guidance to better reveal the number of graphene layers. 77
Figure 5.7. TEM studies of the graphene stacking order: (a) TEM image of the planar view of graphene; (b) FFT of (a); (c) electron diffraction image of graphene. 77
Figure 5.8. A proposed PECVD graphene growth mechanism on silver. 80
Figure 5.9. Comparison of the XPS Ag 3d spectra of silver after 5 months of exposure to ambient condition for (a) a sample fully covered by PECVD-grown graphene and (b) a sample without graphene. Note that the intensity was normalized for better comparison. .. 81
Table S5.1. G and 2D peak positions with various hole doping levels under no strain 82
Figure S5.2. The AFM height images of the sample surface after (a) 15 min, (b) 10 min, and (c) 5 min of PECVD graphene growth, showing significantly increased surface roughness in comparison with (d) for the surface of silver before the PECVD process. 83
Figure S5.3. Comparison of the XRD spectra of the Ag (111) peak taken on samples before the PECVD process and after the PECVD process for graphene growth over different times of 5 min, 10 min and 15 min. 84
Figure S5.4. Si-2p spectra of PECVD-grown graphene on Ag after growth times of (a) 15 min, (b) 10 min, and (c) 5 min. 84
Figure S5.5. XPS C-1s spectra and the first derivative XAES C KLL spectrum after the PECVD with the growth times of (a,d) 15 min, (b,e) 10 min, and (c,f) 5 min. 85

Figure S5.6. XAES C KLL spectra of PECVD-grown graphene on Ag after growth times of (a) 15 min, (b) 10 min, and (c) 5 min, and (d) the C KLL spectrum of xGnP Graphene Nanoplatelets R10, where R10 was used as the reference graphene material to validate the data processing. (e-h) The first derivative of C KLL spectra of (a-d), respectively. The D value for the graphitic reference sample is in agreement with that in a previous report [175]. Before differentiation, the data were smooth by moving average method with a width of 11 data points. The spectra differentiation was executed with the Savitzky–Golay(SG) quadratic method and a smoothing width of 11 data points using CasaXPS software. 85
Figure 6.1 Ramen spectra measurements (a) Raman spectrum of PECVD-grown graphene on ED copper foil with varied growth times at 40W. (b) Optical micrograph showing a graphene sample of an area ~ (1.5×0.8) cm^2 that was transferred onto a SiO_2 substrate after the PECVD growth on an ED copper foil. (c) Raman spectra of graphene samples grown on ED copper foils under different plasma powers for the same 20-minute growth time. (d) Correlation between the positions of the 2D peak (pos(2D)) and the G peak (pos(G)) of PECVD-grown graphene, pre- and post-transfer. The pink solid dot at the cross point of the red and blue lines represents the position of strain-free and undoped graphene for reference. 93
Figure 6.2. SEM images of transferred graphene grown at 40W. The growth time for images (a,c) is 10 minutes, while images (b,d) correspond to a growth time of 20 minutes. Images (a,b) were taken under ET detector, and images (c,d) were taken under in-lens mode. 95
Figure 6.3. TEM and diffraction images (a) HRTEM image of transferred graphene grown at 40W with a growth time of 10min. (b) Electron diffraction of transferred graphene grown at 40W with a growth time of 10min. 96
Figure 6.4. Optical micrographs of the ED copper foil (a) before PECVD and after PECVD at 40W for a growth time of (b)10sec (c) 1min (d)5min (e)10min and (f) 20min, respectively. 97
Figure 6.5. Roughness of ED copper foil after PECVD graphene growth. (a) Variation in roughness with different growth times at 40W. (b) Comparison of roughness with different plasma power at a fixed growth time of 20 minutes. 98
Figure 6.6. EBSD map of an ED copper foil (a) before PECVD and after PECVD at 40W with different growth times of (b)10sec (c) 1min (d)5min (e)10min and (f) 20min, respectively. The scale bar in (a) is 2μm and 100μm for (b) – (f). Grains were defined with a grain detection angle of 10° and the twin boundaries (Σ 3) are indicated with white lines. The color scales for grain orientation is shown in the lower right corner of (a). 99
Figure 6.7. Grain size and activation energy analysis (a) Average grain size as a function of growth time at 40W (b) Cu grain size measured under different plasma power conditions. Growth time is 20 min (c) Plot of ln (t) *vs.* ln (D), the fitted growth exponent n is 14.88. (d) $\ln(D^n/t)$ versus 1/T plot, with n=14.88. 100
Figure 6.8. Inverse pole figures of the ED copper foil (a) before PECVD and after PECVD at 40W with growth times of (b)10sec (c) 1min (d)5min (e)10min and (f) 20min, respectively. 102
Figure 6.9. XPS survey scan of the ED copper foil before PECVD (labeled as ref) and after PECVD at 40W of different growth time. 103

Figure 6.10. XPS C1s spectra of the ED copper foil (a) before PECVD and after PECVD at 40W with growth times of (b)10sec (c) 1min (d)5min (e)10min and (f) 20min, respectively. 103
Figure S6.1. Temperature measurement of the PECVD system. The temperature on the tube wall recorded by thermocouple (Left). T_H indicates the fitted temperature plateau. Showing the attached thermocouple on the PECVD system. (Right) 106
Table S6.1. Measured temperature at the tube wall at different time with 40W. 106
Figure S6.2. Plotting T_H versus the corresponding plasma power. 107
Figure S6.3. The extrapolated substrate temperature under different plasma power using the fitted slope in Figure S6.2. and the midpoint temperature measured using the temperature label at 10W (*i.e.*, the temperature is in the range of 232 ℃ - 260 ℃ at 10 W). 108
Table S6.2. Substrate temperature at different plasma power 108
Figure S6.4. SEM images of the ED copper foil (a) before PECVD and after PECVD at 40W with growth times of (b)10sec (c) 1min (d)5min (e)10min and (f) 20min. The scale bar is 10μm. 109
Figure S6.5. Optical micrographs of the ED copper foil after 20 minutes of PECVD graphene growth with plasma power sof (a) 20W (b) 30W (c) 40W, respectively. 109
Figure S6.6. SEM images of the ED copper foil after 20 minutes of PECVD graphene growth with plasma powers of (a) 20W (b) 30W, and (c) 40W, respectively. The scale bar is 10μm. 109
Figure S6.7. White light interferometry images of the ED copper foil (a) before PECVD and after PECVD at 40W with growth times of (b)10sec (c) 1min, (d)5min, (e)10min, and (f) 20min, respectively. The scale bar is 100 μm. 110
Figure S6.8. White light interferometry images of the ED copper foil after 20 minutes of PECVD graphene growth with plasma powers of (a) 20W, (b) 30W, and (c) 40W, respectively. The scale bar is 100 μm. 110
Figure S6.9. EBSD map of the ED copper foil after 20 minutes of PECVD graphene growth with different plasma power of (a) 20W, (b) 30W, and (c) 40W. The scale bar is 100μm. 111
Figure S6.10. Inverse pole figures of the ED copper foil after 20 minutes of PECVD graphene growth with different plasma powers of (a) 20W, (b) 30W, and (c) 40W. 111
Figure S6.11. XPS survey scan of the ED copper foil after 20 minutes of PECVD graphene growth with different plasma power. Here we note that the detected N and Si elements at 20W originates from the silane derivative coating on the backside of the ED Cu foil. 112
Figure 7.1. The magnitude of source-drain current ($|I_{DS}|$) *vs.* source-gate voltage (V_{GS}), $|I_{DS}|$-*vs.*-$V_{GS,}$ hysteresis curves for (a) heavily n-doped monolayer MoS_2 with a constant source-drain voltage V_{DS} = 0.1 V and (b) regular monolayer MoS_2 with V_{DS} = –1.0 V under different applied magnetic fields (*B*) perpendicular to the MoS_2 layer. Here LRS (HRS) denotes the low (high) resistance states, respectively. The source-drain voltage V_{DS} is applied parallel to the MoS_2 layer whereas the source-gate voltage V_{GS} is applied perpendicular to the MoS_2 layer. These measurements were on MoS_2 FET devices carried out by Duxing Hao. 116
Figure 7.2. Schematic of the band alignment of $Si/SiO_2/MoS_2$ based on the KPFM measurements for (a) regular and (b) heavily doped monolayer MoS_2 FET devices. The units for the numbers indicated in the figure are in eV. 117

Figure 7.3. Magnetic field induced lattice expansion of regular MoS_2. The measurement of Moiré lattice constants using STM were carried out by the research group of Professor Chun-Liang Lin at NYJU in Taiwan. 119
Figure 8.1.1. The initial trial of scaled-up MW-PECVD chamber at Mastek. 120
Figure 8.1.2. Raman spectrum of graphene after the PECVD process using the scaled-up chamber. 121
Figure 8.1.3. Raman modes in graphene. Here the iTO (iLO) phonon refers to in-plane (longitudinal) transverse optical phonon. Adapted from Ref[168]. 121
Figure 8.1.4. The PECVD system previously used for diamond growth at Mastek. 122
Figure 8.1.5. Side views through the chamber viewing port, showing the change of plasma position with respect to the sample (Cu foil) under different power and pressure. 123
Figure 8.1.7. Raman spectrum after the PECVD process using the diamond PECVD chamber. Growth time = 20 min. 124
Figure 8.1.8. Raman spectrum after PECVD using the diamond PECVD chamber. Growth time = 10 min, H2 flow = 240 sccm, power = 1200 W. 125
Figure 8.1.9. Raman spectrum of graphene after the PECVD process using the diamond PECVD chamber. Growth time = 10 min, power = 700 W. 126
Figure 8.1.10. Raman spectrum after PECVD using the diamond PECVD chamber. The substrate is sputtered Cu on Si. 127
Figure 8.1.11. Raman spectrum of graphene after the PECVD process using the diamond PECVD chamber with higher H_2 flow. The substrate is sputtered Cu on Si. 127
Figure 8.1.12. Raman spectrum after PECVD using the diamond PECVD chamber. Growth time 20min, 1200W. 128
Figure 8.1.13 Optical micrograph showing the sputter Cu sample with PECVD graphene before transfer (top) and after transferring onto a SiO_2 substrate (down). 129
Figure 8.2.1. The Raman spectrum of the graphene stripes on the top surface of Ag on sapphire substrate. 131
Figure 8.2.2. The Raman spectrum taken on the top surface of Ag deposited on sapphire substrate after O_2 plasma cleaning of the graphene stripes. 131
Figure 8.2.3. The Raman spectrum of the graphene stripes on the top surface of TiW deposited on sapphire substrate. 132
Figure 8.2.4. The Raman spectrum taken on the top surface of TiW deposited on sapphire substrate after O_2 plasma cleaning. 132
Figure 8.2.5. The Raman spectrum of the graphene stripes at the top surface of Ni on sapphire substrate. 133
Figure 8.2.6. The Raman spectrum taken on the top surface of Ni deposited on sapphire after O_2 plasma cleaning of the surface graphene stripes. 134
Figure 8.2.7. Cross-sectional STEM of Ni on sapphire after PECVD and O_2 plasma cleaning, showing the formation of ~ 300 nm thick multilayer graphene. 135
Figure 8.2.8. Zoomed-in cross-sectional STEM of Ni on sapphire after the PECVD process followed by the O_2 plasma cleaning of graphene stripes on the surface of Ni. The insets show the FFT image of the indicated regions. 136
Figure 8.2.9. ELNES line scan of the interfacial graphene region between Ni and sapphire. 136

Figure 8.2.10. Summary of measuring the interfacial graphene with Raman spectroscopy. 137

C h a p t e r 1

INTRODUCTION

Partially adapted from: Chen-Hsuan Lu; Duxing Hao; Nai-Chang Yeh. A Perspective of Recent Advances in PECVD-Grown Graphene Thin Films for Scientific Research and Technological Applications. Submitted.

1. An overview of graphene and other Van der Waals materials

1.1 Interactions and Applications of Graphene with Various Materials

Graphene, a two-dimensional layer of carbon atoms forming a honeycomb lattice structure (Figure 1.1), has emerged as a transformative material in the landscape of modern technology. With its diverse range of properties, it has shown potential in a multitude of applications, from enhancing the stability of metal electrodes to serving as a solid lubricant. When paired with other functioning materials, graphene bolsters their resistance to environmental effects such as oxidation[1-2] and moisture, thus broadens their potential applications[3-5]. However, employing graphene effectively presents its own set of challenges, including the convoluted and demanding processes required for its optimal utilization[6-9].

Some of the materials that can greatly benefit significantly from the unique properties of graphene include gold, silver, and the organic-inorganic hybrid perovskites. Revered for its biocompatibility and malleability, gold finds widespread use in biosensors and flexible electronics[10-12], while silver, is a favored choice for components in organic light emitting diodes (OLEDs)[13] and biosensors with its pronounced surface plasmon resonance (SPR)[2]. Organic-inorganic hybrid perovskites, such as $CH_3NH_3PbX_3$ (X = I, Br), have gained much research attention due to their improved photovoltaic power conversion efficiency[14-26]. However, these materials present significant hurdles due to their environmental susceptibility[2, 27-31], making the integration with graphene a promising strategy for overcoming such obstacles.

Simultaneously, there is an urgent need for novel techniques that allow the direct growth of graphene on commonly used substrates, such as silicon. This requirement is particularly critical for the development of fully CMOS-compatible optoelectronic devices, capitalizing on the remarkable properties of graphene, including its high electron mobility, large Kerr coefficient, and ultrafast photodetection capabilities[32-36]. Yet, the currently available techniques for graphene synthesis on silicon are limited and necessitate high-temperature processing[37], often leading to the generation of small graphene islands or flakes, which are far from ideal for many applications[38-40].

1.2 Technological and Economic Implications

Specifically, the domain of Flexible Hybrid Electronics (FHE) is rapidly evolving and has emerged as a game-changer in the semiconductor industry. FHE technology combines rigid and flexible electronic components to offer innovative applications transforming various industries. Organizations like NextFlex and SEMI FlexTech in the United States have been at the forefront of driving advancements in FHE. Their relentless efforts to advance research and development in FHE have led to significant progress in the domestic manufacturing capabilities of this transformative technology. The Department of Defense (DoD) has recognized the strategic importance of FHE in maintaining and advancing U.S. leadership in cutting-edge defense technologies. In partnership with NextFlex, the DoD invested a whopping $154 million in 2020 to expedite the commercialization of prototype technologies developed by the Army using FHE[41]. This investment underscores the DoD's commitment to FHE and highlights its potential to revolutionize the defense industry.

Further, the world is grappling with the urgent need to reduce carbon emissions globally, and the United States has launched the Net-Zero Government Initiative to achieve net-zero emissions from national government operations by 2050[42]. This initiative is vital to achieving a more environmentally friendly and sustainable future. The low-temperature plasma-enhanced chemical vapor deposition (PECVD) technique employed in this thesis for graphene growth aligns well with this initiative, because it significantly reduces the energy consumption typically associated with active heating and thus contributes to a greener future.

Additionally, the PECVD method for graphene growth demonstrates its compatibility with the processing of FHE, which further helps driving sustainable practices. For example, the healthcare industry is one of the primary beneficiaries of FHE, with its potential to develop flexible or smart wearable electronics with metallic electrodes. Wearable medical devices can monitor health, track fitness, and provide personal assistance, leading to a staggering growth rate of the wearable medical devices market, reaching a value of USD $26.8 billion in 2022. With a projected growth rate of 25.7% from 2023 to 2030[43], the impact of FHE on the healthcare industry will be significant and is expected to further drive the growth in this sector.

Meanwhile, the global printed electronics market, projected to reach USD $30 billion by 2030[44], provides a compelling avenue for the adoption of FHE technology. Given that this market is growing at a compound annual growth rate (CAGR) of 14.5% from 2022 to 2030[44], the integration of graphene—due to its diverse properties—could substantially augment the capabilities and durability of printed electronics. It is worth noting that the FHE market alone is expected to reach USD $264.39 million by 2026, growing at a CAGR of 16.2% over the 2021-2026[45] period. Therefore, the fusion of graphene with FHE technology has not only scientific implications but also substantial economic potential, making it a critical area of focus for this thesis.

1.3 Research Goals and Future Directions

On the other hand, the future of wireless communication lies beyond 5G/6G technology, offering higher bandwidth and lower latency, crucial for real-time machine responses and autonomous vehicles[46]. Graphene, with its diverse properties such as thermal, optical, electrical, and electronic functionalities, has the potential to play a crucial role in these next-generation technologies.

This thesis aims to explore the application of the PECVD graphene growth technique to a wide range of transition metals, such as copper, gold, and silver, unlocking new technological pathways based on graphene-protected surfaces and electrodes. These projections

demonstrate the incredible potential of this research and the vital role that graphene could play in the future of flexible electronics.

In addition to in-depth studies of the synthesis and properties of graphene on a variety of substrates, this thesis also investigates another van der Waals material, molybdenum disulfide (MoS_2). Like all van der Waals materials such as graphene, hexagonal boron nitride, and transition metal dichalcogenides, bulk MoS_2 exhibits strong in-plane covalent bonds and weak inter-layer van der Waals attraction, which can be reduced to a monolayer that consists of three atomic sheets of sulfur, molybdenum and sulfur, each forming triangular lattice structures, as shown in Figure 1.2. We have discovered that distorted monolayer MoS_2 synthesized by high-temperature chemical vapor deposition (CVD) techniques demonstrated unique ferroelectric properties: Unlike conventional ferroelectric materials, distorted MoS_2 preserves its ferroelectric characteristics even in the ultrathin limit, making it particularly appealing for high-density data storage and energy-efficient photovoltaics. Through a comparative overview, this research aims to dissect the challenges and opportunities associated with employing graphene and MoS_2 in advanced technological applications, thereby extending the frontier of our understanding in the realm of two-dimensional materials.

1.4 Graphene lattice structure

Graphene, a single layer of graphite, consists of a monolayer of carbons forming a honeycomb lattice structure, as shown in Figure 1.1

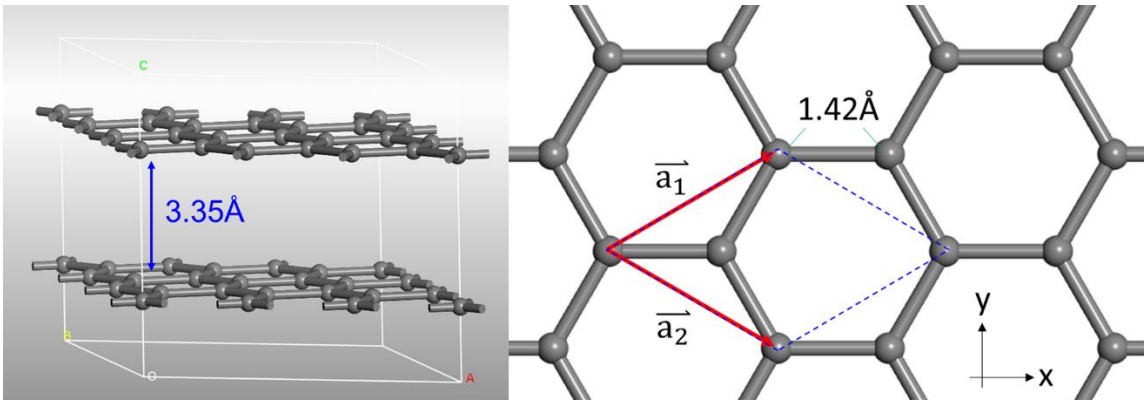

Figure 1.1. Graphite structure (left). The interspacing between graphene layers is 3.35Å. (right) the hexagonal lattice of graphene.

The lattice vectors (in Cartesian coordinates) can be expressed as

$$\overrightarrow{a_1} = a\left(\frac{3}{2}, \frac{\sqrt{3}}{2}\right);\ \overrightarrow{a_2} = a\left(\frac{3}{2}, -\frac{\sqrt{3}}{2}\right) \tag{1.1}$$

where a = 1.42 Å is the C-C sp^2 bond length.

Due to the small lattice constant of the sp^2-bonded two-dimensional honeycomb structure of graphene, only protons and electrons could cross a perfect graphene layer, making it an ideal passivation or anti-corrosion layer. Moreover, since it is only one atom thick, it is optically transparent under visible light, making graphene usable for transparent electrode applications.

For comparison, the lattice structure for a monolayer MoS_2 is shown in Figure 1.2. The 2H phase is characterized by its mirror symmetry, where the top and bottom sulfur (S) layers are arranged in a mirrored configuration. On the other hand, the 1T phase is distinguished by its inversion symmetry, offering a different structural arrangement. Lastly, the 1T' phase represents a unique distorted structure, in which neither mirror nor inversion symmetry is present. This figure illustrates these distinct lattice configurations, highlighting the subtle yet significant differences in their structural symmetries.

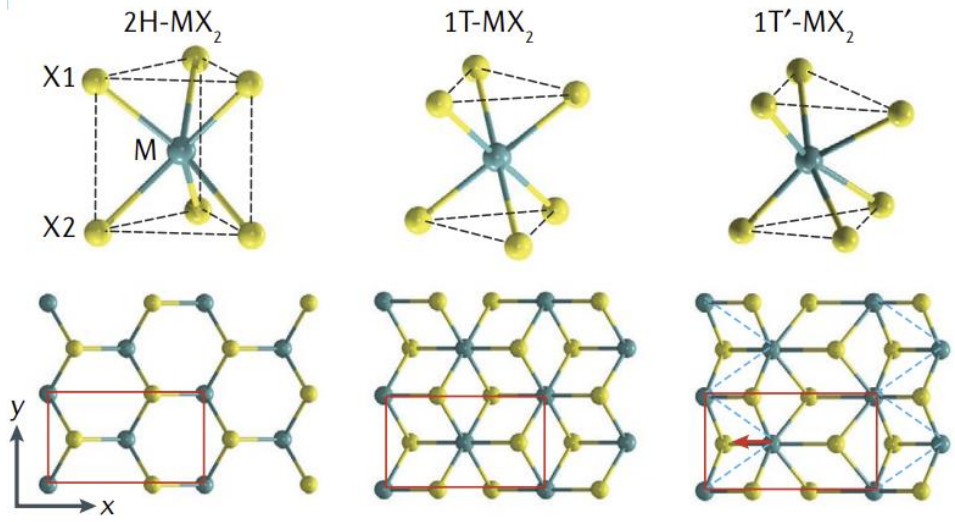

Figure 1.2. Three common structural polymorphs of monolayer MX_2. M represents (Mo,W) and X represents (S, Se, Te). Reproduced from Ref[47]. Copyright © 2021, Springer Nature.

2. Overview of graphene growth method

When it comes to producing graphene, traditional methods include mechanical exfoliation and CVD [48] , along with several other alternatives. Notably, the CVD technique operates under high-temperature conditions, generally close to or exceeding the melting point of the metal catalysts used[49-53], which poses challenges such as high temperatures can result in an aged quartz furnace, potentially leading to contamination issues[54]. While there have been efforts to decrease the CVD growth temperatures[55-57], these approaches typically involve complex preprocessing steps that are not well-suited to industrial-scale production. Moreover, transferring the graphene from the metal foils to the target substrates is an added challenge. This transfer step is not only expensive and time-consuming, but it also often results in weak adhesion between the graphene and the substrates[58], thus restricting its practical applications.

PECVD provides an alternative solution. This technique leverages plasma to establish a highly reactive environment, which facilitates growth at lower temperatures[59]. However, the typically reported growth temperatures for PECVD, ranging from 450 – 700 °C[60-72], are still too elevated for common polymer substrates. Therefore, there is a need for a PECVD process that can operate at lower temperatures compatible with these organic substrates, enabling direct graphene growth.

Considering the growing demand for flexible electronics, it is critical to develop a method that allows for low-temperature graphene growth. This need emphasizes the importance of creating scalable, low-temperature graphene synthesis techniques compatible with a broad spectrum of substrates and seamlessly integrated into industrial processes.

3. The scope of this thesis

This thesis is organized into eight chapters, each tackling a distinct aspect of materials science with a focus on graphene and ferroelectric materials. Chapter 2 centers on the single-step direct growth of graphene on Cu ink using PECVD, with applications aimed at FHE and the IoT. Chapter 3 continues to explore polymer-compatible low-temperature PECVD of graphene on electroplated Cu, concentrating on its roles in FHE and fan-out redistribution layers (RDL). Subsequent chapters delve into different substrates and conditions for PECVD graphene growth, such as on silver and electrodeposited copper foils. Chapter 7 takes a departure from graphene to discuss the ferroelectric properties of monolayer MoS_2, addressing its potential in data storage and neuromorphic computing among other applications. The thesis concludes with Chapter 8, which outlines future work, particularly in scaling up PECVD graphene growth for more impactful results and provides a summary of the thesis.

C h a p t e r I I

SINGLE-STEP DIRECT GROWTH OF GRAPHENE ON CU INK TOWARD FLEXIBLE HYBRID ELECTRONIC APPLICATIONS BY PLASMA-ENHANCED CHEMICAL VAPOR DEPOSITION

Adapted from:
Lu, C. H.; Leu, C. M.; Yeh, N. C. Single-Step Direct Growth of Graphene on Cu Ink toward Flexible Hybrid Electronic Applications by Plasma-Enhanced Chemical Vapor Deposition. ACS Applied Materials & Interfaces 2021, 13 (5), 6951-6959, DOI: 10.1021/acsami.0c22207.

Personal contribution: I participated in the conception of the project, grew the PECVD graphene, performed AFM and Raman measurements, interpreted the data, and I wrote the draft manuscript.

Highly customized and free-formed products in flexible hybrid electronics (FHE) require direct pattern creation such as inkjet printing (IJP) to accelerate the product development. In this work, we demonstrate direct growth of graphene on Cu ink deposited on polyimide (PI) by means of plasma enhanced chemical vapor deposition (PECVD), which provides simultaneous reduction, sintering and passivation of the Cu ink and further reduces its resistivity. We investigate the PECVD growth conditions for optimizing the graphene quality on Cu ink and find that the defect characteristics of graphene are sensitive to the H_2/CH_4 ratio at higher total gas pressure during the growth. The morphology of Cu ink after the PECVD process and the dependence of graphene quality on the H_2/CH_4 ratio may be attributed to the difference in the corresponding electron temperature. This study therefore paves a new pathway towards efficient growth of high-quality graphene on Cu ink for applications to flexible electronics and Internet of Things (IoT).

1. Introduction

Interconnects are an essential component to all electronic devices. Typically, the desired circuits are defined by lithography and then followed by sputter Cu deposition. Such a subtractive process generally leads to low material utilization efficiency and substantial

chemical waste[73]. In addition, it is well recognized that the high cost and time-consuming development of lithographic masks or fine metal masks (FMM) at the panel-level scale cannot easily adapt to the need of wearable devices, flexible hybrid electronics (FHE) and Internet of Things (IoT) applications that involve highly customized and free-formed products[74]. In this context, pattern creation without the need of lithographic masks, such as digital lithography technology (DLT) and inkjet printing (IJP), is a promising paradigm worth pursuing to expedite the product development to meet the demand of highly diversified applications.

Specifically, additive manufacturing such as inkjet printing is promising to greatly lower production costs due to its superior material utilization efficiency by direct patterning and its scalability[75-76]. Inkjet printing has been successfully demonstrated in devices such as printed sensors[77-79], antennas[80-81], interconnects[75-76] and displays[82-83]. However, the high surface-to-volume ratio of the metallic nanoparticles in ink material is susceptible to rapid oxidation. Therefore, substantial emphasis has been made on silver ink due to its resistance to oxidation and the conductive nature of its oxidized surface layer[84]. On the other hand, the drawbacks of silver ink include its high cost and tendency of electromigration[85]. In contrast, copper has a lower material cost and is more resistant to electromigration[86], although copper surfaces are prone to oxidation and the resulting copper oxide is not conductive, which degrades the reliability of electric circuits made of Cu ink. To address this issue, a common practice to remove the oxide shell of Cu nanoparticles is through sintering, which is also a required process to transform the printed layer into continuous and conductive layers[87]. Nonetheless, in the absence of proper protection, copper oxides would inevitably form at a later time. Therefore, it would be ideal to cover the sintered copper ink with a passivation layer without compromising the conductivity.

Graphene is known for its superior properties in electronics, mechanics, and optics at an atomic scale thickness[88-90]. In particular, only protons and electrons could cross a perfect graphene layer due to the small lattice constant of the sp^2-bonded two-dimensional honeycomb structure. Additionally, graphene is electrically conductive, and few-layer

graphene is optically transparent. As a result, graphene has found its position in various applications such as antennas[91], sensors[92], electromagnetic interference (EMI)[93], and for surface protection of air-sensitive materials such as the hybrid perovskites[94] and Cu ink. Indeed, graphene has been demonstrated to be a diffusion barrier for interconnects[95-96], a passivation layer for surface plasmon resonance nanostructures[97] , a surface protection layer for Cu nanowires[98], and as transparent conductive films[99-101].

Over the years, various graphene synthesis methods have been developed, with mechanical exfoliation and high-temperature chemical vapor deposition (CVD) being the most common approaches[48]. However, these methods are either not scalable or incompatible with industrial processes[67]. For example, standard graphene grown by CVD involves temperatures near or above the melting point of metal catalyst and the growth on metal foils[49-53]. The evaporated metal and aged quartz furnace under such high temperature could cause contamination[54]. Although some modifications have been proposed to lower the growth temperature to near room temperature [55-57], those approaches involve specific processes that limit the feasibility of their integration to industrial production. In addition, graphene grown on metal foils would require an additional process to transfer graphene to targeted substrates, which is time-consuming, costly, and often leads to poor adhesion between the transferred graphene and the substrates[58], thus limiting the potential applications.

A feasible approach for low-temperature two-dimensional material synthesis is plasma-enhanced chemical vapor deposition (PECVD), which has the advantage of both scalability and compatibility with industrial processes[60-72, 102-103]. In particular, instead of relying on pyrolysis of precursors to generate reacting species as in thermal CVD, PECVD takes advantage of a rich stock of radicals and energetic species induced by plasma, providing a highly reactive environment and thus lowering the growth temperatures[59]. Despite numerous reports of PECVD graphene synthesis with the growth temperatures lowered to ~ 450 – 700 °C [60-72], however, these temperatures are still much higher than the melting point of common polymers for growth of graphene on Cu ink. Therefore, a PECVD process conducted at

sufficiently low temperatures for organic substrates to withstand will be necessary to achieve direct growth of graphene on Cu ink.

In this study, we demonstrate a single-step PECVD-growth method that can both sinter and passivate the Cu ink without the need of active heating. We also investigate the effect of hydrogen-to-methane ratio and total pressure on the resulting graphene quality. Raman spectroscopic studies were employed to confirm the growth of graphene on Cu ink and to reveal different types of graphene defects under different hydrogen concentrations in the PECVD growth. The surface morphology characterization of graphene on Cu ink by the PeakForce tapping mode of the atomic force microscopy (PFT-AFM) and by scanning electron microscopy (SEM) along with cross-sectional high angle annular dark field scanning transmission electron microscopy (HAADF-STEM), revealed that the extent of sintering was also affected by the hydrogen concentration in the PECVD growth. X-ray photoelectron spectroscopy (XPS) indicated apparent reduction of surface CuO in the Cu ink after the PECVD process, and 4-point electrical transport measurements further demonstrated the reduction of electrical resistivity by more than 75% after PECVD growth of graphene on Cu ink. These findings therefore suggest a promising pathway via direct PECVD growth of graphene on Cu ink for scalable and industrially compatible IJP towards the applications of FHE and IoT.

2. Experimental method

2.1 Preparation of Cu ink on polyimide substrate

Polyimide on glass substrates were prepared by coating liquid polyimide (polyamic acid) on glass substrates by doctor blade and was baked through a series of temperatures at 80℃, 150℃, 220℃ , and 300℃ each for 30 minutes followed by 400℃ for 1 hr. The thickness of the polyimide film after baking was about 24 μm. Subsequently, Cu ink, which consisted of a mixture of Cu nanoparticles of mean diameters 300 nm and 20 nm with 7:3 ratio by weight, was coated on the polyimide layer by doctor blade. To solidify the Cu ink layer, the substrates

were then annealed under forming gas (5% H_2 in N_2) atmosphere for 30 minutes at 250°C. The thickness of Cu ink layer after annealing was about 15 μm.

2.2 PECVD graphene growth

The PECVD system consists of a Sairem microwave solid state generator at 2.45 GHz, an Evenson cavity, a quartz tube of ½" OD and a quartz sample holder. The base pressure of the system is 24 mtorr. Before inserting the samples into the reaction tube, both the interior of the tube and the quartz holder were cleaned first by Ar/O_2 plasma and then followed by Ar/H_2 plasma to remove potential organic residues on the tube wall. Prior to plasma excitation, H_2 and CH_4 gases were introduced simultaneously into the tube and controlled by mass flow controllers with the total gas flow set to 9 sccm. The total pressure was held at either 500 mtorr or 750 mtorr using the throttle valve. After the gas flow stabilized, the power of plasma was set at 10 W and the plasma was ignited with a tesla coil to start the growth. A schematic diagram of the PECVD system is shown in Figure 2.1. An image of how a sample was placed directly inside the plasma is shown in the inset of Figure 2.1. The temperature under this 10 W plasma power was about 160°C[67]. After 5 min, the power was set to zero while the same gas flow was kept to cool the sample.

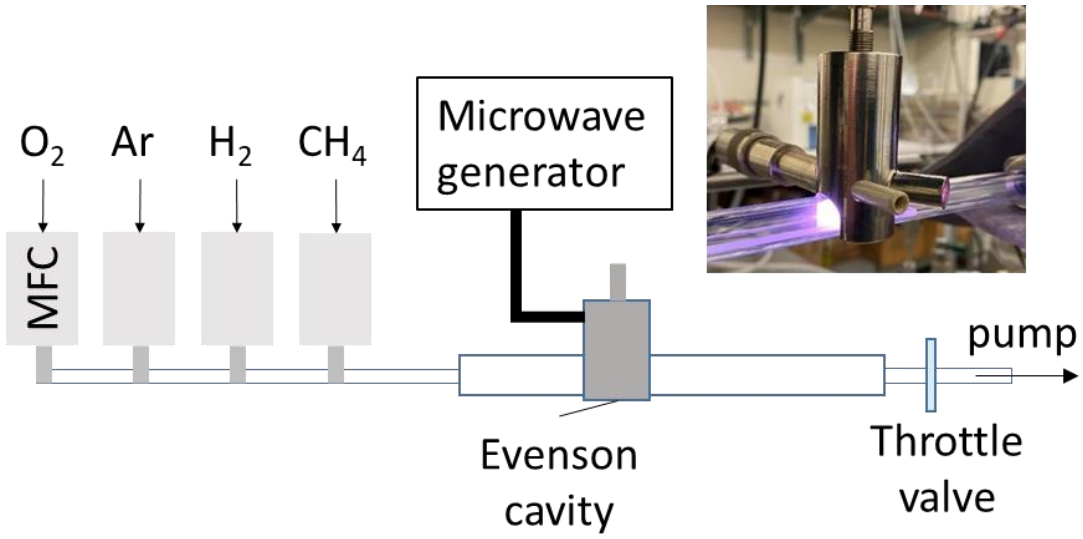

Figure 2.1: A schematic diagram of the PECVD system for direct graphene growth on Cu ink. The inset shows an image of PECVD graphene growth in process, where the sample was placed inside the plasma.

2.3 Characterization

Raman spectra were taken directly on the Cu ink after graphene growth by a Raman spectrometer (Renishaw, In-Via, and Renishaw M1000) with 514.3 nm laser, and the background signal of the Raman spectra was subtracted before peak fitting. The peaks of graphene Raman modes (D, G, D′, 2D) were fitted using the Lorentzian line shape with the peak height denoted as I(D), I(G), I(D′) and I(2D), respectively. The morphology was characterized by the PeakForce tapping mode of an atomic force microscope (PFT-AFM, Bruker Dimension Icon) using the ScanAsyst tip and also by a field emission scanning electron microscope (FESEM, ZEISS 1550VP). Additionally, cross-sectional Cs-corrected high angle annular dark field scanning transmission electron microscopy (HAADF-STEM) images were obtained by JEOL ARM-200F operating at 200kV. Here we note that during the STEM sample preparation, a layer of Os was coated on graphene to create an elemental contrast between graphene and the amorphous carbon. X-ray photoelectron spectroscopy (XPS, VG Scientific ESCALAB 250, monochromatic Al Kα) was used for elemental

analyses of samples. Resistivity of the samples was measured with a 4-point probe (Mitsubishi, MCP-T610) and the distance between electrodes was 1 mm.

3. Results and discussion

Representative sample appearance before and after the PECVD process was shown in Figure S2.1. The brighter appearance of Cu after the PECVD process suggested that surface oxide had been reduced.

Figures 2.2(a) and 2.2(c) are collections of Raman spectra on samples after PECVD under different H_2/CH_4 ratios and for a total pressure of 500 mtorr and 750 mtorr, respectively. We note that the H_2/CH_4 ratio defined here is the flow rate ratio. The presence of G and 2D peaks confirmed that graphene had been grown on Cu ink. Our results therefore indicated that plasma enhanced processes could largely reduce the growth temperature compared to thermal activation.

To make more quantitative analysis, we plotted in Figures 2.2(b) and 2.2(d) the peak intensity ratios of I(D)/I(G) versus the H_2/CH_4 gas ratio. Here we remark that the I(2D)/I(G) ratio was included in supplementary information (Figure. S2.2) for reference only because it was primarily associated with the interlayer coupling of graphene[104]. Instead, we were primarily interested in the analysis of I(D)/I(G), which provided information about the crystalline size and defect/edge density in graphene and so was indicative of the quality of graphene. We found that at a lower total pressure (500 mtorr), the I(D)/I(G) ratio was much less sensitive to the H_2/CH_4 gas ratio (Figs. 2.2(b) and 2.2(d)). This weaker dependence may be attributed to the higher rates of ion bombardment under a lower total pressure because of the longer ionic mean free paths that were less sensitive to the H_2/CH_4 gas ratio.

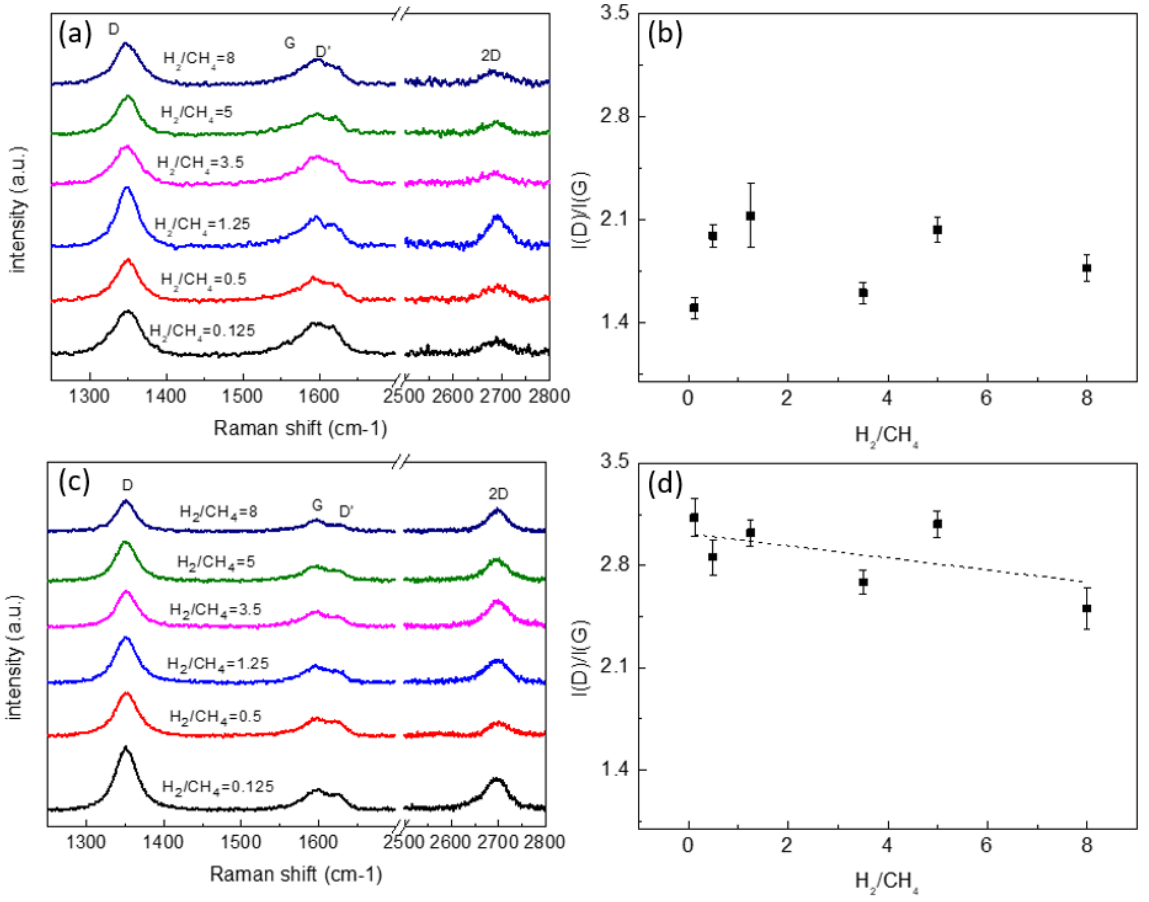

Figure 2.2: Raman spectral characteristics of graphene grown on Cu ink under different PECVD growth conditions: (a) Raman spectra of samples grown under a total gas pressure of 500 mtorr. (b) The intensity ratios of I(D)/I(G) for the spectra shown in (a) *vs* the H_2/CH_4 gas ratio. (c) Raman spectra of samples grown under a total gas pressure of 750 mtorr. (d) The intensity ratios of I(D)/I(G) for the spectra shown in (c) *vs* the H_2/CH_4 gas ratio.

On the other hand, the I(D)/I(G) ratio under a higher total pressure (750 mtorr) exhibited more dependence on the H_2/CH_4 gas ratio. Noting that the ion bombardment was more suppressed under a higher total gas pressure due to reduced ionic mean free paths, the main factor that contributed to the varying graphene quality may be related to the variation of the electron temperature with the H_2/CH_4 ratio. Specifically, it has been shown theoretically[105-106] and verified experimentally[107] that the electron temperature of the plasma containing CH_4 would be lower than that containing H_2 for a given plasma condition because of a larger

ionization energy of H_2 than that of CH_4. As the CH_4 concentration decreased, the electron temperature would increase, thus enhancing the reaction tendency and leading to reduced I(D)/I(G). It is worth noting that the electron temperature is not a strong function of the total gas pressure under high frequency excitation, as discussed in Supplementary section 2.2. Thus, we may attribute the variations of electron temperature in the plasma to the varying H_2/CH_4 gas ratio.

The I(D)/I(G) ratio of graphene is known to be representative of the defect concentration in the sample. While the I(D)/I(G) ratio typically increases with increasing defect concentration, it could exhibit an opposite trend in the limit of high defect concentrations[108-110]. Therefore, to reveal whether the decaying trend of I(D)/I(G) with H_2/CH_4 implied an increase or a decrease of defect concentration, we further considered the I(D′)/I(G) ratio as a function of the H_2/CH_4 gas ratio (see Figure 2.3(a)) and the relationship between I(D)/I(G) and I(D′)/I(G), as shown in Figure 2.3(b). We found that similar to the behavior of I(D)/I(G), the I(D′)/I(G) ratio also exhibited a decreasing trend with H_2/CH_4, and that the ratios of I(D)/I(G) and I(D′)/I(G) showed clear proportionality as expected in the limit of low defect concentration,[111] Our experimental findings therefore suggested that a higher H_2/CH_4 ratio led to a lower defect density because of the resulting increase of electron temperature that enhanced the reaction tendency[107].

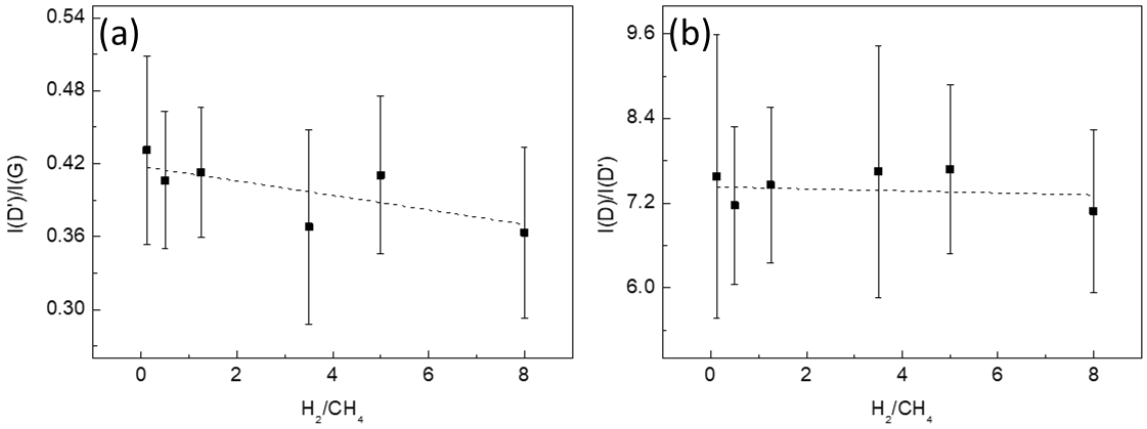

Figure 2.3: Comparison of the I(D′)/I(G) and I(D)/I(D′) ratios of samples of graphene on Cu ink taken under a total pressure of 750mtorr: (a) I(D′)/I(G) *vs.* H_2/CH_4 (b) I(D)/I(D′) *vs.* H_2/CH_4.

As Eckmann *et al*[111] had shown previously, the ratio of I(D)/I(D') plot could also reveal the nature of the defects, which was a method already employed by several works[109, 112]. Following the similar procedure, we note that in Figure 2.3(b), the ratio of I(D)/I(D′) across the entire range of H_2/CH_4 ratios was about 7.2, which may be associated with primary defect structures of vacancies.[58]

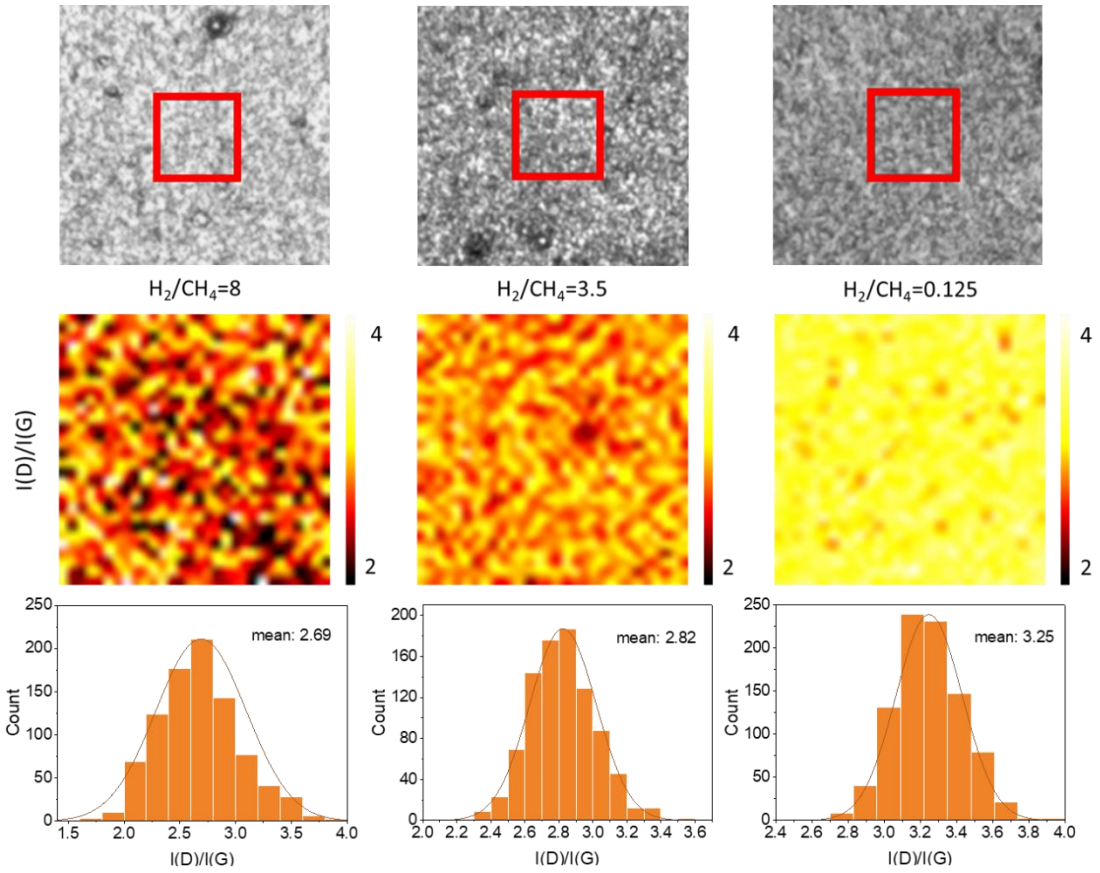

Figure 2.4: Raman spectral maps of graphene grown on Cu ink with three different H_2/CH_4 ratios of 8, 5 and 0.125 at 750 mtorr. The top row are the optical images with the red box indicating the mapped region of (15×15) μm^2. The second row correspond to maps of the I(D)/I(G) ratios taken over areas indicated above, and the third row are the histograms of the I(D)/I(G) maps.

To confirm the validity of aforementioned findings over extended sample areas, we show in Figure 2.4 the Raman spectral maps and histograms taken on (15×15) μm^2 areas of graphene grown on Cu ink with three different H_2/CH_4 ratios under a total pressure of 750 mtorr. The average values of the I(D)/I(G) ratio for H_2/CH_4 = 8, 5 and 0.125 were 2.69, 2.82 and 3.25, respectively, which were in agreement with the trend shown in Figure 2.2.

To understand the effect of PECVD on the surface morphology of Cu ink, we studied the sample images by scanning electron microscopy (SEM) and cross-sectional HAADF-STEM. Figure 2.5 shows the SEM and cross-sectional HAADF-STEM images of Cu ink taken before and after PECVD with a total pressure of 750 mtorr for H_2/CH_4 = 0.125 and 8, respectively. We found that before PECVD, the morphology of Cu ink was consistent with dispersed particles, as shown in Figures 2.5(a) and 2.5(b) for the images taken by SEM and HAADF-STEM, respectively. After PECVD, the Cu ink particles were sintered and became connected, as exemplified in Figures 2.5(c) and 2.5(d) for the SEM and HAADF-STEM images taken on Cu ink with H_2/CH_4 = 0.125, and similarly in Figures 2.5(e) and 2.5(f) for images of Cu ink with H_2/CH_4 = 8. In particular, we note that the connectivity among Cu ink particles was much more complete for PECVD growth with a larger H_2/CH_4 ratio (= 8). Additionally, the HAADF-STEM images revealed that the effective heating depth of the PECVD process was about 1 μm, and that a larger H_2/CH_4 ratio resulted in a slightly deeper heating depth, as exemplified in Figures 2.5(d) and 2.5(f). In contrast to the sub-nanometer heating depth found in the remote plasma process of plasma enhanced atomic layer deposition (PEALD)[113], our PECVD process involving direct plasma apparently facilitated a more energy-efficient thermal process. Thus, for a Cu layer thickness less than 1 μm, we anticipate that the entire Cu layer could undergo the sintering process from PECVD.

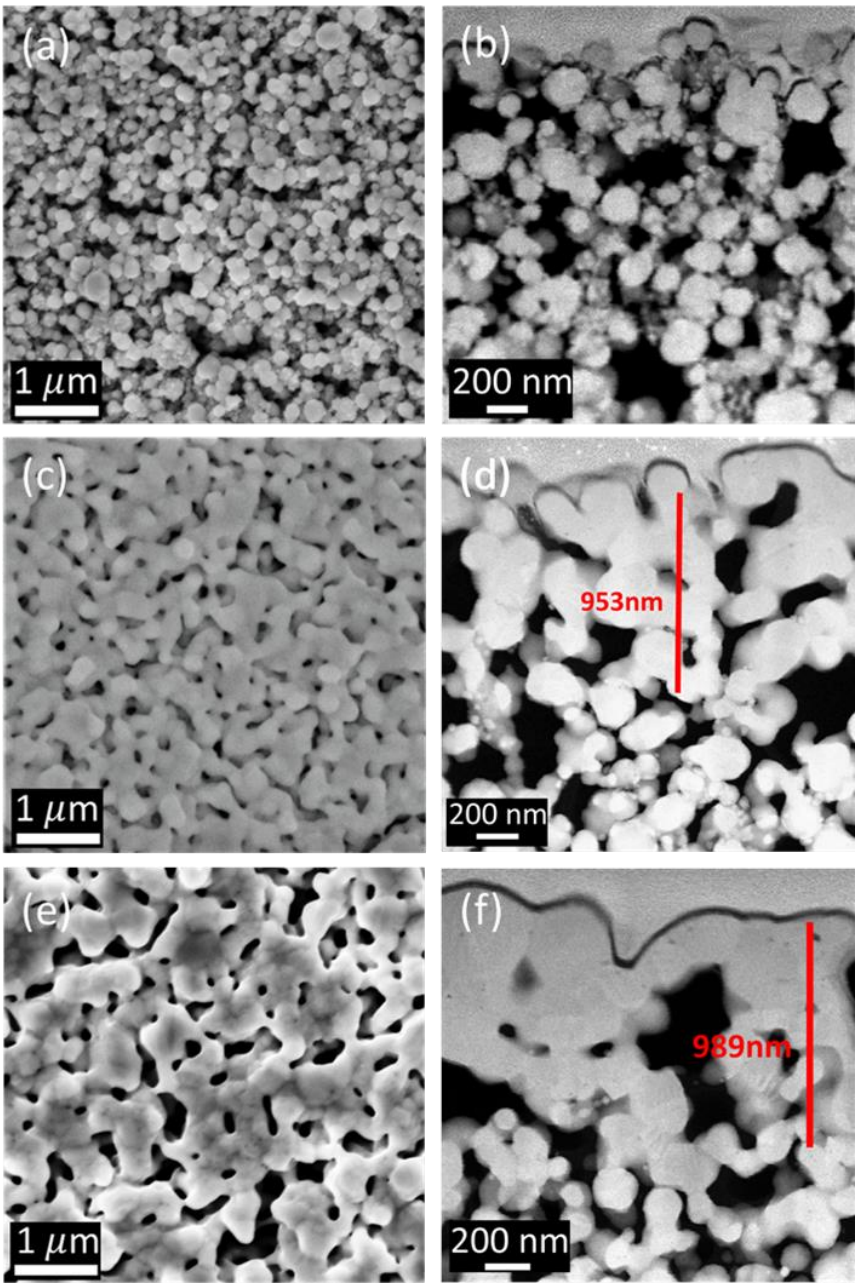

Figure 2.5: SEM and STEM images (a) SEM image of Cu ink before PECVD. (b) HAADF-STEM image of Cu ink before PECVD. (c) SEM and (d) HAADF-STEM images of Cu ink after PECVD with H_2/CH_4 = 0.125 and total pressure = 750 mtorr. (e) SEM and (f) HAADF-STEM images of Cu ink after PECVD with H_2/CH_4 = 8 and total pressure = 750 mtorr. The red lines in (d) and (f) indicate the approximate heating depths of the PECVD process under H_2/CH_4 = 0.125 and 8, respectively. The STEM images were acquired by ITRI.

Under a higher magnification, the Z contrast of HAADF-STEM imaging revealed the thickness of the graphene. As shown in Figure 2.6, the thickness of graphene corresponded to bilayer and monolayer for H_2/CH_4 = 0.125 and H_2/CH_4 = 8 at 750 mtorr, respectively. For comparison, the high-mag HAADF-STEM image of the sample before PECVD was shown in Figure S2.3. In contrast to Figure 2.6, the absence of a clear Z-contrast between Cu and Os in Figure S2.3 indicated that no graphene was present on the Cu surface and that the clear interface Z-contrast in Figure 2.6 was due to the PECVD grown graphene instead of adsorbed carbon from air exposure. The main mechanism of forming monolayer graphene on Cu was dominantly from surface adsorption due to the low carbon solubility of Cu[49]. For PECVD, the active species such as C_2 formed in the plasma environment could deposit on the first layer of graphene, forming bilayer graphene[114].

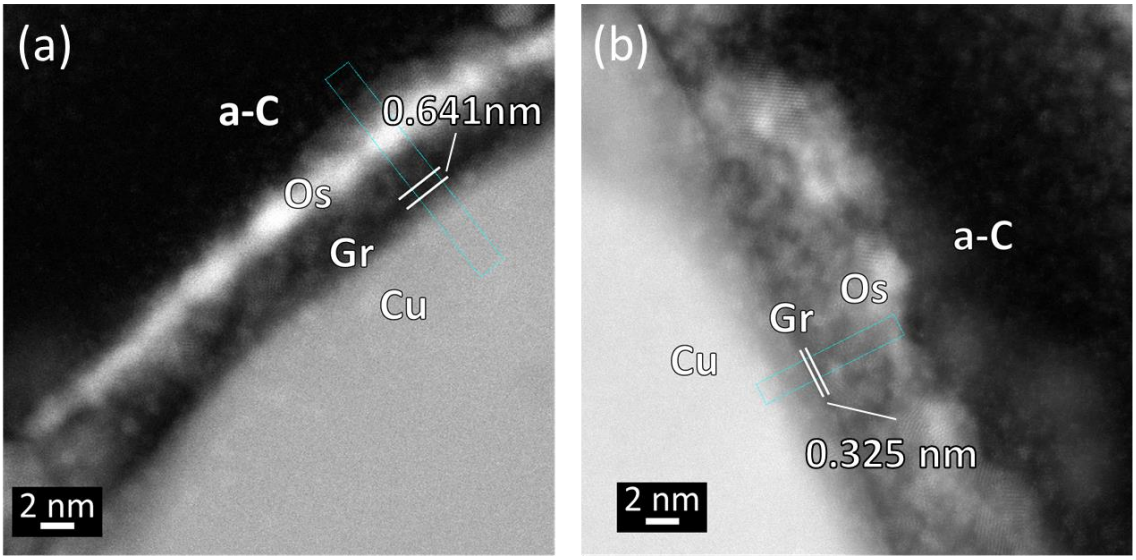

Figure 2.6: Magnified HAADF-STEM images of graphene Cu ink after PECVD with a total pressure of 750 mtorr and H_2/CH_4 (a) = 0.125, (b) = 8. Here "a-C" refers to amorphous carbon and "Gr" represents graphene. The intensity slices (green rectangle region) for both (a) and (b) were included in Figure S2.3. The STEM images were acquired by ITRI.

The aforementioned observation may be understood by the fact that the higher electron temperature associated with a larger H_2/CH_4 ratio in the PECVD process helped enhance the

surface diffusion of the Cu ink[107]. In addition, noting that the energy of ions impinging a surface in contact with the plasma is given by $e\phi$, where e is the electron charge, ϕ represents the floating potential:[105-106]

$$\phi = -\frac{k_B T_e}{2e}\left(1 + \ln\left(\frac{m_i}{2\pi m_e}\right)\right), \tag{2.1}$$

and k_B, T_e, m_i, m_e denote the Boltzmann constant, electron temperature, ion mass and electron mass, respectively, a larger H_2/CH_4 ratio would increase the ion energy according to Eq. (2.1) and facilitate the surface reaction.

Further studies of the surface morphology of Cu ink after PECVD were carried out by atomic force microscopy (AFM). Representative AFM images of samples grown at $H_2/CH_4 = 8$ and $H_2/CH_4 = 0.125$ are shown in Figures 2.7(a) and 2.7(b), respectively. We examined the highly connected regions for both cases as indicated by the red boxes and found that the corresponding RMS roughness was 15.1 nm and 45.2 nm, respectively, indicating smoother surfaces of the connected region after PECVD with a larger H_2/CH_4 ratio, which were more beneficial to better quality graphene growth. A schematic of the observed roughness differences due to different H_2/CH_4 ratios is shown in Figure 2.7(c). It is noted, however, that these measurements are based on single points per sample, which may introduce location-specific bias.

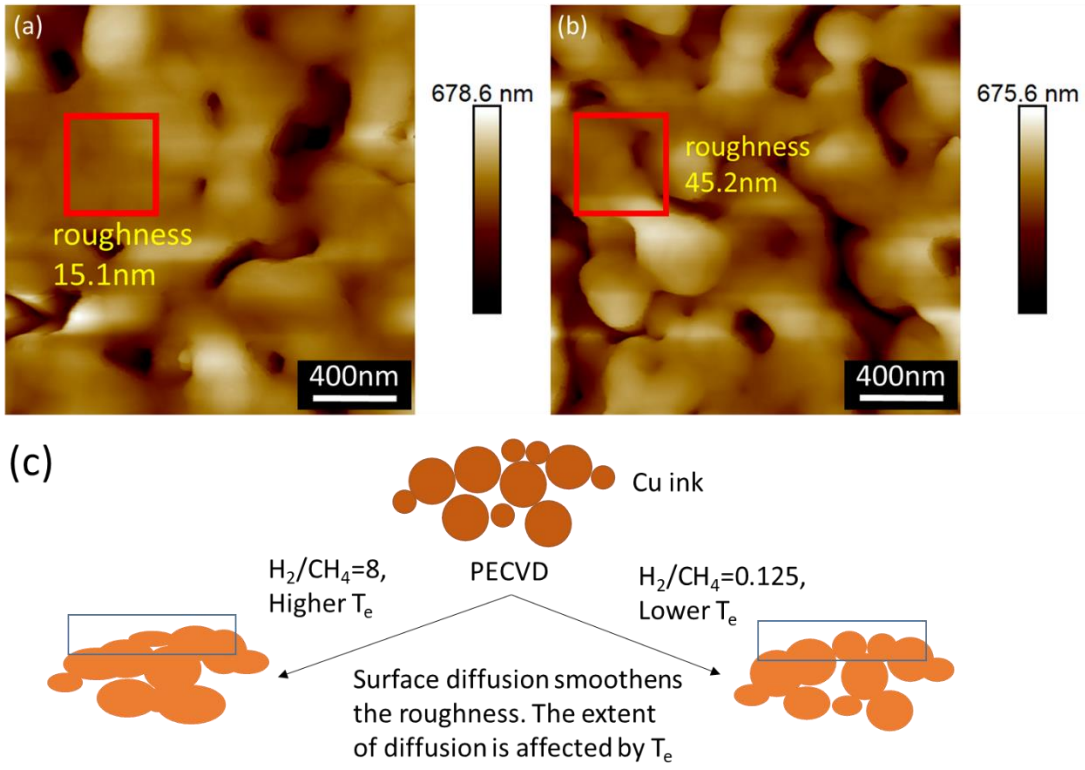

Figure 2.7: AFM images of the samples (a) after PECVD with H_2/CH_4 = 8, 750 mtorr; and (b) after H_2/CH_4 = 0.125, 750 mtorr. Here the values of the surface roughness obtained in the areas indicated by the red boxes in (a) and (b) were obtained by calculating the RMS roughness of the selected regions. (c) A schematic showing the observed roughness differences due to different H_2/CH_4 ratios.

The changes in the chemical state of Cu ink after the PECVD process were examined by X-ray photoelectron spectroscopy (XPS) as shown in Figure 2.8. The absence of the shake-up satellite peaks associated with Cu^{2+} indicated that the graphene covered samples after PECVD were free of CuO. We further note that all samples were stored under ambient condition prior to the XPS studies so that the absence of CuO in graphene-covered samples also demonstrated that graphene was suitable to serve as a passivation layer for Cu ink.

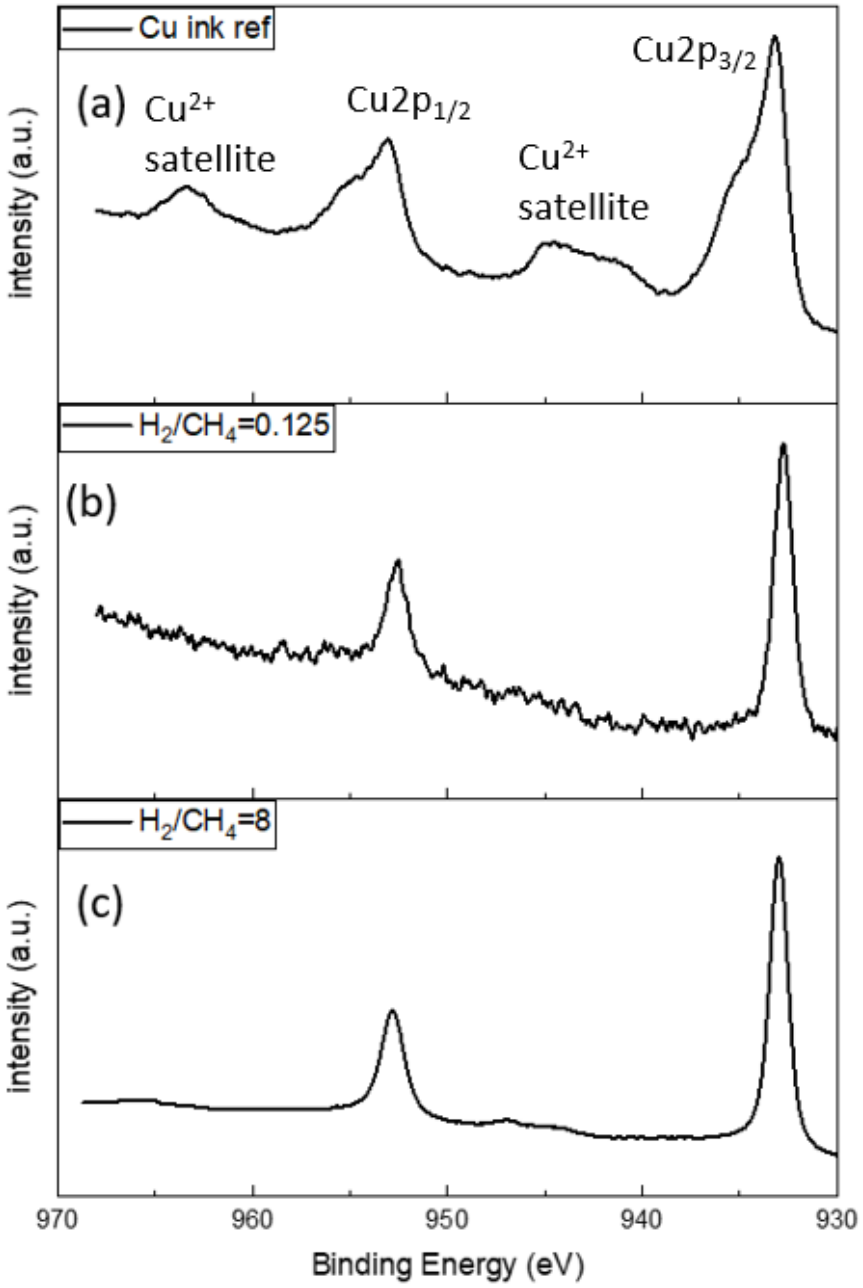

Figure 2.8: XPS Cu-2p spectra taken on Cu-ink samples: (a) before PECVD; (b) after PECVD with growth conditions of H_2/CH_4 = 0.125 and total pressure = 750 mtorr; and (c) after PECVD with H_2/CH_4 = 8 and total pressure = 750 mtorr. The XPS spectra were acquired by ITRI.

Given that Cu^{+} and Cu^{0} were indistinguishable in the XPS Cu-2p spectrum[115], Cu $L_3M_{45}M_{45}$ region were scanned via X-ray excited Auger spectroscopy (XAES) as shown in Figure 2.9 to distinguish between Cu_2O and Cu. The peak-to-peak ratio from Figures 2.9(b) and 2.9(d) suggested that both $H_2/CH_4 = 8$ and $H_2/CH_4 = 0.125$ have similar ratios of Cu_2O : Cu. The absence of a peak at ~ 917.7 eV indicated that there was no Cu^{2+}, which was in line with the absence of Cu^{2+} satellites in the XPS Cu-2p spectra as shown in Figures 2.8(b) and 2.8(c). The reduction of Cu ink from CuO to Cu_2O instead of pure Cu is due to the two-step reduction path of CuO nanoparticles where metallic Cu would not form without long reduction time (> 45 min)[116]. It was also reported that whether the reduction of CuO to Cu underwent a single-step or a two-step process depended on the size of the nanoparticle[116]. Therefore, we expect that further optimization of the particle size of Cu ink and the PECVD process could lead to less surface Cu oxide species.

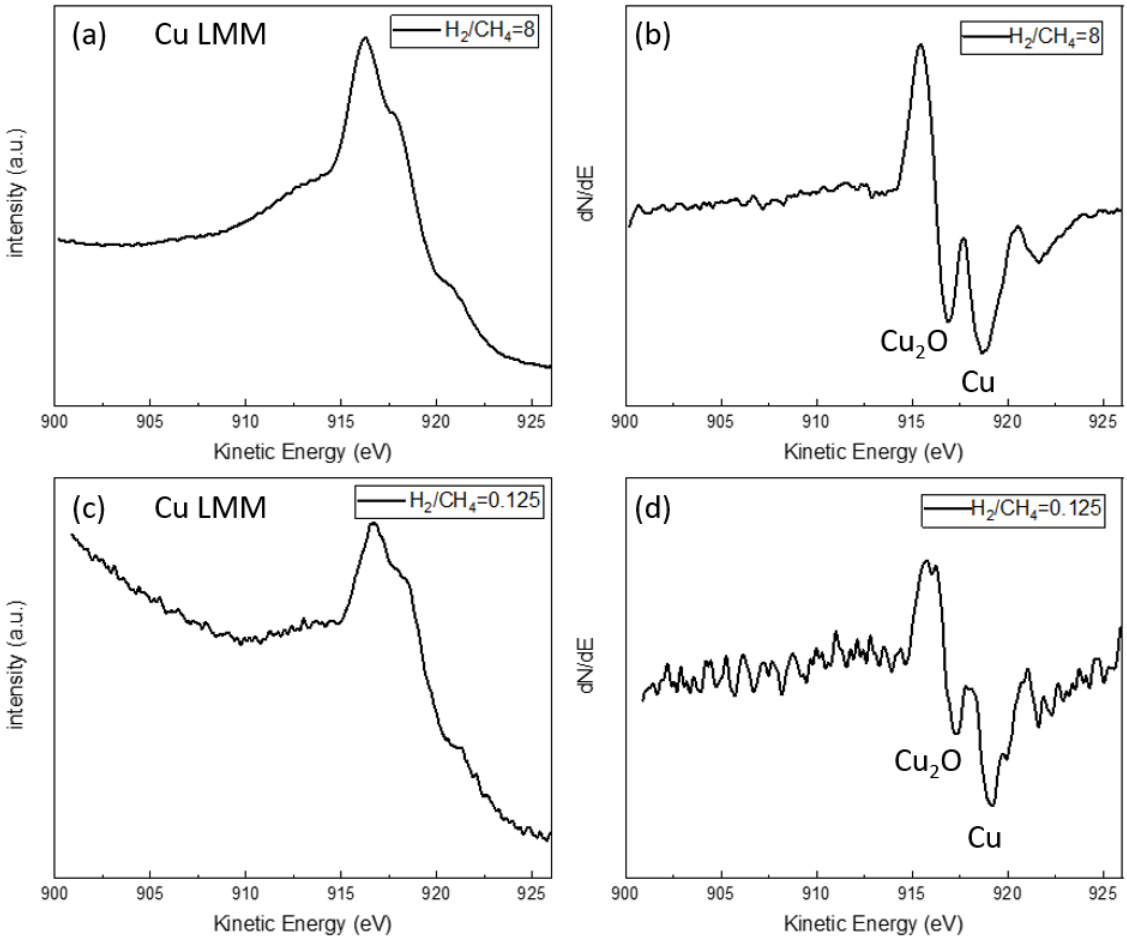

Figure 2.9: XAES Cu LMM spectra of samples after PECVD: (a) with H_2/CH_4 = 8, total pressure = 750 mtorr; (b) differential spectrum of (a); (c) with H_2/CH_4 = 0.125, total pressure = 750 mtorr; and (d) differential spectrum of (c). The XAES spectra were acquired by ITRI.

Finally, we examined the electrical properties of the Cu ink samples before and after the PECVD process, and the resistivity data were tabulated in Table 2.1. The much-reduced resistivity after PECVD may be attributed to both the sintering of Cu ink and the coverage of graphene. The difference in resistivity between the conditions of H_2/CH_4 = 8 and H_2/CH_4 = 0.125 may be attributed to the extent of sintering as shown in Figures 2.5(c) – (f), where

the Cu ink was more connected under the $H_2/CH_4 = 8$ condition and additional conduction paths through graphene were formed so that the resistivity became smaller.

Table 2.1. Resistivity of the Cu ink before and after PECVD. The resistivity were acquired by ITRI.

750 mtorr	Cu ink ref	H_2/CH_4 = 8	H_2/CH_4 = 5	H_2/CH_4 = 3.5	H_2/CH_4 = 1.25	H_2/CH_4 = 0.5	H_2/CH_4 = 0.125
Resistivity ($m\Omega \cdot cm$)	0.154(1)	0.0376(2)	0.0523(4)	0.0552(2)	0.0605(2)	0.0646(7)	0.0817(1)

4. Conclusion

In this work we have demonstrated single-step direct growth of graphene on Cu ink/polyimide by means of PECVD without the need of active heating. The low-temperature process was shown to be compatible with polymer substrates commonly used in flexible electronics. The PECVD process on Cu ink not only reduced and sintered the Cu ink but also created a graphene passivation layer on the ink, which led to prevention of oxidation and significant reduction in the resistivity of the Cu ink. Further investigation of several growth conditions revealed that graphene growth was more sensitive to the H_2/CH_4 ratio under a higher total gas pressure. Additionally, the defect structures in the PECVD-grown graphene were independent on the H_2/CH_4 ratio, showing predominantly vacancy-type defects for the inspected H_2/CH_4 ratio. The morphology of the Cu ink after PECVD and the dependence of graphene quality on the H_2/CH_4 ratio were attributed to the differences in the electron temperature of the plasma under different H_2/CH_4 ratios. Our low-temperature PECVD process for direct graphene growth on Cu ink/polyimide and our understanding of how to control the resulting graphene quality therefore paves a new pathway towards incorporating graphene/Cu ink/polyimide into hybrid flexible electronics.

Supporting Information

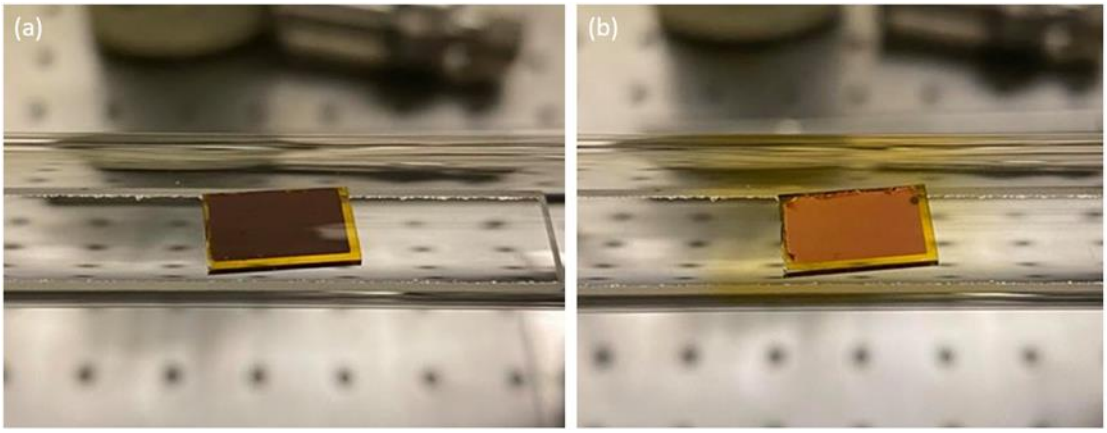

Figure S2.1: Images of the Cu ink sample (a) before PECVD and (b) after PECVD.

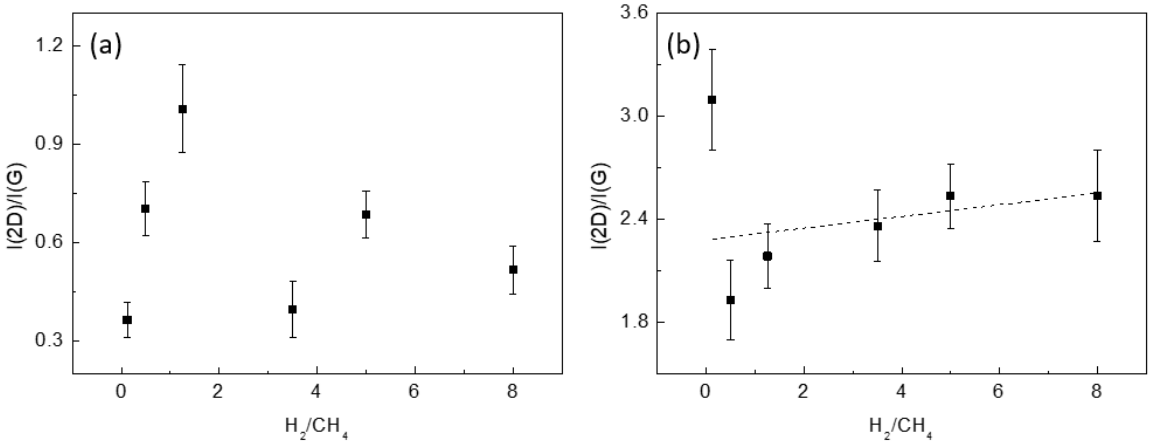

Figure S2.2. I(2D)/I(G) vs H_2/CH_4 at (a) 500 mtorr and (b) 750 mtorr.

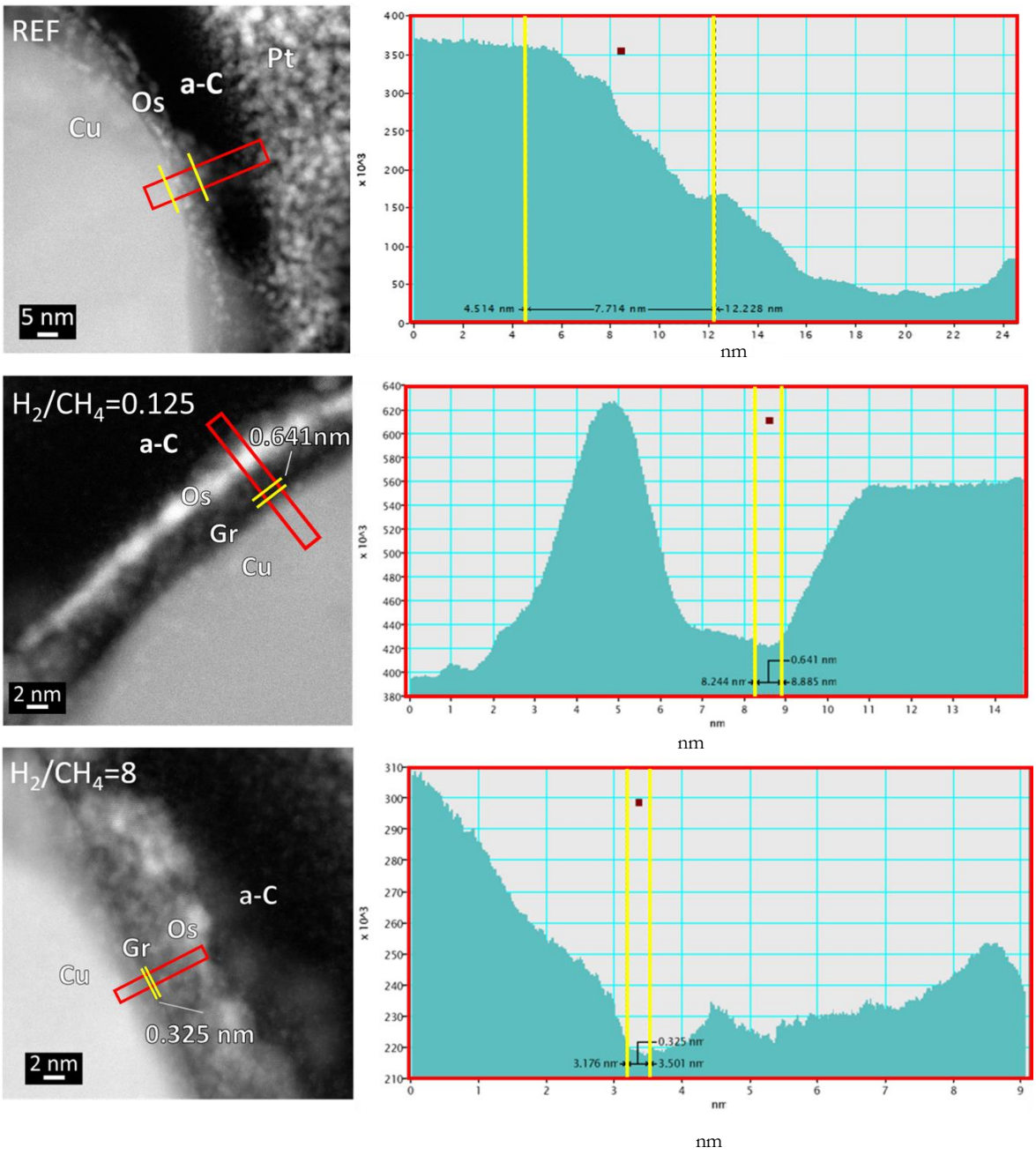

Figure S2.3: HAADF-STEM image of the Cu ink before and after PECVD of 750mtorr with the corresponding intensity slices. The STEM images were acquired by ITRI.

Section 2. Derivation of the dependence of electron temperature on total pressure

The equation of motion of electrons under the applied oscillating electric field E(t) = $E_0\exp(i\omega t)$ may be written as:

$$m_e \frac{dv_e}{dt} = -eE_0 \exp(i\omega t) - m_e \nu \mathrm{v}_e, \tag{1}$$

where E_0: electric field amplitude, ω: the frequency of the applied electric field, ν: the collision frequency between electron and the neutral, which is proportional to pressure, v_e: the velocity of the electron and m_e: the mass of the electron. Solving for v_e yields:

$$\mathrm{v}_e = -\frac{eE(t)}{m_e\,(\nu^2+\omega^2)}(\nu - i\omega). \tag{2}$$

The time-averaged power absorbed by an electron is:

$$\theta_a = Re\left(\frac{F\cdot v_e^*}{2}\right) = Re\left(-\frac{eE\mathrm{v}_e^*}{2}\right) = \frac{e^2}{2m_e}\frac{\nu}{\nu^2+\omega^2}E_0^2 \tag{3}$$

and the time-averaged kinetic energy of the electron is:

$$E_k = \frac{1}{2}m_e Re(\frac{\mathrm{v}_e\mathrm{v}_e^*}{2}) = \frac{3}{2}k_b T_e. \tag{4}$$

Therefore comparing eq(3) and eq(4), we have:

$$\theta_a = 2\nu E_k \text{ or } T_e = \frac{e^2E_0^2}{6k_b m_e}\frac{1}{\nu^2+\omega^2}. \tag{5}$$

Under microwave excitation, where $\frac{\omega}{\nu} \gg 1$ we can approximate eq(5) as:

$$T_e \approx \frac{e^2E_0^2}{6k_b m_e}\frac{1}{\omega^2}. \tag{6}$$

Therefore, the electron temperature is independent of the collision frequency or pressure.

Chapter III

POLYMER-COMPATIBLE LOW-TEMPERATURE PLASMA-ENHANCED CHEMICAL VAPOR DEPOSITION OF GRAPHENE ON ELECTROPLATED CU FOR FLEXIBLE HYBRID ELECTRONICS

Adapted from:
Lu, C.-H.; Leu, C.-M.; Yeh, N.-C. Polymer-Compatible Low-Temperature Plasma-Enhanced Chemical Vapor Deposition of Graphene on Electroplated Cu for Flexible Hybrid Electronics. ACS Applied Materials & Interfaces 2021, 13 (34), 41323-41329, DOI: 10.1021/acsami.1c11510.

Personal contribution: I participated in the conception of the project, grew the PECVD graphene, performed AFM and Raman measurements, interpreted the data, and I wrote the draft manuscript.

Flexible hybrid electronics (FHE) and fan-out redistribution layers (RDL) rely on electroplating Cu on polymer. In this work, direct low-temperature plasma enhanced chemical vapor deposition (PECVD) of graphene on electroplated Cu over polyimide substrates is demonstrated, and the deposition of graphene is found to passivate and strengthen the electroplated Cu circuit. The effect of the H_2/CH_4 ratio on the PECVD graphene growth is also investigated, which is shown to affect not only the quality of graphene but also the durability of Cu. A 100,000 cycles of folding with a bending radius of 2.5 mm and the corresponding resistance tests are carried out, revealing that Cu circuits covered by graphene grown with a higher H_2/CH_4 ratio can sustain many more bending cycles. Additionally, graphene coverage is shown to suppress the formation of copper oxides under ambient environment for at least 8 weeks after the PECVD process.

1. Introduction

Flexible hybrid electronics (FHE) have been under increasing demands because their light weight and flexible characteristics are favorable for a wide range of applications in such areas as automotive sensors,[74] wearable sensors,[117] flexible display,[118] and smart packaging radio-frequency identification (RFID).[119] These applications typically involve heterogeneous

integration of a large number of chips with different functionalities, and therefore require the fan-out wafer/panel-level packaging (FOWLP/FOPLP) where a high-density redistribution layer (RDL) plays an essential role for electrical connections between chips. A typical choice for the metal wiring on the RDL is Cu by electrochemical deposition (ECD). Nevertheless, as the density of Cu wires on the RDL increases, electromigration of Cu due to high current densities becomes a serious issue that must be addressed, and a solution to strengthen the Cu wires on the RDL while maintaining high conductivity is also required.

Meanwhile, two-dimensional (2D) materials have been under the spotlight for applications in flexible electronics because of their atomic-scale thicknesses. In particular, the unique physical properties of graphene have found a variety of applications such as surface passivation,[120] antennas,[121] sensors[122] and transparent conductive films.[123] Additionally, graphene has been shown to effectively improve the reliability and conductivity of Cu wires when deposited on them.[124-125] Therefore, graphene coverage of Cu wires on the RDL is expected to be a viable solution to the aforementioned issues facing the development of FHE.

Among the methods for graphene synthesis, mechanical exfoliation and chemical vapor deposition (CVD) at high temperatures are the most common approaches. Typical thermal CVD graphene synthesis requires a growth temperature near or above the melting point of the metal foils used as the substrates.[49, 51] Under such high temperatures, evaporated metal and the aged quartz furnace could cause contamination[54] in addition to the incompatibility with most device processing. Over the years, progress has been made to lower the CVD growth temperature to 300°C [126] or even close to room temperature.[55-56] Nevertheless, these methods are either incompatible with targeted substrate materials, or involves specific processes that are not scalable for industrial production. For instance, the reported CVD graphene growth temperature reduction involved benzene as the precursor,[126] which could dissolve polymer substrates. Other approaches involve graphene nuclei preparation at 1050°C [55] or the application of high pressure,[56] which are also harsh conditions incompatible with polymer substrates. Although graphene may be synthesized with the aforementioned approaches on metallic substrates and then transferred to polymer substrates, the transfer

process is not only time-consuming but also potentially damaging to graphene quality. Moreover, the transferred graphene typically exhibits poor adhesion to the targeted substrates.[58]

An alternative approach for low-temperature graphene synthesis that is both scalable for industrial processes and compatible with polymer substrates is plasma-enhanced chemical vapor deposition (PECVD). Unlike thermal CVD where reacting species are generated through pyrolysis, PECVD utilizes plasma to generate radicals and energetic species, which creates a reactive environment to lower the growth temperature. However, typical graphene growth temperatures by PECVD are still in the range of around 400-700 °C, which is still higher than the melting point of typical polymers. Thus, it is necessary to develop a PECVD process for graphene synthesis that could be operated at a temperature where organic substrates could withstand.

In this study, we report a polymer-compatible PECVD graphene growth method on electroplated Cu thin films by means of direct plasma without the need of active heating, and demonstrate that the graphene deposition leads to Cu passivation and durability enhancement for folding. The effect of hydrogen-to-methane ratio on the graphene quality is also investigated. To characterize the quality of graphene grown on electroplated Cu, Raman spectroscopic studies and X-ray photoelectron spectroscopy (XPS) were employed. The surface morphology of graphene on electroplated Cu was investigated by the PeakForce tapping atomic force microscopy (PFT-AFM), which revealed that the Cu surface was smoothened after PECVD growth and that the morphology was not strongly dependent on the hydrogen concentration. Studies of the PECVD-grown samples by cross-sectional high-angle annular dark field scanning transmission electron microscopy (HAADF-STEM) further showed that the deposited graphene was bilayer when synthesized under high hydrogen concentrations, which also resulted in better graphene quality. XPS studies confirmed the graphene coverage over electroplated Cu and further indicated that native oxides on the Cu surface were removed during the PECVD process. Moreover, graphene coverage was shown to suppress the formation of copper oxides under ambient environment

for at least 8 weeks after the PECVD process. Measurements of the electrical resistance of graphene on Cu/polymer samples after folding inward for 100,000 times with a bending radius of 2.5 mm uncovered that PECVD graphene not only lowered the resistance but also increased the durability of the Cu circuit significantly. Additionally, the durability enhancement by the deposition of PECVD-grown graphene was found to be dependent on the hydrogen-to-methane ratio. Our work therefore presents the process of direct low-temperature PECVD graphene growth as a scalable and industrially compatible approach to achieving passivation and durability enhancement of electroplated Cu on polymer for FHE applications.

2. Experimental method

2.1 Structure of electroplated Cu substrates

The substrates provided by the Industrial Technology Research Institute (ITRI) consist of the following layered structures from bottom up: polyimide (15 μm), silicon nitride (200 nm), sputtered Ti (100 nm) as an adhesion layer, sputtered Cu (200 nm) as a seed layer, and electroplated Cu (2 μm).

2.2 PECVD graphene synthesis

The PECVD graphene growth chamber consists of a quartz tube of ½" outer diameter and quartz sample holders, which operates with a base pressure of 24 mtorr. The plasma was generated by an Evenson cavity connected to Sairem solid-state microwave generator fixed at 2.45 GHz, which led to direct plasma within the volume of the growth chamber enclosed by the cavity. Before placing the sample into the sample holders, the holders were cleaned with both Piranha solution (H_2SO_4 : H_2O_2 = 3:1 in volume, mixed at room temperature) and Ar/O_2 gas flow, followed by Ar/H_2 plasma cleaning to remove potential organic residues. Note that Piranha solution is highly corrosive and so care must be taken when handling. Before plasma excitation, both H_2 and CH_4 gases were introduced into the growth chamber by mass flow controllers, and the total pressure of the system was fixed at 750 mtorr. The

plasma power was set at 8 W for the PECVD growth, which was started after the gas flow stabilized. The temperature change during the growth was recorded via a thermocouple attached on the quartz tube as shown in Figure S3.1. The maximum temperature reached during the PECVD growth was about 100 ℃. After 10 minutes, the plasma was turned off with the gas flow maintained until the sample completely cooled down to room temperature.

2.3 Characterization

Raman spectra were taken on the graphene covered Cu by a Raman spectrometer (Renishaw, In-Via) with a 514.3 nm laser and a spatial resolution of 0.5 μm. The peaks of graphene Raman modes (D, G, 2D) were fitted by the Lorentzian lineshape. The corresponding peak intensities were denoted as I(D), I(G) and I(2D), respectively. The surface topography and morphology were characterized by the PeakForce tapping atomic force microscopy with a ScanAsyst probe (PTF-AFM, Bruker Dimension Icon). X-ray photoelectron spectroscopy (XPS) was collected via the Surface Science Instruments M-Probe ESCA with Al K_α of 1486.6 eV X-ray source and a hemispherical energy analyzer using a pass energy of 25 eV. The X-ray spot size was (500 × 1200) μm^2, and the instrument work function was calibrated with respect to Au $4f_{7/2}$. Cross-sectional transmission electron microscopy (TEM) images were acquired by Cs-corrected JEOL ARM-200F with 200 kV acceleration voltage under the high-angle annular dark field scanning transmission electron microscopy (HAADF-STEM) mode. A layer of metal oxide was coated during the TEM sample preparation as a protecting layer. The folding test was conducted by using a piece of custom-built equipment at ITRI with a bending radius of 2.5 mm. Electrical resistance of samples was measured using a Keithley 2400 source meter.

3. Results and discussion

In Figure 3.1(a) we show the Raman spectra of PECVD graphene grown at different ratios of H_2/CH_4 flow rates. The distinct signatures of graphene Raman modes (D, G, D′, 2D) indicated successful graphene growth for all H_2/CH_4 ratios. Our results confirmed that PECVD processes could substantially reduce the required growth temperatures when

compared to thermal CVD processes. To evaluate the effect of the H_2/CH_4 ratio on the quality of graphene, the intensity ratio I(D)/I(G) and the estimated graphene grain size L *vs.* H_2/CH_4 were plotted in Figure 1(b). Specifically, the graphene grain size L or distance between defects could be estimated by the I(D)/I(G) ratio as follows:[127]

$$\mathrm{L(nm)} = \frac{560}{E_{laser}^4}\left(\frac{I_D}{I_G}\right)^{-1} \quad (1)$$

where $E_{laser} = 2.41$ eV in our case.

As shown in Figure 3.1(b), higher H_2/CH_4 ratios lead to larger grain sizes of graphene. As we shall discuss later, the grain size is an important factor that affects the durability of the Cu circuit pattern. Additional Raman spectroscopic characterizations of samples grown under different H_2/CH_4 ratios are shown in Figure S3.2 and Figure S3.3 for the I(D)/I(G) and I(2D)/I(G) spatial maps across (30×30) μm^2, respectively, along with the corresponding histograms where each histogram consists of 225 point spectra.

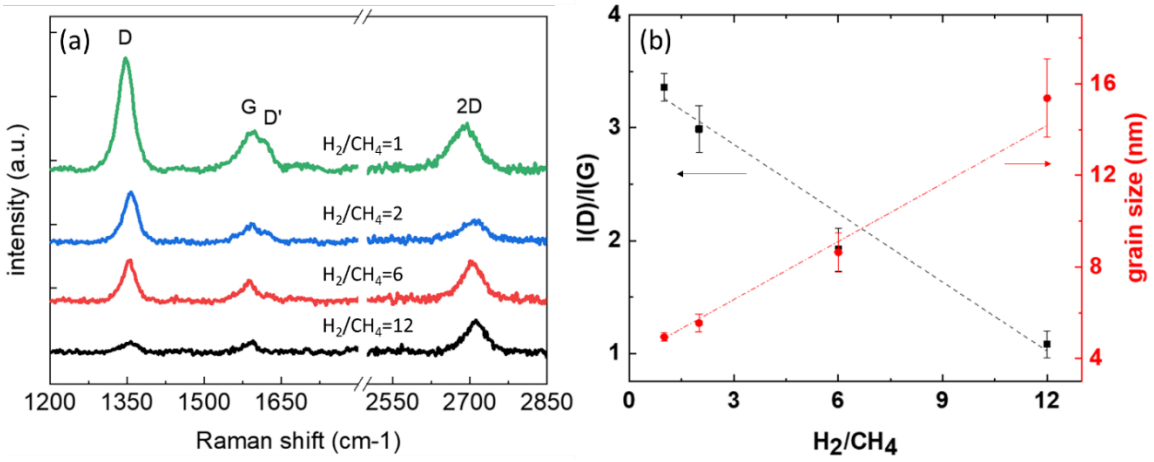

Figure 3.1. Raman spectra measurement (a) Representative Raman spectra of PECVD graphene grown at different H_2/CH_4 ratios. (b) The I(D)/I(G) intensity ratio and graphene grain size L *vs.* H_2/CH_4 ratio. Here the error bar associated with each H_2/CH_4 ratio was calculated from analyzing 225 Raman spectra.

The decreasing trend of I(D)/I(G) *vs.* H_2/CH_4 could be the result of both defective graphene etched by hydrogen[128] and the increased electron temperature in the plasma for higher H_2 concentration.[120] Since the samples were directly in contact with plasma without external bias, the magnitude of the ion bombardment energy due to the floating potential ϕ_f is given by the difference between the floating potential and plasma potential ϕ_p:[105]

$$e|\phi_f - \phi_p| = \frac{k_B T_e}{2}\left(1 + \ln\left(\frac{m_i}{2\pi m_e}\right)\right), \quad (2)$$

where e is the electron charge, k_B the Boltzmann constant, T_e the electron temperature, m_i the ion mass, and m_e the electron mass. While we had found previously that the ion bombardment energy could affect the surface roughness of Cu nanoparticle films,[120] the morphology of the electroplated Cu did not vary as much across for different H_2/CH_4 ratios, as shown by the spatial maps of Peak Force Error images in Figure 3.2. These results indicated that under the PECVD process, the morphology of the electroplated Cu was not as sensitive to ion bombardment as that of Cu nanoparticles, which may be attributed to the much better connectivity of the former prior to the PECVD process. Therefore, the observed reduction in roughness with increasing H_2/CH_4 ratio may be mainly attributed to Cu etching by hydrogen plasma.[129] Moreover, the optical appearance of the electroplated Cu was more reflective after the PECVD process (Figure S3.4), which agreed with the AFM images that the roughness decreased and that the morphology appeared sharper and polished after PECVD (Figure 3.2 and Figure S3.5) as the result of Cu etching by plasma and graphene growth.

Here we remark that our choice of the Peak Force Error images for morphology studies in the place of typical scanning electron microscopy (SEM) is because typical surface cleaning procedure such as O_2 plasma is not suitable for graphene covered samples. For SEM imaging, the graphene covered sample surface would be subject to electron beam induced amorphous carbon deposition due to adsorbed organic molecules from air exposure. An alternative way to obtain detailed morphology for delicate samples is through atomic force microscopy (AFM). Within available AFM modes, the Peak Force tapping mode allows a controllable

force set point to minimize sample damages. Comparing the Peak Force Error images (Figure 3.2) to the height images (Figure S3.5), we find that the former can provide better resolution for the detailed surface morphology. In fact, the Peak Force Error images have been applied to image detailed structures of fragile cells in biology.[130-131]

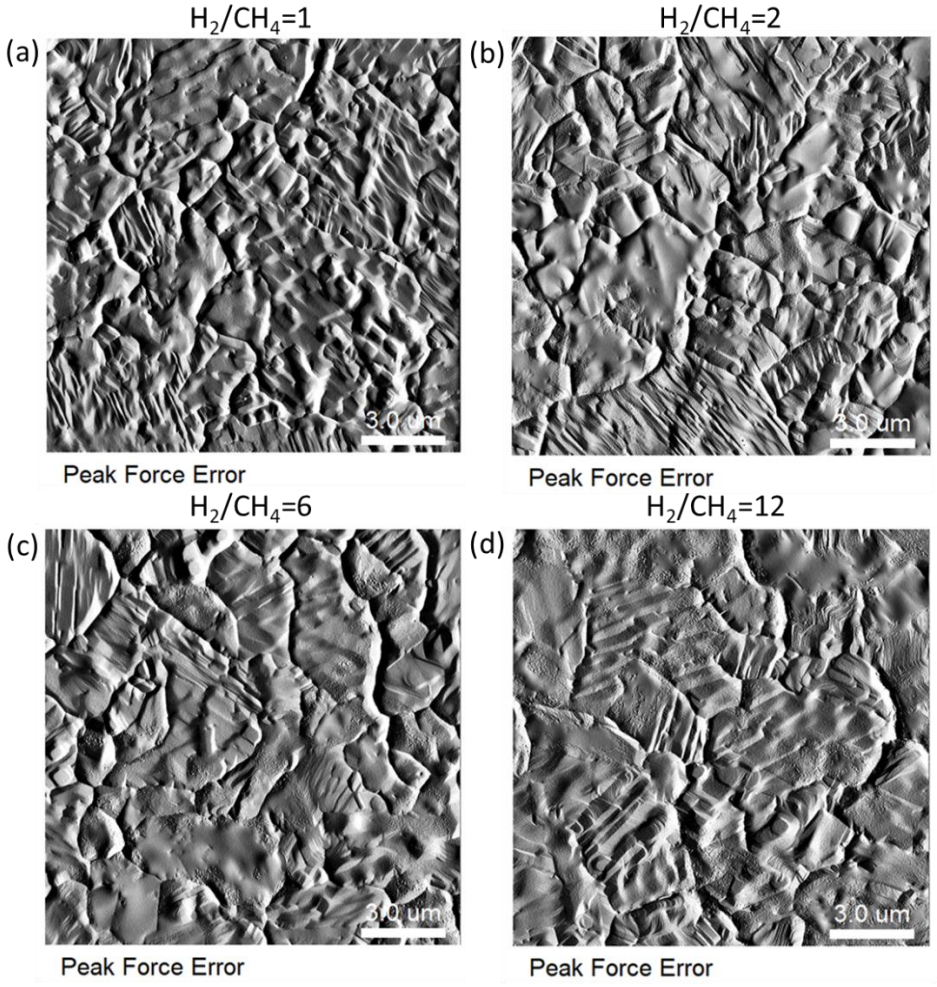

Figure 3.2. Peak Force Error image of electroplated Cu substrates after the PECVD process with (a) H_2/CH_4 = 1, (b) H_2/CH_4 = 2, (c) H_2/CH_4 = 6, and (d) H_2/CH_4 = 12.

To investigate the thickness of graphene grown on electroplated Cu substrates, a typical approach is to consider the I(2D)/I(G) ratio from Raman spectroscopy, and a value of I(2D)/I(G) > 1 is commonly considered as a signature for monolayer graphene.[18] On the other hand, it is also well known that the I(2D)/I(G) ratio is sensitive to interlayer coupling[104] so

that it is not always an accurate indicator for the number of graphene layers. To verify the exact thickness of graphene deposited on the electroplated Cu substrates, cross-sectional image of the sample grown with $H_2/CH_4 = 12$ was taken by HAADF-STEM and shown in Figure 3.3. The image confirmed that the thickness of the graphene to be bilayer, implying that the ratio of I(2D)/I(G) > 1 was associated with turbostratic stacking of the graphene layers.[132-133] For comparison, the HAADF-STEM image of a reference sample was shown in Figure S3.6, which clearly showed that no graphene layer was present, therefore precluding the possibility that the observed layered structure in Figure 3.3 could be from adsorbed molecules due to air exposure.

XPS was employed to investigate the chemical change of the samples. The C-1s spectra of samples after the PECVD process were shown in Figure 3.4. The clear contribution from the sp^2 carbon bond (~ 284.3 eV) further confirmed graphene coverage on Cu, while the presence of C=O bond (~ 288 eV) could be due to exposure to ambient environment.[134] Comparing to the as-received Cu substrate (Figure S3.7 (a)), Cu-2p region scans indicated that PECVD graphene growth process also removed Cu oxides as shown in Figure 3.5, similar to the Cu substrate etched with dilute H_2SO_4 (Figure S3.7 (b)). We further note a blue shift in the C=C component of Figure 3.4(a) for graphene grown under the condition of $H_2/CH_4 = 1$, which may be attributed to the highest defect density of this sample (according to Raman spectroscopic studies) that led to less ideal sp^2 bonding and the formation of sp^3 bonds around defects. Therefore, the averaged C=C component shifted towards a higher binding energy and became closer to the C-C bond. In the same context, the revelation of the lowest intensity of the C-C component in Figure 3.4(d) was consistent with the fact that the sample was grown with the highest H_2/CH_4 ratio and had the lowest defect density.

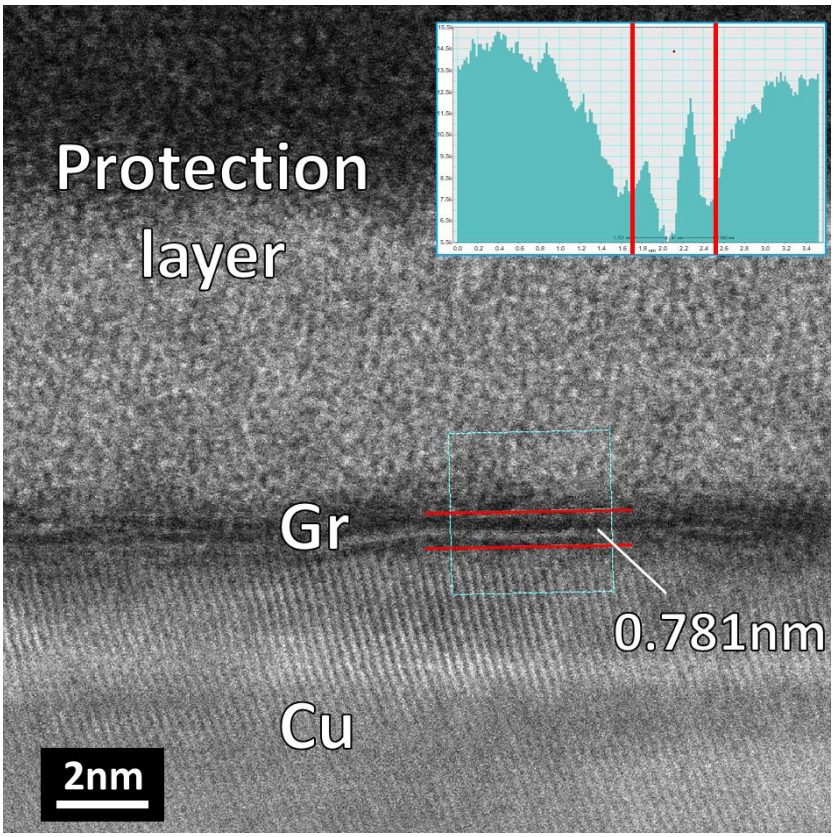

Figure 3.3. HAADF-STEM image of PECVD graphene grown on electroplated Cu with the ratio of H_2/CH_4 = 12. Here "Gr" represents graphene. The inset shows the intensity slice of the indicated region from Cu through graphene to the proprietary protection layer. The STEM image was acquired by ITRI.

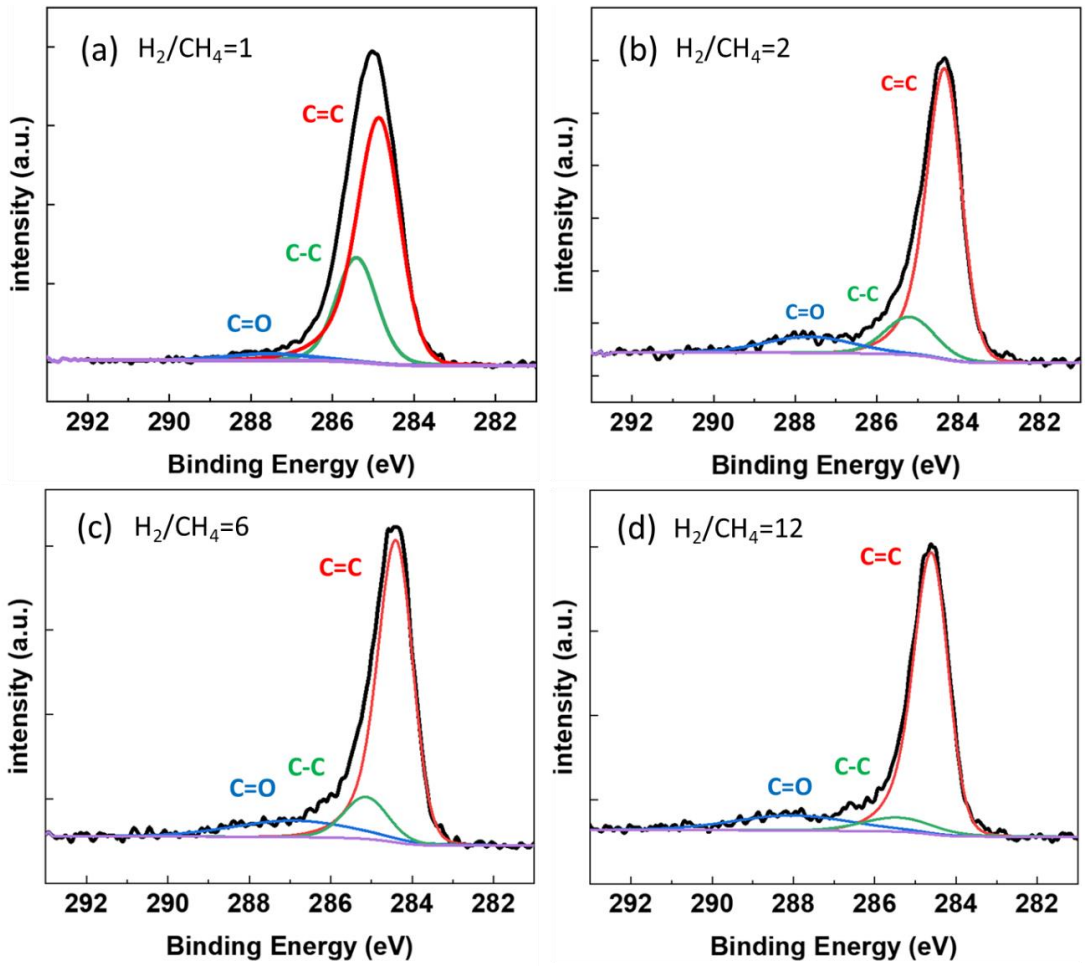

Figure 3.4. XPS C1s spectra collected on PECVD graphene covered samples: (a) after PECVD with H_2/CH_4 = 1, (b) after PECVD with H_2/CH_4 = 2, (c) after PECVD with H_2/CH_4 = 6, (d) after PECVD with H_2/CH_4 = 12.

Furthermore, we found that for samples stored under a normal ambient condition up to 8 weeks, electroplated Cu covered with PECVD-grown graphene showed strongly suppressed Cu oxide satellite formation (Figures 3.5 (b)–(e), (g)–(j) and (l)–(o)), which was in stark contrast to the significant oxidation with time of an etched electroplated Cu substrate without graphene coverage (Figures 3.5(a), (f) and (k)). This finding therefore demonstrated excellent passivation of Cu by the low-temperature PECVD-grown graphene.

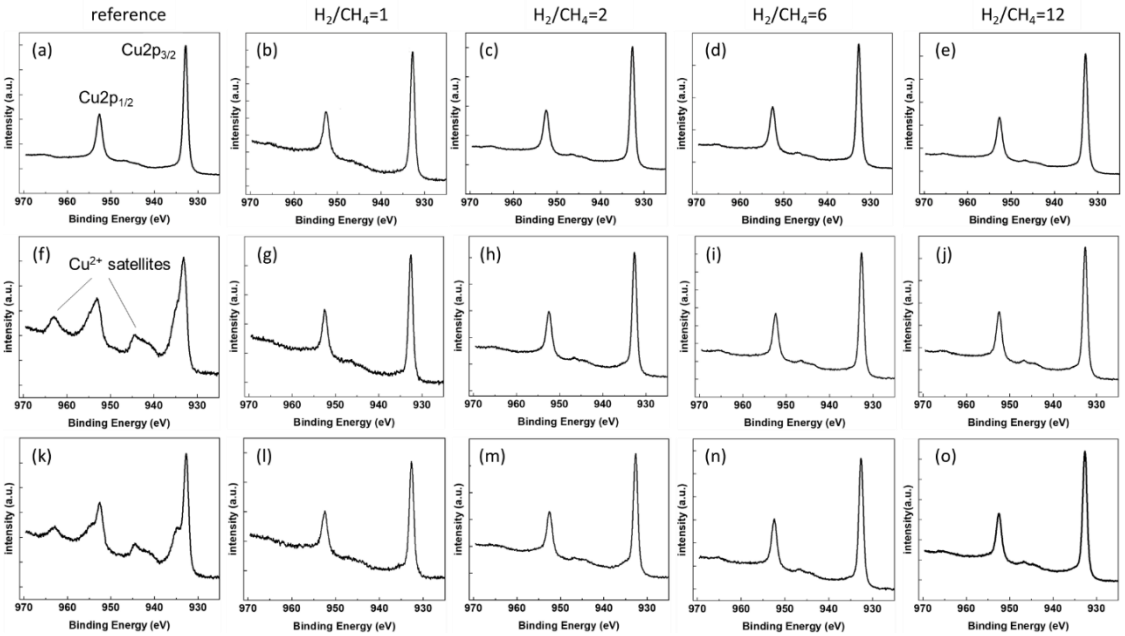

Figure 3.5. XPS Cu 2p spectra. Top panels: XPS Cu 2p peaks of (a) etched Cu substrate and (b-e) samples right after PECVD growth of graphene under different H_2/CH_4 ratios. Middle panels, XPS Cu 2p peaks of samples after stored under normal ambient condition for 4 weeks: (f) etched Cu substrate and (g-j) samples after PECVD growth of graphene under different H_2/CH_4 ratios. Bottom panels: XPS Cu 2p peaks of samples after stored under normal ambient condition for 8 weeks: (k) etched Cu substrate and (l-o) samples after PECVD growth of graphene under different H_2/CH_4 ratios.

The electroplated Cu circuit pattern on the substrates and the folding equipment used for the folding test and resistance measurements of the substrates are shown in Figure S3.8, and the effect of the PECVD-grown graphene coverage on the Cu circuit compared with that without graphene coverage is shown in Figure 3.6. We found that the resistance of the Cu circuit with PECVD-grown graphene coverage was reduced relative to the reference Cu circuit without graphene coverage. Moreover, the durability of the Cu circuit with PECVD-grown graphene was increased significantly: while the reference sample broke down after fewer than 60,000 cycles, the graphene covered samples could maintain electrical conduction (as indicated by measurable resistance values) up to 100,000 cycles of folding. (The measurement up to 200,000 cycles was included in Table S3.2). Here, “broke-down” was defined as the state of

exceedingly high resistance where the resistance was not measurable. In addition, we found that samples covered with graphene grown under higher H_2/CH_4 ratios exhibited better durability enhancement, as tabulated in Table S3.1. Our results also indicated that the underlying polyimide substrate maintained its flexibility after the PECVD process. We further note that the folding test was conducted under ambient condition and that the resistance of the circuit was measured directly on the sample without a typical dielectric passivation layer for FHE. This finding suggests that the graphene coverage can also decrease the passivation thickness in addition to enhancing the reliability of the Cu circuit, which may be attributed to the extra stability provided by graphene to the underlying Cu [135] and is consistent with our XPS studies shown in Figure 3.5.

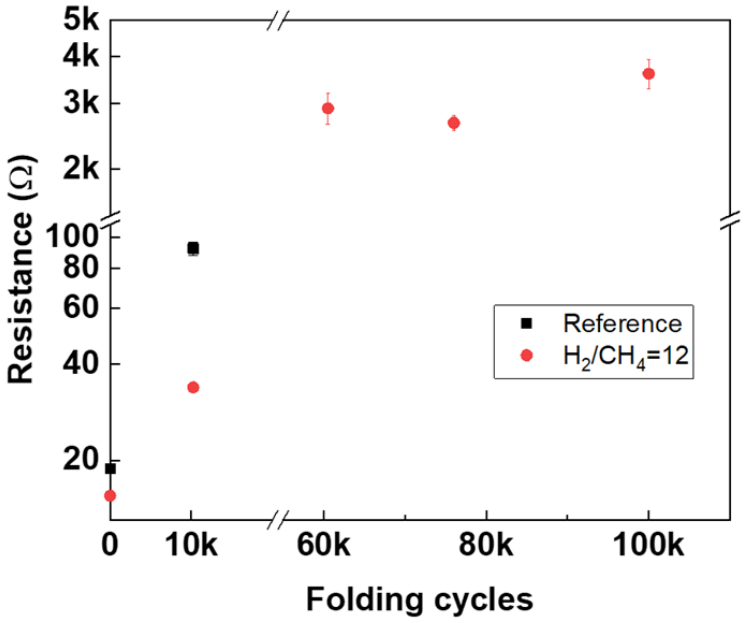

Figure 3.6. Resistance of the Cu circuit *vs.* the number of folding cycles. Note that the reference sample failed after about 60,000 folding cycles. The folding test was performed by ITRI.

4. Conclusion

We have demonstrated direct low-temperature PECVD graphene growth on flexible substrates consisting of electroplated Cu on polymer. An investigation of the PECVD growth conditions revealed that the graphene quality improved with increasing H_2/CH_4 ratio. In addition to the removal of surface oxide from the electroplated Cu substrate and the reduction of surface roughness of Cu by the PECVD process, graphene coverage on the substrate further suppressed the formation of Cu oxide after the samples were stored in ambient environment for 8 weeks and also significantly enhanced the durability of the Cu circuit. For folding tests up to about 100,000 cycles with a bending radius of 2.5 mm, samples covered by graphene grown at higher H_2/CH_4 ratios exhibited significantly better durability. Our successful low-temperature PECVD process for direct growth of graphene on flexible substrates of electroplated Cu on polymer thus opens up new opportunities for strengthening the durability and stability of Cu circuits while reducing the electrical resistance, which are crucial criteria for reliable FHE applications.

Supporting Information

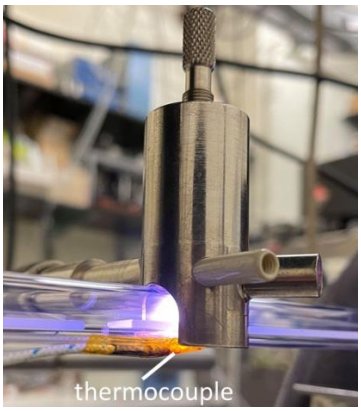

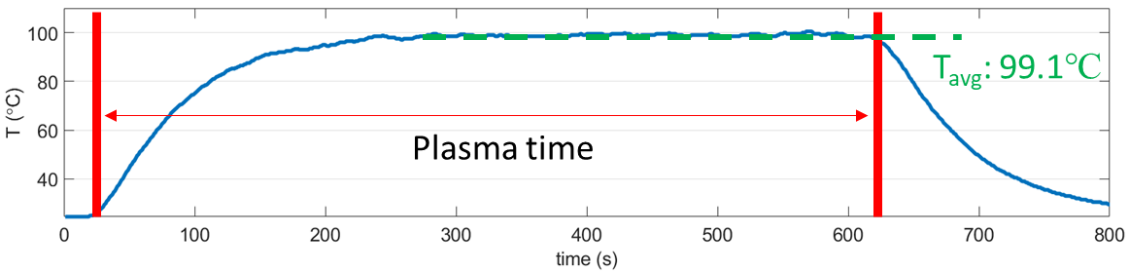

Figure S3.1. Appearance of the PECVD and the temperature measurement. (Top panel) Photograph of the PECVD process in progress. (Bottom panel) The growth chamber temperature change as a function of time during the PECVD process was recorded via thermocouple attached on the quartz tube.

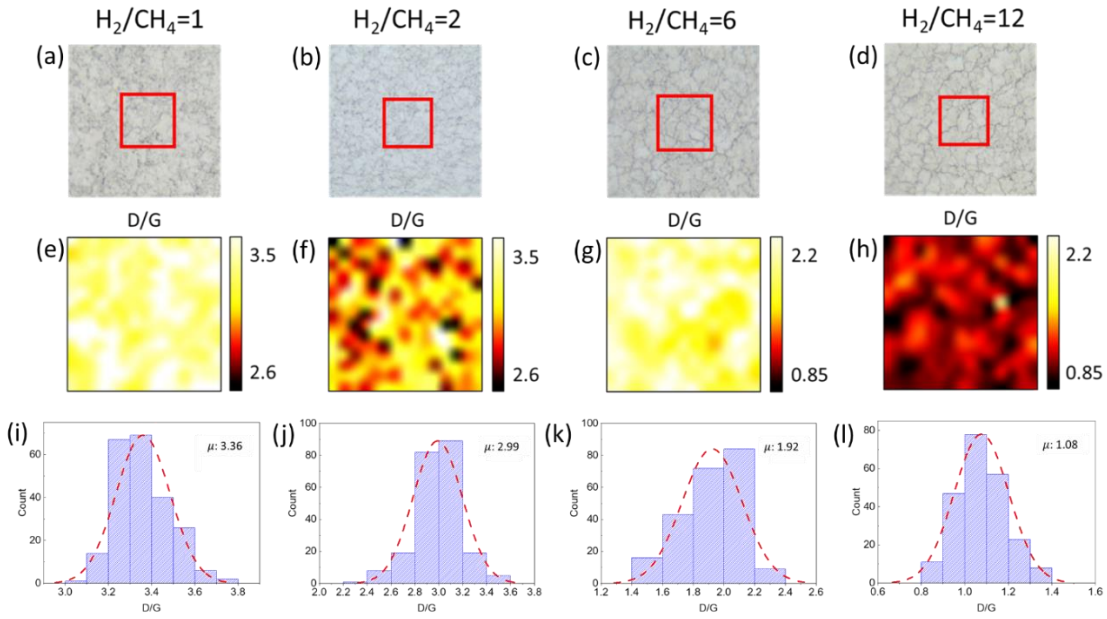

Figure S3.2. Optical images, I(D)/I(G) spatial maps and histograms of the I(D)/I(G) spatial maps of PECVD-grown graphene on electroplated Cu under different ratios of H_2/CH_4: (a,e,i) H_2/CH_4 = 12 (b,f,j) H_2/CH_4 = 6 (c,g,k) H_2/CH_4 = 2, and (d,h,i) H_2/CH_4 = 1. The size of the mapping area in (e-h), which corresponds to the red squares in (a-d), is (30×30) μm^2. Each histogram from (i) to (l) consists of 225 point spectra, and each point spectrum is taken over a spot size with a radius of 0.5 μm.

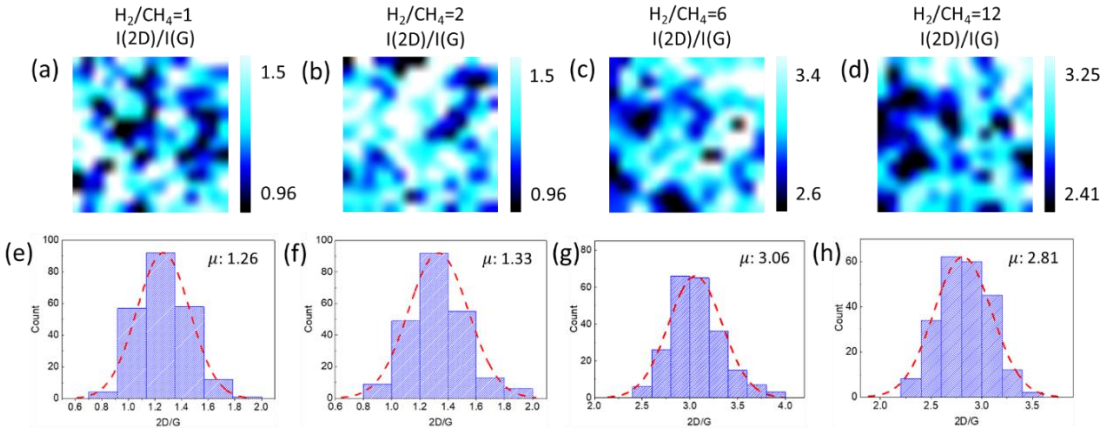

Figure S3.3. I(2D)/I(G) spatial maps and histograms of the I(2D)/I(G) spatial maps of PECVD-grown graphene on electroplated Cu under different ratios of H_2/CH_4 flow rates: (a,e) H_2/CH_4 = 1, (b,f) H_2/CH_4 = 2, (c,g) H_2/CH_4 = 6, and (d,h) H_2/CH_4 = 12. The size of the mapping area in (a-d) is (30×30) μm^2. Each histogram from (e) to (h) consists of 225 point spectra, and each point spectrum is taken over a spot size with a radius of 0.5 μm.

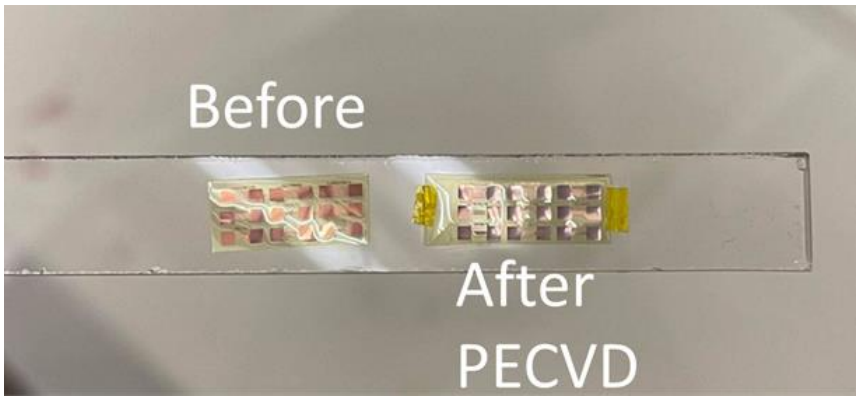

Figure S3.4. Optical image comparing the appearances of the electroplated Cu substrate on polyimide before and after the PECVD process.

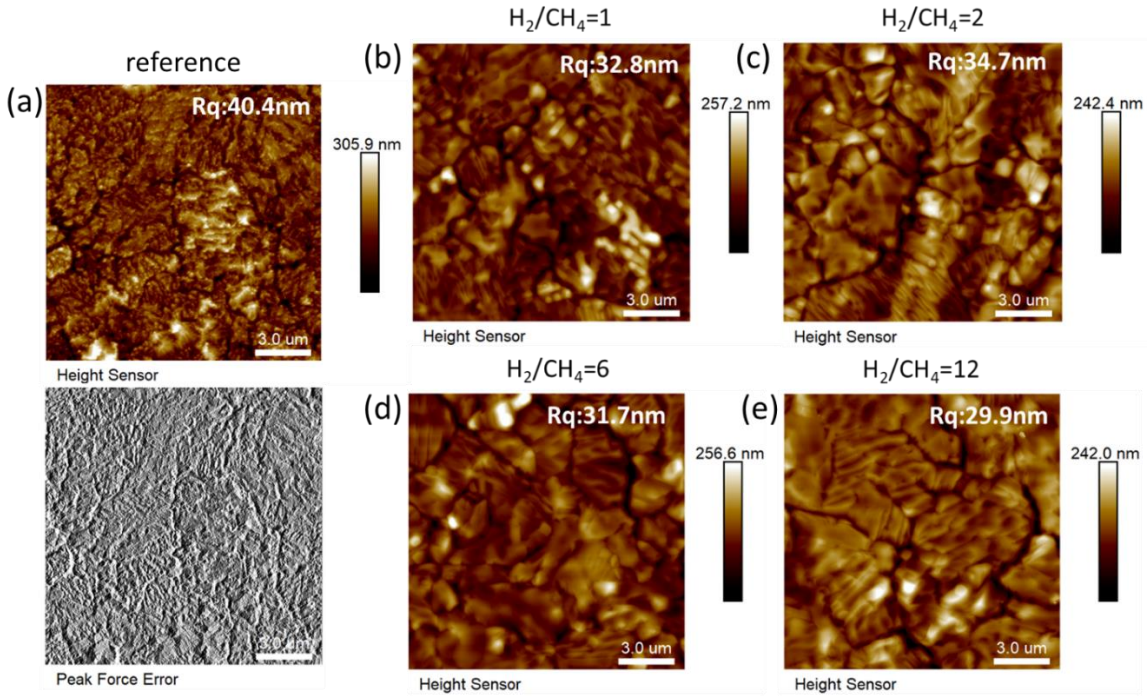

Figure S3.5. Surface morphology of electroplated Cu substrates: (a) AFM image (top panel) and Peak Force channel (bottom panel) of an electroplated Cu substrate before PECVD. (b) AFM image of an electroplated Cu substrate after PECVD with H_2/CH_4 = 1. (c) AFM image of an electroplated Cu substrate after PECVD with H_2/CH_4 = 2. (d) AFM image of an electroplated Cu substrate after PECVD with H_2/CH_4 = 6. (e) AFM image of an electroplated Cu substrate after PECVD with H_2/CH_4 = 12. The RMS roughness of the images were indicated.

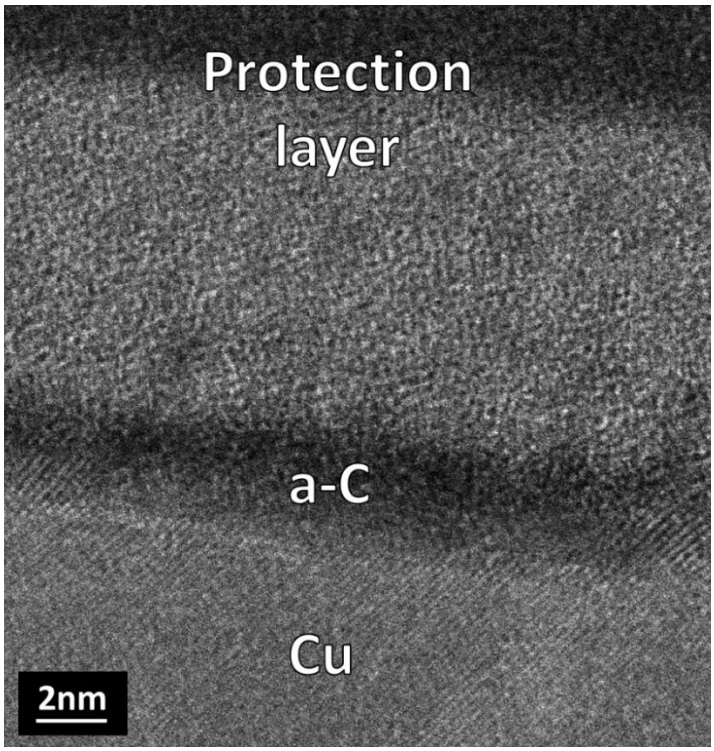

Figure S3.6. HAADF-STEM image of the reference sample. Here a-C between Cu and the protection layer refers to amorphous carbon. The STEM image was acquired by ITRI.

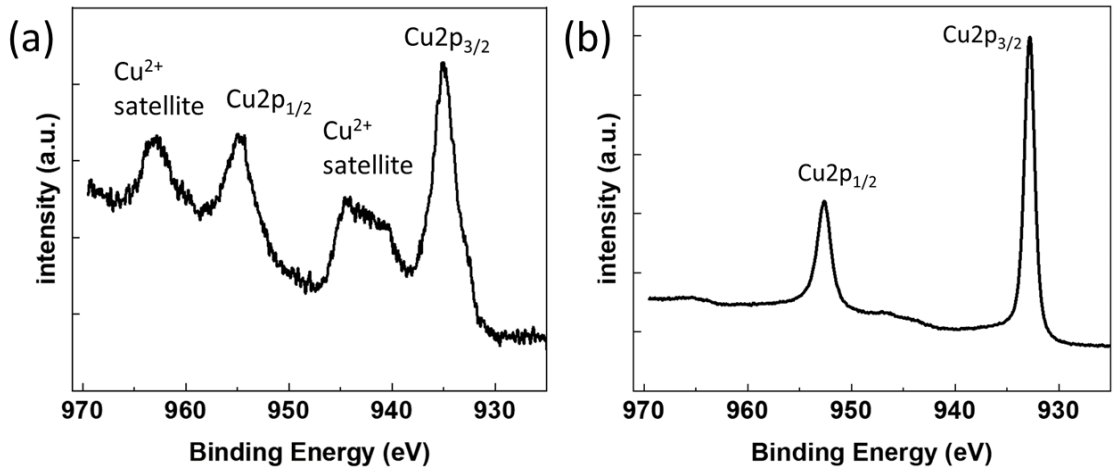

Figure S3.7. Cu2p XPS spectra of (a) as-received electroplated Cu substrate, and (b) the same electroplated Cu substrate after dilute H_2SO_4 etch.

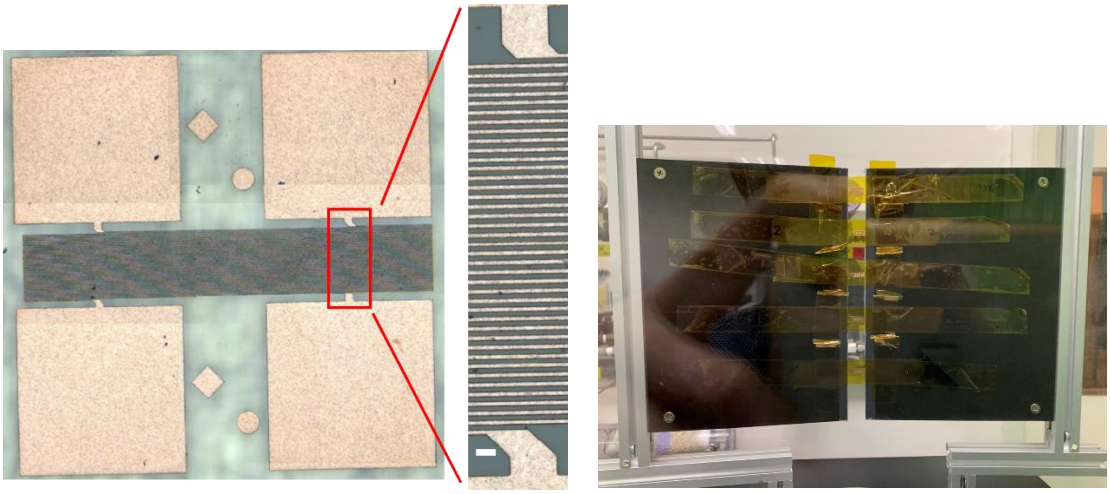

Figure S3.8. The circuit pattern used for the folding test and resistance measurements (Left). The size for each electrical pad is (1×1) mm^2, and the expanded image of the area indicated by the red box is shown on the right, and the scale bar (white) is 20 μm. (Right) Photograph of the equipment for the folding test. The circuit pattern was attached to the center of the equipment.

Table S3.1. Electrical resistance (measured in Ω) of different samples after the indicated number (N) of folding cycles and comparison among samples grown under different H_2/CH_4 ratios. The folding test was performed by ITRI.

Sample / Record number; Folding cycle (N) / Resistance (Ω)		1	2	3	4	5
reference	N	0	10,250	failed	—	—
	Ω	18.8	92.43			
H_2/CH_4=1	N	0	10,250	failed	—	—
	Ω	18.3	33.66			
H_2/CH_4=2	N	0	10,250	60,505	failed	—
	Ω	16.20	16.71	149M		
H_2/CH_4=6	N	0	50,255	65,750	89,750	110,140
	Ω	19.9	2.46k	2.39k	3.12k	3.66k
H_2/CH_4=12	N	0	10,250	60,505	76,000	100,000
	Ω	15.5	33.87	2.91k	2.66k	3.60k

Table S3.2. Electrical resistance (measured in Ω) of different samples after the indicated number (N) of folding cycles up to 200,000 cycles. The folding test was performed by ITRI.

Sample / Record number; Folding cycle (N) / Resistance (Ω)		1	2	3	4	5	6	7
reference	N	0	10,250	failed	—	—	—	—
	Ω	18.82	92.43					
H_2/CH_4=1	N	0	10,250	failed	—	—	—	—
	Ω	18.33	33.66					
H_2/CH_4=2	N	0	10,250	60,505	failed	—	—	—
	Ω	16.20	16.71	149M				
H_2/CH_4=6	N	0	50,255	65,750	89,750	110,140	189,750	200,000
	Ω	19.92	2.46k	2.39k	3.12k	3.66k	6.88k	5.41k
H_2/CH_4=12	N	0	10,250	60,505	76,000	100,000	185,360	200,000
	Ω	15.46	33.87	2.91k	2.66k	3.60k	93M	93M

C h a p t e r I V

GRAPHENE ON GOLD FOR ANTICORROSION IN SMART WEARABLE ELECTRONICS

Adapted from:
Lu, C.-H.; Shang, K.-M.; Lee, S.-R.; Tai, Y.-C.; Yeh, N.-C. Graphene on Nanoscale-Thick Au Films: Implications for Anticorrosion in Smart Wearable Electronics. ACS Applied Nano Materials 2022, 5 (3), 4343-4349, DOI: 10.1021/acsanm.2c00401.

Personal contribution: C.-H. L. participated in the conception of the project, grew the PECVD graphene, performed AFM, XPS and Raman measurements, interpreted the data , and wrote the draft manuscript.

Gold is normally considered inert to chemical reaction. Nevertheless, as a common electrode material, it would suffer from corrosion when exposed to certain solutions such as sweat and body fluids. Here we report low temperature plasma-enhanced chemical vapour deposition (PECVD) of graphene on gold and demonstrate its feasibility for anti-corrosion application. The effects of hydrogen-to-methane ratio and the underlying gold substrate on the graphene growth are investigated, and the growth mechanism of PECVD graphene on gold is proposed. When immersed in an oxygenated saline solution, the PECVD-grown graphene-covered gold surface is found to remain intact after an acceleration soaking test at 90 ℃ for 24 hours, which is in contrast to the degradation of bare gold surface subject to the same test. Our findings suggest that consumer/medical wearables and implantable devices with exposed gold can benefit from the protection of a direct, low-temperature PECVD-grown graphene layer for anti-corrosion, thereby prolonging the efficacy and reliability of gold electrode-based biosensors.

1. Introduction

Since the first successful isolation of monolayer graphene, its unique electronic, optical and mechanical properties have stimulated a wide range of research activities and

applications. Early works of graphene production rely on mechanical exfoliation,[48] which is not scalable for real-world applications. To date, chemical vapor deposition (CVD) is one of the common approaches for large scale graphene synthesis. Typically, it involves both metallic substrates, such as Ni and Cu, and high growth temperatures to facilitate the dissociation of hydrocarbon precursors for graphene formation.[136] Besides Ni and Cu, other transition metal substrates such as Co,[137] Pt,[138] Au[139,140] and Ru[141] have been demonstrated for CVD graphene growth.

Gold has been widely adopted in biosensors for its biocompatibility and in flexible electronics for its ductility.[10,11,12] Despite the common perception that gold is chemically inert for use as electrochemical electrodes, it is still prone to surface oxidation or corrosion.[28,27] Graphene on gold has been demonstrated to stabilize the Au electrodes for electrochemical application.[3] In addition, graphene coverage on gold could enhance the detection sensitivity of DNA molecules compared to bare gold electrodes.[4] Therefore, graphene could enable versatile applications of gold.

In terms of the growth temperature, CVD graphene growth commonly operates at a temperature near the melting points of the metal foils, which is prone to induce contamination due to evaporated metal and aged quartz furnace.[54] In addition, high temperature processes would damage substrates that involve polymeric or temperature sensitive materials, thus limiting their suitability to applications requiring flexible materials.[142] Several approaches have been proposed to lower the graphene growth temperature for thermal CVD. For instance, Jang *et al.*[126] reported the use of benzene precursor to reduce the graphene growth temperature to 100 °C while Fujita *et al.*[55] demonstrated a near room temperature graphene growth through liquid metal nucleation. However these approaches generally involve complicated preprocessing steps that are not compatible with industrial processes for large-area scalable production.[56,55,126]

On the other hand, plasma-enhanced chemical vapor deposition (PECVD) is a scalable process that could enable low-temperature graphene growth. PECVD relies on plasma to create reactive species to lower the required growth temperature. Growth temperature

ranging from 160 ℃ to 700 ℃ have been reported for PECVD graphene synthesis on various substrates.[67, 142,68,61] Considering the aforementioned advantages of Au and graphene, as well as the increasing interest in flexible or smart wearable electronics with gold electrodes,[143,144,145,146] it is highly desirable to find a method for graphene growth on gold under low temperature.

In this work, we demonstrate the feasibility of direct growth of graphene on gold thin films by PECVD at low temperature. Raman spectroscopy and direct transfer of graphene onto SiO_2 confirm the successful growth of graphene. X-ray diffraction (XRD) studies further reveal that the crystallinity of gold thin films improves after the PECVD graphene growth process. A growth mechanism of PECVD graphene on Au is proposed based on studies of the X-ray photoelectron spectroscopy (XPS) and cross-sectional annular dark-field scanning transmission electron microscopy (ADF-STEM) of the PECVD-grown samples. Finally, with accelerated soak testing (AST), we demonstrate excellent anti-corrosion performance of graphene on Au. Therefore, our work demonstrates the feasibility of low-temperature direct growth of graphene on gold by PECVD for anti-corrosion, paving ways to scalable smart medical applications based on PECVD-grown graphene on gold.

2. Experimental method

2.1 Substrate preparation

The Au substrate in this work consists of a Au thin film of 30 nm thickness above a Ti layer of 10 nm thick, both deposited on a SiO_2/Si substrate with a SiO_2 thickness of 285 nm via an electron-beam (e-beam) evaporator. Prior to metal deposition, the SiO_2/Si wafer was cleaned with the piranha solution, which was a mixture of H_2SO_4:H_2O_2 with a 3:1 volume ratio.

2.2 PECVD graphene growth

Prior to the PECVD graphene growth, the quartz tube and sample holders were cleaned with O_2 plasma and H_2 plasma. The plasma system consisted of a microwave generator

fixed at 2.45 GHz and an Evenson cavity. Before plasma ignition by a high frequency coil, CH_4 and H_2 gas were introduced into the quartz tube by mass flow controllers (MFC), and the total pressure was set at 750 mtorr, which was controlled by a throttle valve. Here we define H_2/CH_4 as the ratio of the H_2 gas flow to the CH_4 gas flow. The plasma power was set at 10 W for 5 minutes and the samples were left cooled down with the gas flow continued after the plasma was turned off. Through plasma heating, the temperature during graphene growth was about 120 ℃. To transfer the graphene grown on $Au/Ti/SiO_2/Si$ to a SiO_2/Si substrate, polymethyl methacrylate (PMMA) was spin coated on the graphene-covered $Au/Ti/SiO_2/Si$ substrates followed by gold etching via a gold etchant (TFA, Transene). Subsequently, the transferred graphene on SiO_2/Si was soaked in acetone for PMMA removal.

2.3 Characterization

After growth, Raman spectroscopy was conducted to confirm the graphene growth and graphene quality. The spectra were collected with a Raman spectrometer (InVia, Renishaw) with 514 nm laser. Surface morphology was characterized by atomic force microscopy (AFM, Bruker Dimension Icon) under PeakForce tapping mode and scanning electron microscopy (SEM). XPS (Surface Science Instruments MProbe ESCA) with Al K_α X-ray source and a hemispherical energy analyzer using a pass energy of 25 eV was used to characterize the chemical change after PECVD. The instrument work function was calibrated with respect to Au $4f_{7/2.}$ ADF-STEM images were acquired by aberration-corrected JEOL ARM-200F under 200 kV accelerating voltage. XRD were performed with PANalytical X'Pert PRO with Cu K_α radiation. Accelerated soak testing (AST) was conducted by immersing the samples of graphene grown on $Au/Ti/SiO_2/Si$ as well as controlled samples of $Au/Ti/SiO_2/Si$ without graphene into a saline solution (with 0.9% NaCl) for 24 hours at 90 ℃. The sample edges were sealed with epoxy to prevent from potential reaction of the saline solution with the underlying Ti layer from the edges.

3. Results and Discussion

Figure 4.1(a) shows the optical micrograph image of a graphene sample transferred onto a SiO_2/Si substrate, indicating that graphene had fully covered the Au/Ti/SiO_2/Si substrate of 1x0.5cm^2 despite a short growth time. The Raman spectra of PECVD-grown graphene on Au under different H_2/CH_4 ratios in Figure 4.1(b) further confirm the finding of successful graphene growth: The existence of the characteristic Raman modes of graphene (*i.e.*, the D, G, D´ and 2D peaks) clearly indicated successful low-temperature growth of graphene on Au. Specifically, the distinct 2D peak suggested that our PECVD growth process provided significantly better graphene crystallinity than the thermal CVD method, the latter led to a barely visible 2D peak for a growth temperature of 850 ℃.[139] Ani *et al* [147] have pointed out that the carbon solubility in metal is related to the catalytic activity for hydrocarbon dissociation. The carbon solubility of Au is 0.01%, which is significantly smaller than that of Cu (0.04%) so that CVD growth of graphene on Au is expected to be more difficult than on Cu, consistent with experimental observation.

To further characterize the PECVD-grown graphene on Au, we note that the quality of graphene and its defect types can be inferred from Raman spectroscopic studies through analysing the intensity ratio of D to G peaks (I(D)/I(G)) as well as that of D to D´ peaks (I(D)/I(D´)), respectively.[111,127] As shown in Figure 1(c), the I(D)/I(G) ratio decreased with increasing H_2/CH_4, which could be attributed to increasing hydrogen radicals that facilitated efficient etching of defective graphene.[148] The quality of the synthesized graphene can be estimated by the D/G ratio through the relation[127]

$$L(nm) = \frac{560}{E_{laser}^4}\left(\frac{I_D}{I_G}\right)^{-1} \quad (4.1)$$

where L represents the inter-defect distance or the graphene grain size, and E_{laser} = 2.41eV. Using this formula, the graphene grain size was estimated to be ~ 6 nm. Although the grain size was not ideal, we found that bilayer graphene with a full coverage over the underlying gold surface could still provide excellent passivation for gold, to be elaborated

later in this section. This finding may be attributed to the small interlayer spacing of bilayer graphene (< 0.35 nm), which effectively prevented most ions from diffusing through the graphene layers to reach the gold surface.

In contrast, the I(D)/I(D´) ratio was consistently between 6 and 7 for all H_2/CH_4 values investigated, which implied primarily vacancy defects in the PECVD-grown graphene on Au.[111]

Quantitatively, the amount of biaxial strain of graphene grown on Au could be derived through the use of the following formula:[149]

$$\boldsymbol{\varepsilon = \frac{\Delta\omega}{2\omega_0\gamma_{2D}}}, \tag{4.2}$$

where $\Delta\omega$ denotes the difference between the Raman shift of the 2D band measured directly on the Au/Ti/SiO_2/Si growth substrate and that measured on the same sample after transferred to a SiO_2/Si substrate, ω_0 is the unstrained (*i.e.*, after transferred to a SiO_2/Si substrate) Raman shift of the 2D band, and γ_{2D} = 3.15 is the Grüneisen parameter of the 2D band.[149] The strain values thus derived from using Eq. (4.2) for different H_2/CH_4 ratios are summarized in Figure 4.1(d), which reveal that graphene was compressively strained after direct growth on Au, and that the compressive strain became relieved after transferred to a SiO_2/Si substrate. This finding is in agreement with the previous observation reported by Oznuluer *et al*.[139]

The decreasing magnitude of compressive strain with increasing H_2/CH_4 as shown in Figure 4.1(d) may be attributed to the morphology change illustrated in Figure 4.2 for images taken by an atomic force microscope. Here both the height images (Figure 4.2(a-c)) and the PeakForce error images (Figure 4.2(d-f)) were included because the PeakForce error images could provide more detailed surface morphology than height channel.[150]

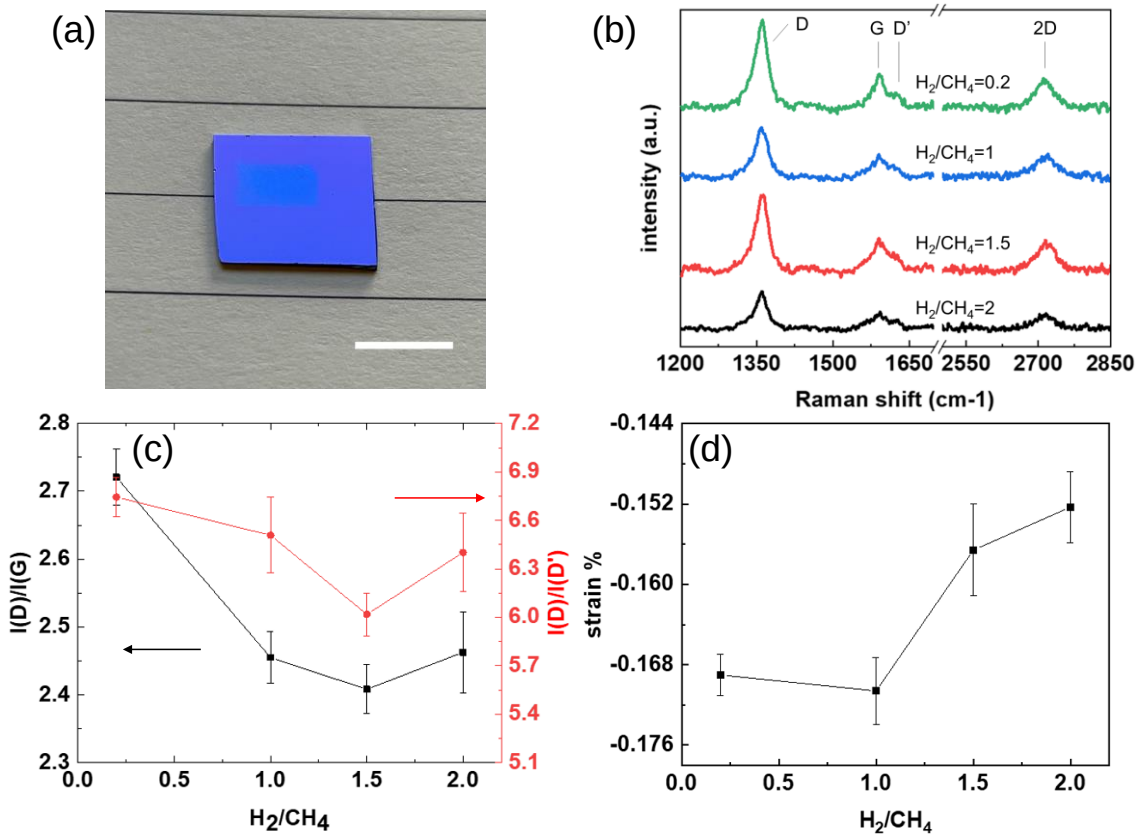

Figure 4.1. Raman spectra measurement (a) Graphene (lighter blue) transferred onto a SiO_2/Si substrate (darker blue) after its growth on Au/Ti/ SiO_2/Si. The scale bar is 1 cm. (b) Raman spectra of PECVD-grown graphene on Au/Ti/ SiO_2/Si under different H_2/CH_4 growth conditions. (c) The intensity ratios I(D)/I(G) and I(D)/I(D´) extracted from (b). (d) The calculated strain of graphene on Au from Eq. (4.2).

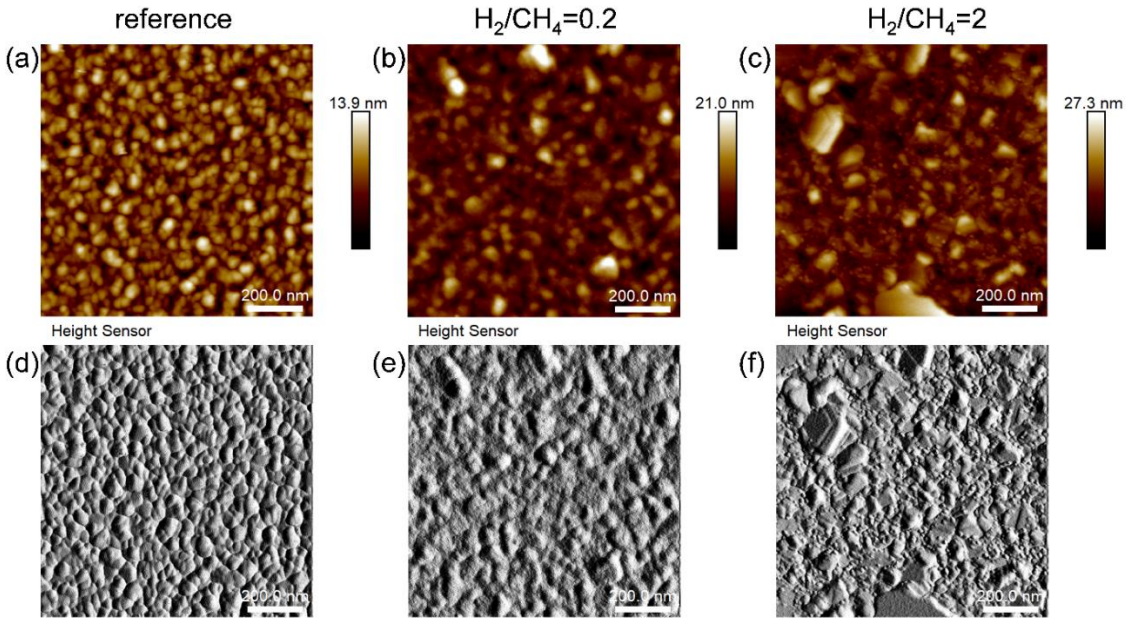

Figure 4.2. The AFM height images and peakforce error images of the sample surface (a,d) before PECVD, (b,e) after PECVD graphene growth at H_2/CH_4 = 0.2, and (c,f) after PECVD graphene growth at H_2/CH_4 = 2. Here the scale bar represents 200 nm.

Before PECVD, the Au surface revealed apparent granular structures (Figure 4.2(a,d)), whereas after PECVD graphene growth, the morphology became dependent on the H_2/CH_4 ratio. Comparing the surface morphology for graphene grown under the growth conditions of H_2/CH_4 = 0.2 and H_2/CH_4 = 2, the Au surface under a higher H_2/CH_4 ratio showed smoother surface structures, leading to reduced compressive strain on graphene. The observation of the smoother surface morphology under a higher H_2/CH_4 ratio may be associated with better etching of Au by H_2 plasma.[151]

To elucidate the growth mechanism of graphene on gold by PECVD, measurements of XPS and ADF-STEM were performed. Figure 4.3 showed the XPS C-1s spectra of the samples after PECVD growth, which further confirmed the formation of graphene on Au from the dominant sp^2 carbon contribution. In addition, the absence of any discernible peak around the binding energy of 283 eV implied that there was no metal carbide formation.[152] The presence of graphene layers under different PECVD growth conditions was further

verified by the ADF-STEM images in Figure 4.4. For $H_2/CH_4 = 0.2$, we observed mainly monolayer graphene, while for $H_2/CH_4 \geq 1$ we found primarily bilayer graphene. Interestingly, for $H_2/CH_4 = 0.2$ a clear amorphous carbon layer was also observed while little amorphous carbon was found for $H_2/CH_4 \geq 1$. Based on these experimental findings, we conjecture the PECVD growth mechanism of graphene on Au as schematically illustrated in Figure 4.5 and further described below.

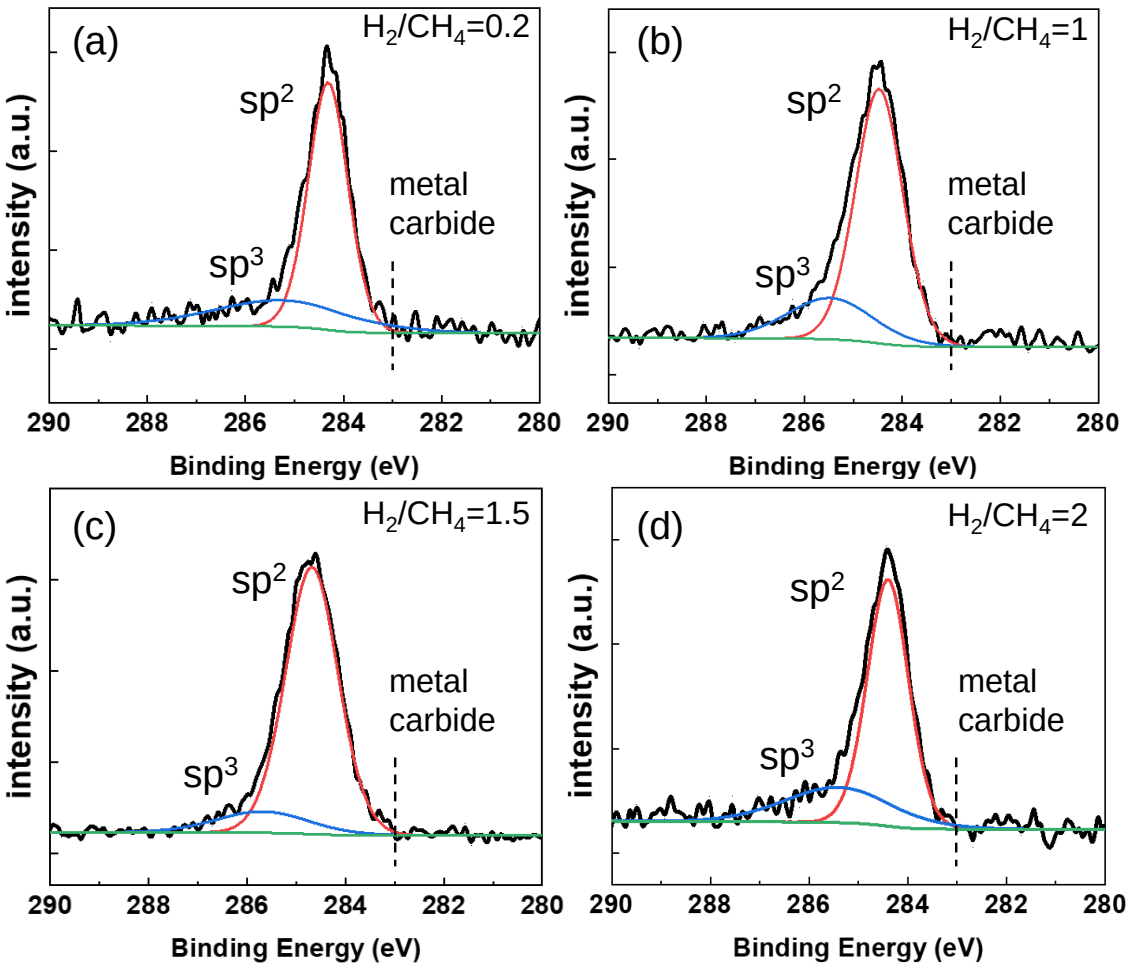

Figure 4.3. XPS C-1s spectra of the graphene samples after the PECVD process under the growth condition with (a) $H_2/CH_4 = 0.2$, (b) $H_2/CH_4 = 1$, (c) $H_2/CH_4 = 1.5$, and (d) $H_2/CH_4 = 2$.

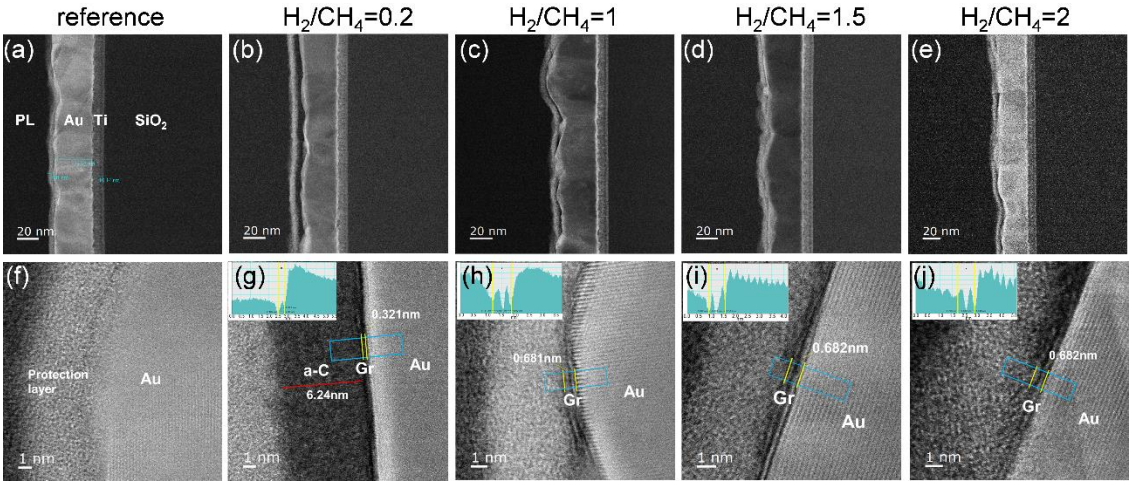

Figure 4.4. ADF-STEM images at a lower magnification (top row) and higher magnification (bottom row) of (a,f) a reference sample without the PECVD process, and samples after the PECVD process with the growth condition of (b,g) H_2/CH_4 = 0.2, (c,h) H_2/CH_4 = 1, (d,i) H_2/CH_4 = 1.5, and (e,j) H_2/CH_4 = 2. Here "PL", "Gr" and "a-C" represent protection layer, graphene, and amorphous carbon, respectively. The STEM images were acquired by ITRI.

First, microwave excitation creates a plasma environment with energetic radicals and reacting species that are dissociated/excited from methane and hydrogen. Plasma also contributes to the heating of the substrates, and the degree of heating depends on the plasma power. Some of the radicals as well as the hydrocarbon species become adsorbed onto the Au surface, and dehydrogenation process of the adsorbed hydrocarbon species takes place before carbon radicals migrate and nucleate into graphene. The low carbon solubility in Au limits the number of graphene layers that can be nucleated on the Au surface, and the dehydrogenation and migration processes for graphene formation are dependent on the temperature and the catalytic activity of the substrate. For small H_2/CH_4 ratios (*e.g.*, H_2/CH_4 = 0.2), monolayer graphene formed through the adsorption of carbon species mentioned above. However, further adsorption of carbon species after the nucleation of monolayer graphene led to the formation of an amorphous carbon layer rather than a second layer of graphene. This finding associated with low H_2/CH_4 ratios may be attributed to

insufficient hydrogen radicals for etching amorphous carbon[148] and the lower electron temperature of the plasma[67, 142] that led to reduced reactivity from the substrate. On the other hand, bilayer graphene without an amorphous carbon layer formed on Au surface with higher H_2/CH_4 ratios (*e.g.*, $H_2/CH_4 \geq 1$), which may be attributed to the higher substrate reactivity from a higher electron temperature in the plasma[67, 142] as well as sufficient hydrogen radicals for etching amorphous carbon. However, layers beyond bilayer graphene could not be developed due to limited carbon solubility in Au and the hinderance of carbon species to penetrate graphene layers to form third layer or more[114]. Although plasma significantly reduced the required growth temperature compared to thermal CVD, we note that no graphene growth on Au could take place when the plasma power was lowered from 10 W to 8 W, while graphene could still grow on Cu at 8 W.[150] This finding may be attributed to the lower catalytic activity of Au than that of Cu so that a higher substrate temperature or plasma power is required for graphene formation. On the other hand, we note that a high plasma power does not necessarily guarantee successful graphene growth, because energetic ion bombardment dominates under a high plasma power, which could lead to significant sample surface damages and removal of adsorbed hydrocarbon species, thus preventing graphene formation.

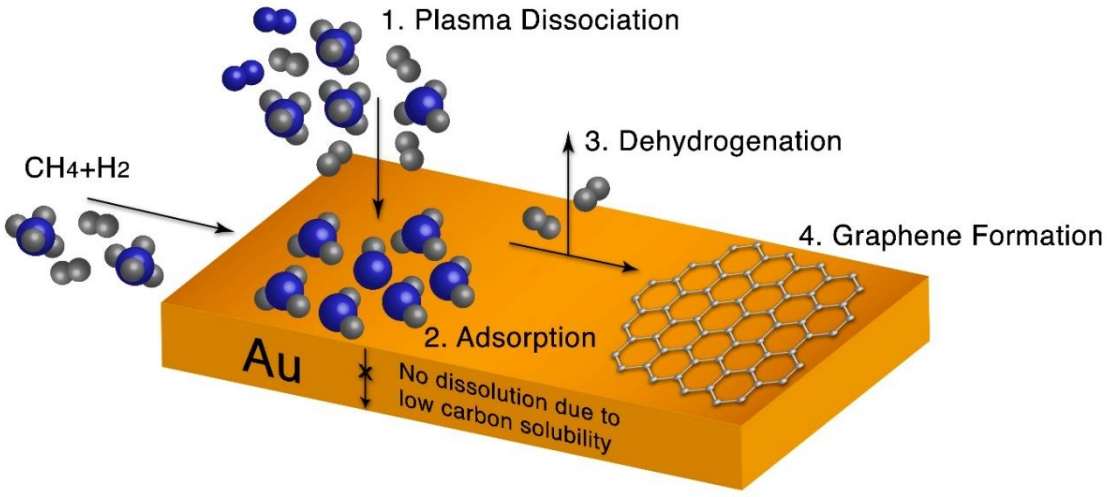

Figure. 4.5 Schematic of the growth mechanism of graphene on gold by PECVD

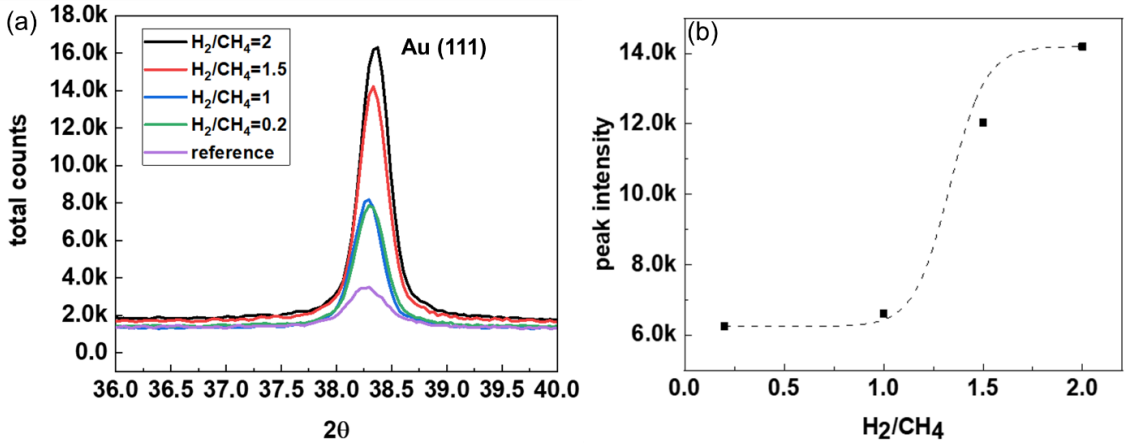

Figure 4.6. XRD measurement (a) XRD of Au (111) region (b) the extracted Au (111) peak intensity plotted versus H_2/CH_4 ratio. Note that the dashed line is for guidance only. The XRD measurements were acquired by ITRI.

XRD were conducted to characterize the changes in Au crystallography after the PECVD process, as shown in Figure 4.6 (a). The Au (111) intensity counts increased with the H_2/CH_4 ratio and were all much larger than that without the PECVD process. The extracted Au (111) peak intensity *vs.* H_2/CH_4 ratio was plotted in Figure 4.6(b). Given that our PECVD process was conducted without any active heating source, the increased crystallinity compared to the reference sample could be attributed to plasma activation that provided sufficient thermal energy, and that the increased crystallinity with the H_2/CH_4 ratio could be due to the increasing electron temperature of the plasma.[142] In addition, similar background counts across the different samples were observed, reinforcing the idea that the variations in Au (111) intensity are indeed indicative of changes in crystallinity. This similarity in background counts helps to rule out influences from instrumental variables, sample preparation differences, and environmental conditions during measurement, thereby supporting the interpretation that the increased crystallinity correlates with the H_2/CH_4 ratio.

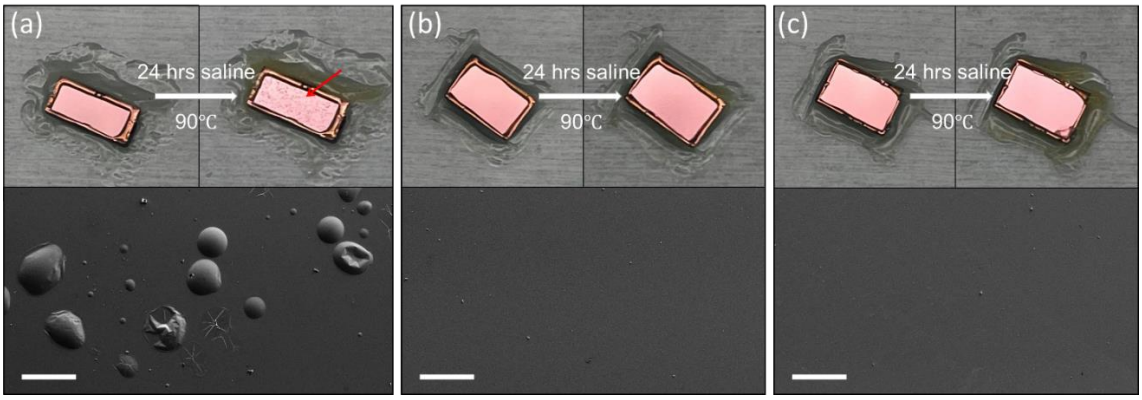

Figure 4.7. SEM images (a) Reference sample without graphene coverage. The red arrow indicates the damaged surface with bubbles. (b) Sample with PECVD graphene coverage grown under the condition H_2/CH_4 = 0.2. (c) Sample with PECVD graphene coverage grown under the condition H_2/CH_4 = 2. The top row shows the optical images before and after AST. The bottom row shows the SEM images taken after AST. The scale bar is 100 μm. The AST tests and SEM images were performed and acquired by K.-M. Shang.

To evaluate if the directly grown graphene on gold could passivate the gold surface, we performed AST by soaking both a bare Au/Ti/SiO_2/Si substrate and a sample of PECVD-grown graphene on Au/Ti/SiO_2/Si into oxygenated saline solution of 0.9% NaCl for 24 hours at 90°C. It is known that body fluids, which may be approximated by the oxygenated saline solution, are highly corrosive to metals.[27,153-154] .

Figure 4.7 shows the SEM images of the indicated samples after AST and the insets show the optical images before and after AST. Clearly the sample without graphene coverage exhibited a damaged surface, while the surface for graphene-covered sample remained intact. In addition, the accelerated soaking test (under 90 °C for 24 hrs) adapted in our work was equivalent to the condition of approximately one month under normal human body temperature[27, 155]. Therefore, our demonstration of graphene-provided protection of gold films in an oxygenated saline solution at 90 °C for 24 hrs is sufficient for such medical applications disposable wearable sensors. On the other hand, although samples synthesized with the ratio of H_2/CH_4 = 0.2 were monolayer graphene, the amorphous carbon above the

graphene layer contributed to enhancing the efficiency of these samples for passivation. On the other hand, for samples synthesized with higher H_2/CH_4 ratios, the resulting bilayer graphene structure made it difficult for ions to diffuse through the layers of a very small interlayer spacing to reach the gold surface. Therefore, excellent passivation could be achieved for samples synthesized with a range of different H_2/CH_4 ratios, as exemplified in Figure 4.7(b) for a sample synthesized under the condition of $H_2/CH_4 = 0.2$, and in Figure 4.7(c) for a sample synthesized under the condition of $H_2/CH_4 = 2$.

4. Conclusion

In conclusion, we reported a low-temperature graphene growth directly on gold by PECVD. Raman spectroscopic studies showed that PECVD-grown graphene underwent a compressive strain on Au and that the defects in the graphene were mainly vacancies. The surface morphology and crystallinity of Au was investigated using AFM and XRD, respectively, was found to be dependent on the H_2/CH_4 ratio used during the PECVD process. ADF-STEM images also verified that the number of graphene layers grown on Au was related to the growth condition of the H_2/CH_4 ratio. A growth mechanism of graphene on Au is proposed based on XPS and ADF-STEM studies of the PECVD-grown samples. Finally, excellent anti-corrosion performance of graphene on Au was demonstrated by AST in oxygenated saline solution. Therefore, our work of low-temperature direct growth of graphene on gold by PECVD appears promising for anti-corrosion in smart wearable, implantable and flexible hybrid electronics.

C h a p t e r V

GRAPHENE ON SILVER WITH LONG-TERM SURFACE PASSIVATION

Adapted from:
Lu, C.-H.; Shang, K.-M.; Lee, S.-R.; Leu, C.-M.; Tai, Y.-C.; Yeh, N.-C. Low-Temperature Direct Growth of Nanocrystalline Multilayer Graphene on Silver with Long-Term Surface Passivation. ACS Appl. Mater. Interfaces 2023, 15, 7, 9883–9891

Personal contribution: C.-H. L. participated in the conception of the project, grew the PECVD graphene, performed AFM, XPS, XRD, and Raman measurements, interpreted the data, and wrote the draft manuscript.

A wide variety of transition metals, including copper and gold, have been successfully used as the substrates for graphene growth. On the other hand, it has been challenging to grow graphene on silver so that realistic applications by combining graphene and silver for improved electrode stability and enhanced surface plasmon resonance (SPR) in organic light emitting diodes (OLEDs) and biosensing have not been realized to date. Here we demonstrate surface passivation of silver through single-step rapid growth of nanocrystalline multilayer graphene on silver via low-temperature plasma-enhanced chemical vapor deposition (PECVD). The effect of the growth time on the graphene quality and the underlying silver characteristics is investigated by Raman spectroscopy, X-ray diffraction (XRD), atomic force microscopy (AFM), X-ray photoelectron spectroscopy (XPS), and cross-sectional annular dark-field scanning transmission electron microscopy (ADF-STEM). These results reveal nanocrystalline graphene structures with turbostratic layer stacking. Based on the XPS and ADF-STEM results, a PECVD growth mechanism of graphene on silver is proposed. The multilayer graphene also provides excellent long-term protection of the underlying silver surface from oxidation after 5 months of air exposure. This development thus paves the way towards realizing technological applications based on graphene-protected silver surfaces and electrodes as well as hybrid graphene-silver plasmonics.

1. Introduction

The unique electronic and optical properties of graphene have stimulated an extensive range of scientific research and technological applications. Additionally, multilayer graphene may be regarded as an alternative to graphite in many graphite-related applications with the benefits of much better scalability in the lateral dimensions[156] and the much smaller thicknesses. For instance, it has been challenging to produce highly oriented pyrolytic graphite (HOPG) to an areal dimension larger than ~ (0.1×0.1) m^2. In the case of graphene growth, chemical vapor deposition (CVD) is a common scalable approach to achieve large-scale high-quality graphene synthesis. Common transition metal substrates such as Ni [157] and Cu [158] are used along with high processing temperatures to pyrolyze hydrocarbon molecules to activate CVD graphene growth. [136] Other transition metal substrates such as Ag, [159] Au, [139,140] Pt, [138] Ru, [141] and Co [137] have been reported for CVD graphene synthesis.

One of the drawbacks of CVD graphene growth is that it is a high-temperature process, typically close to the melting points of the metal foils. Under such conditions, aged quartz furnaces and evaporated metal could lead to contamination.[54] In addition, substrates involving temperature-sensitive materials such as polymers would be damaged under high-temperature processes, preventing their applications for flexible materials.[142] Moreover, the current industrial trend of net zero carbon emission by 2050 makes the high-temperature process unfavorable due to large energy consumption. Research progress has been made to reduce the growth temperature for CVD graphene. For instance, a growth temperature of 100 °C has been reported through the use of benzene precursor.[126] Moreover, near room temperature growth has been demonstrated by utilizing liquid metal nucleation.[55] Despite the fact that these novel approaches have greatly reduced the growth temperature, they require sophisticated processing steps that are incompatible with industrial processes and large-area production.[126,55,56]

On the other hand, a scalable and industrially compatible process for low-temperature graphene growth is the plasma-enhanced chemical vapor deposition (PECVD) method. The key factor that allows PECVD to reduce growth temperature lies in the plasma, which contains reactive species to promote growth. Recently, Kim *et al.*[160] have further lowered the required temperatures for PECVD growth of graphene by forced convection to increase the reaction probability of excited species or radicals on the substrate surface before their recombination. To date, the reported growth temperatures for various PECVD graphene synthesis methods are found to range from 160 °C to 700 °C on various substrates.[61, 67-68, 142, 161-163]

Silver is commonly used as the electrode for organic light emitting diodes (OLEDs) and in biosensing due to its strong surface plasmon resonance (SPR). However, silver is prone to oxidation, which would degrade the device performances.[2] This problem may be mitigated by the combination of graphene with silver, which has been reported to increase the stability of the silver nanowire electrodes [5] and theoretically predicted to enhance the SPR sensitivity while preventing oxidation.[2] On the other hand, the inert nature of silver has made it difficult to be used as a substrate for graphene growth with the standard CVD techniques. Among the limited reports of graphene growth on silver, one approach involves evaporating atomic carbon onto the surface of a single-crystalline Ag(111) substrate at elevated temperatures under ultra-high vacuum (UHV) conditions for in-situ scanning tunnelling microscopy (STM) studies.[164] The other approach utilizes a high-temperature, atmospheric-pressure (AP) CVD process with solid camphor as the carbon precursor and silver foil as the substrate in a gas mixture of Ar and H_2.[159] Despite these progresses, direct graphene growth on silver at low temperatures remain a challenging task.[165]

In this work, we show the viability of direct growth of nanocrystalline multilayer graphene on a silver thin film via low-temperature PECVD, where the growth configuration involves flipping the substrate downwards so that the silver thin film is facing away from the direct plasma. The successful growth of nanocrystalline multilayer graphene is confirmed by Raman spectroscopy. X-ray diffraction (XRD) studies of the silver thin films after the

PECVD process further reveal the improvement of the silver crystallinity. Studies by transmission electron microscopy (TEM) reveal that the resulting multilayer graphene is of turbostratic stacking. We further propose a growth mechanism of graphene on silver from studies of the X-ray photoelectron spectroscopy (XPS) and cross-sectional annular dark-field scanning transmission electron microscopy (ADF-STEM) and demonstrate that XPS data may be used as a non-destructive means to infer the average graphene thickness in agreement with the ADF-STEM results. Confirmed through XPS, the surface of silver fully covered by the directly grown multilayer graphene exhibit no traces of oxidation after 5 months of ambient air exposure, which is in stark contrast to the XPS data of a controlled silver surface without graphene coverage, implying perfect passivation of silver by the PECVD-grown multilayer graphene. The excellent protection of silver from oxidation provided by the PECVD-grown graphene and the improvement of the underlying silver crystallinity after the PECVD process suggests that our approach paves ways towards realistic technological applications of graphene-protected silver electrodes and surfaces as well as hybrid graphene-silver plasmonics.

2. Material and methods

2.1 Substrate preparation

The Ag substrate in this work included a Si substrate covered with a 100 nm thick Ti adhesion layer and a 500 nm thick Ag thin film on top, both deposited via an electron-beam (e-beam) evaporator.

2.2 PECVD graphene growth

Before the PECVD process, the interior of the quartz tube was rinsed with nitric acid to remove potential silver residue, while sample holders were cleaned with piranha solution (H_2SO_4:H_2O_2 = 3:1 in volume) at room temperature. Afterward, O_2 and H_2 plasma were separately used to clean both the quartz tube and the sample holders. The plasma system involved a microwave power source (Sairem) and an Evenson cavity. Prior to plasma

ignition, CH_4 of 1 sccm and H_2 of 4 sccm were added into the quartz tube with a total pressure of 100 mtorr. The Ag side was flipped downward as shown in Figure 5.1.

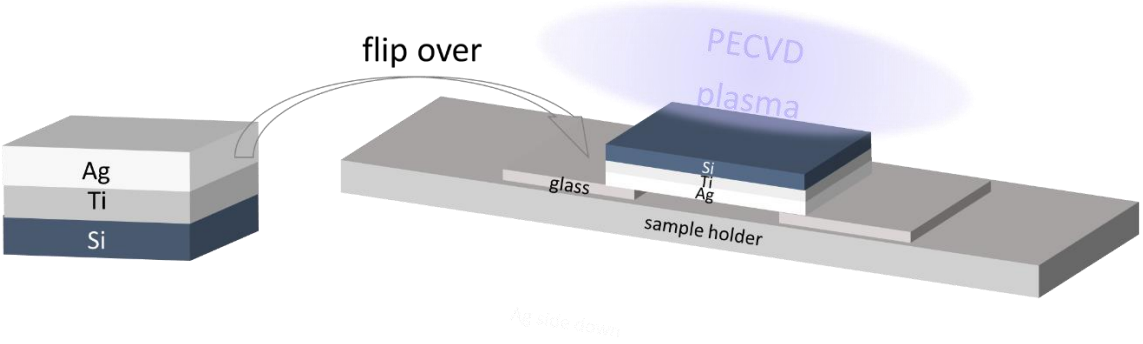

Figure 5.1. Schematic of flipping over the Ag/Ti/Si substrate and placing it onto the sample holder for direct PECVD-graphene growth on Ag.

10 W of plasma power was used along with various growth times. During the PECVD process, the sample was heated only by direct plasma. During the PECVD process, the temperature on the sample was between 232-260 °C, as measured by a temperature label (Wahl TEMP-RECORDER 101-4V). After the PECVD process, polymethyl methacrylate (PMMA) was spin-coated on the silver samples covered with PECVD-grown graphene, which was followed by silver etching with a gold etchant (TFA, Transene) in order to transfer the graphene grown on silver to a SiO_2 substrate to evaluate the graphene coverage. Subsequently, acetone was used to remove the PMMA on the transferred graphene sample. For TEM planar view imaging, the PECVD-grown graphene was transferred onto a Cu grid with a Lacey Formvar film.

2.3 Characterization

Raman spectroscopic characterizations for graphene growth and quality confirmation were made by using a Raman spectrometer (InVia, Renishaw) equipped with a 514 nm laser. Atomic force microscopy (AFM, Bruker Dimension Icon) with PeakForce tapping mode was used for surface morphology characterization. XPS (Kratos Axis Ultra) with monochromated Al K_α X-ray source and a hemispherical energy analyzer under a pass energy of 10 eV was used for the high-resolution scan, whereas a pass energy of 80 eV was used for X-ray induced Auger spectroscopy (XAES) of the C KLL Auger region. In addition, XPS signal was used for estimating the graphene thickness, as elaborated in a later section. The instrument work function was calibrated with respect to the Ag $3d_{5/2}$ signal. Cross-sectional ADF-STEM and TEM plane view images were acquired by aberration-corrected JEOL ARM-200F operated at 200 kV. Selected area diffraction (SAD) was taken with JEOL JEM2100F at 200kV. XRD (Rigaku Smartlab) was performed using Cu K_α radiation and Ge (220) double bounce monochromator for $K_{\alpha 2}$ elimination.

3. Results and Discussion

Figure 5.2(a) shows the Raman spectra of PECVD-grown graphene on silver under different growth times. The observed characteristic Raman modes of graphene (*i.e.*, the D, G, D', 2D and 2D' peaks) confirms the successful low-temperature growth of graphene on silver. The optical micrograph image of a SiO_2 substrate with the transferred graphene as shown in Figure 5.2(b) indicates a full coverage of graphene on the silver substrate of (1.0×0.7) cm^2. Interestingly, despite very high I(D)/I(G) ratios for all samples, the distinct 2D and 2D' peaks indicated a good graphene crystallinity of our PECVD-grown graphene. The 2D and 2D' peaks of graphene result from intervalley and intravalley phonon scattering, respectively; neither has needs for defect activation. [166-167] Therefore, one may expect that as the defect concentration increased, 2D and 2D' peaks would have become worse defined due to imperfect electron dispersion, as demonstrated by Eckmann *et al.*.[168] In this context, had the high I(D)/I(G) ratios found in our graphene samples been related to high defect concentrations, distinct 2D and 2D' peaks would not have existed.

On the other hand, it is known that the grain size of graphene and its defect types may be extracted by analysing the D-to-G Raman mode intensity ratio (I(D)/I(G)) and the D-to-D' Raman mode intensity ratio (I(D)/I(D')), respectively.[111,127] As shown in Figure 5.2(c), the I(D)/I(G) ratio decreased slightly with increasing growth time, which implied changes in the grain size with growth time. The grain size of graphene *L* can be estimated by the I(D)/I(G) ratio through Eq (5.1):[127]

$$\mathrm{L(nm)} = \frac{560}{\mathrm{E_{laser}^4}} \left(\frac{\mathrm{I(D)}}{\mathrm{I(G)}}\right)^{-1} \tag{5.1}$$

where $\mathrm{E_{laser}}$ = 2.41eV. From Eq (1), the graphene grain size was estimated to be ~ 3-4 nm, as plotted in Figure 5.2(d). Therefore, the combined observation of clear and distinct 2D and 2D' peaks and the extracted grain sizes of graphene from the I(D)/I(G) ratios suggest that the graphene grown on silver thin films via our PECVD method was nanocrystalline. Meanwhile, as shown in Figure 5.2(e), the I(D)/I(D') ratio for different growth times was between 8 and 9, suggesting that the defect types were a mixture of sp^3 bonds for I(D)/I(D') = 13 and vacancy defects for I(D)/I(D') = 7, although primarily the vacancy type.[111, 168]

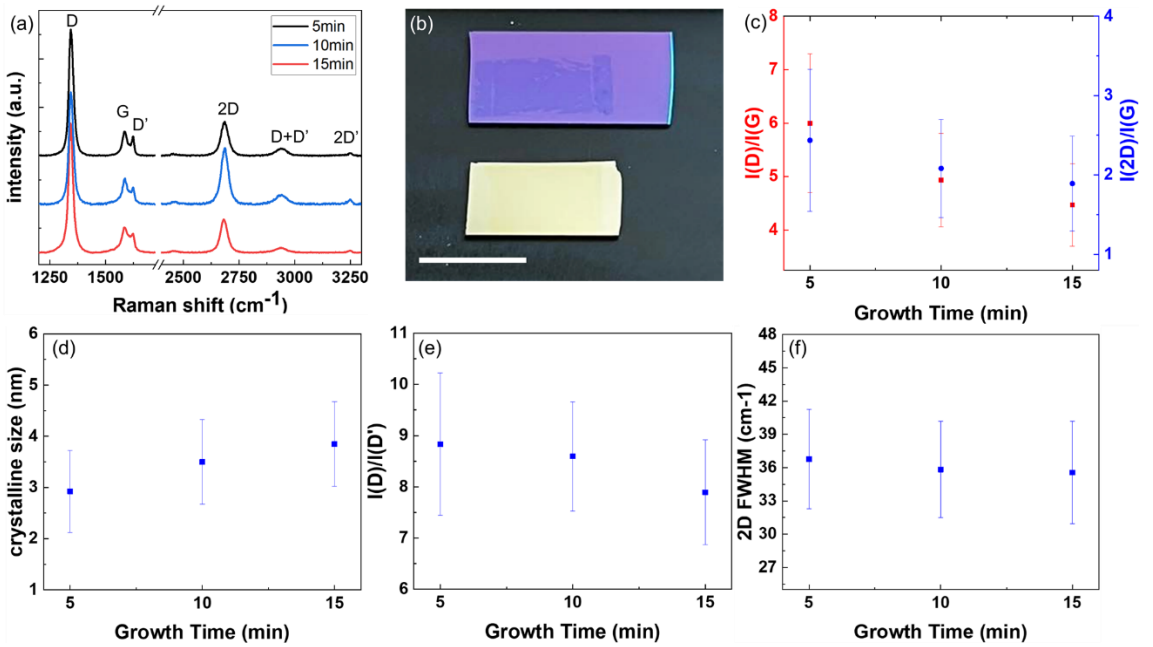

Figure 5.2. Ramen spectra measurements (a) Representative Raman spectrum of the PECVD graphene on silver of different growth times of 5, 10 and 15 minutes. (b) Graphene transferred onto a SiO_2 target substrate after its growth. The growth substrate after the removal of graphene was also included side-by-side with the SiO_2 target substrate to demonstrate the full coverage of graphene on it before graphene removal. The scale bar is 1 cm. (c) The Raman intensity ratios I(D)/I(G) and I(2D)/I(G) for samples of different growth times. (d) The graphene grain sizes of different samples extracted from the I(D)/I(G) ratios and Eq (1). (e) The I(D)/I(D') ratios for samples of different growth times and (f) the FWHM of the 2D peaks for samples of different growth times.

A common perception in the Raman spectral analysis of graphene is that the 2D to G peak intensity ratio I(2D)/I(G) may be used for determining the graphene thickness, with I(2D)/I(G) > 1 implying monolayer graphene. In addition, the full width at half maximum (FWHM) of the 2D peak may provide further information about the number of graphene layers, with an FWHM of ~ 24 cm^{-1} for single-layer graphene [169] and of ~ 50 cm^{-1} for bilayer graphene.[132, 169-170] However, turbostratic stacking of graphene could also give rise to Raman spectral characteristics similar to those of single-layer graphene. In this context, the I(2D)/I(G) ratio and the FWHM of the 2D peak for our PECVD-grown graphene on silver

shown in Figure 5.2(c) and Figure 5.2(f) would imply either single-layer graphene or turbostratic graphene. Therefore, Raman spectral analysis alone appeared insufficient to determine the thickness of graphene conclusively. Additional characterization tools such as TEM and XPS would be necessary to provide more accurate determination of the graphene thickness, as discussed in the following section.

Besides the number of graphene layers and the grain size, Raman spectroscopy could also shed light on the doping and strain of graphene. The spectral shift of either the 2D or G peak, along with the corresponding Grüneisen parameter, could be used to extract the strain effect of graphene.[149] On the other hand, different doping levels of graphene could also lead to a spectral shift of the peak position. As discussed by Lee *et al.*,[171] the doping level and strain effect in graphene may be separated by plotting the 2D peak position versus the G peak position. Following similar analysis, the 2D peak position versus the G peak position of the PECVD-grown graphene on silver showed slightly hole doped and slightly compressively strained, as demonstrated in Figure 5.3, where the relevant numbers used for generating the plot coordinates were summarized in Supporting Information Section S5.1.

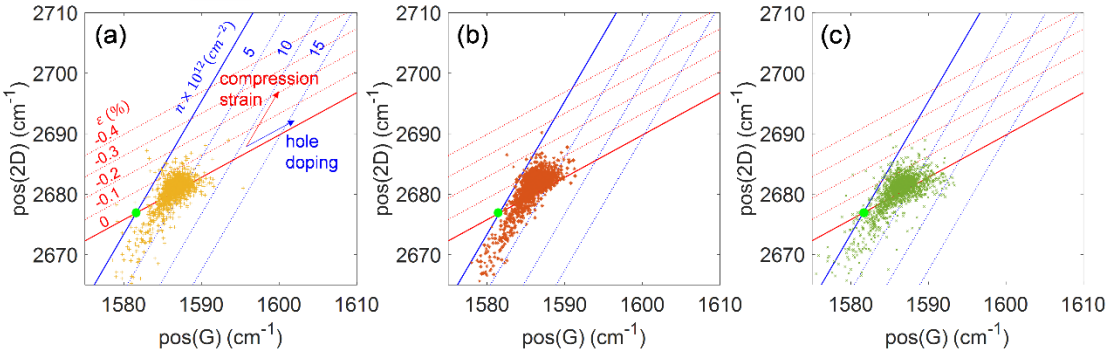

Figure 5.3. 2D peak position "pos(2D)" versus G peak position "pos(G)" of the PECVD graphene on silver samples under growth times of (a) 15 min, (b) 10 min, and (c) 5 min, showing slight hole doping and compressional strain in all samples according to the analysis developed by Lee *et al.*[171] Here the light green solid dot in each panel denotes the strain-free and undoped graphene peak position, and the positive value of the strain corresponds to tensile strain.

To understand the effect of the flipped substrate configuration on the gas flow during the PECVD graphene growth, a computational fluid dynamics (CFD) simulation was carried out. As shown in Figure 5.4, the gas velocity at the top surface (Si side) of the substrate is significantly higher than that of the bottom side (silver side). Therefore, the benefit for using the flipped substrate configuration is two-fold. One is to prevent the energetic plasma from directly damaging the graphene surface. The other is to reduce the gas velocity at the bottom side, which is beneficial to the graphene growth by extending the reaction time between the gas species and the substrate.[172]

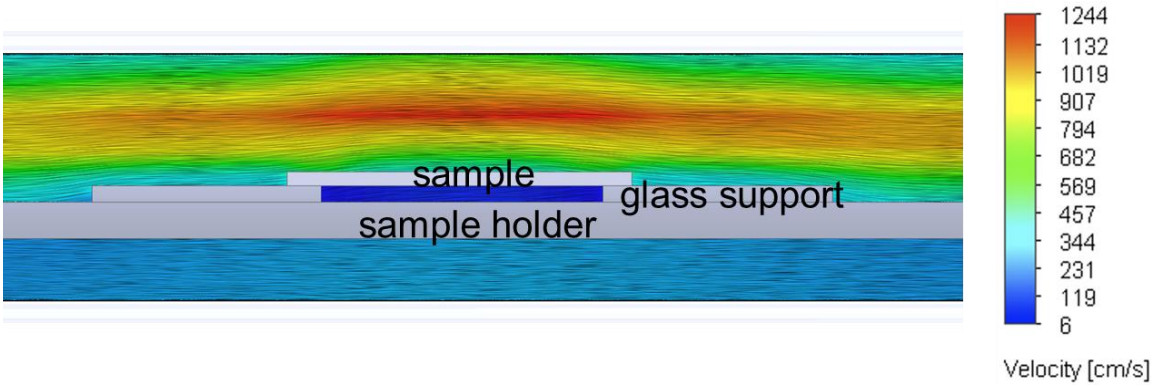

Figure 5.4. A sideview of the gas velocity distribution around the flipped substrate for graphene growth, as obtained by CFD simulations.

Figure S5.2 shows the AFM characterization of the surface morphologies of a sample before and after the PECVD process. After PECVD graphene growth, the AFM image of the surface morphologies was still dominated by the underlying silver layer and revealed a large coalesce of grains and facets, as shown in Figure S2(a-c). In contrast, the silver surface before the PECVD process exhibited apparent granular structures, as shown in Figure S5.2(d). The facet formation after the PECVD process may be attributed to the stabilization of graphene on the metal surface.[173] The increased roughness after PECVD may be attributed to the coalescence of smaller grains, leading to a much larger grain boundary.

Meanwhile, the changes in crystallinity of silver after the PECVD process, as characterized through XRD measurements, were shown in Figure S5.3. The increased Ag (111) intensity

counts after PECVD for different growth times were all much greater than that before the PECVD graphene growth process. Similar peak intensity for all growth times was observed. Given that no active heating source was involved in our PECVD and that the sample temperature was about 232-260 °C through plasma heating, which was much lower than the melting point of silver (961.8 ℃), the improved crystallinity of Ag (111) after the PECVD process when compared to the reference sample may be attributed to the sufficient thermal energy [142] provided by plasma activation. The improved Ag crystallinity could provide added benefits for silver plasmonic applications[174-175].

The chemical changes in the silver thin film quickly after the PECVD process were characterized via XPS as shown in Figure 5.5. Within the Ag-3d spectrum, the silver oxide component was much reduced after the PECVD process (Figure 5.5(a-c)) when compared with the reference sample (Figure 5.5(d)). The O-1s spectrum (Figure 5.5(e-h)) also supported the observation of reduced metal oxide component. Nevertheless, in the O-1s spectrum, peaks associated to SiO_2 were also present. The Si-2p region scans were carried out as shown in Figure S5.4, which confirmed the existence of SiO_2 on the surface. The origin of the SiO_2 will be discussed in a later paragraph.

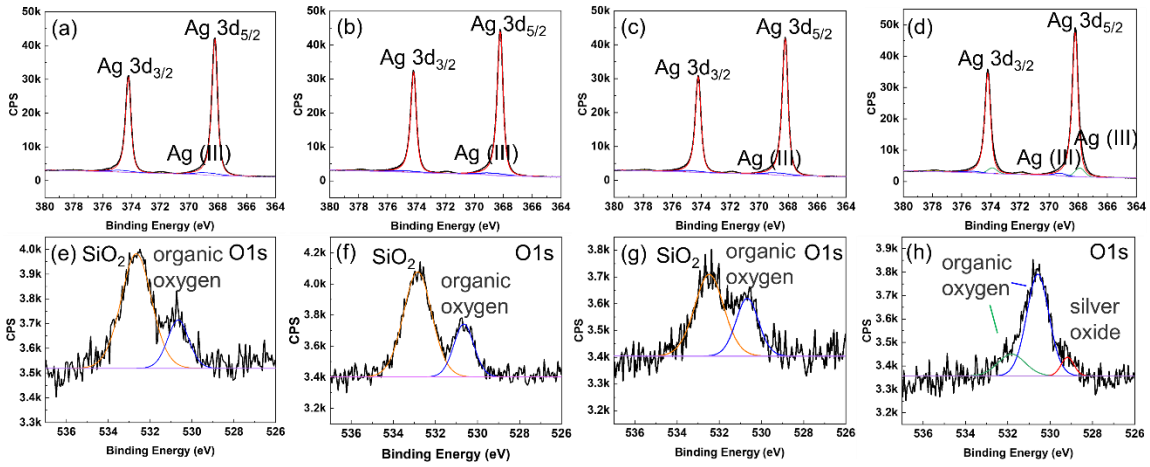

Figure 5.5. XPS Ag-3d and O-1s spectra taken quickly after the PECVD process for growth times of (a,e) 15 min, (b,f) 10 min, (c,g) 5 min, and those of the reference sample (d,h), showing a much reduced silver oxide component for all samples after the PECVD process.

The graphene formation on silver after PECVD was further verified through XPS C-1s spectra as shown in Figure S5.5, which also confirmed the dominant contribution of sp^2 carbon. Moreover, neither metal carbide formation [152] nor bonding between the observed Si and graphene could be inferred from the absence of any apparent peak around the binding energy of 282-283 eV. The extent of hybridization of carbon may be revealed by comparing the "D-parameter" in the C KLL Auger region, where the D-parameter is defined by the peak separation in the first derivative of the Auger spectrum;[176] a larger D parameter would indicate a higher sp^2 hybridization percentage. Using the results from the XAES studies (Figure S5.6), we obtained the first derivative of the spectra for different growth times shown in Figure S6(e-g). In addition to the spectra of different samples before differentiation, the XAES of a graphitic reference has been included in Figure S5.6(d,h) to validate the data processing. As shown in Figure S5.6, the graphene sample with 15 min growth time exhibited the largest D value, suggesting a higher sp^2 percentage than those samples with either 10 min or 5 min growth time. This finding also corroborated the lower I(D)/I(D') ratio shown in Figure 5.1, which implied smaller concentrations of sp^3-like defects.

ADF-STEM images as shown in Figure 5.6 provided direct measure of the number of graphene layers under different PECVD growth times. For the samples with 15 min growth time, we found 3-4 layers of graphene, whereas 2-3 layers for samples with both 10 min and 5min growth times were obtained. To verify the graphene stacking orientation, TEM imaging was performed as shown in Figure 5.7(a). Although the atomic structure was not easily seen, the associated FFT image (Figure 5.7(b)) revealed a six-fold symmetry arc pattern instead of discrete spots, suggesting that the angular orientation of graphene layers was random. Using the TEM electron diffraction imaging as shown in Figure 5.7(c), ring patterns and up to second order diffraction spots were observed. These results further confirmed the turbostratic nature of the multilayer graphene on silver and indicated that our PECVD-grown graphene had good graphene crystallinity despite small grain sizes (or, equivalently, relatively large I(D)/I(G) ratios in the Raman spectrum).

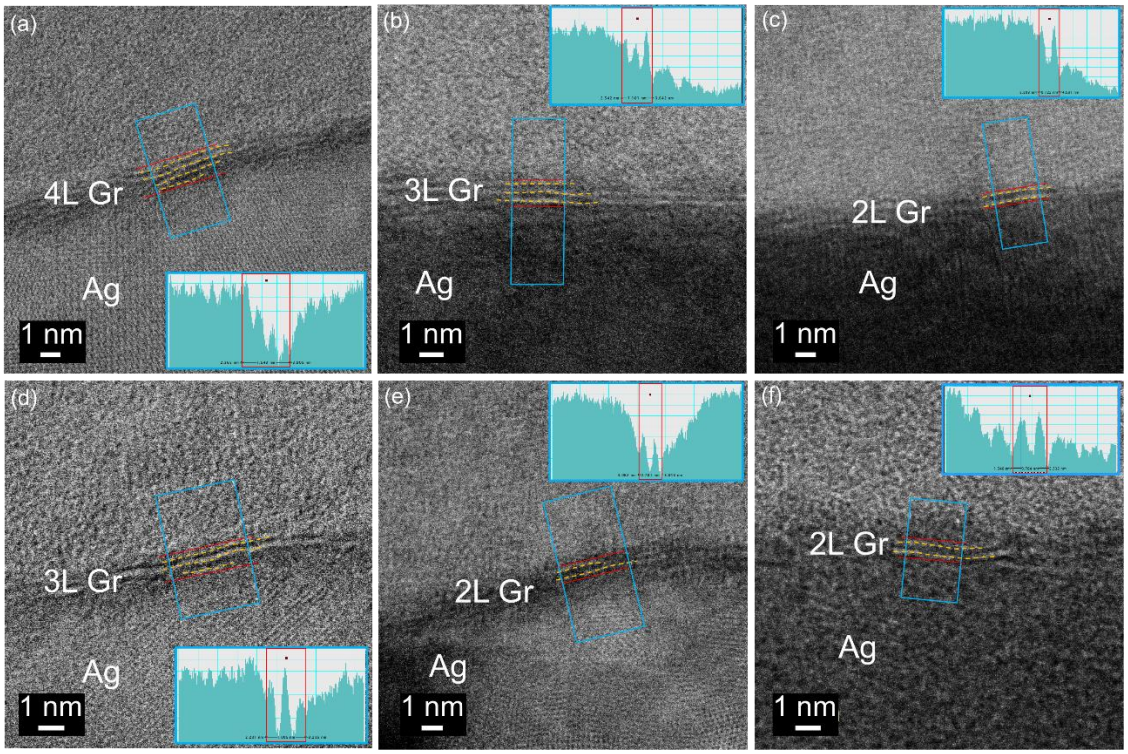

Figure 5.6. Cross-sectional ADF-STEM images for graphene samples with growth times of (a,d) 15 min, (b,e) 10 min, and (c,f) 5 min. The insets showed the averaged intensity profile within the boxed region. The orange dash lines were for guidance to better reveal the number of graphene layers. The STEM images were acquired by ITRI.

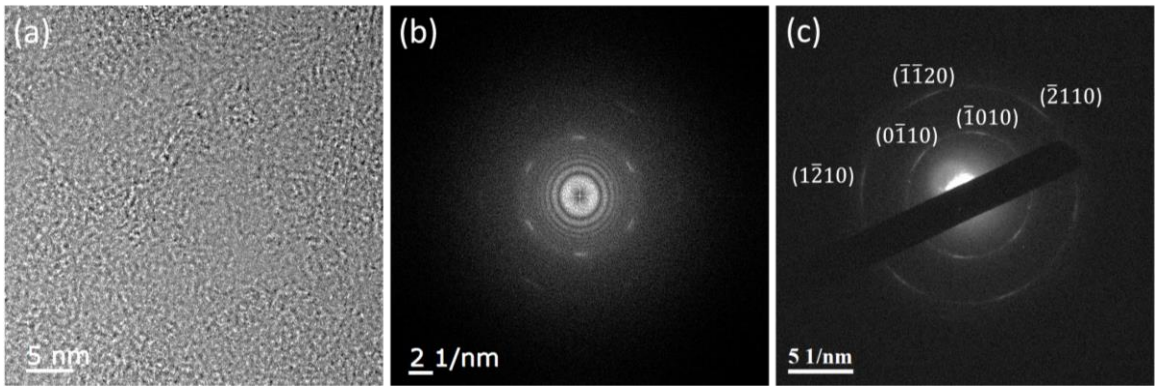

Figure 5.7. TEM studies of the graphene stacking order: (a) TEM image of the planar view of graphene; (b) FFT of (a); (c) electron diffraction image of graphene. The TEM images were acquired by ITRI.

Comparing the direct imaging of graphene layers by ADF-STEM with XPS characterizations, we investigate whether XPS studies may provide useful information about the average number of graphene layers, similar to previous studies by Hill *et al*. that proposed to determine the oxide thin film thickness through XPS [177] and by Cumpson *et al.* that suggested a "thickogram" graphical approach.[178] Specifically, the governing equation for the thickogram is given by

$$\ln\left(\frac{\frac{I_o}{S_o}}{\frac{I_s}{S_s}}\right) - \left[\left(\frac{E_o}{E_s}\right)^{0.75} - 0.5\right]\frac{t}{\lambda_o \cos\theta} - \ln 2 = \ln\left[\sinh\left(\frac{t}{2\lambda_o \cos\theta}\right)\right] \quad (5.2)$$

where I_o and I_s are the integrated spectral area under the peaks from the overlayer and the substrate, respectively; S_o and S_s are the corresponding relative sensitivity factors; E_o and E_s are the kinetic energies of the overlayer element (carbon) and substrate element (silver), respectively; λ_o is the photoelectron inelastic mean free path, t is the overlayer thickness, and θ is the emission angle. In this work, λ_o for graphene was 1.06 nm,[176] and θ for the XPS system was 0°. Additionally, we note that the XPS spectra used for the thickogram analysis must be recorded with the same number of scans and pass energy.

The advancement of computational power since the graphical approach initially proposed by Cumpson *et al.* has enabled numerical computation of sample thicknesses based on given XPS data. Using the XPS data taken on our PECVD-grown graphene on silver samples with different growth times, we find that the extracted overlayer (*i.e.*, graphene) thicknesses for 15 min, 10 min, and 5 min growth times are 1.22, 0.55, and 0.63 nm, respectively, which are in reasonable agreement with the ADF-STEM imaging. Therefore, we have confirmed that XPS data may be used to infer the graphene thickness in addition to Raman spectroscopic analysis and ADF-STEM imaging.

Based on the XPS and ADF-STEM data, we hypothesize the PECVD graphene growth mechanism on silver, which is schematically shown in Figure 5.8. Like all other plasma-enhanced deposition processes, our PECVD growth of graphene on silver begins with the creation of energetic radicals and reacting species through the dissociation or excitation of

methane and hydrogen by microwave excitation. Additionally, the substrates are heated through direct contact with the plasma. While the plasma is on, some reactive species such as radicals and hydrocarbon species diffuse into the silver side and become adsorbed onto the silver surface and then nucleate into graphene. Meanwhile, the top surface of the substrate that directly faces the plasma (*i.e.*, the Si side) undergoes direct bombardment of energetic ions and radicals in the plasma so that some Si atoms/ions are ejected from the substrate into the plasma, leading to incorporation of some Si species during the graphene growth. Given the fact that Ag and Au have the same carbon solubility and therefore the same catalytic activity,[147] the growth mechanism of graphene on silver is expected to be similar to the surface adsorption mechanism on Au. In this context and noting a previous work by Lu *et al.* on PECVD graphene growth on Au that demonstrated bilayer graphene growth for $H_2/CH_4 \geq 1$ after 5 min,[163] our finding of bilayer graphene growth on silver for the same growth time (5 min) with $H_2/CH_4 = 4$ appeared to be consistent with the previous report.

On the other hand, when the growth time was extended to 10 min and 15 min, 3 or 4 graphene layers were observed. As shown from the ADF-STEM images in Figure 5.6, additional graphene layers could grow either from the top or beneath the existing graphene layers. This finding suggests that for PECVD graphene growth on silver, multilayer graphene growth could occur not only through the diffusion of the carbon species from graphene edges but also through the adsorption and nucleation of activated carbon and hydrogen species on the existing graphene layer.

It is worth noting that a penetration graphene growth mechanism has been previously proposed by Wu *et al.*[179]. However, the penetration growth mechanism could not support graphene growth for more than bilayer due to the restricted penetration of carbon atoms,[179] which contradicts our observation.

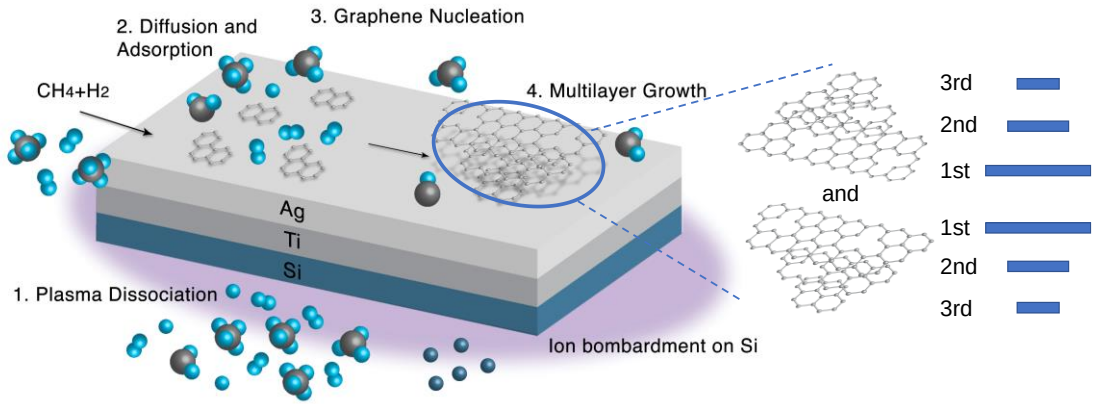

Figure 5.8. A proposed PECVD graphene growth mechanism on silver.

Since the graphene growth temperature is dependent on the plasma power, where higher power results in higher temperatures, it is conceivable to apply plasma power greater than 10 W to achieve larger graphene grain sizes with smaller I(D)/I(G) ratios. However, higher plasma power would lead to more ejected Si species into the plasma and therefore the undesirable result of more Si incorporation into the graphene layers during the growth. This consideration therefore constrains the choice of plasma power during the PECVD growth of graphene on silver.

An important issue to address for the usefulness of our nanocrystalline multilayer graphene is to evaluate its ability for surface passivation, because the small grain sizes are accompanied by many grain boundaries, which may lead to compromised surface passivation because gas molecules could pass through the grain boundaries and reacted with the underlying silver. Fortunately, we found that the multilayer nature and turbostratic stacking of our PECVD-grown graphene could compensate the drawback of many grain boundaries. Figure 5.9 shows the XPS spectra of Ag 3d region after 5 months of exposure to ambient condition. There were negligible changes in the peak shape of the silver covered by directly PECVD-grown multilayer graphene. In contrast, the XPS spectra of the silver sample without graphene protection exhibited significant peak broadening and shoulder formation due to oxidation after 5 months. These findings clearly demonstrate that the silver surface was well protected by the multilayer graphene despite of its nanocrystalline size. The excellent passivation may

be attributed to the fact that multiple graphene layers with turbostratic stacking could significantly hinder the diffusion pathways of moisture or oxygen molecules from reaching the silver surface[163, 180].

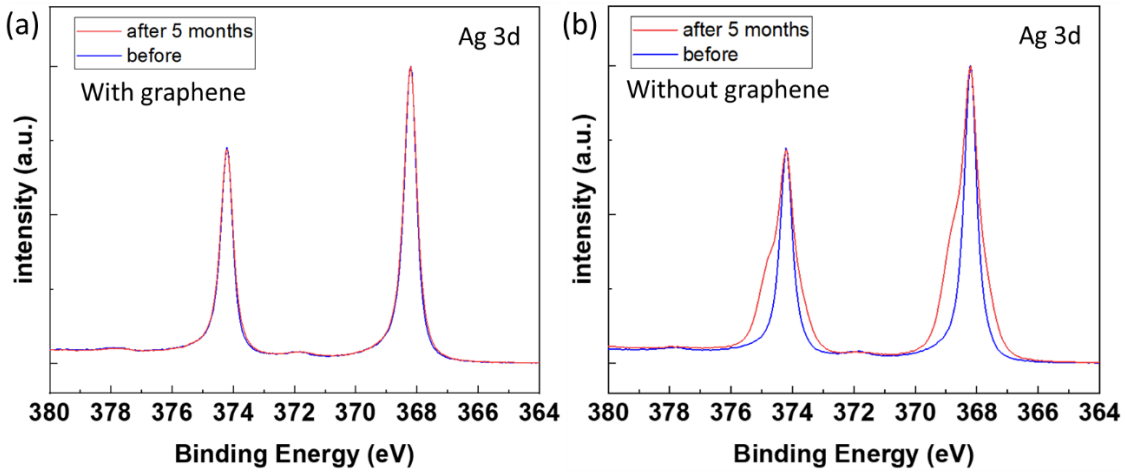

Figure 5.9. Comparison of the XPS Ag 3d spectra of silver after 5 months of exposure to ambient condition for (a) a sample fully covered by PECVD-grown graphene and (b) a sample without graphene. Note that the intensity was normalized for better comparison.

4. Conclusion

In conclusion, we report a low-temperature single-step method for direct graphene growth on silver by PECVD for long-term surface passivation. Raman spectroscopic studies of the graphene-on-silver samples suggested that they consisted of nanocrystals with overall good crystalline quality, underwent a slight compressive strain and exhibited slight hole doping, with vacancies being the primary defects in the samples. Using CFD simulations, the benefit for using the flipped substrate configuration was revealed. From AFM and XRD characterizations, the silver surface morphology and crystallinity after the PECVD process were found to differ from those before the PECVD process, with improved crystallinity after PECVD. The number of graphene layers grown on silver was verified by cross-sectional ADF-STEM images, which varied from 2-4 layers depending on the growth time. The stacking order of the multilayer was confirmed through TEM electron diffraction to be

turbostratic. We further proposed a mechanism for the PECVD-growth of graphene on silver based on findings from the XPS and ADF-STEM studies and demonstrated that XPS data may be used for non-destructive thickness determination of graphene. Moreover, the multilayer graphene was found to protect the underlying silver against oxidation for at least 5 months of ambient air exposure. The combined benefits of passivation and improved crystallinity of silver by PECVD-grown graphene imply that our approach paves the way towards scalable technological applications based on graphene-protected silver surfaces and electrodes as well as hybrid graphene-silver plasmonics.

Supporting Information

Section S5.1. Relevant parameters used to establish the coordinate of strain and doping plots in Figure 5.3

The peak position (G, 2D) for unstrained and undoped graphene is (1581.6, 2676.9) [171]. To generate the strain coordinate, a slope $\left(\frac{\Delta 2D}{\Delta G}\right)_n$ = 0.7 was used, whereas a different slope $\left(\frac{\Delta 2D}{\Delta G}\right)_\varepsilon$ = 2.2 was used to generate the doping coordinate [171]. Additionally, information about the dependence of either the G or 2D peak on different doping levels was necessary to generate the parallel lines shown in Figure 5.3 for different strain and doping levels. We used $\frac{\Delta 2D}{\Delta n} = 0.87$ (an average of 0.7 and 1.04 according to Lee, J. E. *et al* [171]) to generate the 2D peak positions for different hole doping levels. The G and 2D peak positions under no strain and with various hole doping levels have been generated using the aforementioned method, as tabulated below in Table S1.

Table S5.1. G and 2D peak positions with various hole doping levels under no strain

hole doping n x 10^{12} (cm^{-2})	posG (cm^{-1})	pos2D (cm^{-1})
n = 0	1581.600	2676.90
1	1582.843	2677.77

2	1584.086	2678.64
3	1585.329	2679.51
4	1586.571	2680.38
5	1587.814	2681.25
6	1589.057	2682.12
10	1594.029	2685.60
15	1600.243	2689.95

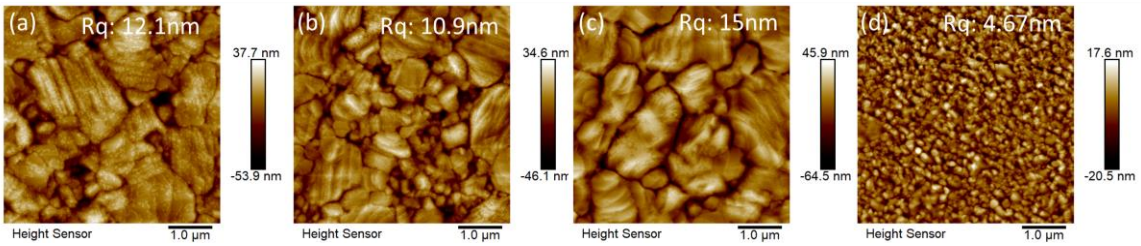

Figure S5.2. The AFM height images of the sample surface after (a) 15 min, (b) 10 min, and (c) 5 min of PECVD graphene growth, showing significantly increased surface roughness in comparison with (d) for the surface of silver before the PECVD process.

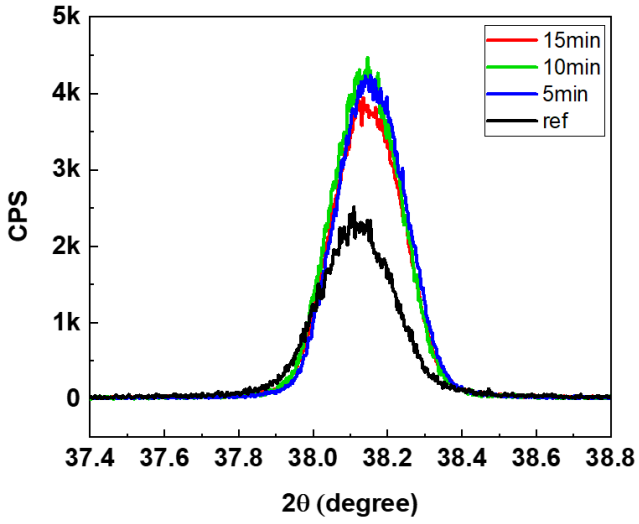

Figure S5.3. Comparison of the XRD spectra of the Ag (111) peak taken on samples before the PECVD process and after the PECVD process for graphene growth over different times of 5 min, 10 min and 15 min.

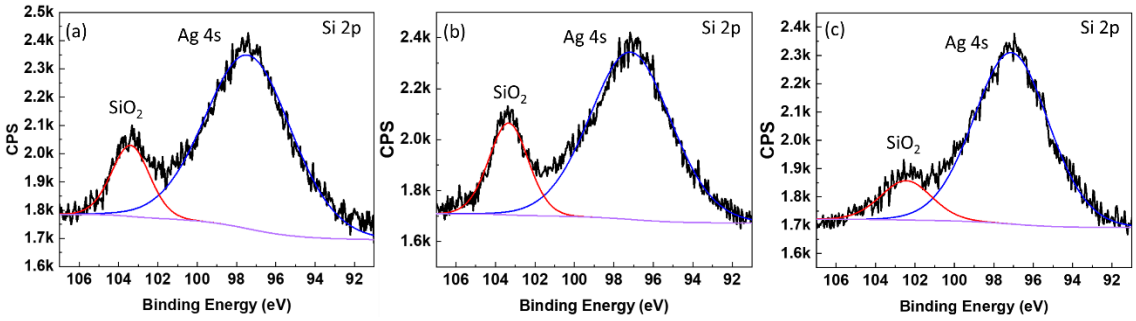

Figure S5.4. Si-2p spectra of PECVD-grown graphene on Ag after growth times of (a) 15 min, (b) 10 min, and (c) 5 min.

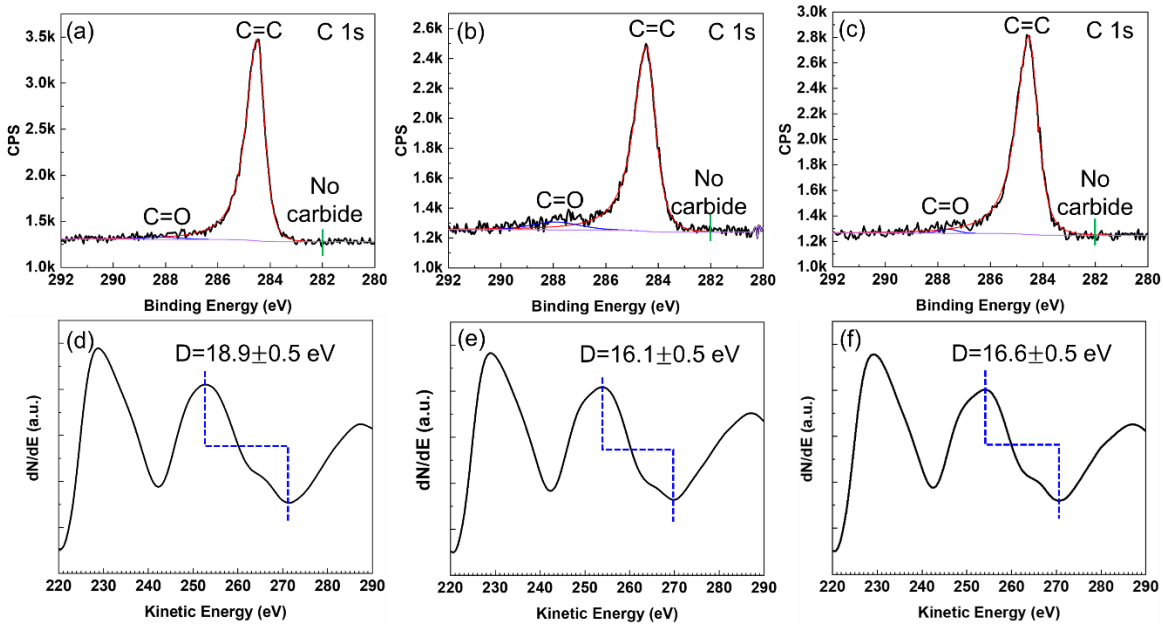

Figure S5.5. XPS C-1s spectra and the first derivative XAES C KLL spectrum after the PECVD with the growth times of (a,d) 15 min, (b,e) 10 min, and (c,f) 5 min.

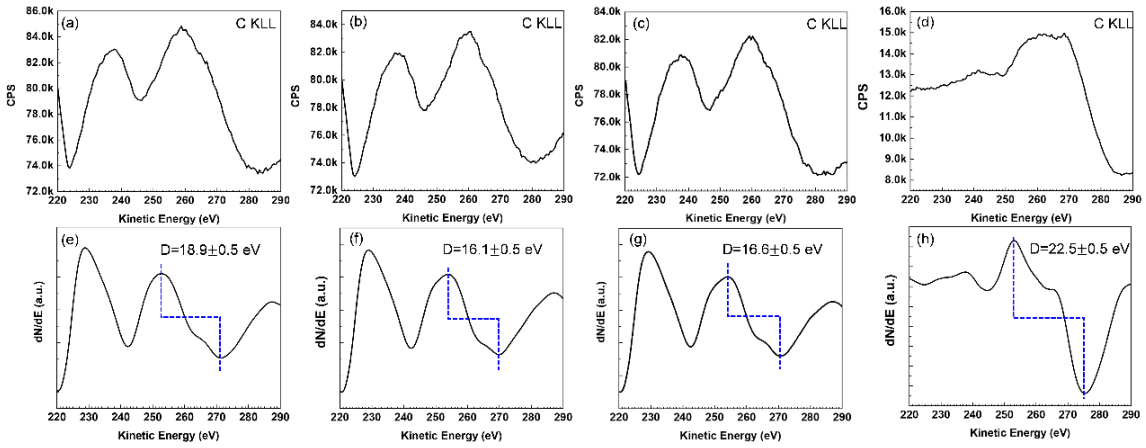

Figure S5.6. XAES C KLL spectra of PECVD-grown graphene on Ag after growth times of (a) 15 min, (b) 10 min, and (c) 5 min, and (d) the C KLL spectrum of xGnP Graphene Nanoplatelets R10, where R10 was used as the reference graphene material to validate the data processing. (e-h) The first derivative of C KLL spectra of (a-d), respectively. The D value for the graphitic reference sample is in agreement with that in a previous report [176]. Before differentiation, the data were smooth by moving average method with a width of 11

data points. The spectra differentiation was executed with the Savitzky–Golay(SG) quadratic method and a smoothing width of 11 data points using CasaXPS software.

Chapter VI

FEASIBILITY AND STRUCTURAL TRANSFORMATION OF ELECTRODEPOSITED COPPER FOILS IN PECVD GRAPHENE GROWTH

Adapted from:
Lu, C.-H.; Shang, K.-M.; Lee, S.-R.; Leu, C.-M.; Tai, Y.-C.; Yeh, N.-C. Feasibility and Structural Transformation of Electrodeposited Copper Foils for Graphene Synthesis by Plasma-Enhanced Chemical Vapor Deposition. Submitted.

Personal contribution: C.-H. L. initiated the idea, grew the PECVD graphene, performed SEM, EBSD, XPS, Raman measurements, interpreted the data, and wrote the draft manuscript.

Large-area graphene has often been synthesized on rolled-annealed copper foils, which requires subsequent transfer to targeted substrates for desirable applications. Here we investigate the quality of large-area graphene directly grown by plasma-enhanced chemical vapor deposition (PECVD) on electrodeposited copper foils that are widely used in lithium-ion batteries and printed circuit boards. Through a series of spectroscopic and microscopic studies, we uncover intricate correlations between the graphene growth dynamics and the growth time and plasma power: For a given plasma power, a minimum growth time is required for comprehensive graphene coverage, which is followed by the formation of complete monolayer graphene and t hen the emergence of multilayer graphene with increasing time, indicating that the PECVD growth of graphene on electrodeposited copper foils is not self-limited. A pivotal finding is the adverse impact of reduced plasma power on the resultant graphene quality because of the effectively lower substrate temperatures. Additionally, the PECVD process initiates significant chemical and structural beneficial alterations to the electrodeposited copper substrate, including efficient removal of the surface Zn layer, increased Cu grain size, reduced surface roughness, and reoriented out-of-plane Cu orientations, which foster optimal graphene growth conditions on these industrially compatible substrates for a wide range of applications.

1. Introduction

Since the initial discovery of isolating graphene as a single atomic layer using the exfoliation method[48], much progress has been made towards the synthesis of graphene, including using the controllable chemical vapor deposition (CVD) method to allow for scalable growth of graphene on copper [158]. While advances in research have indicated that other metal substrates like Co[137], Ru, [141] Pt, [138] Au, [139-140, 163,] Ag, [159, 181] can be used for graphene growth, copper foil remains the most popular choice due to their ease of preparation and availability. The growth of graphene on copper has shown promising results, including enhanced mechanical strength[150], superior electromigration resistance[125], and improved cycle life for anode-free lithium batteries[182].

Most graphene growth on copper to date employs rolled-annealed (RA) copper foils, which are produced through a continuous mechanical rolling process of a copper billet, leading to inherently limited lateral dimensions and minimum thicknesses as well as rolling lines on the foil surface. In contrast, electrodeposited (ED) copper foils, which are typically used in copper-clad laminates (CCL) for printed circuit boards (PCB) and as the current collector for lithium-ion batteries, have their advantages. For instance, in rigid PCBs, ED copper foils are often preferred over RA copper foils due to their cost-effectiveness and improved thickness control.

The production of ED copper foil involves submerging a negatively charged metal drum in a copper sulfate solution. The rotation of the drum facilitates the deposition of copper onto its surface, gradually creating the foil. This process results in a columnar crystallite structure in the ED copper. The ED copper then undergoes surface treatments, such as passivation with Zn or Ni. Despite occasional reports of graphene growth on electroplated copper film[150] and the co-electrodeposition of copper and graphene oxide[183], there have been no reported direct graphene growth on ED copper foil, which may imply challenges associated with the inherent surface roughness and the surface passivation of ED copper foils.

Among various graphene growth methods, plasma-enhanced chemical vapor deposition (PECVD) is a low-temperature process with scalability and industrial compatibility. The reduced growth temperature for PECVD is due to reactive species generated in the plasma that help facilitate the growth. Various studies have reported PECVD graphene synthesis at temperatures varying between 160 °C and 700 °C across different substrate materials.[61, 67-68, 142, 161-163]. Compared to thermal CVD, where a growth temperature approaching the melting temperature of the metallic substrate is used, the PECVD method complies with contemporary industrial shifts towards achieving net zero carbon emission by 2050 through reducing the large thermal budget.

In this work, we demonstrate the feasibility of using PECVD to grow graphene on ED copper foil, an alternative to the commonly used RA copper foil in the realm of graphene growth. The successful graphene growth is substantiated by Raman spectroscopic studies. In addition, accompanying scanning electron microscopy (SEM) analyses reveal significant time dependent transformations in the morphology of the ED copper foil during the PECVD process. High-resolution transmission electron microscopy (HRTEM) and electron diffraction also confirm that the graphene sheet grown on the ED copper foil is monolayer with high crystallinity. Complementing the SEM and HRTEM findings, electron backscatter diffraction (EBSD) studies offer deeper insights into the remarkable crystallographic changes occurring in the ED copper foil, even with a brief exposure to the PECVD process. Further, X-ray photoelectron spectroscopy (XPS) taken on graphene samples synthesized on ED copper foils by PECVD provide evidence for the effective removal of the protective zinc cap layer on the ED copper foil during the initial graphene growth stages and the subsequent development of the graphene signature. This comprehensive study broadens our understanding of the underlying dynamics of graphene growth on ED copper foils, which presents the potential for their more extensive utilization in graphene-based applications.

2. Experimental method

2.1 Sample Preparation

The ED copper foils with a thickness of 18 μm were developed by the Industrial Technology Research Institute. The top surface of these foils was coated by a thin layer (~ 5 nm in thickness) of Zn, while the back surface was covered by silane derivatives as an adhesion promoter. Both treatments are standard industrial practices for the ED copper foils used in PCB applications.

2.2 PECVD Graphene Growth

The PECVD system comprises a 1/2" quartz tube, quartz sample holder, and Evenson cavity equipped with a microwave source. To eliminate copper residue, the quartz tube and sample holders were cleaned with nitric acid. Ar/O_2 and Ar/H_2 plasma were separately utilized to further remove potential carbon residue from the quartz tube and sample holders. A methane (CH_4) flow of 0.005 sccm and a hydrogen (H_2) flow of 5 sccm were introduced into the tube, with a stabilization time of at least 10 minutes provided for the low CH_4 flow. The total pressure was set at 500 mtorr.

The PECVD process utilized a maximum plasma power of 40 W while adjusting the growth time. Heating of the sample during PECVD was exclusively accomplished through direct plasma. It should be noted that higher plasma power often resulted in almost complete Cu etching. More information regarding the temperature estimation inside the plasma is detailed in the supporting information section S1. After the PECVD process, graphene grown on copper was transferred to a SiO_2 substrate for graphene coverage evaluation. The sample transfer and copper etching processes involved the use of polymethyl methacrylate (PMMA) and the treatment with 0.25M ammonium persulfate (APS).

2.3 Characterization

Raman spectroscopic analysis was performed using a Renishaw InVia Raman spectrometer equipped with a 514 nm laser. Field emission scanning electron microscopy (FESEM) with an EBSD detector (ZEISS 1550VP) was utilized to examine the morphology and crystallography of the copper surface. The FESEM was operated at 20 kV for EBSD, while a setting of 5 kV was used for SEM imaging of transferred graphene. The surface roughness of the copper foil was determined using Wytec white light interferometry. High-resolution and survey scans for XPS were conducted using a Kratos Axis Ultra instrument, employing monochromated Al Kα X-ray source with pass energies of 10 eV and 40 eV, respectively. The instrument's work function was calibrated based on the Cu $2p_{3/2}$ signal at 932.6 eV. For HRTEM and electron diffraction, the graphene samples were transferred onto Cu grids coated with a Lacey Formvar film and imaged with JEOL JEM2100F at 80kV.

3. Results and discussion

Figure 6.1(a) shows the Raman spectra of graphene, grown via PECVD on ED copper foil under varying growth times and utilizing a 40W plasma. The spectra show the characteristic G and 2D peaks, confirming successful graphene growth on ED copper when growth periods exceeded five minutes. In contrast, we note that when the growth duration was shorter than five minutes, no characteristic graphene signals could be observed.

Figure 6.1(b) depicts an optical micrograph for a SiO_2 substrate with a transferred PECVD-grown graphene sample on top. This image suggests complete graphene coverage on the ED copper growth substrate, encompassing an area of about (1.5×0.8) cm^2. We further adjusted plasma power levels while maintaining a consistent growth time of 20 minutes. The results, presented in Figure 6.1(c), demonstrate a significant correlation between the quality of the resultant graphene and the plasma power. Interestingly, a distinct D peak appeared at lower powers of 30 W and 20 W, while the 2D peak vanished at 20 W. The 2D peak, known to indicate graphene's crystallinity, stems from intervalley phonon scattering. Decreasing the plasma power limits the available energy needed to dissociate or excite the methane and

hydrogen required for growth. As our system employs direct plasma without active heating, the substrate temperature corresponds directly to the plasma power. Thus, lower plasma power implies a lower substrate temperature—a condition less favorable for graphene growth. Consequently, a decrease in plasma power leads to a decline in the quality of the resultant graphene. On the other hand, excess plasma power could lead to damages incurred by the bombardment of energetic ions and radicals in the plasma. Thus, proper balance between supplying sufficient dissociation energy for methane in graphene growth and preventing damages to graphene by energetic particles in the plasma is necessary to achieve high quality graphene growth on the ED copper substrate.

Raman spectroscopy is a common tool for identifying strain and doping levels in graphene by analyzing the positions of the 2D and G peaks[171, 181]. As shown in Figure 6.1(d), graphene samples grown on ED copper foil appeared to be electron-doped and under compressive strain. The electron doping level was approximately 7×10^{12} cm^{-2}. Using the formula $E_F = \hbar|v_F|\sqrt{\pi n}$[184], where v_F is the Fermi velocity in graphene (1.1×10^6 m/s), $\hbar$ is the reduced Planck constant (6.58×10^{-16} eV·s), and n is the two-dimensional charge density, we calculated the Fermi level shift to be around 0.34eV. This value aligns with the reported value for graphene on a Cu crystal[185-186]. The observed compressive strain can be attributed to the difference in thermal expansion coefficients between Cu and graphene[186-187]. After transferring the graphene onto SiO_2, the strain considerably relaxed, and the doping level slightly shifted to hole-doping.

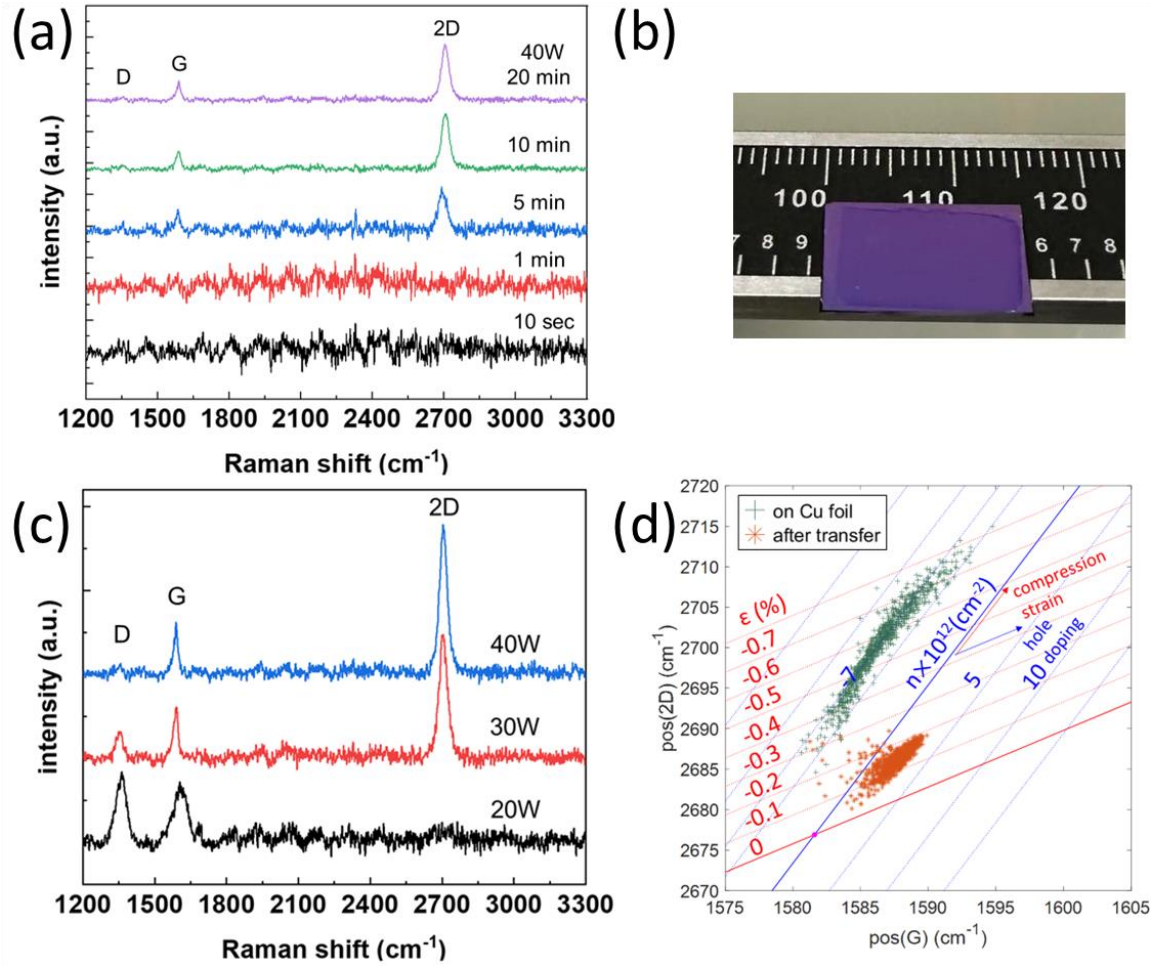

Figure 6.1 Ramen spectra measurements (a) Raman spectrum of PECVD-grown graphene on ED copper foil with varied growth times at 40W. (b) Optical micrograph showing a graphene sample of an area ~ (1.5×0.8) cm² that was transferred onto a SiO_2 substrate after the PECVD growth on an ED copper foil. (c) Raman spectra of graphene samples grown on ED copper foils under different plasma powers for the same 20-minute growth time. (d) Correlation between the positions of the 2D peak (pos(2D)) and the G peak (pos(G)) of PECVD-grown graphene, pre- and post-transfer. The pink solid dot at the cross point of the red and blue lines represents the position of strain-free and undoped graphene for reference.

To inspect the graphene boundaries and the number of layers, Figure 6.2(a,b) presents the SEM image taken with a standard Everhart-Thornley (ET) detector, showcasing transferred

graphene with growth times of 10 and 20 minutes at 40W, respectively. The images do not exhibit noticeable signs of multilayer graphene formation. However, when using in-lens detector (Figure 6.2(c,d)), the existence of graphene boundaries and multilayer domains becomes clear. The image corresponding to the 10-minute growth duration (Figure 6.2(c)) does not show signs of multilayer domains while the image from the 20-minute growth duration (Figure 6.2(d)), on the other hand, exhibits several multilayer graphene domains of approximately 1μm. This observation suggests that, unlike thermal CVD graphene growth[158], the growth of graphene by PECVD is not self-limiting. This is largely attributed to the abundant supply of C_2 radicals generated by microwave plasma,[67] which play a crucial role in the formation of sp^2 bonds.[188]

Here we note that the increased visibility of grain boundaries and multilayer domains when utilizing an in-lens detector can be attributed to reduced signals from the Type III secondary electrons (SE3), the latter originate from backscattered electron scattering within the SEM chamber. Although a standard ET detector in principle could also image the boundary/multilayer domain contrast, it requires optimization of accelerating voltage and working distance to reduce the SE3 signal[189], which makes direct imaging of the boundary/multilayer domain contrast using the ET detector more difficult. In contrast, using an in-lens detector is more straightforward and provides a simpler approach to achieve the same result, making it highly sensitive to variations in the graphene structure.

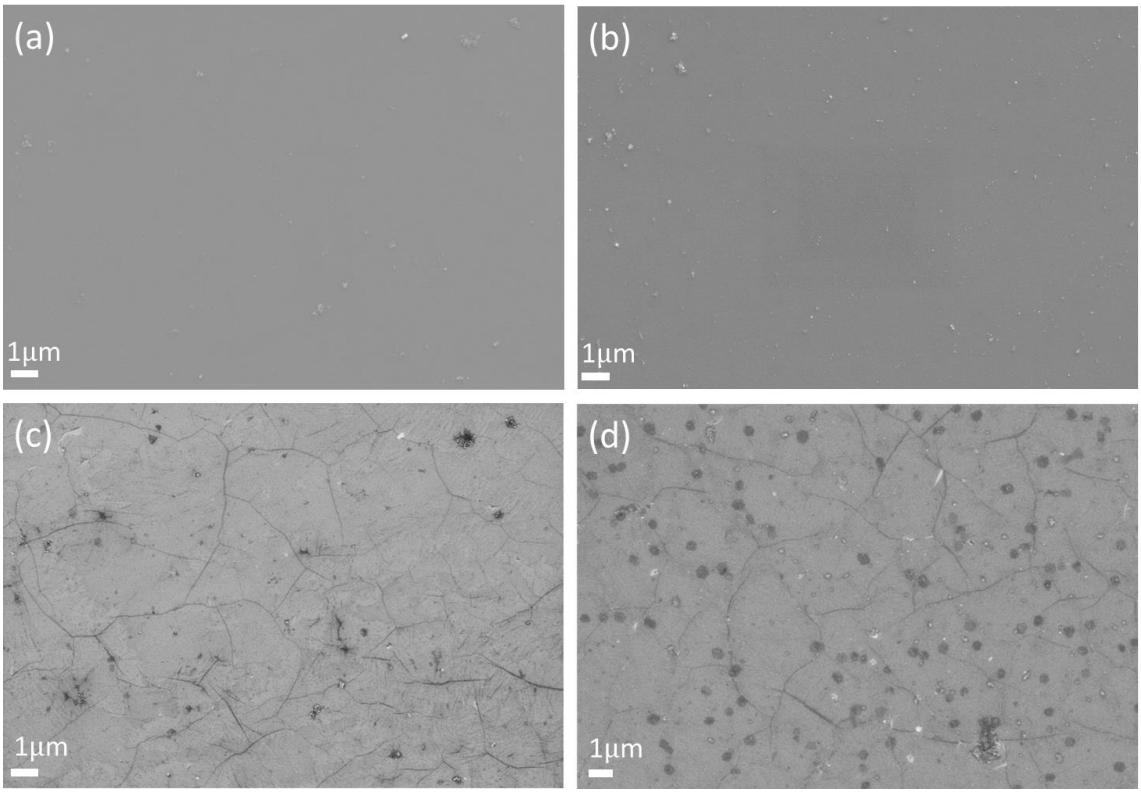

Figure 6.2. SEM images of transferred graphene grown at 40W. The growth time for images (a,c) is 10 minutes, while images (b,d) correspond to a growth time of 20 minutes. Images (a,b) were taken under ET detector, and images (c,d) were taken under in-lens mode.

To further verify the quality and the numbers of layers of graphene, HRTEM imaging and electron diffraction were performed as shown in Figure 6.3. The clear honeycomb lattice and six-fold diffraction spots indicate that the graphene is of monolayer and highly crystalline, which also corroborates with the negligible D/G ratio from the Raman spectrum.

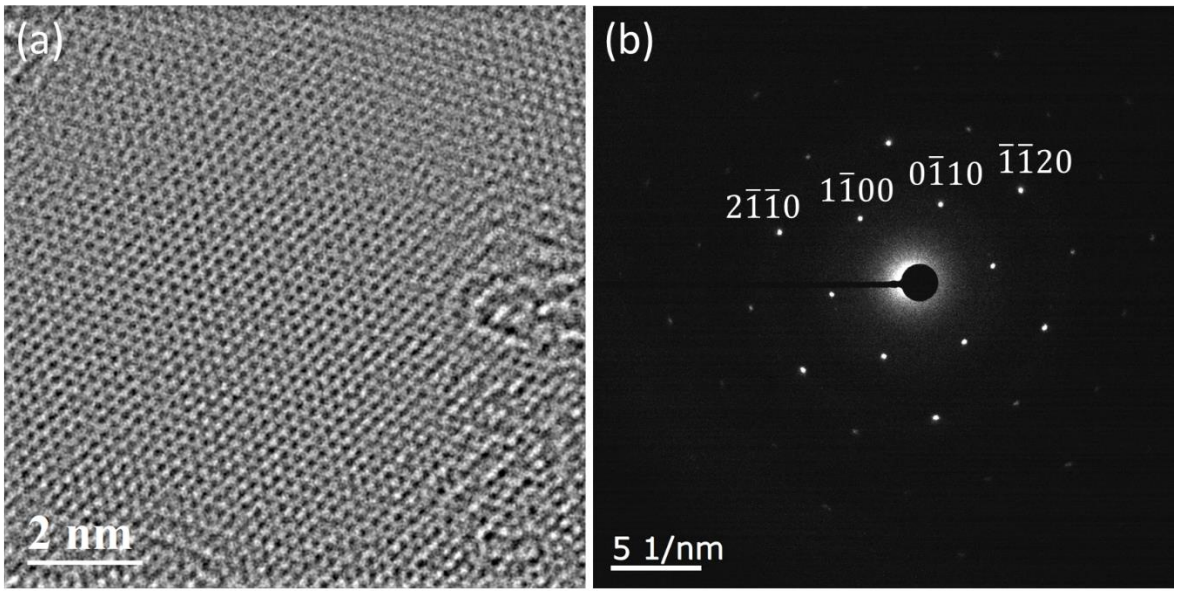

Figure 6.3. TEM and diffraction images (a) HRTEM image of transferred graphene grown at 40W with a growth time of 10min. (b) Electron diffraction of transferred graphene grown at 40W with a growth time of 10min. The TEM images were acquired by ITRI.

An examination of the evolution of the ED copper foil following the PECVD graphene process offers intriguing insights. Figure 6.4 features an optical micrograph of the ED copper foil after different durations of graphene growth. As the growth time increases, the grain boundaries of the Cu foil become better defined and deepen, while the ragged surface is gradually eliminated. This observation is further substantiated by the SEM images in Figure S6.4.

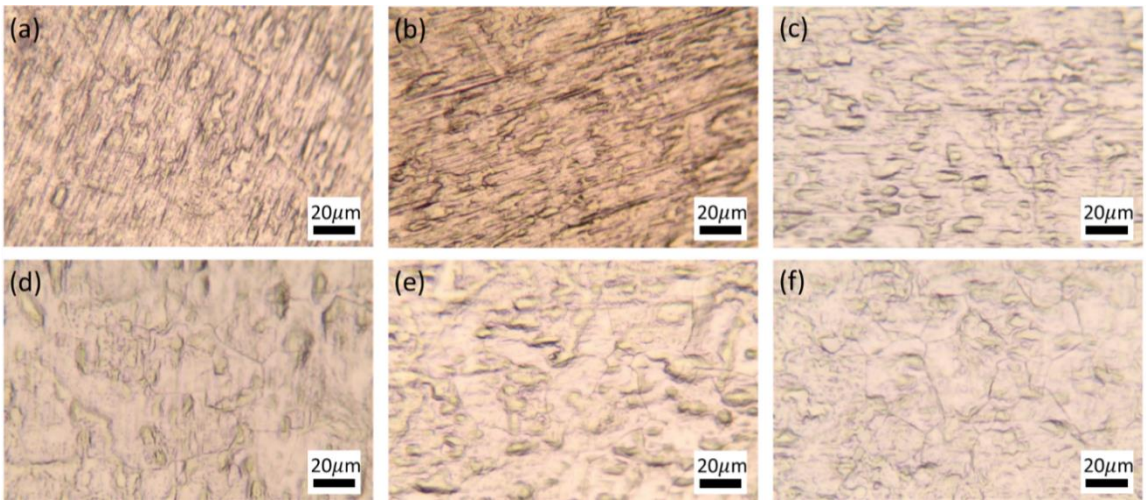

Figure 6.4. Optical micrographs of the ED copper foil (a) before PECVD and after PECVD at 40W for a growth time of (b)10sec (c) 1min (d)5min (e)10min and (f) 20min, respectively.

On the contrary, optical micrographs shown in Figure S6.5 and SEM images in Figures S6.6 suggest that a reduced plasma power (20W and 30W) has minimal impact on the surface morphology, which largely maintains its ragged appearance. While the surface appears smoother under SEM after graphene growth at 40W, measurements using a white light interferometer (Figures S6.7 and S6.8) reveal an increase in roughness as the growth time extends (Figure 6.5(a)). In contrast, the roughness stays relatively constant for smaller plasma power of 20 W and 30 W, and then increases at 40 W (Figure 6.5(b)). Under elevated plasma power, grain boundaries are etched at a faster rate, resulting in their significant deepening. While this process may smooth individual grains, the increased depth of the grain boundaries contributes to an overall increase in surface roughness.

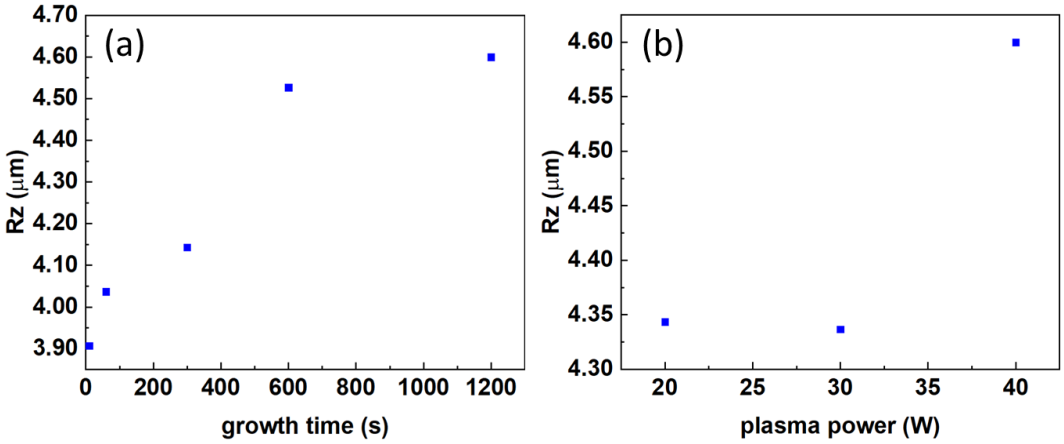

Figure 6.5. Roughness of ED copper foil after PECVD graphene growth. (a) Variation in roughness with different growth times at 40W. (b) Comparison of roughness with different plasma power at a fixed growth time of 20 minutes.

The EBSD mapping of an ED copper foil, both before and after PECVD graphene growth for different growth times at 40W, is exhibited in Figure 6.6. The average grain size is calculated and plotted in Figure 6.7(a). The activation energy of Cu grain growth in this context is calculated by analyzing the grain size dependence at different temperatures. Given the direct dependence between temperature and plasma power in our study, we also measured the Cu grain size under varying plasma power conditions (Figure S6.9), as summarized in Figure 6.7(b). The conversion of plasma power to substrate temperature is explained in the supplementary information section S6.1.

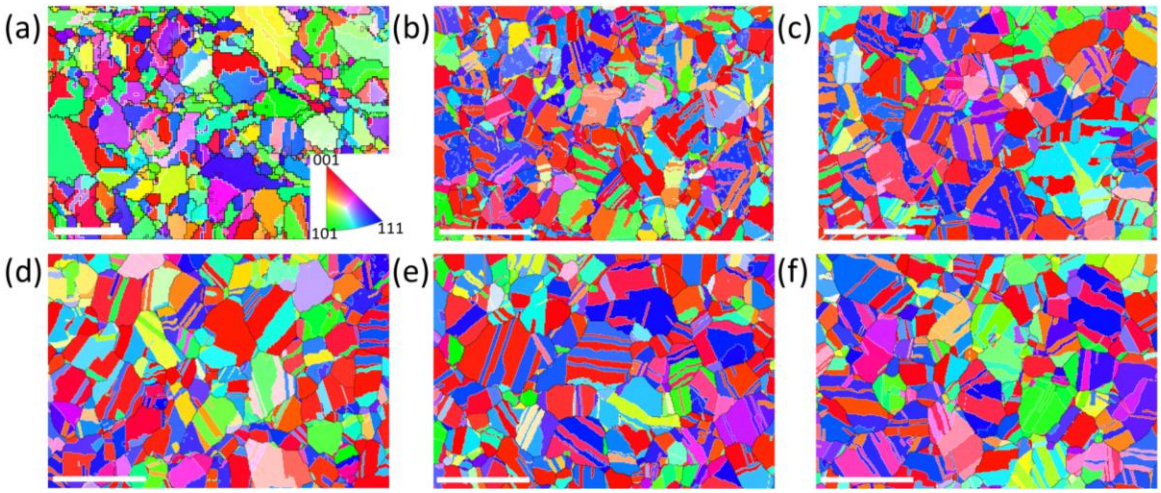

Figure 6.6. EBSD map of an ED copper foil (a) before PECVD and after PECVD at 40W with different growth times of (b)10sec (c) 1min (d)5min (e)10min and (f) 20min, respectively. The scale bar in (a) is 2μm and 100μm for (b) – (f). Grains were defined with a grain detection angle of 10° and the twin boundaries (Σ 3) are indicated with white lines. The color scales for grain orientation is shown in the lower right corner of (a).

A general model of grain growth kinetics can be described by the equation[190]

$$D^n = Kt \qquad \text{(Eq 6.1.)}$$

where n represents the growth exponent, K is the growth coefficient, D is the grain size, and t is the growth time. The growth exponent n can be determined by examining the slope when plotting ln (t) *vs.* ln (D), as shown in Figure 6.7(c). Here, the value of n is determined to be 14.88. To deduce the activation energy, we note that the growth coefficient can be expressed as

$$K = K_0 e^{-(\frac{Q}{RT})} \qquad \text{(Eq 6.2.)}$$

where Q is the activation energy and R is the gas constant. Integrating this with Equation 1, we obtain

$$\ln\left(\frac{D^n}{t}\right) = \ln(K_0) - \frac{Q}{R}\frac{1}{T} \quad \text{(Eq 6.3.)}$$

as demonstrated in Figure 6.7(d). The slope magnitude $\frac{Q}{R}$ is determined to be 50906, corresponding to an activation energy of 423.2kJ/mol.

The comparison of both the growth exponent and activation energy with the ideal case—where n = 2 and the grain boundary diffusion of Cu is 91.67kJ/mol[191]—indicates that the Cu grain growth during PECVD graphene growth is substantially impeded.

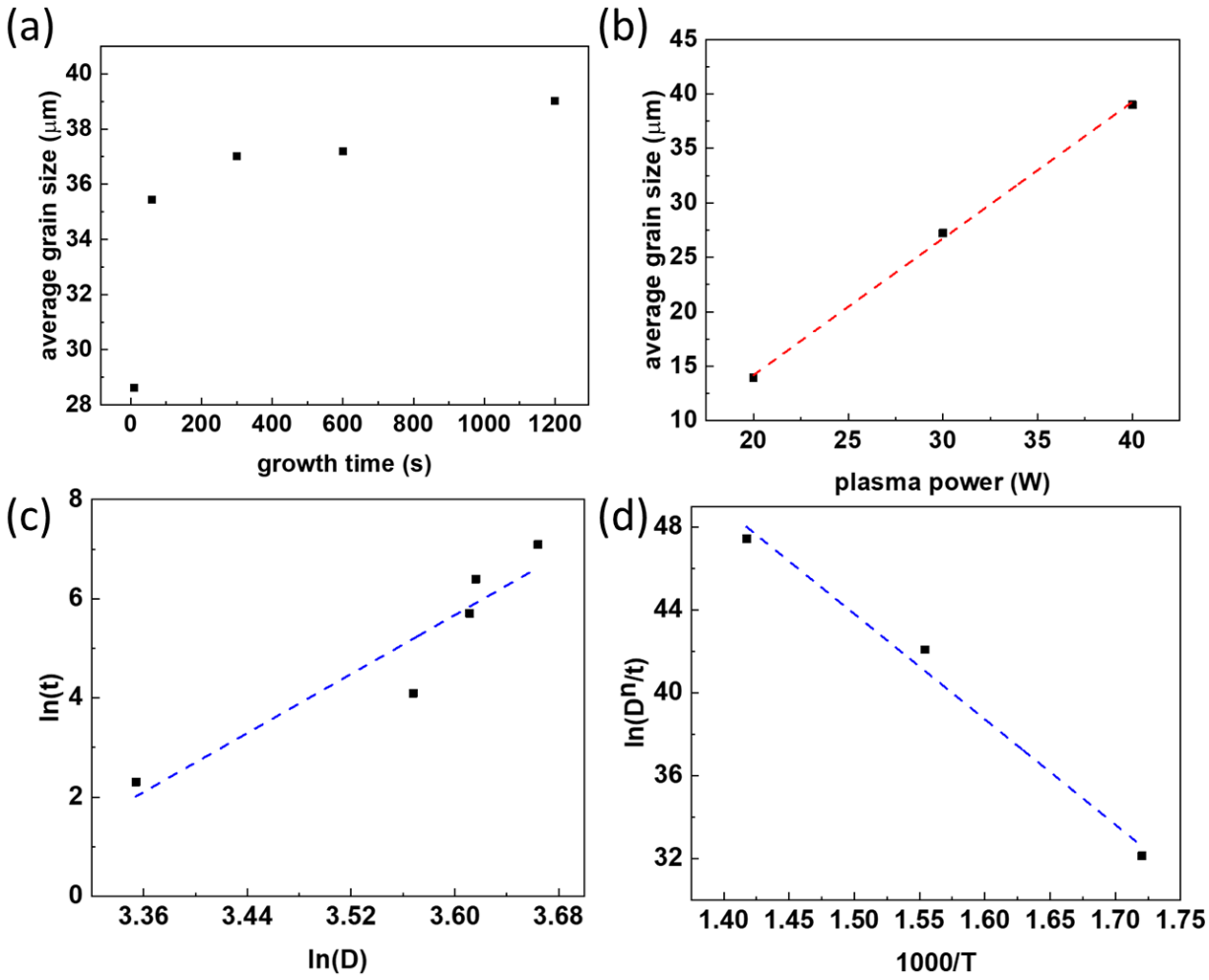

Figure 6.7. Grain size and activation energy analysis (a) Average grain size as a function of growth time at 40W (b) Cu grain size measured under different plasma power conditions.

Growth time is 20 min (c) Plot of ln (t) *vs.* ln (D), the fitted growth exponent n is 14.88. (d) $\ln(D^n/t)$ versus 1/T plot, with n=14.88.

Figure 6.8 displays the crystallographic orientation information obtained through EBSD analysis. The inverse pole figures reveal that the primary out-of-plane orientation of the ED copper is (001). Remarkably, within a brief duration of merely 10 seconds, a significant transformation in the crystallographic orientation occurs, even though the substrate temperature remains well below ~0.3 Tm (melting point) of Cu. This suggests an additional driving force, potentially chemical etching, facilitating the rapid evolution of crystal orientation at relatively low temperatures[160]. Following this initial shift, the dominant orientations observed are (001) and (111), with no significant variations for the growth time afterwards. Interestingly, even under lower plasma power conditions during PECVD graphene growth (Figure S10), the dominant orientations remain (001) and (111).

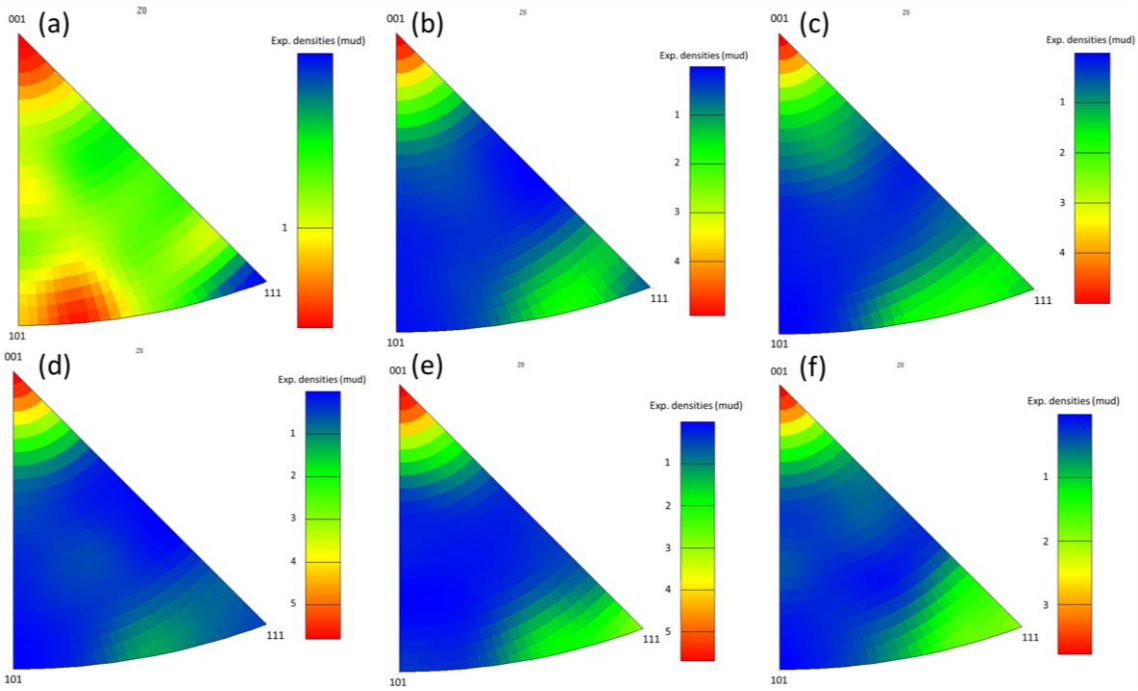

Figure 6.8. Inverse pole figures of the ED copper foil (a) before PECVD and after PECVD at 40W with growth times of (b)10sec (c) 1min (d)5min (e)10min and (f) 20min, respectively.

Turning to the chemical evolution of the ED copper foil during PECVD graphene growth, Figure 6.9 presents the XPS survey spectra of the ED copper foil before and after PECVD at 40W for varying growth durations. A mere 10 seconds into the process, the surface Zn layer is removed, exposing the underlying Cu surface. Figure S6.11 displays the XPS survey spectra for different plasma powers, demonstrating that the Zn layer is also removed at reduced plasma power.

As the growth continues, the increasing C1s signal suggests the onset of graphene growth on the surface. Figure 6.10 illustrates the C1s XPS spectra before graphene growth and after varying growth durations. The sp^2 carbon signal becomes visible after 5 minutes of growth, corroborating the Raman spectra in Figure 6.1(a), where graphene signature peaks emerged after 5 minutes of growth. However, the presence of functional groups (*i.e.,* O-C=O and C-O) in the 5-minute growth period also implies that the graphene growth was not complete within this time.

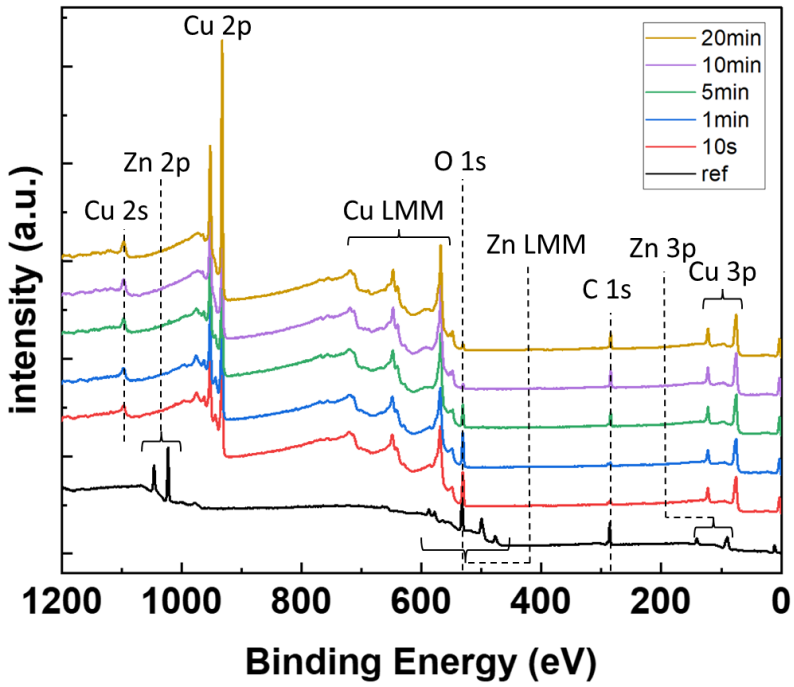

Figure 6.9. XPS survey scan of the ED copper foil before PECVD (labeled as ref) and after PECVD at 40W of different growth time.

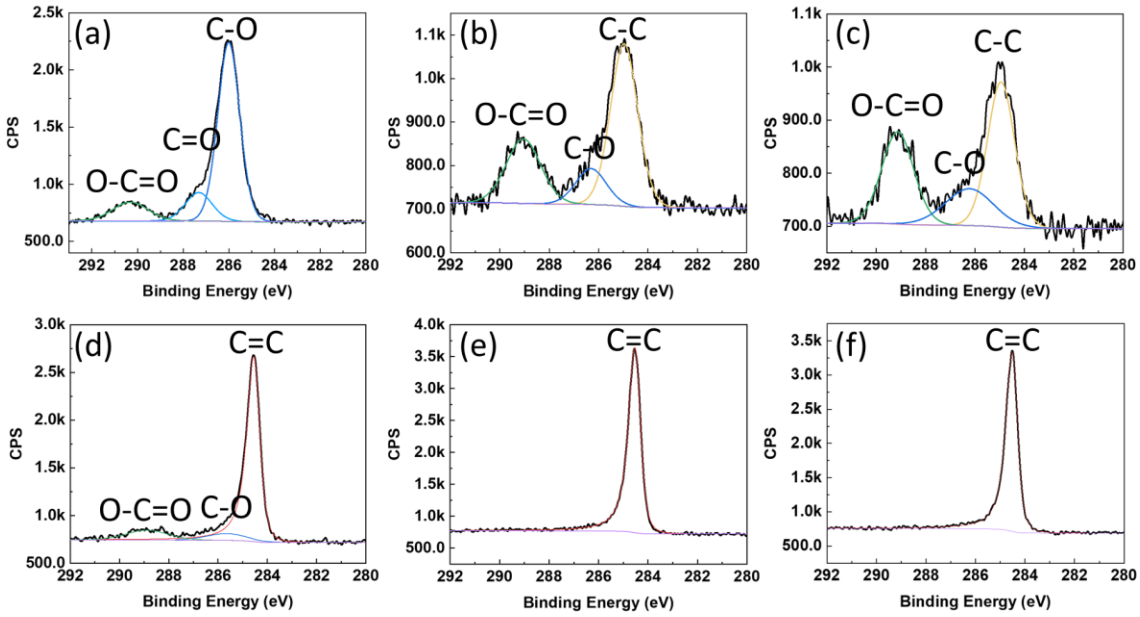

Figure 6.10. XPS C1s spectra of the ED copper foil (a) before PECVD and after PECVD at 40W with growth times of (b)10sec (c) 1min (d)5min (e)10min and (f) 20min, respectively.

Drawing on the SEM, EBSD, and XPS data, we can hypothesize the growth mechanism of PECVD graphene on ED copper foil as follows: Initially, the rough surface and Zn coating hinder graphene formation. The initial plasma phase removes the top Zn layer, exposing the Cu surface. As plasma heating continues, the microscopic roughness begins to smooth out, coinciding with the reorientation of out-of-plane Cu orientations, specifically (001) and (111), which are common for graphene growth[192-193]. When heated for an adequate duration (>5min), the substrate temperature becomes high enough to work in conjunction with the plasma activation of methane and hydrogen, thus inducing graphene growth. When the growth period extends (>10min), several multilayer domains begin to form on the existing graphene, as observed in Figure 6.2(d). Concurrently, during graphene growth, the copper grain size also gradually increases, further facilitating graphene growth.

4. Conclusion

In summarizing, this research provides an in-depth understanding of the mechanisms and conditions governing the growth of graphene through PECVD on ED copper foil. By utilizing Raman spectroscopy, SEM imaging, HRTEM, EBSD, and XPS, we unravel the detailed relationship between growth time, plasma power, and the resultant quality of graphene.

Our analyses indicate that a minimum of five minutes of growth time is necessary for complete graphene coverage on the ED copper substrate. More interestingly, at the 10-minute mark, HRTEM confirmed the presence of monolayer graphene. Furthermore, SEM images reveal the development of multilayer graphene for growth times exceeding 20 minutes, suggesting that PECVD graphene growth on ED copper is not inherently self-terminating.

A critical observation from our research is that decreasing plasma power directly adversely impacts the quality of the resultant graphene. This effect can be attributed to the strong correlation between plasma power and substrate temperature in our experimental setup, which provides less conducive conditions for graphene growth with decreasing plasma

power. Notably, the Cu crystal orientation rapidly transforms into predominantly (001) and (111) upon merely 10 sec of PECVD process, and then remains essentially the same with increasing growth time, as revealed through the EBSD studies.

Our research also highlights notable chemical and structural modifications to the ED copper substrate during the PECVD process. Within just a few seconds of commencing the process, the surface Zn layer is efficiently removed, exposing the underlying Cu surface. As the process progresses, we observe an increase in Cu grain size, a reduction in surface roughness, and a reorientation of out-of-plane Cu orientations – all these changes collectively create a more suitable environment for graphene growth.

The knowledge gained from this study significantly enhances our comprehension of the interplay between the process parameters, substrate preparation, and the quality of the resulting graphene growth on ED copper foils using PECVD. These insights are expected to contribute towards optimizing the direct graphene growth on these substrates that are widely used in industrial applications.

Supporting Information

S1. Substrate temperature estimation:

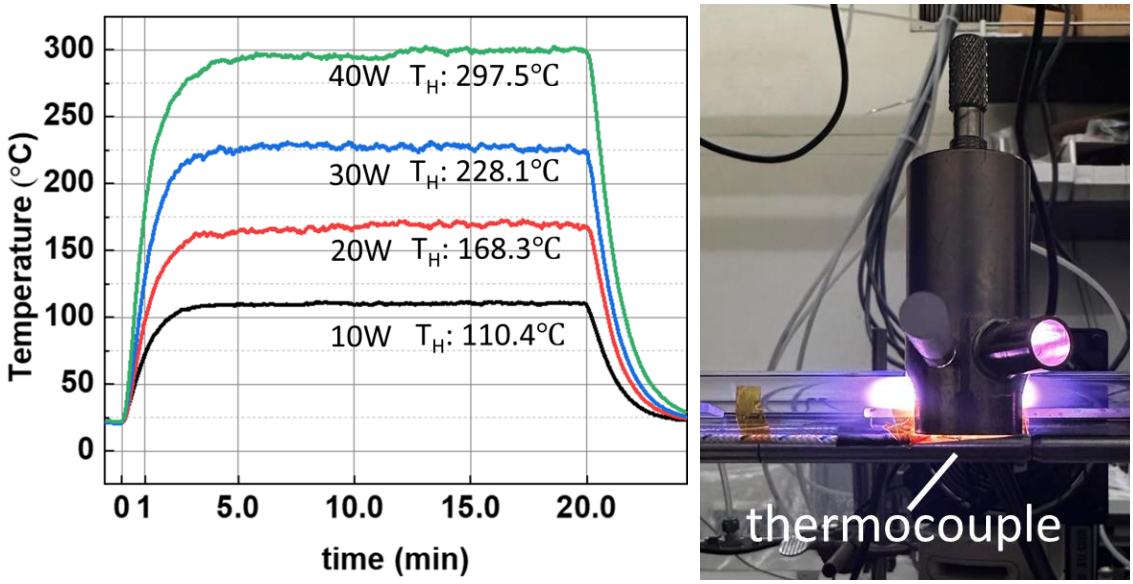

Figure S6.1. Temperature measurement of the PECVD system. The temperature on the tube wall recorded by thermocouple (Left). T_H indicates the fitted temperature plateau. Showing the attached thermocouple on the PECVD system. (Right)

The measured temperature at the tube wall at different time is summarized in Table S6.1.

Table S6.1. Measured temperature at the tube wall at different time with 40W.

Time (at 40W)	T (°C)
10s	33
1min	184
5min	293
10min	$=T_H$
20min	$=T_H$

With the temperature plateau under different plasma power, a linear correspondence of T_H versus plasma power is observed as shown in Figure S6.2.

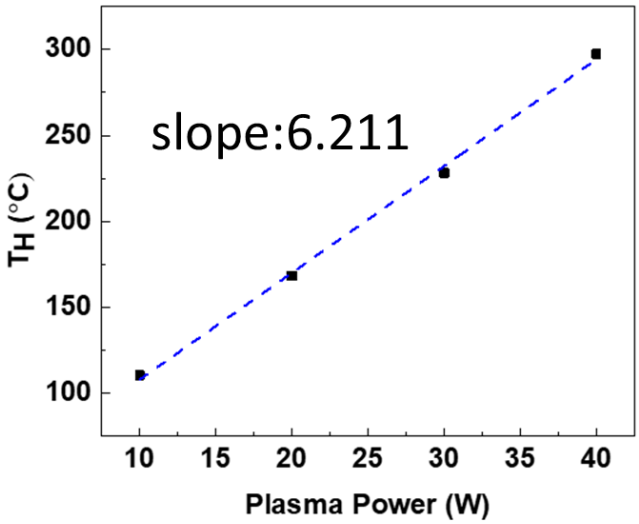

Figure S6.2. Plotting T_H versus the corresponding plasma power.

Next, assuming that the interior temperature also follows the same plasma power dependence ((*i.e.*, slope=6.211 (℃/W)) and using the substrate temperature measured through temperature label at 10W, which suggested the temperature range between 232 and 260℃. For estimation, we take the midpoint temperature (246℃) as the representative substrate temperature at 10W. With these, the substrate temperature at higher plasma power is extrapolated and plotted in Figure S6.3. The substrate temperature at different plasma power is summarized in Table S6.2.

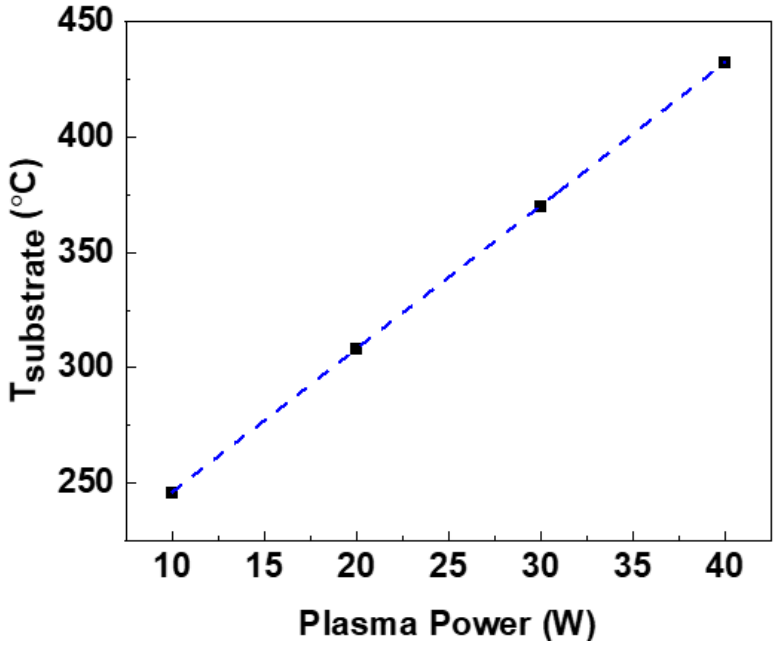

Figure S6.3. The extrapolated substrate temperature under different plasma power using the fitted slope in Figure S6.2. and the midpoint temperature measured using the temperature label at 10W (*i.e.*, the temperature is in the range of 232 ℃ - 260 ℃ at 10 W).

Table S6.2. Substrate temperature at different plasma power

Power (W)	Tsubstrate (℃)
40	432.2 (extrapolated)
30	370.2 (extrapolated)
20	308.1 (extrapolated)
10	246.0 (temperature label)

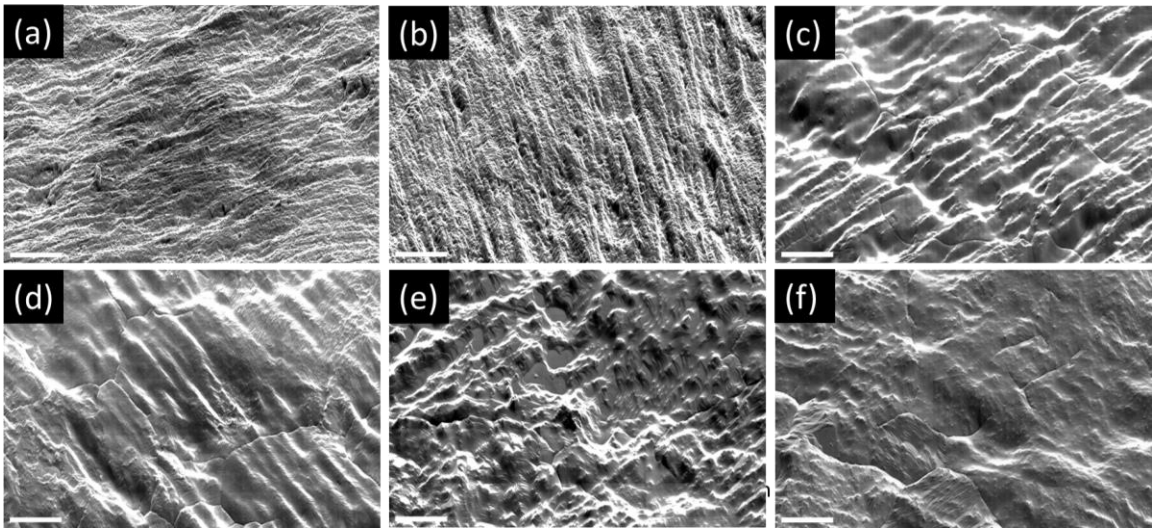

Figure S6.4. SEM images of the ED copper foil (a) before PECVD and after PECVD at 40W with growth times of (b)10sec (c) 1min (d)5min (e)10min and (f) 20min. The scale bar is 10μm.

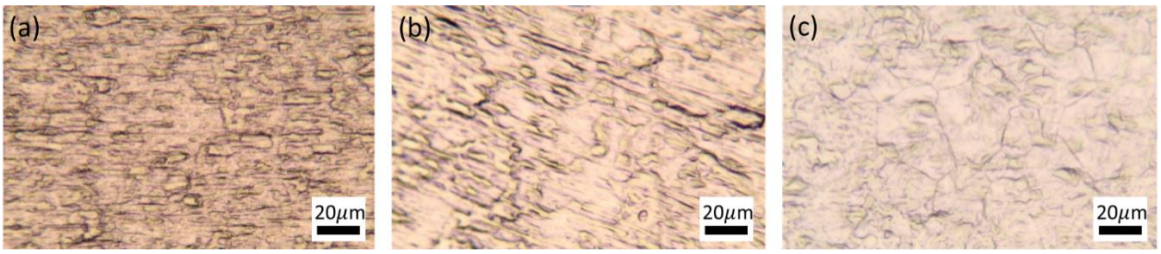

Figure S6.5. Optical micrographs of the ED copper foil after 20 minutes of PECVD graphene growth with plasma power sof (a) 20W (b) 30W (c) 40W, respectively.

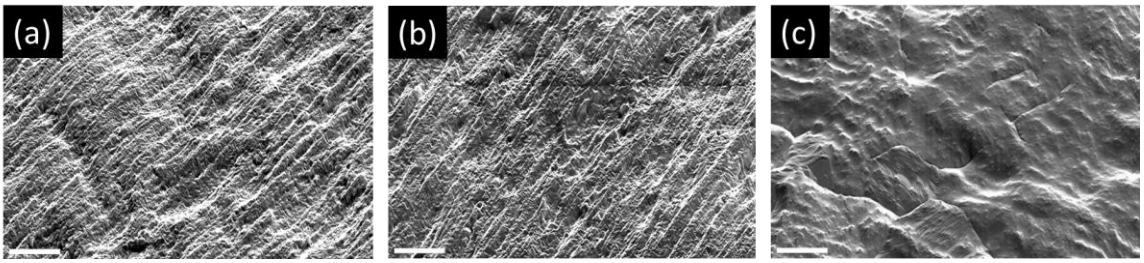

Figure S6.6. SEM images of the ED copper foil after 20 minutes of PECVD graphene growth with plasma powers of (a) 20W (b) 30W, and (c) 40W, respectively. The scale bar is 10μm.

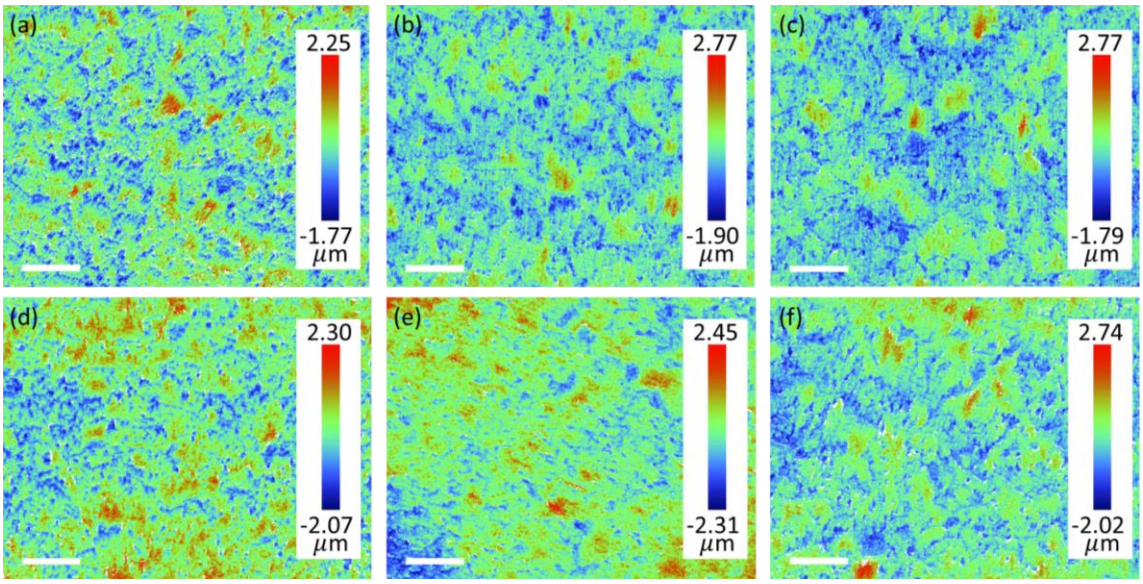

Figure S6.7. White light interferometry images of the ED copper foil (a) before PECVD and after PECVD at 40W with growth times of (b)10sec (c) 1min, (d)5min, (e)10min, and (f) 20min, respectively. The scale bar is 100 μm. The interferometry images were acquired by K. -M. Shang.

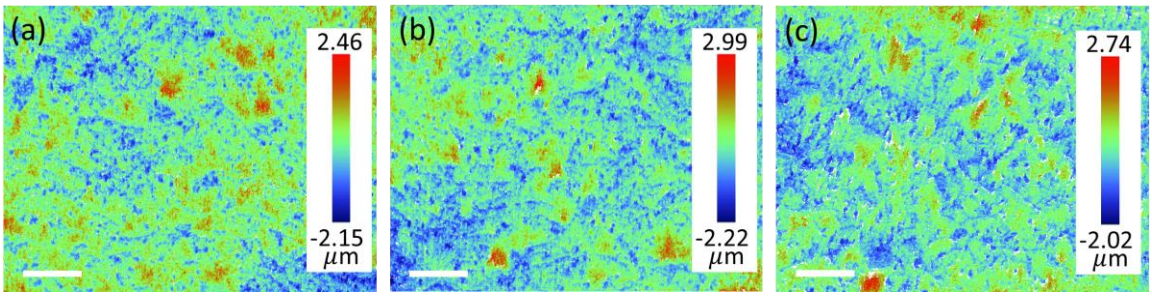

Figure S6.8. White light interferometry images of the ED copper foil after 20 minutes of PECVD graphene growth with plasma powers of (a) 20W, (b) 30W, and (c) 40W, respectively. The scale bar is 100 μm. The interferometry images were acquired by K. -M. Shang.

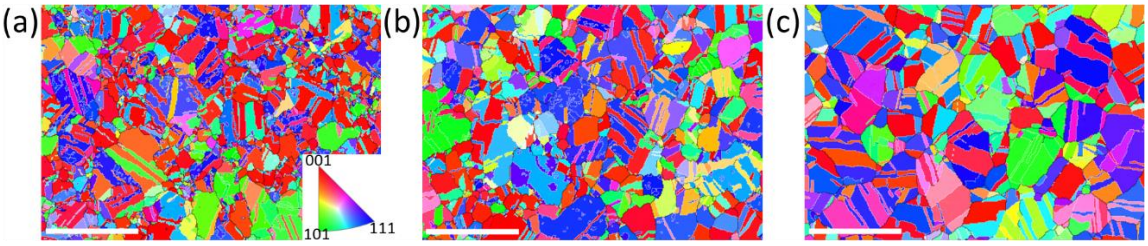

Figure S6.9. EBSD map of the ED copper foil after 20 minutes of PECVD graphene growth with different plasma power of (a) 20W, (b) 30W, and (c) 40W. The scale bar is 100μm.

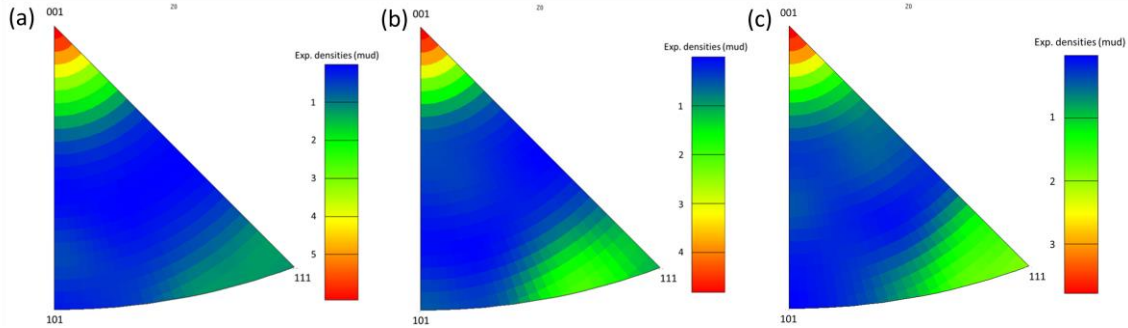

Figure S6.10. Inverse pole figures of the ED copper foil after 20 minutes of PECVD graphene growth with different plasma powers of (a) 20W, (b) 30W, and (c) 40W.

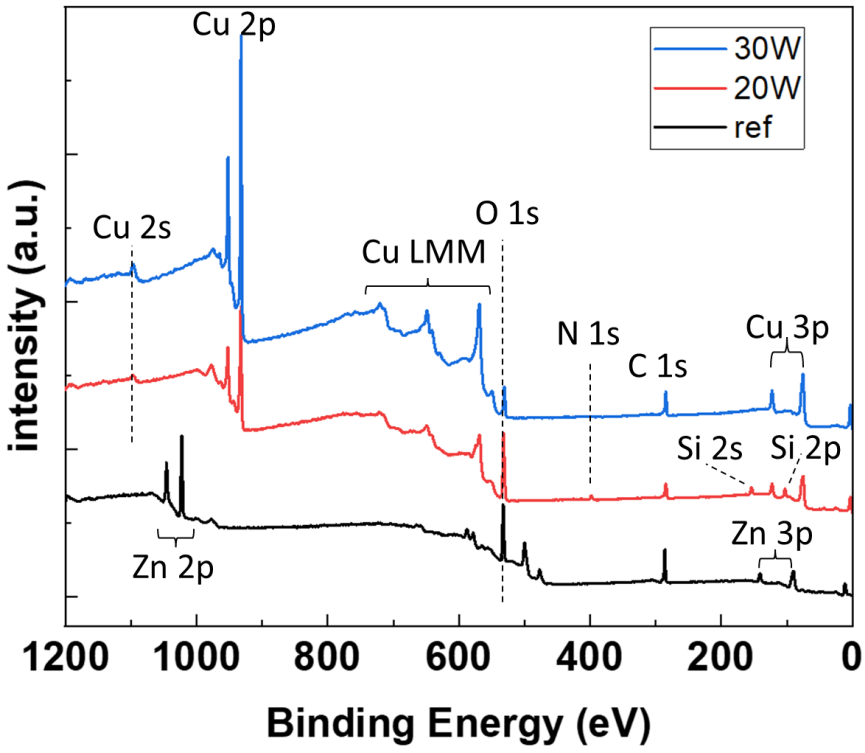

Figure S6.11. XPS survey scan of the ED copper foil after 20 minutes of PECVD graphene growth with different plasma power. Here we note that the detected N and Si elements at 20W originates from the silane derivative coating on the backside of the ED Cu foil.

Chapter VII

DIPOLE ORDERING IN MONOLAYER MoS_2

Partially adapted from:
Duxing Hao, Wen-Hao Chang, Yu-Chen Chang, Wei-Tung Liu, Chen-Hsuan Lu, Tilo H. Yang, Naoya Kawakami, Ming-Hao Liu, Chun-Liang Lin, Ting-Hua Lu, Yann-Wen Lan and Nai-Chang Yeh. Magnetic Field-Induced Ferroelectric Responses in Monolayer MoS_2 Transistors. In preparation

Personal contribution: C.-H.L. carried out the PF-KPFM measurements and estimated the carrier concentrations and sulfur vacancies.

Introduction

Ferroelectric materials are distinguished by their spontaneous electric polarization, a property that can be manipulated through an external electric field. This unique characteristic has led to significant technological advancements, finding applications in high-density data storage[194], non-volatile memories, ferroelectric random-access memory (FeRAM)[195], negative capacitance field-effect transistors (NCFETs)[196-198], and neuromorphic computing[199]. However, conventional ferroelectric materials, such as those with perovskite structures like lead zirconate titanate (PZT), face substantial challenges when miniaturized to nanoscale dimensions. These challenges mainly arise from the depolarization effect, which compromises their ferroelectric properties[200-201]. Moreover, the incompatibility of perovskites with CMOS processes further restricts their application.

A key criterion for ferroelectricity is the existence of a non-centrosymmetric space group in the material's structure[202]. Notably, progress in fluorite-structured oxide thin films—such as HfO_2[203] and ZrO_2[204]or their solid solutions[205]—has demonstrated the crucial role of stabilizing the high-pressure orthorhombic phase (o-phase) through confinement to achieve ferroelectricity. Impressively, the minimum thickness for ferroelectricity in $Hf_xZr_{1-x}O_2$ films has been reported to be as low as 1 nm[206], highlighting the necessity of further research to explore the lower thickness limit for ultrathin ferroelectric films[207].

On the other hand, the advent of 2D materials presents new opportunities for overcoming these challenges. Materials like monolayer molybdenum disulfide (MoS_2) have been shown to preserve their ferroelectric properties even when reduced to atomic scales[208-209]. A distorted-1T structure in monolayer MoS_2 disrupts centrosymmetry, thereby enabling a net electric polarization and the onset of ferroelectricity[208-209]. However, the practical application of ferroelectric MoS_2 in field effect transistor (FET) devices is still an open area of research, necessitating further investigation. Our latest findings delve deeper into this area, showing a compelling differentiation between heavily doped and regular MoS_2 in terms of their ferroelectric or dipole ordering responses.

Growth methods of MoS_2

Before diving into our results, it is essential to compare the prevailing growth methods for MoS_2 and graphene. The four predominant techniques—CVD, metal-organic chemical vapor deposition (MOCVD), PECVD, and plasma-enhanced atomic layer deposition (PEALD)—each have their merits and limitations, especially concerning operational temperatures and film quality.

CVD is celebrated for its ability to produce MoS_2 flakes but operates at elevated temperatures ranging from 600°C to 800°C[210] . Such high thermal requirements often exclude its use in temperature-sensitive applications[211-212]. Additionally, the scalability of CVD is hampered by its sensitivity to various parameters, including partial pressure[213], temperature[214], and substrate orientation[215] .

Metal-organic chemical vapor deposition (MOCVD), a variant of CVD, uses organic metal precursors and offers scalability with excellent film coverage[216]. It operates at more moderate temperatures between 320°C and 550°C[214]. However, the reliance of MOCVD on toxic precursors and hazardous byproducts poses environmental and safety risks[216].

As a more versatile alternative, PECVD allows for quicker film deposition at significantly lower temperatures of 150°C to 300°C[217]. It also utilizes safer precursors like molybdenum

pentachloride ($MoCl_5$) and elemental sulfur (S_8), reducing the need for hazardous chemicals such as H_2S[211]. Despite these advantages, PECVD generally results in MoS_2 films with multiple layers[218].

For precise control over film thickness, ALD is the method of choice. Its self-limiting nature ensures accurate control at an Ångström scale while maintaining uniformity and conformality[219]. While thermal ALD allows MoS_2 growth at temperatures as low as 60°C, it necessitates post-annealing for crystallization[220]. PEALD, in contrast, operates between 300°C and 450°C and also shows self-limiting behavior[221]. However, it often yields films that are either amorphous or polycrystalline, which are not ideal for electronic applications[211].

In summary, CVD stands out for flake production, but its elevated operating temperatures are limiting. PECVD and MOCVD present more thermally lenient options, each with its own trade-offs. PEALD provides the most temperature flexibility but compromises film quality.

Dipole ordering responses in monolayer MoS_2

Our experiments indicate contrasting behavior between heavily n-doped MoS_2 and regular MoS_2 back-gate field-effect transistor (FET) devices. As shown in Figure 7.1(a)-(b), while the former exhibits a ferroelectric response without the need for an external magnetic field, the latter requires one to manifest similar hysteresis curve. The inset in Figure 7.1(b) shows the absence of hysteresis response for the regular MoS_2 device at zero magnetic field. This difference is central to understanding the underlying mechanisms that facilitate dipole ordering in MoS_2 devices.

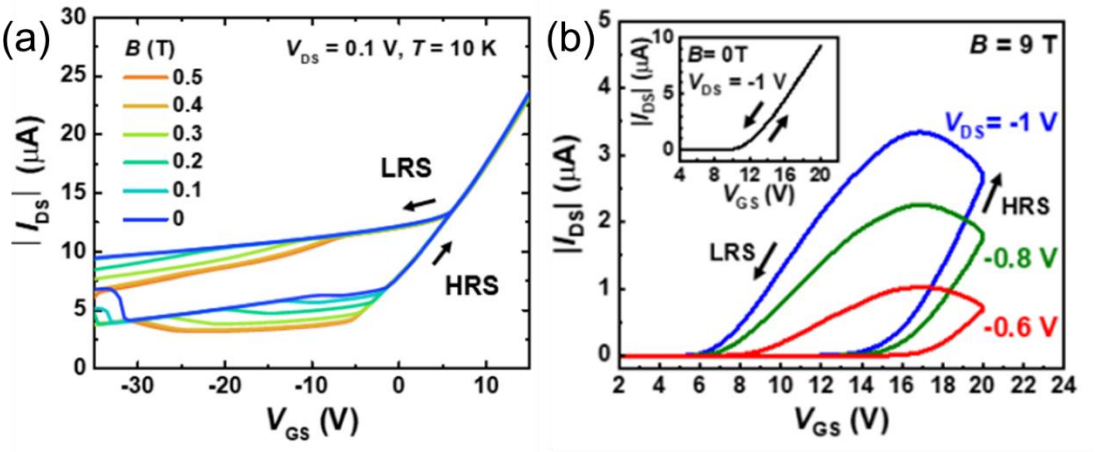

Figure 7.1. The magnitude of source-drain current ($|I_{DS}|$) *vs.* source-gate voltage (V_{GS}), $|I_{DS}|$-*vs.*-V_{GS}, hysteresis curves for (a) heavily n-doped monolayer MoS_2 with a constant source-drain voltage V_{DS} = 0.1 V and (b) regular monolayer MoS_2 with V_{DS} = –1.0 V under different applied magnetic fields (*B*) perpendicular to the MoS_2 layer. Here LRS (HRS) denotes the low (high) resistance states, respectively. The source-drain voltage V_{DS} is applied parallel to the MoS_2 layer whereas the source-gate voltage V_{GS} is applied perpendicular to the MoS_2 layer. These measurements were on MoS_2 FET devices carried out by Duxing Hao.

Work function measurements and estimating the sulfur vacancies

The work function of the monolayer MoS_2 was measured by Peak Force Kelvin Probe Force Microscopy (PF-KPFM) calibrated with respect to the work function of gold at 4.82 eV[222]. The contact potential difference (CPD) between the tip and the sample is given by $\Delta V_{CPD} = \phi_{sample} - \phi_{tip}$, where ϕ represents work function. Therefore, the work function of the MoS_2 sample is given by $\phi_{MoS_2} = \phi_{tip} + \Delta V_{CPD}^{MoS_2} = \phi_{Au} + \Delta V_{CPD}^{MoS_2} - \Delta V_{CPD}^{Au}$.

For the heavily doped MoS_2, $\Delta V_{CPD}^{MoS_2}$ was measured to be (1.89 ± 0.21) V, while ΔV_{CPD}^{Au} was measured to be (2.43 ± 0.23) V. The Fermi level E_F was then determined from ϕ_{MoS_2} ~ 4.3 eV, which was 0.1 eV above the conduction band minimum.

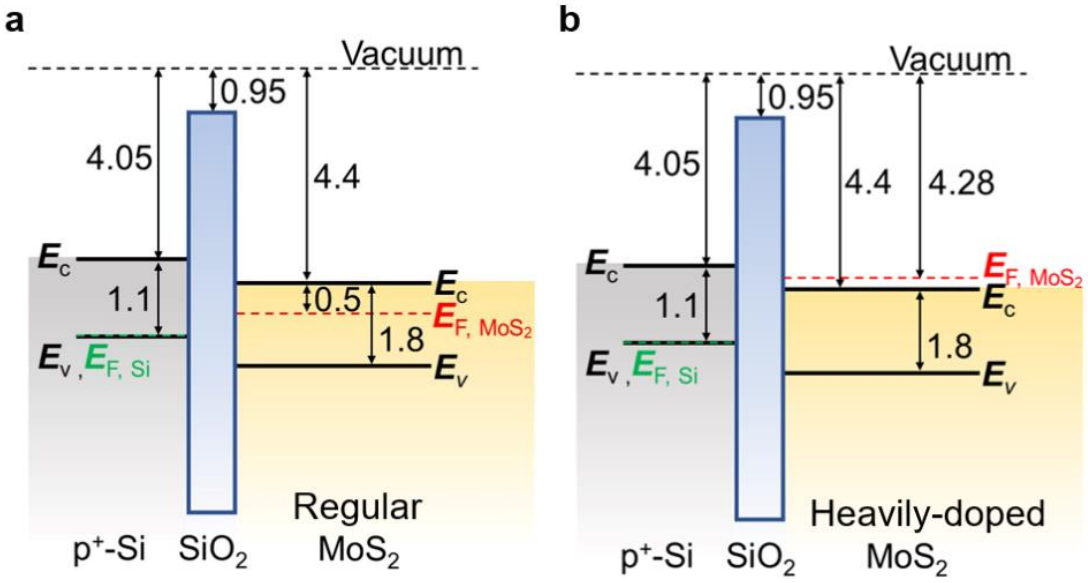

Figure 7.2. Schematic of the band alignment of $Si/SiO_2/MoS_2$ based on the KPFM measurements for (a) regular and (b) heavily doped monolayer MoS_2 FET devices. The units for the numbers indicated in the figure are in eV.

On the other hand, for the regular MoS_2, $\Delta V_{CPD}^{MoS_2}$ was measured to be (0.52 ± 0.23) V, while ΔV_{CPD}^{Au} was measured to be (0.39 ± 0.22) V. The Fermi level E_F was therefore determined to be ϕ_{MoS_2}~4.9eV, which was located at ~ 0.5 eV below the conduction band minimum. The schematics of band alignments for both cases were shown in Figure 7.2.

Assuming sulfur vacancies contribute to the doping of MoS_2, the sulfur vacancy concentration for both cases could be estimated. The majority carrier concentration of MoS_2 could be calculated with the following approximating formula $n = n_i e^{\frac{E_F - E_i}{k_b T}}$,where k_b is Boltmann constant, T is the temperature, n_i, E_F, E_i are the intrinsic electron concentration, Fermi level, and the intrinsic Fermi level of MoS_2, respectively. Here we note that we approximated E_i as the mid gap since $E_i = \frac{E_c + E_v}{2} + \frac{k_b T}{2} \ln\left(\frac{m_p^*}{m_n^*}\right) \sim \frac{E_c + E_v}{2}$, where m_p^* and m_n^* are the effective mass of holes and electrons of MoS_2, respectively. With n_i ~ 10^6 cm^{-2} at room temperature[223] and measured E_F - E_i = 0.4 eV, the corresponding electron concentration

of the regular MoS_2 sample was estimated as $n \approx 4.8\times10^{12}$ cm^{-2} . Assuming those electrons were induced by sulfur vacancies, the order of magnitude of sulfur vacancy population density can be estimated as $na^2\sqrt{3}/4 \sim 0.2\%$, where a = 0.318 nm is the lattice constant of MoS_2.

On the other hand, for heavily doped MoS_2, the above approximation no longer holds when the Fermi level is above the conduction band minimum. In this case we have to use the Fermi-Dirac distribution of electrons to calculate the carrier concentration:

$n = \int_{E_c}^{\infty} \frac{g_s g_v m_n^*}{2\pi\hbar^2} \frac{1}{1+e^{\frac{E-E_F}{kT}}} dE = \frac{g_s g_v m_n^* k_B T}{2\pi\hbar^2} \ln\left(e^{\frac{E_F-E_c}{k_B T}} + 1\right)$,where, $g_s = g_v = 2$ are spin and valley degeneracy, respectively, $m_n^* = 0.5\ m_0$ is the effective mass averaged over DFT calculations[224-226]. Therefore, the carrier density was estimated to be 5.1×10^{13} cm^2 and the sulfur vacancy density was about 2.2%. The estimation of sulfur vacancy for heavily doped MoS_2 is in agreement with the XPS measurements, where an average of (5.0% ± 3.7%) sulfur vacancy density was obtained. These vacancies are instrumental in inducing the structural distortions that result in a non-centrosymmetric lattice arrangement, thereby facilitating the observed ferroelectricity.

Mechanisms underlying dipole ordering response

For both types of MoS_2, our data indicate that a non-centrosymmetric structure is essential for ferroelectric/dipole ordering behavior. In the case of heavily doped MoS_2, it appears that an excess of sulfur vacancies triggers dipole ordering response through lattice symmetry breaking.

However, for regular MoS_2, the situation is more complex. While it initially exhibits no ferroelectric response at zero magnetic field, we observed a change in hysteresis behavior under the influence of an external magnetic field. In addition, lattice expansion was detected in regular MoS_2 when subjected to a magnetic field (Figure 7.3), implying a structural modification that enables its dipole ordering properties, although the microscopic mechanism for this magnetic field-induced effect is still unknown.

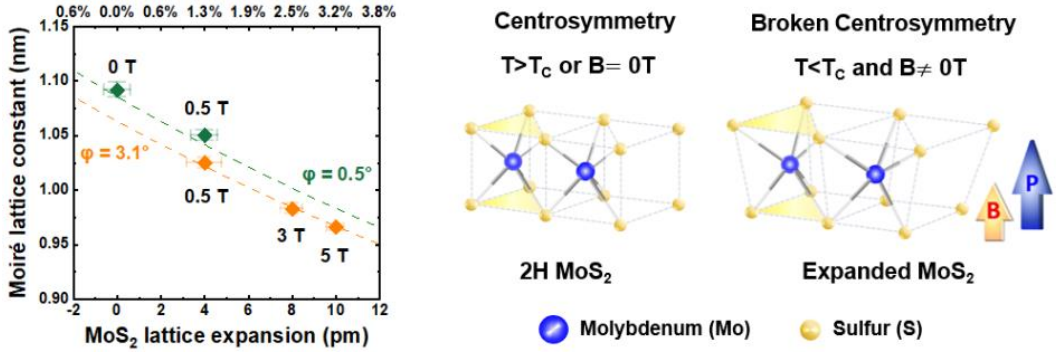

Figure 7.3. Magnetic field induced lattice expansion of regular MoS_2. The measurement of Moiré lattice constants using STM were carried out by the research group of Professor Chun-Liang Lin at NYJU in Taiwan.

Conclusion

Our findings reveal the appearance of dipole ordering properties in monolayer MoS_2, underlining the critical role of doping levels and sulfur vacancies. While the heavily doped MoS_2 can display these properties without an external magnetic field, regular MoS_2 remains dependent on external magnetic fields. These observations emphasize the need for further investigation into the underlying physics.

Chapter VIII

FUTURE WORK AND SUMMARY

Future Work

1. Large-area PECVD graphene growth

The sample dimensions in our PECVD system have been limited by the size of the Evenson cavity, leading to a maximum sample size of approximately (1×2) cm^2. The results presented in this thesis would be more impactful if the PECVD graphene synthesis could be scaled up. In collaboration with the Industrial Technology Research Institute (ITRI) and Mastek in Taiwan, we have demonstrated the feasibility of scaling up the direct-plasma PECVD graphene growth to a sample dimension larger than (3×3) cm^2 in size.

The initial trial of the scaled up PECVD system consists of a cylindrical chamber with the substrate holder inserted within, as depicted in Figure 8.1.1. By adjusting the growth condition to the following parameters: H_2 = 250 sccm, CH_4 = 125 sccm, P = 2.3torr, plasma power = 200 W, and growth time = 30 min, we were able to detect the characteristic Raman modes of 2D, G and D peaks in the graphene synthesized in this scaled-up PECVD system, as shown in Figure 8.1.2.

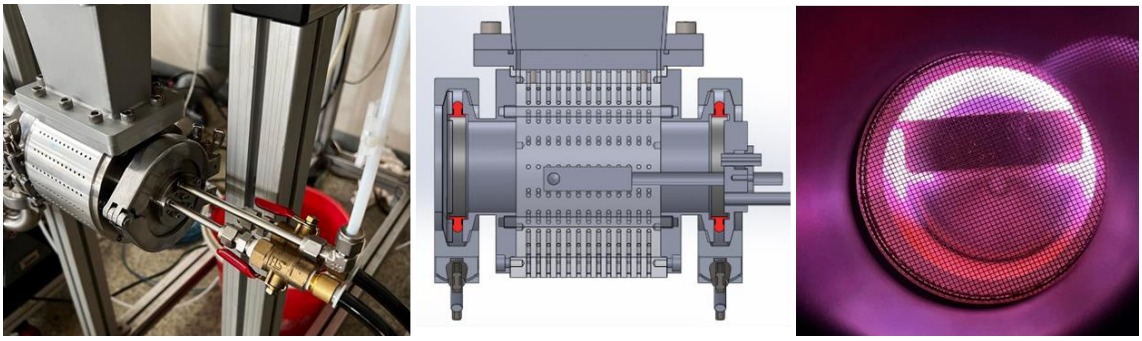

Figure 8.1.1. The initial trial of scaled-up MW-PECVD chamber at Mastek.

Our criterion for successful graphene growth is the formation of the 2D peak. This peak originates from scattering off the well-defined in-plane transverse optical (iTO) phonon mode around the K-point of the graphene Brillouin zone (Figure 8.1.3). Specifically, the emergence of the 2D peak (also known as G′ in some publications) involves the double or triple resonances of iTO phonon scattering between two valleys, which is a feature unique to the graphitic in-plane honeycomb crystalline structures.

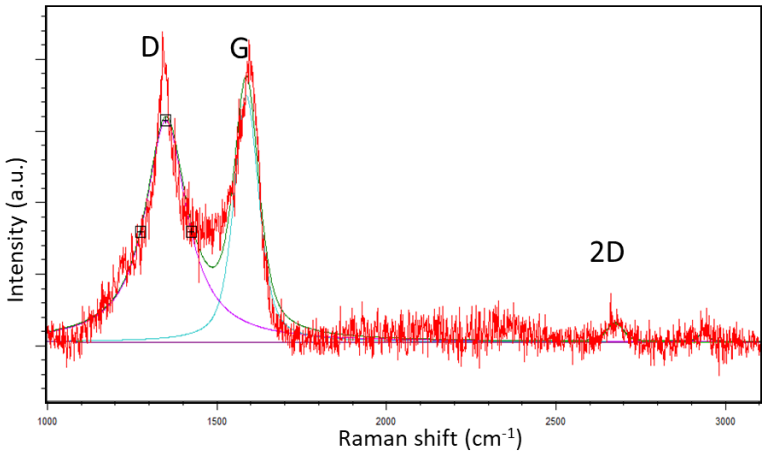

Figure 8.1.2. Raman spectrum of graphene after the PECVD process using the scaled-up chamber.

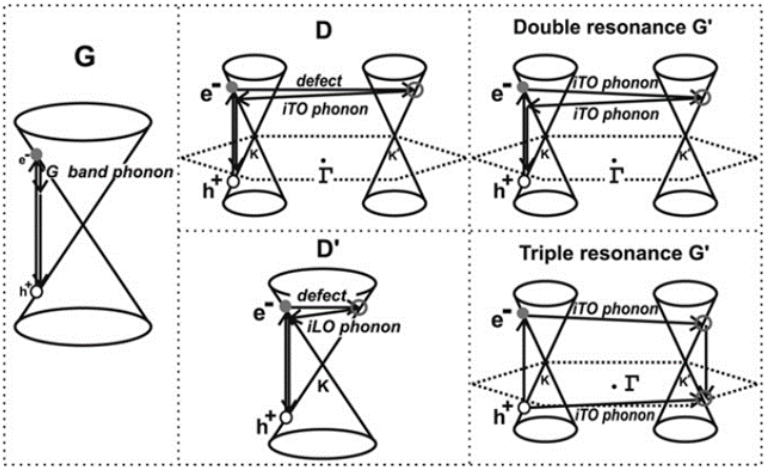

Figure 8.1.3. Raman modes in graphene. Here the iTO (iLO) phonon refers to in-plane (longitudinal) transverse optical phonon. Adapted from Ref[169].

Despite these promising results, the chamber conditions proved unstable. Therefore, we opted to use the existing PECVD system at Mastek, which was previously used for diamond growth (Figure 8.1.4). As depicted in Figure 8.1.5, the plasma is much closer to the sample than in Figure 8.1.1. Additionally, we observed a substantial variation in plasma position relative to total pressure. Thus, we adjusted the growth pressure accordingly to ensure that the plasma was as close to the sample as possible, mimicking the direct plasma condition in the lab.

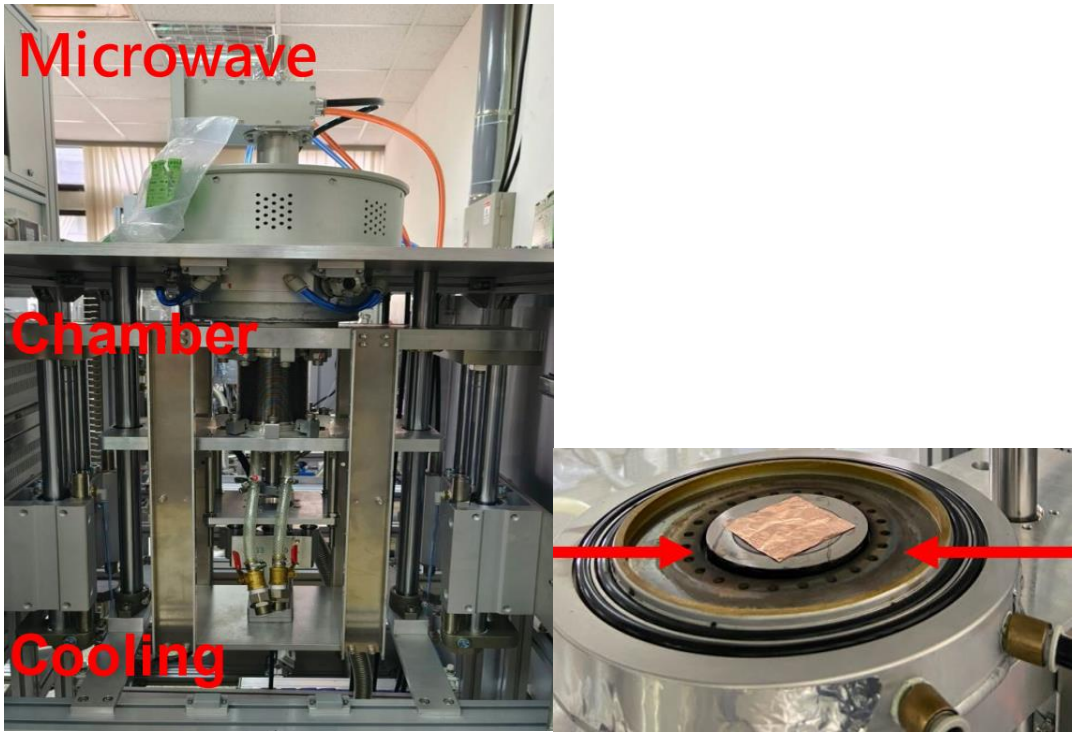

Figure 8.1.4. The PECVD system previously used for diamond growth at Mastek.

Figure 8.1.5. Side views through the chamber viewing port, showing the change of plasma position with respect to the sample (Cu foil) under different power and pressure.

By implementing the following parameters for the growth: H_2 = 120 sccm, CH_4 = 5sccm, P =12 torr, plasma power = 1200 W, and growth time = 10 min, a clear 2D peak could be observed, as demonstrated in Figure 8.6. The relatively high D/G ratio (D/G = 5.97) suggests that growth conditions could be further improved. When we extend the growth time to 20 min, the D/G ratio is lowered to 3.99 as shown in Figure 8.1.7.

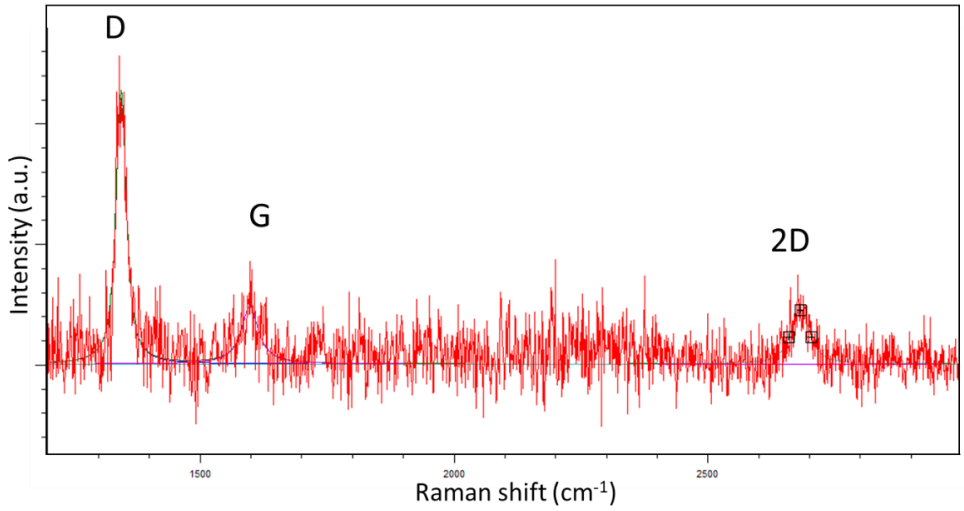

Figure 8.1.6. Raman spectrum of graphene after the PECVD process using the diamond PECVD chamber. Growth time = 10 min.

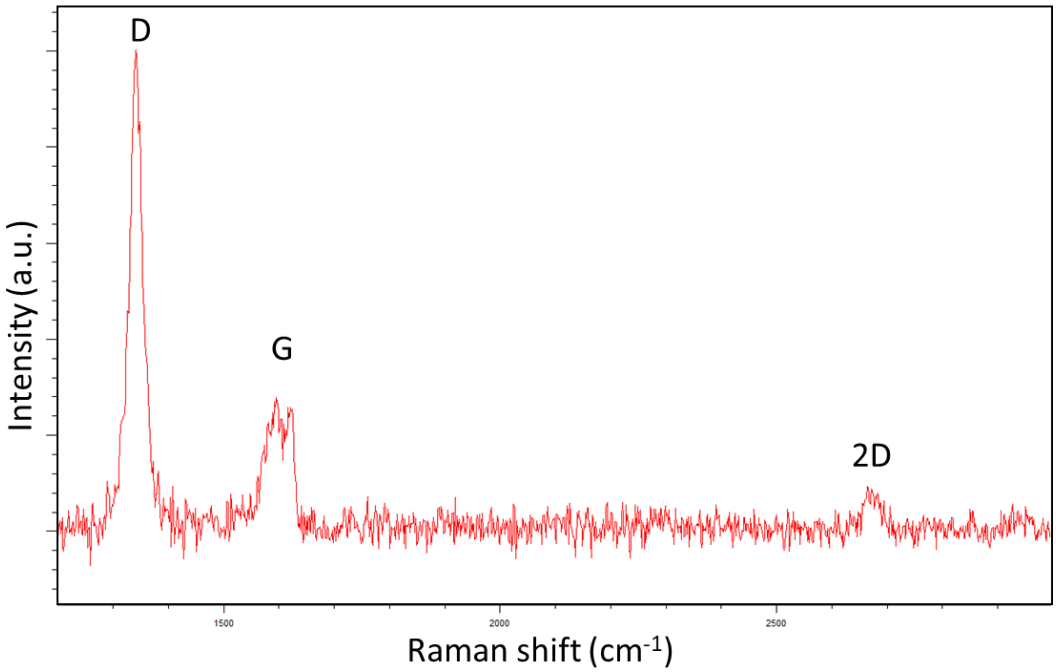

Figure 8.1.7. Raman spectrum after the PECVD process using the diamond PECVD chamber. Growth time = 20 min.

In addition to the growth time, our prior research indicates that a higher H_2/CH_4 ratio can also enhance the graphene quality. Increasing the H_2 gas flow to 240 sccm while keeping CH_4 at 5 sccm and a growth time of 10 min, the D/G ratio dramatically decreased to 1.85, as shown in Figure 8.1.8.

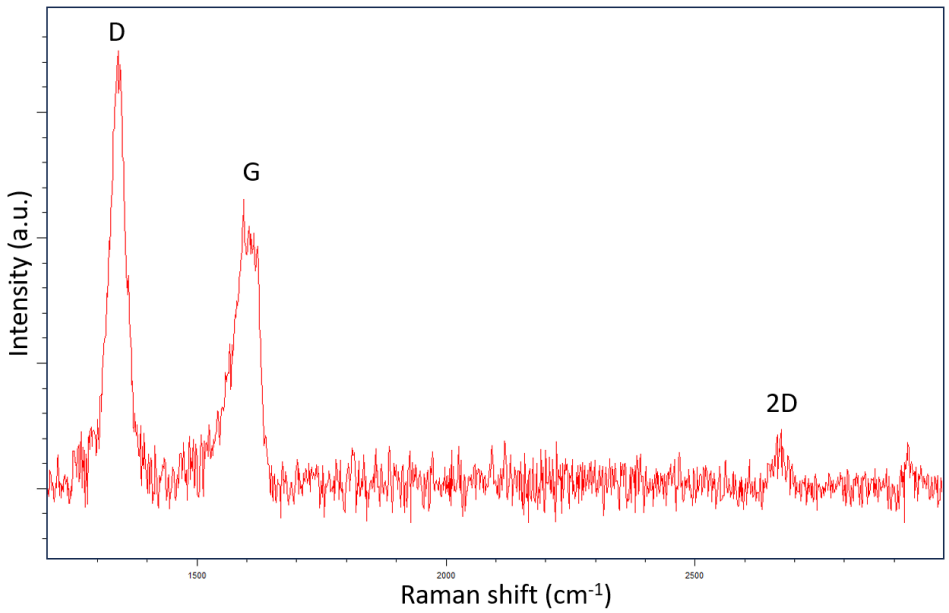

Figure 8.1.8. Raman spectrum after PECVD using the diamond PECVD chamber. Growth time = 10 min, H2 flow = 240 sccm, power = 1200 W.

Conversely, given our direct plasma configuration, the plasma power directly influences the sample temperature. As demonstrated in Figure 8.1.9, when the plasma power was reduced to 700 W and the gas flow was fixed at H_2 = 120 sccm and CH_4 = 5 sccm for a growth time of 10 min, the D/G ratio became 2.71, higher than that grown at 1200 W.

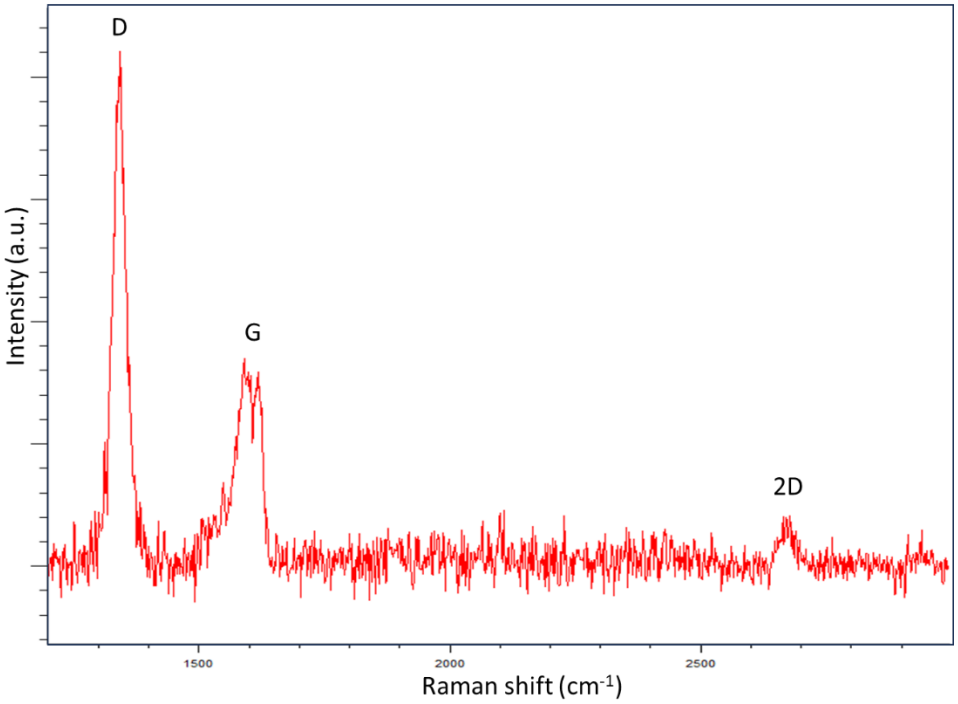

Figure 8.1.9. Raman spectrum of graphene after the PECVD process using the diamond PECVD chamber. Growth time = 10 min, power = 700 W.

Next, we tried PECVD graphene growth on sputtered Cu on Si as the substrate. Implementing the following growth parameters: H_2 = 120 sccm, CH_4 = 5 sccm, P = 20 torr, plasma power = 700 W, and growth time = 20 min, we obtained a much more distinct 2D peak in the Raman spectrum of the resulting graphene, as shown in Figure 8.1.10. The D/G ratio dramatically decreased to 0.79 compared to that for graphene growth on Cu foils.

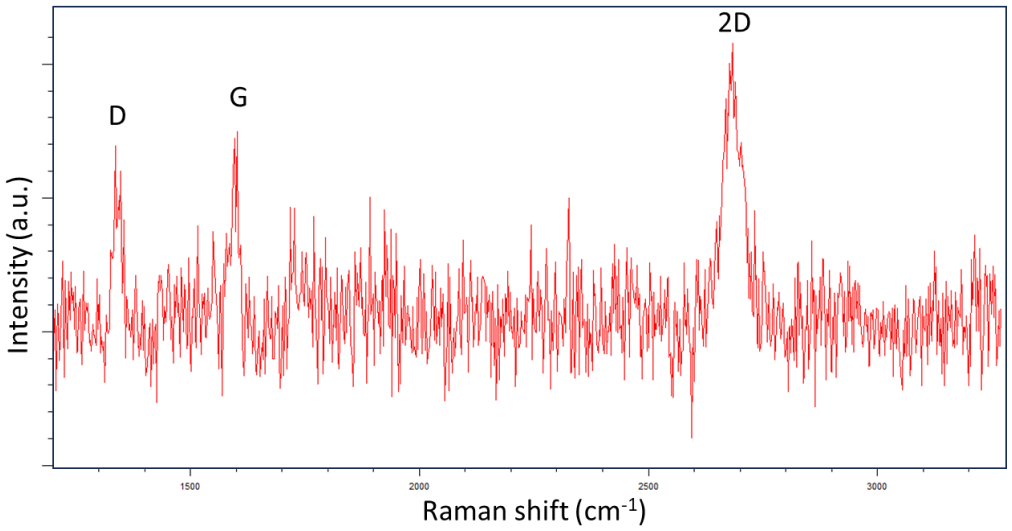

Figure 8.1.10. Raman spectrum after PECVD using the diamond PECVD chamber. The substrate is sputtered Cu on Si.

When the hydrogen gas flow is further increased to 240sccm while keeping other parameters fixed, the D/G ratio decreased to 0.76 as shown in Figure 8.1.11.

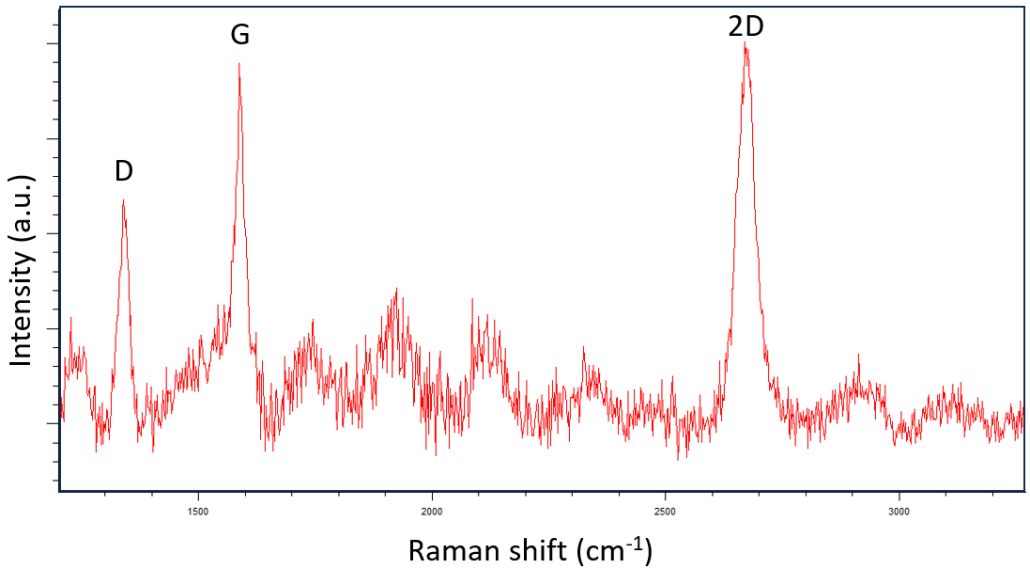

Figure 8.1.11. Raman spectrum of graphene after the PECVD process using the diamond PECVD chamber with higher H_2 flow. The substrate is sputtered Cu on Si.

When we increase the plasma power, that is, implementing the following parameters: H_2 = 240 sccm; CH_4 = 5 sccm; P = 20 torr; plasma power = 1200 W; growth time = 20 min, not only a clear 2D peak could be observed, the D/G ratio dramatically decreased to 0.34 as shown in Figure 8.1.12. It is also worth noting that during the growth, the water cooling of the sample stage is enabled.

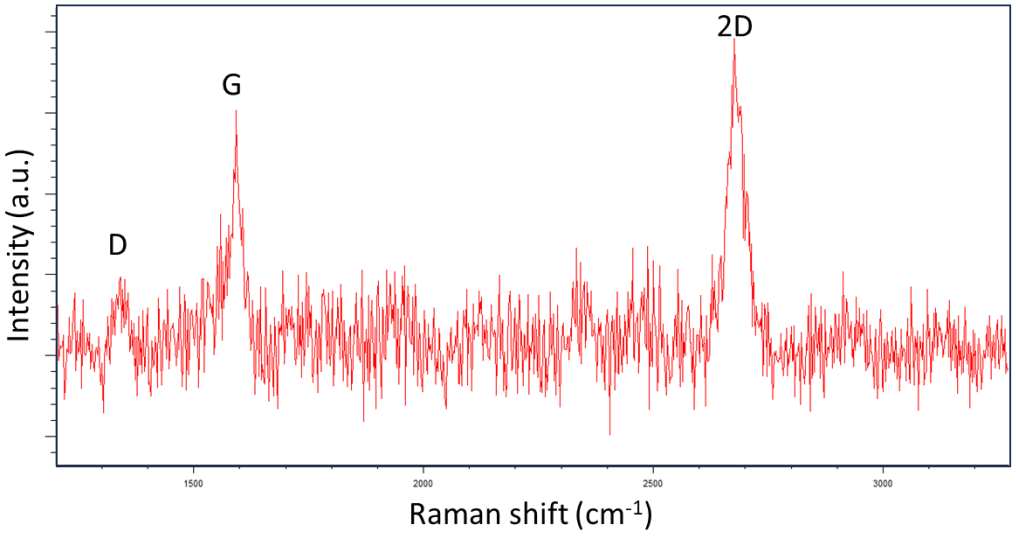

Figure 8.1.12. Raman spectrum after PECVD using the diamond PECVD chamber. Growth time 20min, 1200W.

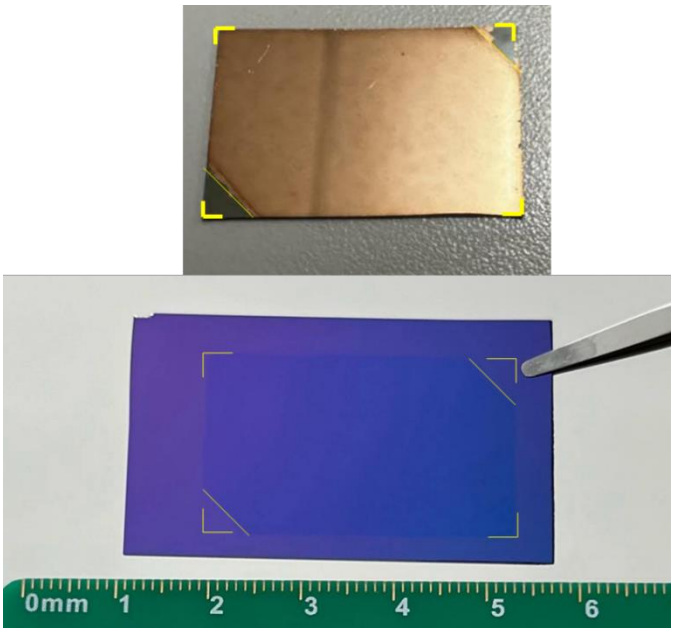

Figure 8.1.13 Optical micrograph showing the sputter Cu sample with PECVD graphene before transfer (top) and after transferring onto a SiO_2 substrate (down).

In order to assess the completeness of the graphene coverage achieved via the diamond PECVD system, the synthesized graphene was transferred onto a SiO_2 substrate for visual analysis. As depicted in Figure 8.1.13, the area covered by graphene precisely coincides with the dimensions of the sputtered Cu substrate, thereby confirming the successful attainment of full graphene coverage.

In summary, we have showcased the potential of scaling up direct-plasma PECVD graphene growth without active heating, achieving a sample size exceeding (3×3) cm^2. The presence of the 2D peak attests to the successful graphene growth. While the graphene produced on Cu foil exhibited a high D/G ratio, indicating either a notable defect concentration or small grain sizes, a shift to sputtered Cu on Si substrates remarkably reduced this ratio. Crucially, the complete coverage of the substrate by graphene has been verified through transfer to a SiO_2 substrate. Overall, with further refinement of the growth process, we believe the quality of graphene synthesized via the scaled-up PECVD system can be further optimized so that large-area PECVD graphene growth for practical applications becomes feasible.

2. Interfacial graphene growth

Introduction

Here we aim to address the issue of signal losses in high-frequency applications, often originating from the interface between the metal and the dielectric. We hypothesize that introducing graphene at this interface could mitigate such losses. However, conventional graphene transfer processes may introduce impurities and excess deformation/strain. Therefore, this section presents our methodology and findings for interfacial graphene growth on different metal thin films deposited on sapphire substrates.

Methodology

We employed PECVD for graphene growth under the following conditions: H_2 at 3 sccm, CH_4 at 1 sccm, a pressure of 500 mtorr, plasma power set at 50W, and a growth time of 3 minutes.

Experiment with Ag

We initiated our experiment by sputtering a 10nm Ag film onto a sapphire substrate. Following the PECVD process, the top surface was covered with black graphene stripes, as shown in Figure 8.2.1. To investigate the existence of interfacial graphene, we applied O_2 plasma to remove the top graphene stripes. However, as illustrated in Figure 8.2.2, no interfacial graphene was observed in this case.

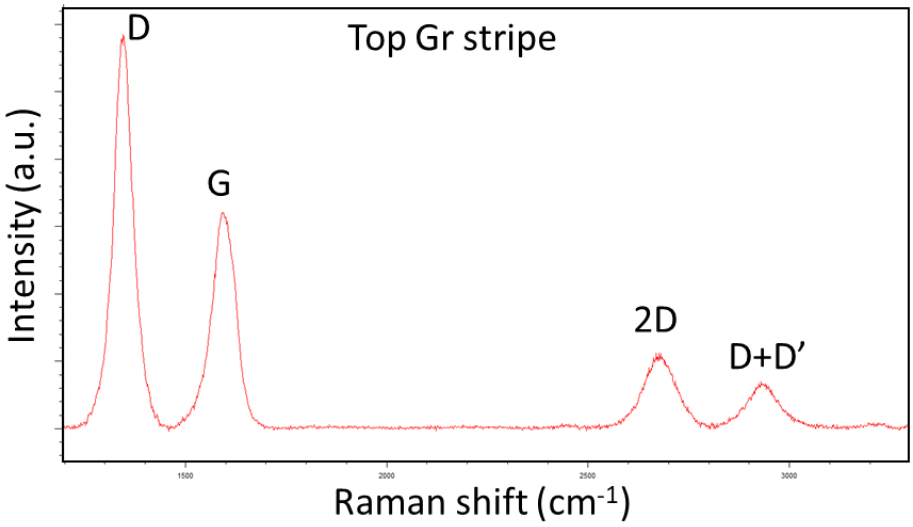

Figure 8.2.1. The Raman spectrum of the graphene stripes on the top surface of Ag on sapphire substrate.

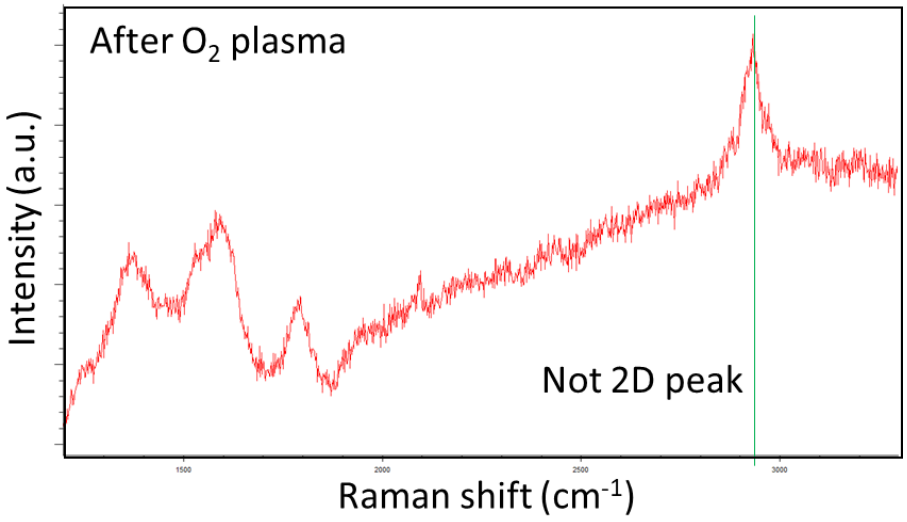

Figure 8.2.2. The Raman spectrum taken on the top surface of Ag deposited on sapphire substrate after O_2 plasma cleaning of the graphene stripes.

Experiment with TiW

Next, we explore TiW (10nm thickness) as the metal layer sputtered on the sapphire substrate. Similar to the Ag experiment, the results after PECVD and after O_2 plasma treatment are shown in Figures 8.2.3 and 8.2.4, respectively. Here too, there were substantial graphene stripes grown on top of TiW, but no interfacial graphene was found after the removal of graphene stripes.

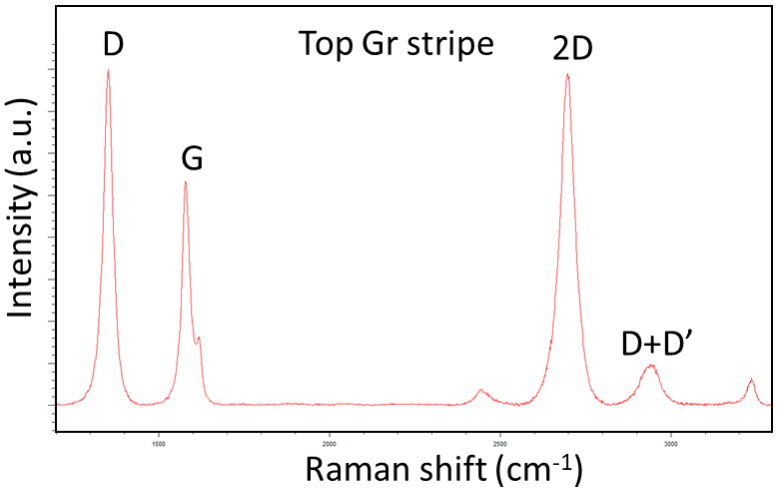

Figure 8.2.3. The Raman spectrum of the graphene stripes on the top surface of TiW deposited on sapphire substrate.

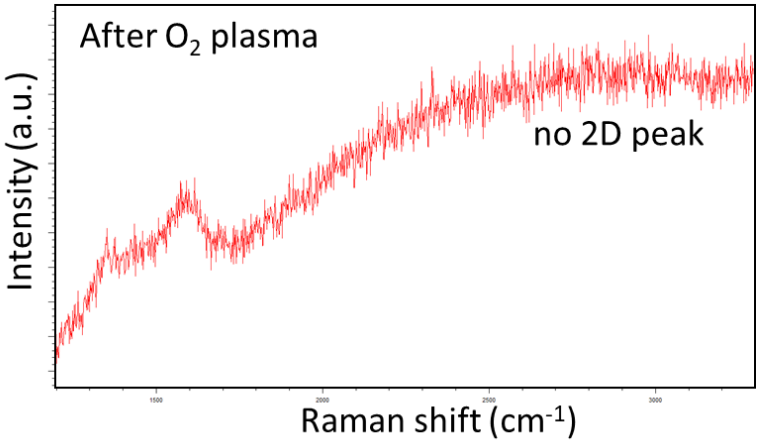

Figure 8.2.4. The Raman spectrum taken on the top surface of TiW deposited on sapphire substrate after O_2 plasma cleaning.

Experiment with Ni

Given the high carbon solubility of Ni, we further explored the feasibility of growing interfacial graphene by depositing a 20 nm thick of Ni film was sputtered onto sapphire, despite the suboptimal characteristics Ni for high-frequency circuits. The Raman spectrum after the PECVD process and subsequent O_2 plasma treatment are shown in Figures 8.2.5 and 8.2.6, respectively. A distinct graphene signal remained after O_2 plasma treatment, suggesting interfacial graphene formation. Additionally, the doublet feature at the 2D peak in the Raman spectrum, suggest the presence of multilayer graphene.

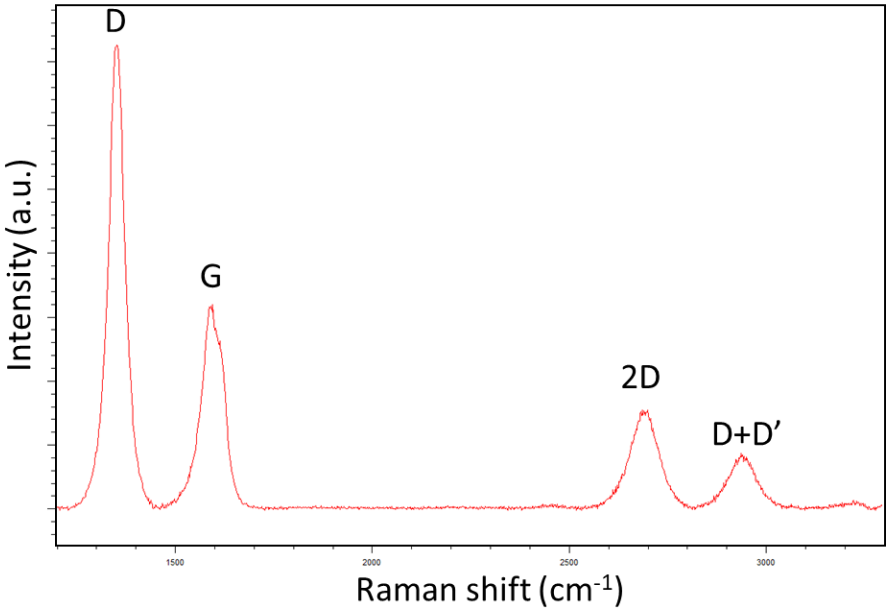

Figure 8.2.5. The Raman spectrum of the graphene stripes at the top surface of Ni on sapphire substrate.

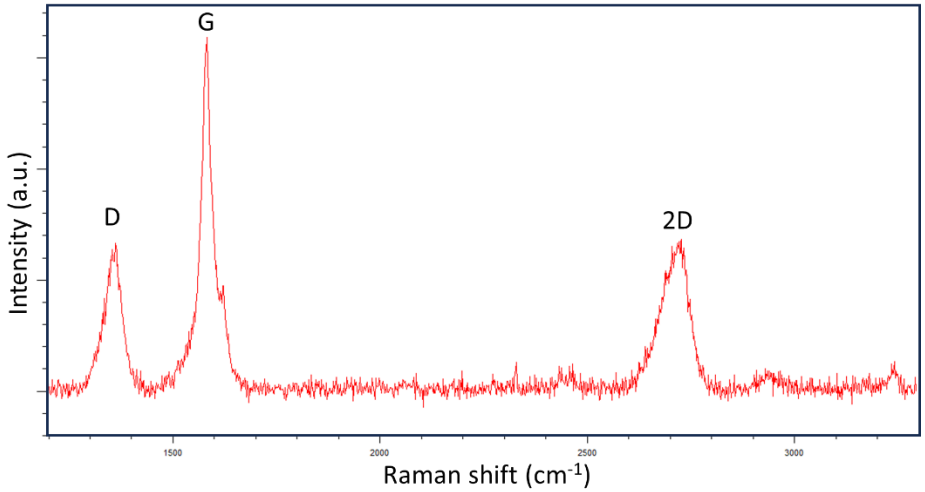

Figure 8.2.6. The Raman spectrum taken on the top surface of Ni deposited on sapphire after O_2 plasma cleaning of the surface graphene stripes.

Cross-sectional STEM was performed to further confirm our findings of interfacial graphene growth, as shown in Figure 8.2.7. Remarkably, around 300 nm of graphene layers were formed within just 3 minutes of growth. Figure 8.2.8 shows a zoomed-in image around the graphene-sapphire interface, where a layer of amorphous carbon was observed adjacent to the sapphire surface. The Electron Energy Loss Near Edge Structures (ELNES) line scans, as shown in Figure 8.2.9, demonstrated the bonding difference between the amorphous carbon at the graphene-sapphire interface and the graphene itself. Specifically, the absence of the 1s $\rightarrow$ σ^* fine structure near or at the graphene-sapphire interface (as observed at locations marked as spot 1 and 2) contrasts with its clear presence in the multilayer graphene regions (indicated by spots 3 to 5), further confirming the distinct bonding characteristics between these areas.

.

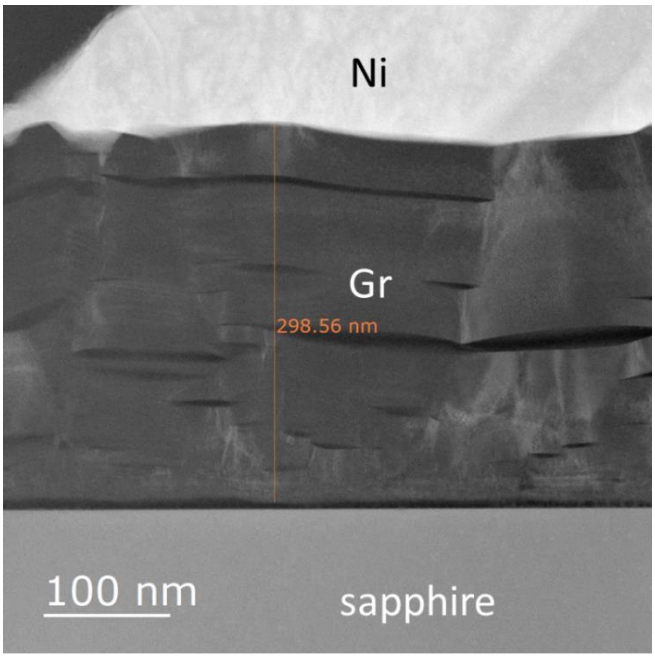

Figure 8.2.7. Cross-sectional STEM of Ni on sapphire after PECVD and O_2 plasma cleaning, showing the formation of ~ 300 nm thick multilayer graphene. The STEM image was acquired by ITRI.

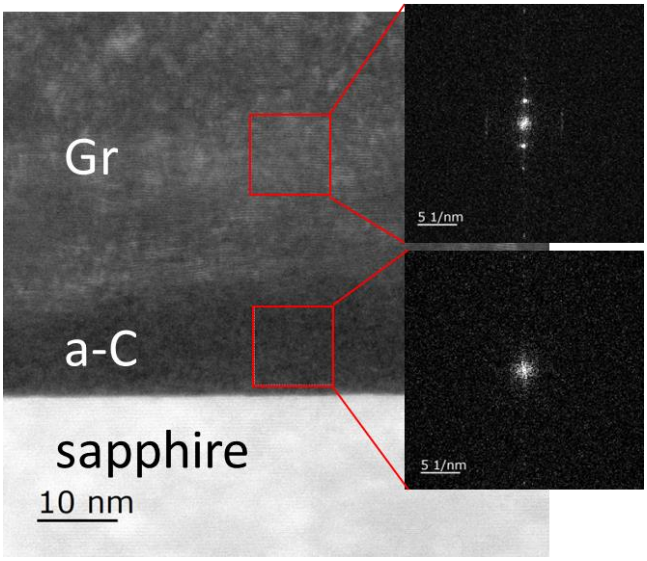

Figure 8.2.8. Zoomed-in cross-sectional STEM of Ni on sapphire after the PECVD process followed by the O_2 plasma cleaning of graphene stripes on the surface of Ni. The insets show the FFT image of the indicated regions. The STEM image was acquired by ITRI.

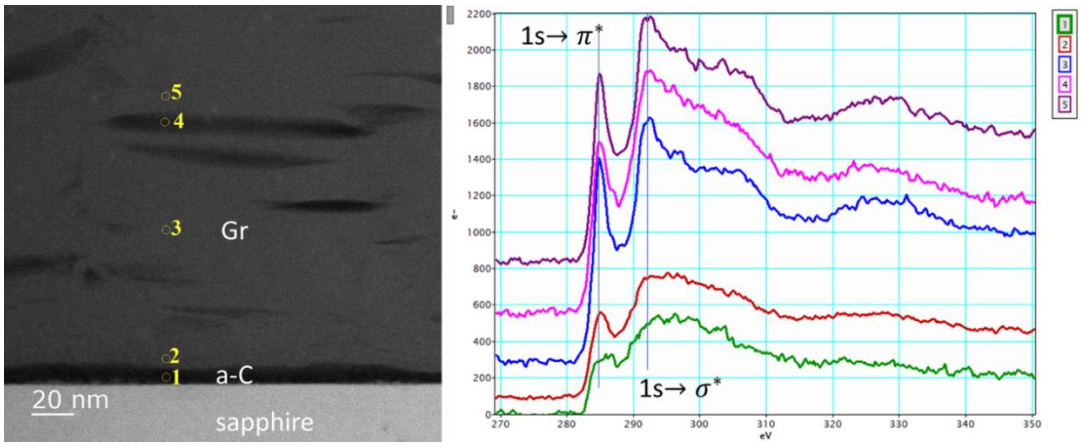

Figure 8.2.9. ELNES line scan of the interfacial graphene region between Ni and sapphire. The ELNES line scan was acquired by ITRI.

Summary

Figure 8.2.10 summarizes the Raman spectroscopy measurements for interfacial graphene. It is noteworthy that the thin metal layer enabled the detection of Raman signals from the

interfacial graphene beneath. Additionally, the adhesion between the metal layer and sapphire weakened after interfacial graphene formation, allowing us to peel off the surface metal layer and measure the interfacial graphene directly.

This section presents promising indications for using Ni to evaluate interfacial graphene growth, although it's worth noting that Ni is not typically suitable for high-frequency applications. No interfacial graphene was observed when using Ag and TiW. Future work should explore the scalability of this technique and its real-world applicability, potentially with metals more suited for high-frequency use.

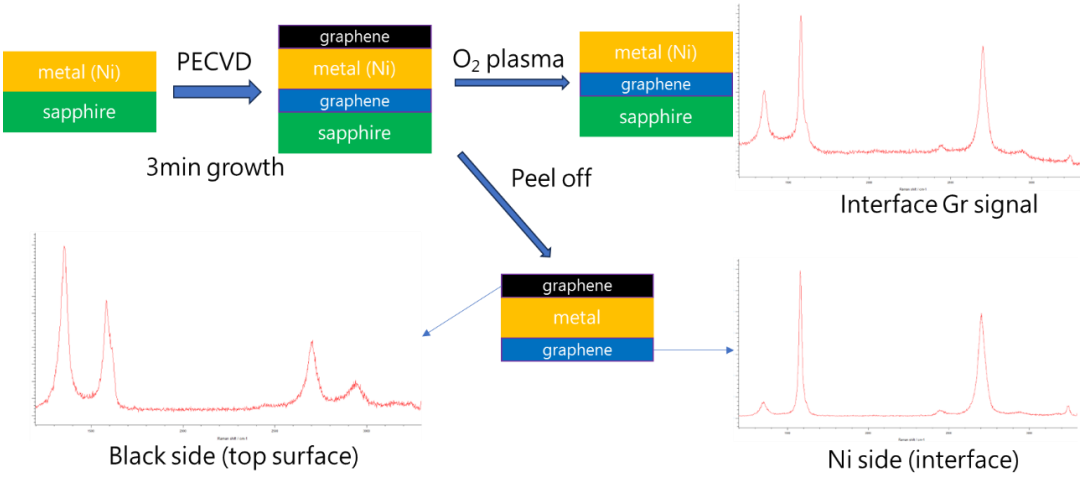

Figure 8.2.10. Summary of measuring the interfacial graphene with Raman spectroscopy.

SUMMARY

The development of single-step plasma-enhanced chemical vapor deposition (PECVD) techniques without active heating have revolutionized the synthesis process of graphene to become scalable and industrially compatible at low temperatures, thus offering versatile applications across a variety of substrates. This thesis provides a comprehensive exploration of this technique, emphasizing its impact on flexible electronics, biosensing, and more.

Initially, the study focuses on the optimization of PECVD growth conditions, which leads to the successful production of high-quality graphene on copper ink. This development sets the stage for potential applications in flexible electronics and IoT devices, with clear benefits for the resilience and environmental stability of copper circuits. The research further establishes that PECVD is effective for growing graphene directly on electroplated copper over polyimide substrates, which not only provides better electrical conductivity and chemical stability but also leads to much improved mechanical durability, adding another layer of versatility to this method.

Expanding on this foundation, the thesis further investigates the application of PECVD in growing graphene on gold. This novel approach presents opportunities to significantly enhance the anti-corrosion properties of gold, extending its lifespan, particularly in the context of electrode-based biosensors.

A significant breakthrough is achieved with the single-step growth of nanocrystalline multilayer graphene on silver. This development not only exhibits exceptional resistance to oxidation but also unveils new opportunities in the field of hybrid graphene-silver plasmonic technologies.

Additionally, the thesis delves into the complexities of using ED copper foils, which are being used in a wide range of applications, as the substrate for graphene growth. Through meticulous experimental studies and analyses, significant transformations in the properties

of the ED copper foils are revealed after the PECVD process, thus demonstrating the feasibility of direct growth of graphene on the ED copper foils.

While the primary focus of the research is on graphene, the thesis also briefly explores the unique dipole ordering properties of monolayer MoS_2, which is a semiconducting van der Waals material. Although not the main focus, this inclusion provides valuable comparative insights, particularly for the synthesis methods and in the context of high-density data storage and non-volatile memories.

Towards the conclusion, the thesis examines the prospects of both large-area PECVD graphene growth and interfacial graphene growth, identifying new directions for future research and innovation.

The insights and findings presented in this thesis contribute to a broader understanding of low-temperature graphene synthesis through PECVD. They serve as a valuable resource for researchers, technology developers, and industry professionals seeking to harness the novel applications of graphene across various sectors. The research outcome of this thesis not only advances our current knowledge of PECVD synthesis of graphene but also stimulates new quest into the ever-expanding field of graphene technology.

BIBLIOGRAPHY

(1) Chen, S.; Brown, L.; Levendorf, M.; Cai, W.; Ju, S.-Y.; Edgeworth, J.; Li, X.; Magnuson, C. W.; Velamakanni, A.; Piner, R. D.; Kang, J.; Park, J.; Ruoff, R. S. Oxidation Resistance of Graphene-Coated Cu and Cu/Ni Alloy. *ACS Nano* **2011,** *5* (2), 1321-1327, DOI: 10.1021/nn103028d.
(2) Choi, S. H.; Kim, Y. L.; Byun, K. M. Graphene-On-Silver Substrates for Sensitive Surface Plasmon Resonance Imaging Biosensors. *Opt. Express* **2011,** *19* (2), 458-466, DOI: 10.1364/OE.19.000458.
(3) Yasuda, S.; Kumagai, R.; Nakashima, K.; Murakoshi, K. Electrochemical Potential Stabilization of Reconstructed Au(111) Structure by Monolayer Coverage with Graphene. *The Journal of Physical Chemistry Letters* **2015,** *6* (17), 3403-3409, DOI: 10.1021/acs.jpclett.5b01488.
(4) Song, B.; Li, D.; Qi, W.; Elstner, M.; Fan, C.; Fang, H. Graphene on Au(111): A Highly Conductive Material with Excellent Adsorption Properties for High-Resolution Bio/Nanodetection and Identification. *ChemPhysChem* **2010,** *11* (3), 585-589, DOI: https://doi.org/10.1002/cphc.200900743.
(5) Lee, D.; Lee, H.; Ahn, Y.; Jeong, Y.; Lee, D.-Y.; Lee, Y. Highly Stable and Flexible Silver Nanowire–Graphene Hybrid Transparent Conducting Electrodes for Emerging Optoelectronic Devices. *Nanoscale* **2013,** *5* (17), 7750-7755, DOI: 10.1039/C3NR02320F.
(6) Li, R.; Li, Z.; Pambou, E.; Gutfreund, P.; Waigh, T. A.; Webster, J. R. P.; Lu, J. R. Determination of PMMA Residues on a Chemical-Vapor-Deposited Monolayer of Graphene by Neutron Reflection and Atomic Force Microscopy. *Langmuir* **2018,** *34* (5), 1827-1833, DOI: 10.1021/acs.langmuir.7b03117.
(7) Liang, X.; Sperling, B. A.; Calizo, I.; Cheng, G.; Hacker, C. A.; Zhang, Q.; Obeng, Y.; Yan, K.; Peng, H.; Li, Q.; Zhu, X.; Yuan, H.; Hight Walker, A. R.; Liu, Z.; Peng, L.-m.; Richter, C. A. Toward Clean and Crackless Transfer of Graphene. *ACS Nano* **2011,** *5* (11), 9144-9153, DOI: 10.1021/nn203377t.
(8) Jin, Z.; McNicholas, T. P.; Shih, C.-J.; Wang, Q. H.; Paulus, G. L. C.; Hilmer, A. J.; Shimizu, S.; Strano, M. S. Click Chemistry on Solution-Dispersed Graphene and Monolayer CVD Graphene. *Chemistry of Materials* **2011,** *23* (14), 3362-3370, DOI: 10.1021/cm201131v.
(9) Jin, Z.; Yao, J.; Kittrell, C.; Tour, J. M. Large-Scale Growth and Characterizations of Nitrogen-Doped Monolayer Graphene Sheets. *ACS Nano* **2011,** *5* (5), 4112-4117, DOI: 10.1021/nn200766e.
(10) Li, Y.; Schluesener, H. J.; Xu, S. Gold Nanoparticle-Based Biosensors. *Gold Bulletin* **2010,** *43* (1), 29-41, DOI: 10.1007/BF03214964.
(11) Khan, Y.; Pavinatto, F. J.; Lin, M. C.; Liao, A.; Swisher, S. L.; Mann, K.; Subramanian, V.; Maharbiz, M. M.; Arias, A. C. Inkjet-Printed Flexible Gold Electrode Arrays for Bioelectronic Interfaces. *Advanced Functional Materials* **2016,** *26* (7), 1004-1013, DOI: https://doi.org/10.1002/adfm.201503316.

(12) Ferrario, A.; Scaramuzza, M.; Pasqualotto, E.; De Toni, A.; Paccagnella, A. Development of a Disposable Gold Electrodes-Based Sensor for Electrochemical Measurements of cDNA Hybridization. *Procedia Chemistry* **2012,** *6*, 36-45, DOI: https://doi.org/10.1016/j.proche.2012.10.128.
(13) Jeong, C.; Park, Y.-B.; Guo, L. J. Tackling Light Trapping in Organic Light-Emitting Diodes by Complete Elimination of Waveguide Modes. *Science Advances* **2021,** *7* (26), eabg0355, DOI: doi:10.1126/sciadv.abg0355.
(14) Kojima, A.; Teshima, K.; Shirai, Y.; Miyasaka, T. Organometal Halide Perovskites as Visible-Light Sensitizers for Photovoltaic Cells. *Journal of the American Chemical Society* **2009,** *131* (17), 6050-6051, DOI: 10.1021/ja809598r.
(15) Im, J.-H.; Lee, C.-R.; Lee, J.-W.; Park, S.-W.; Park, N.-G. 6.5% Efficient Perovskite Quantum-Dot-Sensitized Solar Cell. *Nanoscale* **2011,** *3* (10), 4088-4093, DOI: 10.1039/C1NR10867K.
(16) Lee, M. M.; Teuscher, J.; Miyasaka, T.; Murakami, T. N.; Snaith, H. J. Efficient Hybrid Solar Cells Based on Meso-Superstructured Organometal Halide Perovskites. *Science* **2012,** *338* (6107), 643-647, DOI: doi:10.1126/science.1228604.
(17) Burschka, J.; Pellet, N.; Moon, S.-J.; Humphry-Baker, R.; Gao, P.; Nazeeruddin, M. K.; Grätzel, M. Sequential Deposition as a Route to High-Performance Perovskite-Sensitized Solar Cells. *Nature* **2013,** *499* (7458), 316-319, DOI: 10.1038/nature12340.
(18) Kim, H.-S.; Mora-Sero, I.; Gonzalez-Pedro, V.; Fabregat-Santiago, F.; Juarez-Perez, E. J.; Park, N.-G.; Bisquert, J. Mechanism of Carrier Accumulation in Perovskite Thin-Absorber Solar Cells. *Nature Communications* **2013,** *4* (1), 2242, DOI: 10.1038/ncomms3242.
(19) Jeon, N. J.; Noh, J. H.; Yang, W. S.; Kim, Y. C.; Ryu, S.; Seo, J.; Seok, S. I. Compositional Engineering of Perovskite Materials for High-Performance Solar Cells. *Nature* **2015,** *517* (7535), 476-480, DOI: 10.1038/nature14133.
(20) Nie, W.; Tsai, H.; Asadpour, R.; Blancon, J.-C.; Neukirch, A. J.; Gupta, G.; Crochet, J. J.; Chhowalla, M.; Tretiak, S.; Alam, M. A.; Wang, H.-L.; Mohite, A. D. High-Efficiency Solution-Processed Perovskite Solar Cells with Millimeter-Scale Grains. *Science* **2015,** *347* (6221), 522-525, DOI: doi:10.1126/science.aaa0472.
(21) Li, X.; Bi, D.; Yi, C.; Décoppet, J.-D.; Luo, J.; Zakeeruddin, S. M.; Hagfeldt, A.; Grätzel, M. A Vacuum Flash-Assisted Solution Process for High-Efficiency Large-Area Perovskite Solar Cells. *Science* **2016,** *353* (6294), 58-62, DOI: doi:10.1126/science.aaf8060.
(22) Lin, C.-H.; Hu, L.; Guan, X.; Kim, J.; Huang, C.-Y.; Huang, J.-K.; Singh, S.; Wu, T. Electrode Engineering in Halide Perovskite Electronics: Plenty of Room at the Interfaces. *Adv Mater* **2022,** *34* (18), 2108616, DOI: https://doi.org/10.1002/adma.202108616.
(23) Guan, X.; Wan, T.; Hu, L.; Lin, C.-H.; Yang, J.; Huang, J.-K.; Huang, C.-Y.; Shahrokhi, S.; Younis, A.; Ramadass, K.; Liu, K.; Vinu, A.; Yi, J.; Chu, D.; Wu, T. A Solution-Processed All-Perovskite Memory with Dual-Band Light Response and Tri-Mode Operation. *Advanced Functional Materials* **2022,** *32* (16), 2110975, DOI: https://doi.org/10.1002/adfm.202110975.
(24) Guan, X.; Lei, Z.; Yu, X.; Lin, C.-H.; Huang, J.-K.; Huang, C.-Y.; Hu, L.; Li, F.; Vinu, A.; Yi, J.; Wu, T. Low-Dimensional Metal-Halide Perovskites as High-Performance Materials for Memory Applications. *Small* **2022,** *18* (38), 2203311, DOI: https://doi.org/10.1002/smll.202203311.

(25) Huang, C.-Y.; Li, H.; Wu, Y.; Lin, C.-H.; Guan, X.; Hu, L.; Kim, J.; Zhu, X.; Zeng, H.; Wu, T. Inorganic Halide Perovskite Quantum Dots: A Versatile Nanomaterial Platform for Electronic Applications. *Nano-Micro Letters* **2022,** *15* (1), 16, DOI: 10.1007/s40820-022-00983-6.
(26) Younis, A.; Lin, C.-H.; Guan, X.; Shahrokhi, S.; Huang, C.-Y.; Wang, Y.; He, T.; Singh, S.; Hu, L.; Retamal, J. R. D.; He, J.-H.; Wu, T. Halide Perovskites: A New Era of Solution-Processed Electronics. *Adv Mater* **2021,** *33* (23), 2005000, DOI: https://doi.org/10.1002/adma.202005000.
(27) Li, W.; Rodger, D. C.; Meng, E.; Weiland, J. D.; Humayun, M. S.; Tai, Y. Wafer-Level Parylene Packaging With Integrated RF Electronics for Wireless Retinal Prostheses. *Journal of Microelectromechanical Systems* **2010,** *19* (4), 735-742, DOI: 10.1109/JMEMS.2010.2049985.
(28) Brummer, S. B.; Makrides, A. C. Surface Oxidation of Gold Electrodes. *J Electrochem Soc* **1964,** *111* (10), 1122, DOI: 10.1149/1.2425933.
(29) Leijtens, T.; Eperon, G. E.; Noel, N. K.; Habisreutinger, S. N.; Petrozza, A.; Snaith, H. J. Stability of Metal Halide Perovskite Solar Cells. *Advanced Energy Materials* **2015,** *5* (20), 1500963, DOI: https://doi.org/10.1002/aenm.201500963.
(30) Zhao, X.; Park, N.-G. Stability Issues on Perovskite Solar Cells. *Photonics* **2015,** *2* (4), 1139-1151.
(31) Philippe, B.; Park, B.-W.; Lindblad, R.; Oscarsson, J.; Ahmadi, S.; Johansson, E. M. J.; Rensmo, H. Chemical and Electronic Structure Characterization of Lead Halide Perovskites and Stability Behavior under Different Exposures—A Photoelectron Spectroscopy Investigation. *Chemistry of Materials* **2015,** *27* (5), 1720-1731, DOI: 10.1021/acs.chemmater.5b00348.
(32) Phare, C. T.; Daniel Lee, Y.-H.; Cardenas, J.; Lipson, M. Graphene Electro-Optic Modulator with 30 GHz Bandwidth. *Nature Photonics* **2015,** *9* (8), 511-514, DOI: 10.1038/nphoton.2015.122.
(33) Huidobro, P. A.; Kraft, M.; Maier, S. A.; Pendry, J. B. Graphene as a Tunable Anisotropic or Isotropic Plasmonic Metasurface. *ACS Nano* **2016,** *10* (5), 5499-5506, DOI: 10.1021/acsnano.6b01944.
(34) Casalino, M.; Sassi, U.; Goykhman, I.; Eiden, A.; Lidorikis, E.; Milana, S.; De Fazio, D.; Tomarchio, F.; Iodice, M.; Coppola, G.; Ferrari, A. C. Vertically Illuminated, Resonant Cavity Enhanced, Graphene–Silicon Schottky Photodetectors. *ACS Nano* **2017,** *11* (11), 10955-10963, DOI: 10.1021/acsnano.7b04792.
(35) Chang, P.-H.; Tsai, Y.-C.; Shen, S.-W.; Liu, S.-Y.; Huang, K.-Y.; Li, C.-S.; Chang, H.-P.; Wu, C.-I. Highly Sensitive Graphene–Semiconducting Polymer Hybrid Photodetectors with Millisecond Response Time. *ACS Photonics* **2017,** *4* (9), 2335-2344, DOI: 10.1021/acsphotonics.7b00626.
(36) Levy, U.; Grajower, M.; Gonçalves, P. A. D.; Mortensen, N. A.; Khurgin, J. B. Plasmonic Silicon Schottky Photodetectors: The Physics behind Graphene Enhanced Internal Photoemission. *APL Photonics* **2017,** *2* (2), DOI: 10.1063/1.4973537.
(37) Hwang, J.; Kim, M.; Campbell, D.; Alsalman, H. A.; Kwak, J. Y.; Shivaraman, S.; Woll, A. R.; Singh, A. K.; Hennig, R. G.; Gorantla, S.; Rümmeli, M. H.; Spencer, M. G. van der Waals Epitaxial Growth of Graphene on Sapphire by Chemical Vapor Deposition without a Metal Catalyst. *ACS Nano* **2013,** *7* (1), 385-395, DOI: 10.1021/nn305486x.

(38) Tai, L.; Zhu, D.; Liu, X.; Yang, T.; Wang, L.; Wang, R.; Jiang, S.; Chen, Z.; Xu, Z.; Li, X. Direct Growth of Graphene on Silicon by Metal-Free Chemical Vapor Deposition. *Nano-Micro Letters* **2017,** *10* (2), 20, DOI: 10.1007/s40820-017-0173-1.
(39) Trung, P. T.; Joucken, F.; Campos-Delgado, J.; Raskin, J.-P.; Hackens, B.; Sporken, R. Direct Growth of Graphitic Carbon on Si(111). *Applied Physics Letters* **2013,** *102* (1), 013118, DOI: 10.1063/1.4773989.
(40) Hong, G.; Wu, Q.-H.; Ren, J.; Lee, S.-T. Mechanism of Non-Metal Catalytic Growth of Graphene on Silicon. *Applied Physics Letters* **2012,** *100* (23), 231604, DOI: 10.1063/1.4726114.
(41) Affairs;, U. S. A. C. A. R. L. P. DOD awards $154 million to Army-led flexible electronics project. https://www.army.mil/article/237275/dod_awards_154_million_to_army_led_flexible_electronics_project.
(42) Net-Zero Emissions Operations by 2050, including a 65% reduction by 2030. https://www.sustainability.gov/federalsustainabilityplan/emissions.html.
(43) Wearable Medical Device Market Size, Share & Trends Analysis Report By Type (Diagnostic, Therapeutic), By Site (Handheld, Headband, Strap, Shoe Sensors), By Application, By Region, And Segment Forecasts, 2022-2030. https://www.grandviewresearch.com/industry-analysis/wearable-medical-devices-market.
(44) Global Printed Electronics Industry. https://www.reportlinker.com/p05959782/Global-Printed-Electronics-Industry.html?utm_source=GNW.
(45) Flexible Hybrid Electronics (FHE) Market Size & Share Analysis - Growth Trends & Forecasts (2023 - 2028). https://www.mordorintelligence.com/industry-reports/flexible-hybrid-electronics-market.
(46) 5G/6G Wireless Networks. https://www.dhs.gov/science-and-technology/5g6g.
(47) Li, W.; Qian, X.; Li, J. Phase Transitions in 2D Materials. *Nature Reviews Materials* **2021,** *6* (9), 829-846, DOI: 10.1038/s41578-021-00304-0.
(48) Novoselov, K. S.; Geim, A. K.; Morozov, S. V.; Jiang, D.; Zhang, Y.; Dubonos, S. V.; Grigorieva, I. V.; Firsov, A. A. Electric Field Effect in Atomically Thin Carbon Films. *Science* **2004,** *306* (5696), 666-9, DOI: 10.1126/science.1102896.
(49) Li, X.; Cai, W.; An, J.; Kim, S.; Nah, J.; Yang, D.; Piner, R.; Velamakanni, A.; Jung, I.; Tutuc, E.; Banerjee, S. K.; Colombo, L.; Ruoff, R. S. Large-Area Synthesis of High-Quality and Uniform Graphene Films on Copper Foils. *Science* **2009,** *324* (5932), 1312-4, DOI: 10.1126/science.1171245.
(50) Miseikis, V.; Convertino, D.; Mishra, N.; Gemmi, M.; Mashoff, T.; Heun, S.; Haghighian, N.; Bisio, F.; Canepa, M.; Piazza, V.; Coletti, C. Rapid CVD Growth of Millimetre-Sized Single Crystal Graphene Using a Cold-Wall Reactor. *2d Materials* **2015,** *2* (1), 014006, DOI: 10.1088/2053-1583/2/1/014006.
(51) Wu, Y. A.; Fan, Y.; Speller, S.; Creeth, G. L.; Sadowski, J. T.; He, K.; Robertson, A. W.; Allen, C. S.; Warner, J. H. Large Single Crystals of Graphene on Melted Copper Using Chemical Vapor Deposition. *ACS Nano* **2012,** *6* (6), 5010-7, DOI: 10.1021/nn3016629.
(52) Reina, A.; Jia, X.; Ho, J.; Nezich, D.; Son, H.; Bulovic, V.; Dresselhaus, M. S.; Kong, J. Large Area, Few-Layer Graphene Films on Arbitrary Substrates by Chemical Vapor Deposition. *Nano Lett* **2009,** *9* (1), 30-5, DOI: 10.1021/nl801827v.

(53) Li, X.; Magnuson, C. W.; Venugopal, A.; An, J.; Suk, J. W.; Han, B.; Borysiak, M.; Cai, W.; Velamakanni, A.; Zhu, Y.; Fu, L.; Vogel, E. M.; Voelkl, E.; Colombo, L.; Ruoff, R. S. Graphene Films with Large Domain Size by a Two-Step Chemical Vapor Deposition Process. *Nano Lett* **2010,** *10* (11), 4328-34, DOI: 10.1021/nl101629g.
(54) Lisi, N.; Dikonimos, T.; Buonocore, F.; Pittori, M.; Mazzaro, R.; Rizzoli, R.; Marras, S.; Capasso, A. Contamination-Free Graphene by Chemical Vapor Deposition in Quartz Furnaces. *Sci Rep* **2017,** *7* (1), 9927, DOI: 10.1038/s41598-017-09811-z.
(55) Fujita, J. I.; Hiyama, T.; Hirukawa, A.; Kondo, T.; Nakamura, J.; Ito, S. I.; Araki, R.; Ito, Y.; Takeguchi, M.; Pai, W. W. Near Room Temperature Chemical Vapor Deposition of Graphene with Diluted Methane and Molten Gallium Catalyst. *Sci Rep* **2017,** *7* (1), 12371, DOI: 10.1038/s41598-017-12380-w.
(56) Kwak, J.; Chu, J. H.; Choi, J. K.; Park, S. D.; Go, H.; Kim, S. Y.; Park, K.; Kim, S. D.; Kim, Y. W.; Yoon, E.; Kodambaka, S.; Kwon, S. Y. Near Room-Temperature Synthesis of Transfer-Free Graphene Films. *Nat Commun* **2012,** *3*, 645, DOI: 10.1038/ncomms1650.
(57) Hawaldar, R.; Merino, P.; Correia, M. R.; Bdikin, I.; Gracio, J.; Mendez, J.; Martin-Gago, J. A.; Singh, M. K. Large-Area High-Throughput Synthesis of Monolayer Graphene Sheet by Hot Filament Thermal Chemical Vapor Deposition. *Sci Rep* **2012,** *2*, 682, DOI: 10.1038/srep00682.
(58) Lee, E.; Lee, S. G.; Cho, K. Direct Growth of Substrate-Adhered Graphene on Flexible Polymer Substrates for Soft Electronics. *Chemistry of Materials* **2019,** *31* (12), 4451-4459, DOI: 10.1021/acs.chemmater.9b00948.
(59) Kumar, A.; Voevoclin, A. A.; Zemlyanov, D.; Zakharov, D. N.; Fisher, T. S. Rapid Synthesis of Few-Layer Graphene over Cu Foil. *Carbon* **2012,** *50* (4), 1546-1553, DOI: 10.1016/j.carbon.2011.11.033.
(60) Li, M.; Liu, D.; Wei, D.; Song, X.; Wei, D.; Wee, A. T. Controllable Synthesis of Graphene by Plasma-Enhanced Chemical Vapor Deposition and Its Related Applications. *Adv Sci (Weinh)* **2016,** *3* (11), 1600003, DOI: 10.1002/advs.201600003.
(61) Guo, L. C.; Zhang, Z. Y.; Sun, H. Y.; Dai, D.; Cui, J. F.; Li, M. Z.; Xu, Y.; Xu, M. S.; Du, Y. F.; Jiang, N.; Huang, F.; Lin, C. T. Direct Formation of Wafer-Scale Single-Layer Graphene Films on the Rough Surface Substrate by PECVD. *Carbon* **2018,** *129*, 456-461, DOI: 10.1016/j.carbon.2017.12.023.
(62) Kim, Y. S.; Joo, K.; Jerng, S. K.; Lee, J. H.; Yoon, E.; Chun, S. H. Direct Growth of Patterned Graphene on SiO2 Substrates without the use of Catalysts or Lithography. *Nanoscale* **2014,** *6* (17), 10100-5, DOI: 10.1039/c4nr02001d.
(63) Sun, J. Y.; Chen, Y. B.; Cai, X.; Ma, B. J.; Chen, Z. L.; Priydarshi, M. K.; Chen, K.; Gao, T.; Song, X. J.; Ji, Q. Q.; Guo, X. F.; Zou, D. C.; Zhang, Y. F.; Liu, Z. F. Direct Low-Temperature Synthesis of Graphene on Various Glasses by Plasma-Enhanced Chemical Vapor Deposition for Versatile, Cost-Effective Electrodes. *Nano Research* **2015,** *8* (11), 3496-3504, DOI: 10.1007/s12274-015-0849-0.
(64) Woehrl, N.; Ochedowski, O.; Gottlieb, S.; Shibasaki, K.; Schulz, S. Plasma-Enhanced Chemical Vapor Deposition of Graphene on Copper Substrates. *Aip Advances* **2014,** *4* (4), 047128, DOI: 10.1063/1.4873157.
(65) Malesevic, A.; Vitchev, R.; Schouteden, K.; Volodin, A.; Zhang, L.; Tendeloo, G. V.; Vanhulsel, A.; Haesendonck, C. V. Synthesis of Few-Layer Graphene via Microwave

Plasma-Enhanced Chemical Vapour Deposition. *Nanotechnology* **2008,** *19* (30), 305604, DOI: 10.1088/0957-4484/19/30/305604.
(66) Munoz, R.; Martinez, L.; Lopez-Elvira, E.; Munuera, C.; Huttel, Y.; Garcia-Hernandez, M. Direct Synthesis of Graphene on Silicon Oxide by Low Temperature Plasma Enhanced Chemical Vapor Deposition. *Nanoscale* **2018,** *10* (26), 12779-12787, DOI: 10.1039/c8nr03210f.
(67) Boyd, D. A.; Lin, W. H.; Hsu, C. C.; Teague, M. L.; Chen, C. C.; Lo, Y. Y.; Chan, W. Y.; Su, W. B.; Cheng, T. C.; Chang, C. S.; Wu, C. I.; Yeh, N. C. Single-Step Deposition of High-Mobility Graphene at Reduced Temperatures. *Nat Commun* **2015,** *6*, 6620, DOI: 10.1038/ncomms7620.
(68) Terasawa, T.; Saiki, K. Growth of Graphene on Cu by Plasma Enhanced Chemical Vapor Deposition. *Carbon* **2012,** *50* (3), 869-874, DOI: 10.1016/j.carbon.2011.09.047.
(69) Zhang, Y. J.; Ren, W.; Jiang, Z. D.; Yang, S. M.; Jing, W. X.; Shi, P.; Wu, X. Q.; Ye, Z. G. Low-Temperature Remote Plasma-Enhanced Atomic Layer Deposition of Graphene and Characterization of its Atomic-Level Structure. *Journal of Materials Chemistry C* **2014,** *2* (36), 7570-7574, DOI: 10.1039/c4tc00849a.
(70) Zheng, S.; Zhong, G. F.; Wu, X. Y.; D'Arsie, L.; Robertson, J. Metal-Catalyst-Free Growth of Graphene on Insulating Substrates by Ammonia-Assisted Microwave Plasma-Enhanced Chemical Vapor Deposition. *RSC Advances* **2017,** *7* (53), 33185-33193, DOI: 10.1039/c7ra04162d.
(71) Yeh, N. C.; Hsu, C. C.; Bagley, J.; Tseng, W. S. Single-Step Growth of Graphene and Graphene-Based Nanostructures by Plasma-Enhanced Chemical Vapor Deposition. *Nanotechnology* **2019,** *30* (16), 162001, DOI: 10.1088/1361-6528/aafdbf.
(72) Su, C. Y.; Lu, A. Y.; Wu, C. Y.; Li, Y. T.; Liu, K. K.; Zhang, W.; Lin, S. Y.; Juang, Z. Y.; Zhong, Y. L.; Chen, F. R.; Li, L. J. Direct Formation of Wafer Scale Graphene Thin Layers on Insulating Substrates by Chemical Vapor Deposition. *Nano Lett* **2011,** *11* (9), 3612-6, DOI: 10.1021/nl201362n.
(73) Albrecht, A.; Rivadeneyra, A.; Abdellah, A.; Lugli, P.; Salmeron, J. F. Inkjet Printing and Photonic Sintering of Silver and Copper Oxide Nanoparticles for Ultra-Low-Cost Conductive Patterns. *Journal of Materials Chemistry C* **2016,** *4* (16), 3546-3554, DOI: 10.1039/c6tc00628k.
(74) Khan, Y.; Thielens, A.; Muin, S.; Ting, J.; Baumbauer, C.; Arias, A. C. A New Frontier of Printed Electronics: Flexible Hybrid Electronics. *Adv Mater* **2020,** *32* (15), e1905279, DOI: 10.1002/adma.201905279.
(75) Roshanghias, A.; Ma, Y.; Dreissigacker, M.; Braun, T.; Bretthauer, C.; Becker, K.-F.; Schneider-Ramelow, M. The Realization of Redistribution Layers for FOWLP by Inkjet Printing. *Proceedings* **2018,** *2* (13), 703, DOI: 10.3390/proceedings2130703.
(76) Khorramdel, B.; Liljeholm, J.; Laurila, M. M.; Lammi, T.; Martensson, G.; Ebefors, T.; Niklaus, F.; Mantysalo, M. Inkjet Printing Technology for Increasing the I/O Density of 3D TSV Interposers. *Microsystems & Nanoengineering* **2017,** *3* (1), 17002, DOI: 10.1038/micronano.2017.2.
(77) Quintero, A. V.; Molina-Lopez, F.; Smits, E. C. P.; Danesh, E.; van den Brand, J.; Persaud, K.; Oprea, A.; Barsan, N.; Weimar, U.; de Rooij, N. F.; Briand, D. Smart RFID Label with a Printed Multisensor Platform for Environmental Monitoring. *Flexible and Printed Electronics* **2016,** *1* (2), 025003, DOI: 10.1088/2058-8585/1/2/025003.

(78) Lesch, A.; Jović, M.; Baudoz, M.; Zhu, Y.; Tacchini, P.; Gumy, F.; Girault, H. H. (Invited) Point-of-Care Diagnostics with Inkjet-Printed Microchips. *Ecs Transactions* **2017,** *77* (7), 73-81, DOI: 10.1149/07707.0073ecst.
(79) Tsangarides, C. P.; Ma, H.; Nathan, A. ZnO Nanowire Array Growth on Precisely ControlledPatterns of Inkjet-Printed Cinc Acetate at Low-Temperatures. *Nanoscale* **2016,** *8* (22), 11760-5, DOI: 10.1039/c6nr02962k.
(80) Arrese, J.; Vescio, G.; Xuriguera, E.; Medina-Rodriguez, B.; Cornet, A.; Cirera, A. Flexible Hybrid Circuit Fully Inkjet-Printed: Surface Mount Devices Assembled by Silver Nanoparticles-based Inkjet Ink. *Journal of Applied Physics* **2017,** *121* (10), 104904, DOI: 10.1063/1.4977961.
(81) Abutarboush, H. F.; Shamim, A. Paper-Based Inkjet-Printed Tri-Band U-Slot Monopole Antenna for Wireless Applications. *IEEE Antennas and Wireless Propagation Letters* **2012,** *11*, 1234-1237, DOI: 10.1109/Lawp.2012.2223751.
(82) C, A.; Szymanski, M. Z.; Luszczynska, B.; Ulanski, J. Inkjet Printing of Super Yellow: Ink Formulation, Film Optimization, OLEDs Fabrication, and Transient Electroluminescence. *Scientific Reports* **2019,** *9* (1), 8493, DOI: 10.1038/s41598-019-44824-w.
(83) Hu, Z.; Yin, Y.; Ali, M. U.; Peng, W.; Zhang, S.; Li, D.; Zou, T.; Li, Y.; Jiao, S.; Chen, S. J.; Lee, C. Y.; Meng, H.; Zhou, H. Inkjet Printed Uniform Quantum Dots as Color Conversion Layers for Full-Color OLED Displays. *Nanoscale* **2020,** *12* (3), 2103-2110, DOI: 10.1039/c9nr09086j.
(84) Lu, C.-A.; Lin, P.; Lin, H.-C.; Wang, S.-F. Effects of Silver Oxide Addition on the Electrical Resistivity and Microstructure of Low-Temperature-Curing Metallo-Organic Decomposition Silver Pastes. *Japanese Journal of Applied Physics* **2007,** *46* (7A), 4179-4183, DOI: 10.1143/jjap.46.4179.
(85) Nakamoto, M. Application 4 - Microelectronics packaging by metal nanoparticle pastes. In *Nanoparticle Technology Handbook (Second Edition)*; Hosokawa, M.; Nogi, K.; Naito, M.; Yokoyama, T., Eds.; Elsevier: Amsterdam, 2012; pp 434-438.
(86) Yang, W. D.; Liu, C. Y.; Zhang, Z. Y.; Liu, Y.; Nie, S. D. Copper Inks Formed using Short Carbon Chain Organic Cu-Precursors. *Rsc Advances* **2014,** *4* (104), 60144-60147, DOI: 10.1039/c4ra09318f.
(87) Hermerschmidt, F.; Burmeister, D.; Ligorio, G.; Pozov, S. M.; Ward, R.; Choulis, S. A.; List-Kratochvil, E. J. W. Truly Low Temperature Sintering of Printed Copper Ink Using Formic Acid. *Advanced Materials Technologies* **2018,** *3* (12), 1800146, DOI: 10.1002/admt.201800146.
(88) Geim, A. K.; Novoselov, K. S. The Rise of Graphene. *Nature Materials* **2007,** *6* (3), 183-191, DOI: 10.1038/nmat1849.
(89) Papageorgiou, D. G.; Kinloch, I. A.; Young, R. J. Mechanical Properties of Graphene and Graphene-Based Nanocomposites. *Progress in Materials Science* **2017,** *90*, 75-127, DOI: 10.1016/j.pmatsci.2017.07.004.
(90) Falkovsky, L. A. Optical Properties of Graphene. *Journal of Physics: Conference Series* **2008,** *129*, 012004, DOI: 10.1088/1742-6596/129/1/012004.
(91) Scida, A.; Haque, S.; Treossi, E.; Robinson, A.; Smerzi, S.; Ravesi, S.; Borini, S.; Palermo, V. Application of Graphene-Based Flexible Antennas in Consumer Electronic Devices. *Materials Today* **2018,** *21* (3), 223-230, DOI: 10.1016/j.mattod.2018.01.007.

(92) Sriram, P.; Manikandan, A.; Chuang, F. C.; Chueh, Y. L. Hybridizing Plasmonic Materials with 2D-Transition Metal Dichalcogenides toward Functional Applications. *Small* **2020,** *16* (15), e1904271, DOI: 10.1002/smll.201904271.
(93) Lee, S.; Jo, I.; Kang, S.; Jang, B.; Moon, J.; Park, J. B.; Lee, S.; Rho, S.; Kim, Y.; Hong, B. H. Smart Contact Lenses with Graphene Coating for Electromagnetic Interference Shielding and Dehydration Protection. *ACS Nano* **2017,** *11* (6), 5318-5324, DOI: 10.1021/acsnano.7b00370.
(94) Tseng, W. S.; Jao, M. H.; Hsu, C. C.; Huang, J. S.; Wu, C. I.; Yeh, N. C. Stabilization of Hybrid Perovskite CH3NH3PbI3 Thin Films by Graphene Passivation. *Nanoscale* **2017,** *9* (48), 19227-19235, DOI: 10.1039/c7nr06510h.
(95) Hong, J.; Lee, S.; Lee, S.; Han, H.; Mahata, C.; Yeon, H. W.; Koo, B.; Kim, S. I.; Nam, T.; Byun, K.; Min, B. W.; Kim, Y. W.; Kim, H.; Joo, Y. C.; Lee, T. Graphene as an Atomically Thin Barrier to Cu Diffusion into Si. *Nanoscale* **2014,** *6* (13), 7503-11, DOI: 10.1039/c3nr06771h.
(96) Mehta, R.; Chugh, S.; Chen, Z. Transfer-Free Multi-Layer Graphene as a Diffusion Barrier. *Nanoscale* **2017,** *9* (5), 1827-1833, DOI: 10.1039/c6nr07637h.
(97) Li, Y. F.; Dong, F. X.; Chen, Y.; Zhang, X. L.; Wang, L.; Bi, Y. G.; Tian, Z. N.; Liu, Y. F.; Feng, J.; Sun, H. B. As-Grown Graphene/Copper Nanoparticles Hybrid Nanostructures for Enhanced Intensity and Stability of Surface Plasmon Resonance. *Scientific Reports* **2016,** *6*, 37190, DOI: 10.1038/srep37190.
(98) Manikandan, A.; Lee, L.; Wang, Y. C.; Chen, C. W.; Chen, Y. Z.; Medina, H.; Tseng, J. Y.; Wang, Z. M. M.; Chueh, Y. L. Graphene-Coated Copper Nanowire Networks as a Highly Stable Transparent Electrode in Harsh Environments toward Efficient Electrocatalytic Hydrogen Evolution Reactions. *Journal of Materials Chemistry A* **2017,** *5* (26), 13320-13328, DOI: 10.1039/c7ta01767g.
(99) Alotaibi, F.; Tung, T. T.; Nine, M. J.; Coghlan, C. J.; Losic, D. Silver Nanowires with Pristine Graphene Oxidation Barriers for Stable and High Performance Transparent Conductive Films. *ACS Applied Nano Materials* **2018,** *1* (5), 2249-2260, DOI: 10.1021/acsanm.8b00255.
(100) Jeong, G.; Koo, D.; Seo, J.; Jung, S.; Choi, Y.; Lee, J.; Park, H. Suppressed Interdiffusion and Degradation in Flexible and Transparent Metal Electrode-Based Perovskite Solar Cells with a Graphene Interlayer. *Nano Letters* **2020,** *20* (5), 3718-3727, DOI: 10.1021/acs.nanolett.0c00663.
(101) AlAmri, A. M.; Leung, S. F.; Vaseem, M.; Shamim, A.; He, J. H. Fully Inkjet-Printed Photodetector Using a Graphene/Perovskite/Graphene Heterostructure. *IEEE Transactions on Electron Devices* **2019,** *66* (6), 2657-2661, DOI: 10.1109/Ted.2019.2911715.
(102) Medina, H.; Li, J. G.; Su, T. Y.; Lan, Y. W.; Lee, S. H.; Chen, C. W.; Chen, Y. Z.; Manikandan, A.; Tsai, S. H.; Navabi, A.; Zhu, X. D.; Shih, Y. C.; Lin, W. S.; Yang, J. H.; Thomas, S. R.; Wu, B. W.; Shen, C. H.; Shieh, J. M.; Lin, H. N.; Javey, A.; Wang, K. L.; Chueh, Y. L. Wafer-Scale Growth of WSe2 Monolayers Toward Phase-Engineered Hybrid WOx/WSe2 Films with Sub-ppb NOx Gas Sensing by a Low-Temperature Plasma-Assisted Selenization Process. *Chemistry of Materials* **2017,** *29* (4), 1587-1598, DOI: 10.1021/acs.chemmater.6b04467.
(103) Chen, Y. Z.; Lee, S. H.; Su, T. Y.; Wu, S. C.; Chen, P. J.; Chueh, Y. L. Phase-Modulated 3D-Hierarchical 1T/2H WSe2 Nanoscrews by a Plasma-Assisted Selenization

Process as High Performance NO Gas Sensors with a ppb-Level Detection Limit. *Journal of Materials Chemistry A* **2019,** *7* (39), 22314-22322, DOI: 10.1039/c9ta05348d.
(104) Alrefae, M. A.; Kumar, A.; Pandita, P.; Candadai, A.; Bilionis, I.; Fisher, T. S. Process Optimization of Graphene Growth in a Roll-to-Roll Plasma CVD System. *AIP Advances* **2017,** *7* (11), 115102, DOI: 10.1063/1.4998770.
(105) Moisan, M.; Pelletier, J. Hydrodynamic Description of a Plasma. In *Physics of Collisional Plasmas: Introduction to High-Frequency Discharges*; Springer Netherlands: Dordrecht, 2012; pp 203-335.
(106) von Keudell, A.; Schulz-von der Gathen, V. Foundations of Low-Temperature Plasma Physics—An Introduction. *Plasma Sources Science and Technology* **2017,** *26* (11), 113001, DOI: 10.1088/1361-6595/aa8d4c.
(107) Park, H. J.; Shin, J.-h.; Lee, K.-i.; Choi, Y. S.; Song, Y. I.; Suh, S. J.; Jung, Y. H. Effective Control of CH4/H2 Plasma Condition to Synthesize Graphene Nano-walls with Controlled Morphology and Structural Quality. *Applied Science and Convergence Technology* **2017,** *26* (6), 179-183, DOI: 10.5757/asct.2017.26.6.179.
(108) Beams, R.; Gustavo Cancado, L.; Novotny, L. Raman Characterization of Defects and Dopants in Graphene. *J Phys Condens Matter* **2015,** *27* (8), 083002, DOI: 10.1088/0953-8984/27/8/083002.
(109) Zandiatashbar, A.; Lee, G. H.; An, S. J.; Lee, S.; Mathew, N.; Terrones, M.; Hayashi, T.; Picu, C. R.; Hone, J.; Koratkar, N. Effect of Defects on the Intrinsic Strength and Stiffness of Graphene. *Nature Communication* **2014,** *5* (1), 3186, DOI: 10.1038/ncomms4186.
(110) Nair, R. R.; Ren, W.; Jalil, R.; Riaz, I.; Kravets, V. G.; Britnell, L.; Blake, P.; Schedin, F.; Mayorov, A. S.; Yuan, S.; Katsnelson, M. I.; Cheng, H. M.; Strupinski, W.; Bulusheva, L. G.; Okotrub, A. V.; Grigorieva, I. V.; Grigorenko, A. N.; Novoselov, K. S.; Geim, A. K. Fluorographene: a Two-Dimensional Counterpart of Teflon. *Small* **2010,** *6* (24), 2877-84, DOI: 10.1002/smll.201001555.
(111) Eckmann, A.; Felten, A.; Mishchenko, A.; Britnell, L.; Krupke, R.; Novoselov, K. S.; Casiraghi, C. Probing the Nature of Defects in Graphene by Raman Spectroscopy. *Nano Lett* **2012,** *12* (8), 3925-30, DOI: 10.1021/nl300901a.
(112) Paton, K. R.; Varrla, E.; Backes, C.; Smith, R. J.; Khan, U.; O'Neill, A.; Boland, C.; Lotya, M.; Istrate, O. M.; King, P.; Higgins, T.; Barwich, S.; May, P.; Puczkarski, P.; Ahmed, I.; Moebius, M.; Pettersson, H.; Long, E.; Coelho, J.; O'Brien, S. E.; McGuire, E. K.; Sanchez, B. M.; Duesberg, G. S.; McEvoy, N.; Pennycook, T. J.; Downing, C.; Crossley, A.; Nicolosi, V.; Coleman, J. N. Scalable Production of Large Quantities of Defect-Free Few-Layer Graphene by Shear Exfoliation in Liquids. *Nature Materials* **2014,** *13* (6), 624-30, DOI: 10.1038/nmat3944.
(113) Lee, W. H.; Kao, W. C.; Yin, Y. T.; Yi, S. H.; Huang, K. W.; Lin, H. C.; Chen, M. J. Sub-Nanometer Heating Depth of Atomic Layer Annealing. *Applied Surface Science* **2020,** *525*, 146615, DOI: ARTN 146615
10.1016/j.apsusc.2020.146615.
(114) Lee, H. C.; Liu, W.-W.; Chai, S.-P.; Mohamed, A. R.; Aziz, A.; Khe, C.-S.; Hidayah, N. M. S.; Hashim, U. Review of the Synthesis, Transfer, Characterization and Growth Mechanisms of Single and Multilayer Graphene. *RSC Advances* **2017,** *7* (26), 15644-15693, DOI: 10.1039/c7ra00392g.

(115) Dulle, J.; Thirunavukkarasu, K.; Mittelmeijer-Hazeleger, M. C.; Andreeva, D. V.; Shiju, N. R.; Rothenberg, G. Efficient Three-Component Coupling Catalysed by Mesoporous Copper–Aluminum Based Nanocomposites. *Green Chemistry* **2013,** *15* (5), 1238, DOI: 10.1039/c3gc36607c.
(116) Pike, J.; Chan, S. W.; Zhang, F.; Wang, X. Q.; Hanson, J. Formation of stable Cu2O from reduction of CuO nanoparticles. *Applied Catalysis a-General* **2006,** *303* (2), 273-277, DOI: 10.1016/j.apcata.2006.02.008.
(117) Khan, Y.; Garg, M.; Gui, Q.; Schadt, M.; Gaikwad, A.; Han, D.; Yamamoto, N. A. D.; Hart, P.; Welte, R.; Wilson, W.; Czarnecki, S.; Poliks, M.; Jin, Z.; Ghose, K.; Egitto, F.; Turner, J.; Arias, A. C. Flexible Hybrid Electronics: Direct Interfacing of Soft and Hard Electronics for Wearable Health Monitoring. *Advanced Functional Materials* **2016,** *26* (47), 8764-8775, DOI: 10.1002/adfm.201603763.
(118) Chen, W.-C.; Liou, W.-T.; Jung, C.-W.; Chen, G.; Ho, J.-C.; Chen, J.; Lee, C.-C. P-178: Flexible AMOLED Display Fabricated by Mask-less Digital Lithography Technology. *SID Symposium Digest of Technical Papers* **2019,** *50* (1), 1903-1906, DOI: 10.1002/sdtp.13335.
(119) Song, L.; Myers, A. C.; Adams, J. J.; Zhu, Y. Stretchable and Reversibly Deformable Radio Frequency Antennas Based on Silver Nanowires. *ACS Applied Materials & Interfaces* **2014,** *6* (6), 4248-4253, DOI: 10.1021/am405972e.
(120) Lu, C. H.; Leu, C. M.; Yeh, N. C. Single-Step Direct Growth of Graphene on Cu Ink toward Flexible Hybrid Electronic Applications by Plasma-Enhanced Chemical Vapor Deposition. *ACS Applied Materials & Interfaces* **2021,** *13* (5), 6951-6959, DOI: 10.1021/acsami.0c22207.
(121) Sa'don, S. N. H.; Kamarudin, M. R.; Ahmad, F.; Jusoh, M.; Majid, H. A. Graphene Array Antenna for 5G Applications. *Applied Physics A* **2017,** *123* (2), 118, DOI: 10.1007/s00339-016-0749-5.
(122) Yuan, W.; Shi, G. Graphene-Based Gas Sensors. *Journal of Materials Chemistry A* **2013,** *1* (35), 10078, DOI: 10.1039/c3ta11774j.
(123) Kim, K. S.; Zhao, Y.; Jang, H.; Lee, S. Y.; Kim, J. M.; Ahn, J. H.; Kim, P.; Choi, J. Y.; Hong, B. H. Large-scale Pattern Growth of Graphene Films for Stretchable Transparent Electrodes. *Nature* **2009,** *457* (7230), 706.
(124) Li, L.; Zhu, Z.; Yoon, A.; Wong, H. S. P. In-Situ Grown Graphene Enabled Copper Interconnects With Improved Electromigration Reliability. *IEEE Electron Device Letters* **2019,** *40* (5), 815-817, DOI: 10.1109/led.2019.2908426.
(125) Son, M.; Jang, J.; Lee, Y.; Nam, J.; Hwang, J. Y.; Kim, I. S.; Lee, B. H.; Ham, M.-H.; Chee, S.-S. Copper-Graphene Heterostructure for Back-End-of-Line Compatible High-Performance Interconnects. *npj 2D Materials and Applications* **2021,** *5* (1), 41, DOI: 10.1038/s41699-021-00216-1.
(126) Jang, J.; Son, M.; Chung, S.; Kim, K.; Cho, C.; Lee, B. H.; Ham, M.-H. Low-Temperature-Grown Continuous Graphene Films from Benzene by Chemical Vapor Deposition at Ambient Pressure. *Scientific Reports* **2015,** *5* (1), 17955, DOI: 10.1038/srep17955.
(127) Dresselhaus, M. S.; Jorio, A.; Souza Filho, A. G.; Saito, R. Defect Characterization in Graphene and Carbon Nanotubes using Raman Spectroscopy. *Philos Trans A Math Phys Eng Sci* **2010,** *368* (1932), 5355-77, DOI: 10.1098/rsta.2010.0213.

(128) Vlassiouk, I.; Regmi, M.; Fulvio, P.; Dai, S.; Datskos, P.; Eres, G.; Smirnov, S. Role of Hydrogen in Chemical Vapor Deposition Growth of Large Single-Crystal Graphene. *ACS Nano* **2011,** *5* (7), 6069-76, DOI: 10.1021/nn201978y.
(129) Baklanov, M. R.; Shamiryan, D. G.; Tökei, Z.; Beyer, G. P.; Conard, T.; Vanhaelemeersch, S.; Maex, K.; L., V.; Y.-C., J.; R., B. P.; S., P. Characterization of Cu Surface Cleaning by Hydrogen Plasma. *Journal of Vacuum Science & Technology B: Microelectronics and Nanometer Structures Processing, Measurement, and Phenomena* **2001,** *19* (4), 1201-1211, DOI: 10.1116/1.1387084.
(130) Wang, X.; Bleher, R.; Wang, L.; Garcia, J. G. N.; Dudek, S. M.; Shekhawat, G. S.; Dravid, V. P. Imatinib Alters Agonists-mediated Cytoskeletal Biomechanics in Lung Endothelium. *Scientific Reports* **2017,** *7* (1), 14152, DOI: 10.1038/s41598-017-14722-0.
(131) Su, H.-N.; Li, K.; Zhao, L.-S.; Yuan, X.-X.; Zhang, M.-Y.; Liu, S.-M.; Chen, X.-L.; Liu, L.-N.; Zhang, Y.-Z. Structural Visualization of Septum Formation in Staphylococcus warneri Using Atomic Force Microscopy. *Journal of Bacteriology* **2020,** *202* (19), e00294-20, DOI: 10.1128/jb.00294-20.
(132) Ferrari, A. C.; Meyer, J. C.; Scardaci, V.; Casiraghi, C.; Lazzeri, M.; Mauri, F.; Piscanec, S.; Jiang, D.; Novoselov, K. S.; Roth, S.; Geim, A. K. Raman Spectrum of Graphene and Graphene Layers. *Phys Rev Lett* **2006,** *97* (18), 187401, DOI: 10.1103/PhysRevLett.97.187401.
(133) Dimiev, A.; Kosynkin, D. V.; Sinitskii, A.; Slesarev, A.; Sun, Z.; Tour, J. M. Layer-by-Layer Removal of Graphene for Device Patterning. *Science* **2011,** *331* (6021), 1168-1172, DOI: 10.1126/science.1199183.
(134) Chang, J.-K.; Hsu, C.-C.; Liu, S.-Y.; Wu, C.-I.; Gharib, M.; Yeh, N.-C. Spectroscopic Studies of the Physical Origin of Environmental Aging Effects on Doped Graphene. *Journal of Applied Physics* **2016,** *119* (23), 235301, DOI: 10.1063/1.4953815.
(135) Li, L.; Zhu, Z.; Wang, T.; Currivan-Incorvia, J. A.; Yoon, A.; Wong, H. P. In *BEOL Compatible Graphene/Cu with Improved Electromigration Lifetime for Future Interconnects*, 2016 IEEE International Electron Devices Meeting (IEDM), 3-7 Dec. 2016; 2016; pp 9.5.1-9.5.4.
(136) Liu, W.; Li, H.; Xu, C.; Khatami, Y.; Banerjee, K. Synthesis of High-Quality Monolayer and Bilayer Graphene on Copper Using Chemical Vapor Deposition. *Carbon* **2011,** *49* (13), 4122.
(137) Ramón, M. E.; Gupta, A.; Corbet, C.; Ferrer, D. A.; Movva, H. C. P.; Carpenter, G.; Colombo, L.; Bourianoff, G.; Doczy, M.; Akinwande, D.; Tutuc, E.; Banerjee, S. K. CMOS-Compatible Synthesis of Large-Area, High-Mobility Graphene by Chemical Vapor Deposition of Acetylene on Cobalt Thin Films. *ACS Nano* **2011,** *5* (9), 7198-7204, DOI: 10.1021/nn202012m.
(138) Kang, B. J.; Mun, J. H.; Hwang, C. Y.; Cho, B. J. Monolayer Graphene Growth on Sputtered Thin Film Platinum. *Journal of Applied Physics* **2009,** *106* (10), 104309, DOI: 10.1063/1.3254193.
(139) Oznuluer, T.; Pince, E.; Polat, E. O.; Balci, O.; Salihoglu, O.; Kocabas, C. Synthesis of Graphene on Gold. *Applied Physics Letters* **2011,** *98* (18), 183101, DOI: 10.1063/1.3584006.

(140) Terasawa, T.-o.; Taira, T.; Yasuda, S.; Obata, S.; Saiki, K.; Asaoka, H. Effect of Hydrogen on Chemical Vapor Deposition Growth of Graphene on Au Substrates. *Japanese Journal of Applied Physics* **2019,** *58* (SI), SIIB17, DOI: 10.7567/1347-4065/ab19ae.
(141) Sutter, P.; Ciobanu, C. V.; Sutter, E. Real-Time Microscopy of Graphene Growth on Epitaxial Metal Films: Role of Template Thickness and Strain. *Small* **2012,** *8* (14), 2250-2257, DOI: https://doi.org/10.1002/smll.201200196.
(142) Lu, C.-H.; Leu, C.-M.; Yeh, N.-C. Single-Step Direct Growth of Graphene on Cu Ink toward Flexible Hybrid Electronic Applications by Plasma-Enhanced Chemical Vapor Deposition. *ACS Applied Materials & Interfaces* **2021,** *13* (5), 6951-6959, DOI: 10.1021/acsami.0c22207.
(143) Jeerapan, I.; Poorahong, S. Review—Flexible and Stretchable Electrochemical Sensing Systems: Materials, Energy Sources, and Integrations. *J Electrochem Soc* **2020,** *167* (3), 037573, DOI: 10.1149/1945-7111/ab7117.
(144) Li, Z.; Wang, G.; Li, Z.; Cheng, Z.; Zhou, G.; Li, S. Flexible Transparent Electrodes Based on Gold Nanomeshes. *Nanoscale Research Letters* **2019,** *14* (1), 132, DOI: 10.1186/s11671-019-2973-3.
(145) Ling, Y.; Lyu, Q.; Zhai, Q.; Zhu, B.; Gong, S.; Zhang, T.; Dyson, J.; Cheng, W. Design of Stretchable Holey Gold Biosensing Electrode for Real-Time Cell Monitoring. *ACS Sensors* **2020,** *5* (10), 3165-3171, DOI: 10.1021/acssensors.0c01297.
(146) Wang, R.; Zhai, Q.; An, T.; Gong, S.; Cheng, W. Stretchable Gold Fiber-Based Wearable Textile Electrochemical Biosensor for Lactate Monitoring in Sweat. *Talanta* **2021,** *222*, 121484, DOI: https://doi.org/10.1016/j.talanta.2020.121484.
(147) Ani, M. H.; Kamarudin, M. A.; Ramlan, A. H.; Ismail, E.; Sirat, M. S.; Mohamed, M. A.; Azam, M. A. A Critical Review on the Contributions of Chemical and Physical Factors toward the Nucleation and Growth of Large-Area Graphene. *Journal of Materials Science* **2018,** *53* (10), 7095-7111, DOI: 10.1007/s10853-018-1994-0.
(148) Vlassiouk, I.; Regmi, M.; Fulvio, P.; Dai, S.; Datskos, P.; Eres, G.; Smirnov, S. Role of Hydrogen in Chemical Vapor Deposition Growth of Large Single-Crystal Graphene. *ACS Nano* **2011,** *5* (7), 6069.
(149) Jiang, T.; Wang, Z.; Ruan, X.; Zhu, Y. Equi-Biaxial Compressive Strain in Graphene: Grüneisen Parameter and Buckling Ridges. *2D Materials* **2018,** *6* (1), DOI: 10.1088/2053-1583/aaf20a.
(150) Lu, C.-H.; Leu, C.-M.; Yeh, N.-C. Polymer-Compatible Low-Temperature Plasma-Enhanced Chemical Vapor Deposition of Graphene on Electroplated Cu for Flexible Hybrid Electronics. *ACS Applied Materials & Interfaces* **2021,** *13* (34), 41323-41329, DOI: 10.1021/acsami.1c11510.
(151) Green, T. A. Gold Etching for Microfabrication. *Gold Bulletin* **2014,** *47* (3), 205-216, DOI: 10.1007/s13404-014-0143-z.
(152) Wiltner, A.; Linsmeier, C. Formation of Endothermic Carbides on Iron and Nickel. *physica status solidi (a)* **2004,** *201* (5), 881-887, DOI: https://doi.org/10.1002/pssa.200304362.
(153) Kamachimudali, U.; Sridhar, T. M.; Raj, B. Corrosion of Bio Implants. *Sadhana* **2003,** *28* (3), 601-637, DOI: 10.1007/BF02706450.

(154) Shang, K. M.; Shen, H.; Dai, N.; Kong, D.; Hsiai, T.; Tai, Y. C. In *Micron-Sized Parylene-In-Oil Water Protection Layer*, 2023 IEEE 36th International Conference on Micro Electro Mechanical Systems (MEMS), 15-19 Jan. 2023; 2023; pp 53-56.
(155) Janting, J.; Theander, J. G.; Egesborg, H. On Thermal Acceleration of Medical Device Polymer Aging. *IEEE Transactions on Device and Materials Reliability* **2019,** *19* (2), 313-321, DOI: 10.1109/TDMR.2019.2907080.
(156) Mogi, H.; Bamba, T.; Murakami, M.; Kawashima, Y.; Yoshimura, M.; Taninaka, A.; Yoshida, S.; Takeuchi, O.; Oigawa, H.; Shigekawa, H. Ultimate High Conductivity of Multilayer Graphene Examined by Multiprobe Scanning Tunneling Potentiometry on Artificially Grown High-Quality Graphite Thin Film. *ACS Applied Electronic Materials* **2019,** *1* (9), 1762-1771, DOI: 10.1021/acsaelm.9b00298.
(157) Kim, K. S.; Zhao, Y.; Jang, H.; Lee, S. Y.; Kim, J. M.; Kim, K. S.; Ahn, J.-H.; Kim, P.; Choi, J.-Y.; Hong, B. H. Large-Scale Pattern Growth of Graphene Films for Stretchable Transparent Electrodes. *Nature* **2009,** *457* (7230), 706-710, DOI: 10.1038/nature07719.
(158) Li, X.; Cai, W.; An, J.; Kim, S.; Nah, J.; Yang, D.; Piner, R.; Velamakanni, A.; Jung, I.; Tutuc, E.; Banerjee, S. K.; Colombo, L.; Ruoff, R. S. Large-Area Synthesis of High-Quality and Uniform Graphene Films on Copper Foils. *Science* **2009,** *324* (5932), 1312-1314, DOI: doi:10.1126/science.1171245.
(159) Ayhan, M. E.; Kalita, G.; Sharma, S.; Tanemura, M. Chemical Vapor Deposition of Graphene on Silver Foil as a Tarnish-Resistant Coating. *physica status solidi (RRL) - Rapid Research Letters* **2013,** *7* (12), 1076-1079, DOI: 10.1002/pssr.201308159.
(160) Kim, J.; Sakakita, H.; Itagaki, H. Low-Temperature Graphene Growth by Forced Convection of Plasma-Excited Radicals. *Nano Letters* **2019,** *19* (2), 739-746, DOI: 10.1021/acs.nanolett.8b03769.
(161) Lu, C.-H.; Leu, C.-M.; Yeh, N.-C. Polymer-Compatible Low-Temperature Plasma-Enhanced Chemical Vapor Deposition of Graphene on Electroplated Cu for Flexible Hybrid Electronics. *ACS Applied Materials & Interfaces* **2021**, DOI: 10.1021/acsami.1c11510.
(162) Lu, C.-H.; Leu, C.-M.; Lee, T.-M.; Yeh, N.-C. P-60: Single-Step Plasma-Enhanced Chemical Vapor Deposition of Graphene on Cu Ink and Sputtered Cu Thin Films. *SID Symposium Digest of Technical Papers* **2020,** *51* (1), 1565-1568, DOI: https://doi.org/10.1002/sdtp.14190.
(163) Lu, C.-H.; Shang, K.-M.; Lee, S.-R.; Tai, Y.-C.; Yeh, N.-C. Graphene on Nanoscale-Thick Au Films: Implications for Anticorrosion in Smart Wearable Electronics. *ACS Applied Nano Materials* **2022,** *5* (3), 4343-4349, DOI: 10.1021/acsanm.2c00401.
(164) Kiraly, B.; Iski, E. V.; Mannix, A. J.; Fisher, B. L.; Hersam, M. C.; Guisinger, N. P. Solid-Source Growth and Atomic-Scale Characterization of Graphene on Ag(111). *Nature Communications* **2013,** *4* (1), DOI: 10.1038/ncomms3804.
(165) Batzill, M. The Surface Science of Graphene: Metal Interfaces, CVD Synthesis, Nanoribbons, Chemical Modifications, and Defects. *Surface Science Reports* **2012,** *67* (3-4), 83-115, DOI: 10.1016/j.surfrep.2011.12.001.
(166) Ferrari, A. C.; Basko, D. M. Raman Spectroscopy as a Versatile Tool for Studying the Properties of Graphene. *Nat Nanotechnol* **2013,** *8* (4), 235-46, DOI: 10.1038/nnano.2013.46.
(167) Wu, J.-B.; Lin, M.-L.; Cong, X.; Liu, H.-N.; Tan, P.-H. Raman Spectroscopy of Graphene-Based Materials and Its Applications in Related Devices. *Chemical Society Reviews* **2018,** *47* (5), 1822-1873, DOI: 10.1039/C6CS00915H.

(168) Eckmann, A.; Felten, A.; Verzhbitskiy, I.; Davey, R.; Casiraghi, C. Raman Study on Defective Graphene: Effect of the Excitation Energy, Type, and Amount of Defects. *Physical Review B* **2013,** *88* (3), DOI: 10.1103/PhysRevB.88.035426.
(169) Malard, L. M.; Pimenta, M. A.; Dresselhaus, G.; Dresselhaus, M. S. Raman Spectroscopy in Graphene. *Physics Reports* **2009,** *473* (5-6), 51-87, DOI: 10.1016/j.physrep.2009.02.003.
(170) Lee, S.; Lee, K.; Zhong, Z. Wafer Scale Homogeneous Bilayer Graphene Films by Chemical Vapor Deposition. *Nano Lett.* **2010,** *10* (11), 4702.
(171) Lee, J. E.; Ahn, G.; Shim, J.; Lee, Y. S.; Ryu, S. Optical Separation of Mechanical Strain from Charge Doping in Graphene. *Nat Commun* **2012,** *3*, 1024, DOI: 10.1038/ncomms2022.
(172) Li, N.; Zhen, Z.; Zhang, R.; Xu, Z.; Zheng, Z.; He, L. Nucleation and Growth Dynamics of Graphene Grown by Radio Frequency Plasma-Enhanced Chemical Vapor Deposition. *Sci Rep* **2021,** *11* (1), 6007, DOI: 10.1038/s41598-021-85537-3.
(173) Ananthakrishnan, G.; Surana, M.; Poss, M.; Yaacoub, J. J.; Zhang, K.; Admal, N.; Pochet, P.; Tawfick, S.; Johnson, H. T. Graphene-Mediated Stabilization of Surface Facets on Metal Substrates. *Journal of Applied Physics* **2021,** *130* (16), DOI: 10.1063/5.0065107.
(174) Abd El-Fattah, Z. M.; Mkhitaryan, V.; Brede, J.; Fernández, L.; Li, C.; Guo, Q.; Ghosh, A.; Echarri, A. R.; Naveh, D.; Xia, F.; Ortega, J. E.; García de Abajo, F. J. Plasmonics in Atomically Thin Crystalline Silver Films. *ACS Nano* **2019,** *13* (7), 7771-7779, DOI: 10.1021/acsnano.9b01651.
(175) Toropov, N. A.; Leonov, N. B.; Vartanyan, T. A. Influence of Silver Nanoparticles Crystallinity on Localized Surface Plasmons Dephasing Times. *physica status solidi (b)* **2018,** *255* (3), 1700174, DOI: https://doi.org/10.1002/pssb.201700174.
(176) Kaciulis, S.; Mezzi, A.; Calvani, P.; Trucchi, D. M. Electron Spectroscopy of the Main Allotropes of Carbon. *Surface and Interface Analysis* **2014,** *46* (10-11), 966-969, DOI: https://doi.org/10.1002/sia.5382.
(177) Hill, J. M.; Royce, D. G.; Fadley, C. S.; Wagner, L. F.; Grunthaner, F. J. Properties of Oxidized Silicon as Determined by Angular-Dependent X-ray Photoelectron Spectroscopy. *Chem Phys Lett* **1976,** *44* (2), 225-231, DOI: https://doi.org/10.1016/0009-2614(76)80496-4.
(178) Cumpson, P. J. The Thickogram: A Method for Easy Film Thickness Measurement in XPS. *Surface and Interface Analysis* **2000,** *29* (6), 403-406, DOI: https://doi.org/10.1002/1096-9918(200006)29:6<403::AID-SIA884>3.0.CO;2-8.
(179) Wu, P.; Zhai, X.; Li, Z.; Yang, J. Bilayer Graphene Growth via a Penetration Mechanism. *The Journal of Physical Chemistry C* **2014,** *118* (12), 6201-6206, DOI: 10.1021/jp4108156.
(180) Choi, K.; Nam, S.; Lee, Y.; Lee, M.; Jang, J.; Kim, S. J.; Jeong, Y. J.; Kim, H.; Bae, S.; Yoo, J.-B.; Cho, S. M.; Choi, J.-B.; Chung, H. K.; Ahn, J.-H.; Park, C. E.; Hong, B. H. Reduced Water Vapor Transmission Rate of Graphene Gas Barrier Films for Flexible Organic Field-Effect Transistors. *ACS Nano* **2015,** *9* (6), 5818-5824, DOI: 10.1021/acsnano.5b01161.
(181) Lu, C.-H.; Shang, K.-M.; Lee, S.-R.; Leu, C.-M.; Tai, Y.-C.; Yeh, N.-C. Low-Temperature Direct Growth of Nanocrystalline Multilayer Graphene on Silver with Long-

Term Surface Passivation. *ACS Applied Materials & Interfaces* **2023,** *15* (7), 9883-9891, DOI: 10.1021/acsami.2c21809.
(182) Assegie, A. A.; Chung, C.-C.; Tsai, M.-C.; Su, W.-N.; Chen, C.-W.; Hwang, B.-J. Multilayer-Graphene-Stabilized lithium Deposition for Anode-Free Lithium-Metal Batteries. *Nanoscale* **2019,** *11* (6), 2710-2720, DOI: 10.1039/C8NR06980H.
(183) Song, G.; Fu, Q.; Pan, C. Copper-Graphene Composite Foils via Electro-Deposition: A Mini Review. *MRS Advances* **2018,** *3* (1), 37-44, DOI: 10.1557/adv.2018.28.
(184) Novoselov, K. S.; Geim, A. K.; Morozov, S. V.; Jiang, D.; Katsnelson, M. I.; Grigorieva, I. V.; Dubonos, S. V.; Firsov, A. A. Two-Dimensional Gas of Massless Dirac Fermions in Graphene. *Nature* **2005,** *438* (7065), 197-200, DOI: 10.1038/nature04233.
(185) Walter, A. L.; Nie, S.; Bostwick, A.; Kim, K. S.; Moreschini, L.; Chang, Y. J.; Innocenti, D.; Horn, K.; McCarty, K. F.; Rotenberg, E. Electronic Structure of Graphene on Single-Crystal Copper Substrates. *Physical Review B* **2011,** *84* (19), 195443, DOI: 10.1103/PhysRevB.84.195443.
(186) Frank, O.; Vejpravova, J.; Holy, V.; Kavan, L.; Kalbac, M. Interaction Between Graphene and Copper Substrate: The Role of Lattice Orientation. *Carbon* **2014,** *68*, 440-451, DOI: https://doi.org/10.1016/j.carbon.2013.11.020.
(187) Lee, U.; Han, Y.; Lee, S.; Kim, J. S.; Lee, Y. H.; Kim, U. J.; Son, H. Time Evolution Studies on Strain and Doping of Graphene Grown on a Copper Substrate Using Raman Spectroscopy. *ACS Nano* **2020,** *14* (1), 919-926, DOI: 10.1021/acsnano.9b08205.
(188) Jeon, I.; Yang, H.; Lee, S.-H.; Heo, J.; Seo, D. H.; Shin, J.; Chung, U. I.; Kim, Z. G.; Chung, H.-J.; Seo, S. Passivation of Metal Surface States: Microscopic Origin for Uniform Monolayer Graphene by Low Temperature Chemical Vapor Deposition. *ACS Nano* **2011,** *5* (3), 1915-1920, DOI: 10.1021/nn102916c.
(189) Huang, L.; Zhang, D.; Zhang, F.-H.; Feng, Z.-H.; Huang, Y.-D.; Gan, Y. High-Contrast SEM Imaging of Supported Few-Layer Graphene for Differentiating Distinct Layers and Resolving Fine Features: There is Plenty of Room at the Bottom. *Small* **2018,** *14* (22), 1704190, DOI: https://doi.org/10.1002/smll.201704190.
(190) Humphreys, J.; Rohrer, G. S.; Rollett, A. Chapter 5 - Mobility and Migration of Boundaries. In *Recrystallization and Related Annealing Phenomena (Third Edition)*; Humphreys, J.; Rohrer, G. S.; Rollett, A., Eds.; Elsevier: Oxford, 2017; pp 145-197.
(191) Hu, C. K.; Lee, K. L.; Gupta, D.; Blauner, P. Electromigration and Diffusion in Pure Cu and Cu(Sn) Alloys. *MRS Online Proceedings Library* **1996,** *427* (1), 95-106, DOI: 10.1557/PROC-427-95.
(192) Liu, H.; Liu, Y. Controlled Chemical Synthesis in CVD Graphene. *Physical Sciences Reviews* **2017,** *2* (4), DOI: doi:10.1515/psr-2016-0107.
(193) Wood, J. D.; Schmucker, S. W.; Lyons, A. S.; Pop, E.; Lyding, J. W. Effects of Polycrystalline Cu Substrate on Graphene Growth by Chemical Vapor Deposition. *Nano Lett* **2011,** *11* (11), 4547-54, DOI: 10.1021/nl201566c.
(194) Mikolajick, T.; Slesazeck, S.; Park, M. H.; Schroeder, U. Ferroelectric Hafnium Oxide for Ferroelectric Random-Access Memories and Ferroelectric Field-Effect Transistors. *MRS Bulletin* **2018,** *43* (5), 340-346, DOI: 10.1557/mrs.2018.92.
(195) Kohlstedt, H.; Mustafa, Y.; Gerber, A.; Petraru, A.; Fitsilis, M.; Meyer, R.; Böttger, U.; Waser, R. Current Status and Challenges of Ferroelectric Memory Devices.

Microelectronic Engineering **2005,** *80*, 296-304, DOI: https://doi.org/10.1016/j.mee.2005.04.084.
(196) Salahuddin, S.; Datta, S. Use of Negative Capacitance to Provide Voltage Amplification for Low Power Nanoscale Devices. *Nano Letters* **2008,** *8* (2), 405-410, DOI: 10.1021/nl071804g.
(197) Cheng, P.-H.; Yin, Y.-T.; Tsai, I. N.; Lu, C.-H.; Li, L.-J.; Pan, S. C.; Shieh, J.; Shiojiri, M.; Chen, M.-J. Negative Capacitance from the Inductance of Ferroelectric Switching. *Communications Physics* **2019,** *2* (1), 32, DOI: 10.1038/s42005-019-0120-1.
(198) Jiang, Y.-S.; Jeng, Y.-E.; Yin, Y.-T.; Huang, K.-W.; Chang, T.-J.; Wang, C.-I.; Chao, Y.-T.; Wu, C.-H.; Chen, M.-J. Operation Bandwidth of Negative Capacitance Characterized by the Frequency Response of Capacitance Magnification in Ferroelectric/Dielectric Stacks. *Journal of Materials Chemistry C* **2021,** *9* (4), 1401-1409, DOI: 10.1039/D0TC04025H.
(199) Mulaosmanovic, H.; Ocker, J.; Müller, S.; Noack, M.; Müller, J.; Polakowski, P.; Mikolajick, T.; Slesazeck, S. In *Novel ferroelectric FET based synapse for neuromorphic systems*, 2017 Symposium on VLSI Technology, 5-8 June 2017; 2017; pp T176-T177.
(200) Dawber, M.; Rabe, K. M.; Scott, J. F. Physics of Thin-Film Ferroelectric Oxides. *Rev Mod Phys* **2005,** *77* (4), 1083-1130, DOI: DOI 10.1103/RevModPhys.77.1083.
(201) Fong, D. D.; Stephenson, G. B.; Streiffer, S. K.; Eastman, J. A.; Auciello, O.; Fuoss, P. H.; Thompson, C. Ferroelectricity in Ultrathin Perovskite Films. *Science* **2004,** *304* (5677), 1650-1653, DOI: doi:10.1126/science.1098252.
(202) Fridkin, V.; Ducharme, S. Ferroelectricity and Ferroelectric Phase Transition. In *Ferroelectricity at the Nanoscale*; 2014; Chapter 1, pp 1-9.
(203) Polakowski, P.; Müller, J. Ferroelectricity in Undoped Hafnium Oxide. *Applied Phyics Letters* **2014,** *106*, 232905.
(204) Lin, B. T.; Lu, Y. W.; Shieh, J.; Chen, M. J. Induction of Ferroelectricity in Nanoscale ZrO2 Thin Films on Pt Electrode without Post-Annealing. *Journal of the European Ceramic Society* **2017,** *37* (3), 1135-1139, DOI: 10.1016/j.jeurceramsoc.2016.10.028.
(205) Müller, J.; Böscke, T. S.; Schröder, U.; Mueller, S.; Bräuhaus, D.; Böttger, U.; Frey, L.; Mikolajick, T. Ferroelectricity in Simple Binary ZrO2 and HfO2. *Nano Letters* **2012,** *12* (8), 4318-4323, DOI: 10.1021/nl302049k.
(206) Cheema, S. S.; Kwon, D.; Shanker, N.; dos Reis, R.; Hsu, S.-L.; Xiao, J.; Zhang, H.; Wagner, R.; Datar, A.; McCarter, M. R.; Serrao, C. R.; Yadav, A. K.; Karbasian, G.; Hsu, C.-H.; Tan, A. J.; Wang, L.-C.; Thakare, V.; Zhang, X.; Mehta, A.; Karapetrova, E.; Chopdekar, R. V.; Shafer, P.; Arenholz, E.; Hu, C.; Proksch, R.; Ramesh, R.; Ciston, J.; Salahuddin, S. Enhanced Ferroelectricity in Ultrathin Films Grown Directly on Silicon. *Nature* **2020,** *580* (7804), 478-482, DOI: 10.1038/s41586-020-2208-x.
(207) Salahuddin, S.; Ni, K.; Datta, S. The Era of Hyper-Scaling in Electronics. *Nature Electronics* **2018,** *1* (8), 442-450, DOI: 10.1038/s41928-018-0117-x.
(208) Shirodkar, S. N.; Waghmare, U. V. Emergence of Ferroelectricity at a Metal-Semiconductor Transition in a 1T Monolayer of MoS2. *Physical Review Letters* **2014,** *112* (15), 157601, DOI: 10.1103/PhysRevLett.112.157601.
(209) Lipatov, A.; Chaudhary, P.; Guan, Z.; Lu, H.; Li, G.; Crégut, O.; Dorkenoo, K. D.; Proksch, R.; Cherifi-Hertel, S.; Shao, D.-F.; Tsymbal, E. Y.; Íñiguez, J.; Sinitskii, A.; Gruverman, A. Direct Observation of Ferroelectricity in Two-Dimensional MoS2. *npj 2D Materials and Applications* **2022,** *6* (1), 18, DOI: 10.1038/s41699-022-00298-5.

(210) Gong, Y.; Ye, G.; Lei, S.; Shi, G.; He, Y.; Lin, J.; Zhang, X.; Vajtai, R.; Pantelides, S. T.; Zhou, W.; Li, B.; Ajayan, P. M. Synthesis of Millimeter-Scale Transition Metal Dichalcogenides Single Crystals. *Advanced Functional Materials* **2016,** *26* (12), 2009-2015, DOI: https://doi.org/10.1002/adfm.201504633.
(211) Mattinen, M.; Gity, F.; Coleman, E.; Vonk, J. F. A.; Verheijen, M. A.; Duffy, R.; Kessels, W. M. M.; Bol, A. A. Atomic Layer Deposition of Large-Area Polycrystalline Transition Metal Dichalcogenides from 100 °C through Control of Plasma Chemistry. *Chemistry of Materials* **2022,** *34* (16), 7280-7292, DOI: 10.1021/acs.chemmater.2c01154.
(212) Batude, P.; Brunet, L.; Fenouillet-Beranger, C.; Andrieu, F.; Colinge, J. P.; Lattard, D.; Vianello, E.; Thuries, S.; Billoint, O.; Vivet, P.; Santos, C.; Mathieu, B.; Sklenard, B.; Lu, C. M. V.; Micout, J.; Deprat, F.; Mercado, E. A.; Ponthenier, F.; Rambal, N.; Samson, M. P.; Cassé, M.; Hentz, S.; Arcamone, J.; Sicard, G.; Hutin, L.; Pasini, L.; Ayres, A.; Rozeau, O.; Berthelon, R.; Nemouchi, F.; Rodriguez, P.; Pin, J. B.; Larmagnac, D.; Duboust, A.; Ripoche, V.; Barraud, S.; Allouti, N.; Barnola, S.; Vizioz, C.; Hartmann, J. M.; Kerdiles, S.; Alba, P. A.; Beaurepaire, S.; Beugin, V.; Fournel, F.; Besson, P.; Loup, V.; Gassilloud, R.; Martin, F.; Garros, X.; Mazen, F.; Previtali, B.; Euvrard-Colnat, C.; Balan, V.; Comboroure, C.; Zussy, M.; Mazzocchi; Faynot, O.; Vinet, M. In *3D Sequential Integration: Application-driven technological achievements and guidelines*, 2017 IEEE International Electron Devices Meeting (IEDM), 2-6 Dec. 2017; 2017; pp 3.1.1-3.1.4.
(213) Wang, S.; Rong, Y.; Fan, Y.; Pacios, M.; Bhaskaran, H.; He, K.; Warner, J. H. Shape Evolution of Monolayer MoS2 Crystals Grown by Chemical Vapor Deposition. *Chemistry of Materials* **2014,** *26* (22), 6371-6379, DOI: 10.1021/cm5025662.
(214) Park, J.-H.; Lu, A.-Y.; Shen, P.-C.; Shin, B. G.; Wang, H.; Mao, N.; Xu, R.; Jung, S. J.; Ham, D.; Kern, K.; Han, Y.; Kong, J. Synthesis of High-Performance Monolayer Molybdenum Disulfide at Low Temperature. *Small Methods* **2021,** *5* (6), 2000720, DOI: https://doi.org/10.1002/smtd.202000720.
(215) Wang, S.; Pacios, M.; Bhaskaran, H.; Warner, J. H. Substrate Control for Large Area Continuous Films of Monolayer MoS2 by Atmospheric Pressure Chemical Vapor Deposition. *Nanotechnology* **2016,** *27* (8), 085604, DOI: 10.1088/0957-4484/27/8/085604.
(216) Kang, T.; Tang, T. W.; Pan, B.; Liu, H.; Zhang, K.; Luo, Z. Strategies for Controlled Growth of Transition Metal Dichalcogenides by Chemical Vapor Deposition for Integrated Electronics. *ACS Materials Au* **2022,** *2* (6), 665-685, DOI: 10.1021/acsmaterialsau.2c00029.
(217) Kim, H.; Ahn, C.; Arabale, G.; Lee, C.; Kim, T. Synthesis of MoS2 Atomic Layer using PECVD. *Ecs Transactions* **2013,** *58* (8), 47, DOI: 10.1149/05808.0047ecst.
(218) Beaudette, C. A.; Held, J. T.; Mkhoyan, K. A.; Kortshagen, U. R. Nonthermal Plasma-Enhanced Chemical Vapor Deposition of Two-Dimensional Molybdenum Disulfide. *ACS Omega* **2020,** *5* (34), 21853-21861, DOI: 10.1021/acsomega.0c02947.
(219) Johnson, R. W.; Hultqvist, A.; Bent, S. F. A Brief Review of Atomic Layer Deposition: From Fundamentals to Applications. *Materials Today* **2014,** *17* (5), 236-246, DOI: 10.1016/j.mattod.2014.04.026.
(220) Jurca, T.; Moody, M. J.; Henning, A.; Emery, J. D.; Wang, B.; Tan, J. M.; Lohr, T. L.; Lauhon, L. J.; Marks, T. J. Low-Temperature Atomic Layer Deposition of MoS2 Films. *Angewandte Chemie International Edition* **2017,** *56* (18), 4991-4995, DOI: https://doi.org/10.1002/anie.201611838.

(221) Sharma, A.; Verheijen, M. A.; Wu, L.; Karwal, S.; Vandalon, V.; Knoops, H. C. M.; Sundaram, R. S.; Hofmann, J. P.; Kessels, W. M. M.; Bol, A. A. Low-Temperature Plasma-Enhanced Atomic Layer Deposition of 2-D MoS2: Large Area, Thickness Control and Tuneable Morphology. *Nanoscale* **2018,** *10* (18), 8615-8627, DOI: 10.1039/C8NR02339E.
(222) Panchal, V.; Pearce, R.; Yakimova, R.; Tzalenchuk, A.; Kazakova, O. Standardization of Surface Potential Measurements of Graphene Domains. *Scientific Reports* **2013,** *3* (1), 2597, DOI: 10.1038/srep02597.
(223) Ma, X. Y. Study of the Electrical Properties of Monolayer MoS2 Semiconductor. *Advanced Materials Research* **2013,** *651*, 193-197, DOI: 10.4028/www.scientific.net/AMR.651.193.
(224) Kadantsev, E. S.; Hawrylak, P. Electronic Structure of a Single MoS2 Monolayer. *Solid State Commun* **2012,** *152* (10), 909-913, DOI: https://doi.org/10.1016/j.ssc.2012.02.005.
(225) Yu, S.; Xiong, H. D.; Eshun, K.; Yuan, H.; Li, Q. Phase Transition, Effective Mass and Carrier Mobility of MoS2 Monolayer under Tensile Strain. *Applied Surface Science* **2015,** *325*, 27-32, DOI: https://doi.org/10.1016/j.apsusc.2014.11.079.
(226) Phuc, H. V.; Hieu, N. N.; Hoi, B. D.; Hieu, N. V.; Thu, T. V.; Hung, N. M.; Ilyasov, V. V.; Poklonski, N. A.; Nguyen, C. V. Tuning the Electronic Properties, Effective Mass and Carrier Mobility of MoS2 Monolayer by Strain Engineering: First-Principle Calculations. *Journal of Electronic Materials* **2018,** *47* (1), 730-736, DOI: 10.1007/s11664-017-5843-8.